

The Pennsylvania State University
The Graduate School
Department of Aerospace Engineering

**IN-FLIGHT PERFORMANCE OPTIMIZATION FOR ROTORCRAFT WITH
REDUNDANT CONTROLS**

A Dissertation in
Aerospace Engineering
by
Gurbuz Taha Ozdemir

© 2013 Gurbuz Taha Ozdemir

Submitted in Partial Fulfillment
of the Requirements
for the Degree of

Doctor of Philosophy

December 2013

The dissertation of Gurbuz Taha Ozdemir was reviewed and approved* by the following:

Joseph F. Horn
Associate Professor of Aerospace Engineering
Dissertation Advisor
Chair of Committee

Edward C. Smith
Professor of Aerospace Engineering

Kenneth S. Brentner
Professor of Aerospace Engineering

Christopher Rahn
Professor of Mechanical Engineering

Farhan Gandhi
Rosalind and John J. Redfern Jr. Chair in Engineering at Rensselaer Polytechnic Institute
Special Member

David B. Spencer
Professor of Aerospace Engineering
Director of Graduate Studies of the Department of Aerospace Engineering

*Signatures are on file in the Graduate School

ABSTRACT

A conventional helicopter has limits on performance at high speeds because of the limitations of main rotor, such as compressibility issues on advancing side or stall issues on retreating side. Auxiliary lift and thrust components have been suggested to improve performance of the helicopter substantially by reducing the loading on the main rotor. Such a configuration is called the compound rotorcraft. Rotor speed can also be varied to improve helicopter performance. In addition to improved performance, compound rotorcraft and variable RPM can provide a much larger degree of control redundancy. This additional redundancy gives the opportunity to further enhance performance and handling qualities.

A flight control system is designed to perform in-flight optimization of redundant control effectors on a compound rotorcraft in order to minimize power required and extend range. This “Fly to Optimal” (FTO) control law is tested in simulation using the GENHEL model. A model of the UH-60, a compound version of the UH-60A with lifting wing and vectored thrust ducted propeller (VTDP), and a generic compound version of the UH-60A with lifting wing and propeller were developed and tested in simulation. A model following dynamic inversion controller is implemented for inner loop control of roll, pitch, yaw, heave, and rotor RPM. An outer loop controller regulates airspeed and flight path during optimization.

A Golden Section search method was used to find optimal rotor RPM on a conventional helicopter, where the single redundant control effector is rotor RPM. The FTO builds off of the Adaptive Performance Optimization (APO) method of Gilyard by performing low frequency sweeps on a redundant control for a fixed wing aircraft. A method based on the APO method was used to optimize trim on a compound rotorcraft with several redundant control effectors. The controller can be used to optimize rotor RPM and compound control effectors through flight test or simulations in order to establish a schedule. The method has been expanded to search a two-dimensional control space. Simulation results demonstrate the ability to maximize range by

optimizing stabilator deflection and an airspeed set point. Another set of results minimize power required in high speed flight by optimizing collective pitch and stabilator deflection. Results show that the control laws effectively hold the flight condition while the FTO method is effective at improving performance. Optimizations show there can be issues when the control laws regulating altitude push the collective control towards its limits. So a modification was made to the control law to regulate airspeed and altitude using propeller pitch and angle of attack while the collective is held fixed or used as an optimization variable. A dynamic trim limit avoidance algorithm is applied to avoid control saturation in other axes during optimization maneuvers.

Range and power optimization FTO simulations are compared with comprehensive sweeps of trim solutions and FTO optimization shown to be effective and reliable in reaching an optimal when optimizing up to two redundant controls. Use of redundant controls is shown to be beneficial for improving performance.

The search method takes almost 25 minutes of simulated flight for optimization to be complete. The optimization maneuver itself can sometimes drive the power required to high values, so a power limit is imposed to restrict the search to avoid conditions where power is more than 5% higher than that of the initial trim state. With this modification, the time the optimization maneuver takes to complete is reduced down to 21 minutes without any significant change in the optimal power value.

TABLE OF CONTENTS

LIST OF FIGURES	vii
LIST OF TABLES	xiv
LIST OF SYMBOLS	xvi
ACKNOWLEDGEMENTS	xix
Chapter 1 Introduction	1
1.1 Background	1
1.2 Literature Review	2
1.2.1 Conventional Helicopter and Limitations	3
1.2.2 Compound Rotorcraft	6
1.2.2.1 Lift Compounding	7
1.2.2.2 Thrust Compounding	8
1.2.2.3 Full Compounding	10
1.2.3 Variable Rotor Speed	14
1.2.4 Trim Optimization	15
1.2.5 Optimization Methods	15
1.3 Research Objectives	18
Chapter 2 Aircraft Dynamic Model	21
2.1 GENHEL Model Background	21
2.1.1 Modifications on GENHEL-PSU for Variable Rotor Speed	24
2.1.2 Modifications on GENHEL-PSU for Compound Helicopter Model	24
2.1.3 Recent Modifications on GENHEL-PSU	28
2.2 Vehicle Properties	28
2.3.1 Wing Model – Lift Compounding	31
2.3.2 Propeller Model – Thrust Compounding	33
2.3 Basic Theory on Trim	36
2.3.1 Force and Moment Equilibrium	36
2.3.1.1 Main Rotor	40
2.3.1.2 Tail Rotor	41
2.3.1.3 Fuselage	41
2.3.1.4 Propeller	42
2.3.1.5 Wings	43
2.3.1.6 Horizontal/Vertical Tail	43
2.3.2 Change in Trim with Redundant Controls	44
2.3.3 Trim Analysis with the Nonlinear Simulation	51
Chapter 3 Integrated Flight Control System Design	55
3.1 Control System Design	56
3.1.1 Inner Loop Control Law	59

3.1.2 Outer Loop Control Law	69
3.1.2.1 Low Speed Mode – Translational Rate Command Control Law	70
3.1.2.2 Cruise Speed Mode Control Law	71
3.1.2.3 High-Speed Mode Control Law	72
3.2 Control System Evaluation with Nonlinear Simulation	75
3.2.1 Longitudinal Axis Evaluation	75
3.2.2 Lateral Axis Evaluation.....	78
3.2.3 Heave Axis Evaluation.....	84
Chapter 4 In-Flight Optimization Algorithm	88
4.1 Optimization Method Study	88
4.1.1 Steepest Descent Method	89
4.1.2 Golden Section Method.....	89
4.1.3 Adaptive Performance Optimization.....	91
4.2 Fly-to-Optimal Controller Design.....	92
4.3 Nonlinear Simulation Results	96
4.3.1 Single Parameter Optimization using Golden Section Method.....	96
4.3.2 Single Parameter Optimization of Multiple Control Effectors using Adaptive Performance Optimization Method.....	100
4.3.3 Multiple Parameter Optimization of Multiple Control Effectors Using Adaptive Performance Optimization Method.....	111
4.3.3.1 Maximum Range Optimization	113
4.3.3.2 Minimum Power Optimization.....	118
Chapter 5 Conclusion and Future Work	138
5.1 Conclusion	138
5.2 Future Work	140
Appendix A Figures for Lift, Drag and Moment Coefficients of the Fuselage	142
Appendix B Figures for Lift and Drag Coefficients of the Horizontal and Vertical Tails	158
Appendix C Lift, Drag and Pitching Moment Coefficients of the Wing	166
Appendix D Calculations of Thrust and Power Coefficients of the Propeller	181
References.....	183

LIST OF FIGURES

Figure 1-1: The Effect of Forward Flight Velocity on a Helicopter Main Rotor [6].....	5
Figure 1-2: Rotary-Wing Flight Aerodynamics [15].....	6
Figure 1-3: Sikorsky XH-59A [38].....	10
Figure 1-4: Sikorsky X2 Technology™ Demonstrator [38].....	10
Figure 1-5: Eurocopter’s X3 [42].	11
Figure 1-6: Tip Path Plane Attitudes over the Speed Range [29].....	13
Figure 1-7: Body and Wing Pitch Attitudes over the Speed Range [29].....	13
Figure 1-8: Aircraft Response to Forced-Excitation Maneuver during APO Flight Test [57].....	17
Figure 1-9: Variation of Incremental Drag with Symmetric Aileron Deflection [57].....	18
Figure 2-1: Structure of GENHEL [62].....	22
Figure 2-2: The VLRCOE Rotorcraft Simulation Facility	22
Figure 2-3: The UH-60L/VTDP Aircraft Model	25
Figure 2-4: Piasecki X-49A SpeedHawk VTDP Technology Demonstrator	25
Figure 2-5: Structure of Compound-Modified GENHEL [62].....	26
Figure 2-6: The Generic Compound Rotorcraft Configuration	27
Figure 2-7: Structure of Generic Compound Rotorcraft –Modified GENHEL [62]	27
Figure 2-8: Propeller Efficiency Map.....	35
Figure 2-9: Propeller Thrust Map and Propeller Pitch Schedule with Airspeed	35
Figure 2-10: Free Body Diagram of The Generic Compound Rotorcraft Configuration- Top View.....	38
Figure 2-11: Free Body Diagram of The Generic Compound Rotorcraft Configuration- Side View	39
Figure 2-12: Free Body Diagram of The Generic Compound Rotorcraft Configuration- Rear View	39

Figure 2.13: The Main Rotor Forces and Moments.....	40
Figure 2.14: The Fuselage Forces and Moments.....	42
Figure 2-15: Acceleration in a Baseline Helicopter Configuration	46
Figure 2-16: Acceleration in a Compound Helicopter Configuration	48
Figure 2-17: Rotor Lift Response Derivative for Collective Pitch [70]	50
Figure 2-18: Rotor Lift Response Derivative for Collective Pitch of the Generic Compound Rotorcraft Model	51
Figure 2-19: Propulsive Forces at Different Propeller Pitch Angles at 160 kts Level Flight ..	52
Figure 2-20: Pitch Attitude and TPP Deflection at Different Propeller Pitch Angles	53
Figure 2-21: Lift Forces at Different Propeller Pitch Angles at 160 kts Level Flight	53
Figure 2-22: Collective Pitch at Blade Root with Different Propeller Pitch Angles at 160 kts Level Flight	54
Figure 3-1: General Layout of the Integrated Flight Control System for Low Speed Flight ..	57
Figure 3-2: General Layout of the Integrated Flight Control System for Cruise Speed Flight	57
Figure 3-3: General Layout of the Integrated Flight Control System for High Speed Flight	58
Figure 3-4: Model Following and Dynamic Inversion Control for ACAH	60
Figure 3-5: Model Following and Dynamic Inversion Control for RCAH	60
Figure 3.6: Dynamic Inversion Control Scheme for Roll, Pitch and Rotor Speed Axes.....	68
Figure 3.7: Dynamic Inversion Control Scheme for Yaw and Heave Axes	69
Figure 3-8: Model Following and Model Inversion Control for Translational Rate Command Controller – Low Speed Mode	71
Figure 3-9: Model Following and Model Inversion Control for Airspeed Axis of High- Speed Mode Outer Loop Controller.....	74
Figure 3-10: Model Following and Model Inversion Control for Heave Axis of High Speed Mode Outer Loop Controller.....	74
Figure 3-11: GENHEL-PSU Simulation at Nominal RPM, V=20 kts, Airspeed Command = 15 knots.....	76

Figure 3-12: GENHEL-PSU Simulation at Nominal RPM, V=100 kts, Airspeed Command = 15 knots	77
Figure 3-13: GENHEL-PSU Simulation at 80% of Nominal RPM, V=200 kts, Airspeed Command = 5 knots	78
Figure 3-14: GENHEL-PSU Simulation at Nominal RPM, V=20 kts, Lateral Velocity Doublet = ± 9 knots.....	79
Figure 3-15: GENHEL-PSU Simulation at Nominal RPM, V=20 kts, Lateral Velocity Doublet = ± 18 knots.....	80
Figure 3-16: GENHEL-PSU Simulation at Nominal RPM, V=100 kts, Roll Command= ± 18 degrees	81
Figure 3-17: GENHEL-PSU Simulation at Nominal RPM, V=100 kts, Roll Command= ± 30 degrees	82
Figure 3-18: GENHEL-PSU Simulation at Nominal RPM, V=200 kts, Roll Command= ± 18 degrees	83
Figure 3-19: GENHEL-PSU Simulation at Nominal RPM, V=200 kts, Roll Command= ± 30 degrees	84
Figure 3-20: GENHEL-PSU Simulation at Nominal RPM, V=20 kts, Vertical Speed Command= 21 ft/s.....	85
Figure 3-21: GENHEL-PSU Simulation at Nominal RPM, V=100 kts, Vertical Speed Command= 21 ft/s.....	86
Figure 3-22: GENHEL-PSU Simulation at Nominal RPM, V=200 kts, Vertical Speed Command= 40 ft/s.....	87
Figure 4-1: Golden Section Method Iteration Step Diagram.....	90
Figure 4-2: Schematic of Control Margin Approach.....	95
Figure 4-3: Layout of the Fly-to-Optimal Component of the Controller.....	95
Figure 4-4: Rotor Speed Optimization at 40 knots using Golden Section Method	96
Figure 4-5: Longitudinal Response at 40 knots during Golden Section Method	97
Figure 4-6: Rotor Speed Optimization at 80 knots using Golden Section Method	97
Figure 4-7: Longitudinal Response at 80 knots during Golden Section Method	98
Figure 4-8: Rotor Speed Optimization at 120 knots using Golden Section Method	98
Figure 4-9: Longitudinal Response at 120 knots during Golden Section Method	99

Figure 4-10: Power Required for Different Airspeed using Golden Section Method for FTO	100
Figure 4-11: Adaptive Performance Optimization Results at 150 knots	103
Figure 4-12: Aircraft Response during APO at 150 knots.....	105
Figure 4-13: Adaptive Performance Optimization Results for Rotor Speed at 150 knots.....	106
Figure 4-14: Power Required vs. Rotor Speed at 150 knots during APO	106
Figure 4-15: Adaptive Performance Optimization Results for Propeller Pitch at 150 knots...	107
Figure 4-16: Power Required vs. Propeller Pitch at 150 knots during APO	107
Figure 4-17: Adaptive Performance Optimization Results for Elevator Deflection at 150 knots.....	108
Figure 4-18: Power Required vs. Elevator Deflection at 150 knots during APO.....	108
Figure 4-19: Adaptive Performance Optimization Results for Symmetric Flaperon at 150 knots.....	109
Figure 4-20: Power Required vs. Symmetric Flaperon at 150 knots during APO.....	109
Figure 4-21: Adaptive Performance Optimization Results for Differential Flaperon at 150 knots.....	110
Figure 4-22: Power Required vs. Differential Flaperon at 150 knots during APO	110
Figure 4-23: Control Stick Positions and Engine Throttle Position during APO at 150 knots.....	111
Figure 4-24: Trim Analysis for the Maximum Range Search	115
Figure 4-25: Range Optimization Maneuver starting at 120 knots.....	116
Figure 4-26: Range Optimization Maneuver starting at 100 knots.....	116
Figure 4-27: Response of the Aircraft during Range Optimization Maneuver starting at 120 knots	117
Figure 4-28: Response of the Aircraft during Range Optimization Maneuver starting at 100 knots	117
Figure 4-29: Trim Analysis for the Minimum Power Search at 180 knots with Trim Boundaries	123
Figure 4-30: Trim Analysis for the Minimum Power Search at 180 knots	124

Figure 4-31: Optimization with Collective Pitch and Stabilator Deflection for Minimum Power Required at 180 knots	124
Figure 4-32: Response of the Aircraft during Power Optimization Maneuver at 180 knots ...	125
Figure 4-33: Lift and Thrust Sharing between Main Rotor, Wing and Propeller during Power Optimization Maneuver at 180 knots.....	125
Figure 4-34: Flapping of the Rotor and Main Rotor Controls during Power Optimization Maneuver at 180 knots	126
Figure 4-35: Lift Distribution over the Main Rotor Disk before and after the Power Optimization Maneuver at 180 knots [lbs].....	126
Figure 4-36: Inflow Distribution over the Main Rotor Disk before and after the Power Optimization Maneuver at 180 knots.....	127
Figure 4-37: Trim Analysis for the Minimum Power Search at 200 knots with Trim Boundaries	127
Figure 4-38: Trim Analysis for the Minimum Power Search at 200 knots	128
Figure 4-39: Optimization with Collective Pitch and Stabilator Deflection for Minimum Power Required at 200 knots	128
Figure 4-40: Response of the Aircraft during Power Optimization Maneuver at 200 knots ...	129
Figure 4-41: Lift and Thrust Sharing between Main Rotor, Wing and Propeller during Power Optimization Maneuver at 200 knots.....	129
Figure 4-42: Flapping of the Rotor and Main Rotor Controls during Power Optimization Maneuver at 200 knots	130
Figure 4-43: Lift Distribution over the Main Rotor Disk before and after the Power Optimization Maneuver at 200 knots.....	130
Figure 4-44: Inflow Distribution over the Main Rotor Disk before and after the Power Optimization Maneuver at 200 knots	131
Figure 4-45: Optimization with Collective Pitch and Stabilator Deflection for Minimum Power Required at 180 knots with Low Power Limit.....	131
Figure 4-46: Response of the Aircraft during Power Optimization Maneuver at 180 knots with Low Power Limit	132
Figure 4-47: Lift and Thrust Sharing between Main Rotor, Wing and Propeller during Power Optimization Maneuver at 180 knots with Low Power Limit	132
Figure 4-48: Flapping of the Rotor and Main Rotor Controls during Power Optimization Maneuver at 180 knots with Low Power Limit	133

Figure 4-49: Lift Distribution over the Main Rotor Disk before and after the Power Optimization Maneuver at 180 knots with Low Power Limit [lbs]	133
Figure 4-50: Inflow Distribution over the Main Rotor Disk before and after the Power Optimization Maneuver at 180 knots with Low Power Limit	134
Figure 4-51: Optimization with Collective Pitch and Stabilator Deflection for Minimum Power Required at 200 knots with Low Power Limit.....	134
Figure 4-52: Response of the Aircraft during Power Optimization Maneuver at 200 knots with Low Power Limit	135
Figure 4-53: Lift and Thrust Sharing between Main Rotor, Wing and Propeller during Power Optimization Maneuver at 200 knots with Low Power Limit	135
Figure 4-54: Flapping of the Rotor and Main Rotor Controls during Power Optimization Maneuver at 200 knots with Low Power Limit	136
Figure 4-55: Lift Distribution over the Main Rotor Disk before and after the Power Optimization Maneuver at 200 knots with Low Power Limit [lbs]	136
Figure 4-56: Inflow Distribution over the Main Rotor Disk before and after the Power Optimization Maneuver at 200 knots with Low Power Limit	137
Figure A-1: Fuselage Drag Coefficient Due to Angle of Attack [61]	142
Figure A-2: Fuselage Drag Coefficient Due to Angle of Attack [61]	143
Figure A-3: Incremental Fuselage Drag Coefficient Due to Sideslip [61]	144
Figure A-4: Incremental Fuselage Drag Coefficient Due to Sideslip [61]	145
Figure A-5: Fuselage Sideforce Coefficient Due to Sideslip [61].....	146
Figure A-6: Fuselage Sideforce Coefficient Due to Sideslip [61].....	147
Figure A-7: Fuselage Lift Coefficient Due to Angle of Attack [61]	148
Figure A-8: Fuselage Lift Coefficient Due to Angle of Attack [61]	149
Figure A-9: Incremental Fuselage Lift Coefficient Due to Sideslip [61]	150
Figure A-10: Fuselage Rolling Moment Coefficient Due to Sideslip [61].....	151
Figure A-11: Fuselage Rolling Moment Coefficient Due to Sideslip [61].....	152
Figure A-12: Fuselage Pitching Moment Coefficient Due to Angle of Attack [61].....	153
Figure A-13: Fuselage Pitching Moment Coefficient Due to Angle of Attack [61].....	154

Figure A-14 : Incremental Fuselage Pitching Moment Coefficient Due to Sideslip [61]	155
Figure A-15 : Fuselage Yawing Moment Coefficient Due to Sideslip [61]	156
Figure A-16 : Fuselage Yawing Moment Coefficient Due to Sideslip [61]	157
Figure B-1 : Horizontal Tail Lift Coefficient Due to Angle of Attack [61]	158
Figure B-2 : Horizontal Tail Lift Coefficient Due to Angle of Attack [61]	159
Figure B-3 : Horizontal Tail Drag Coefficient Due to Angle of Attack [61]	160
Figure B-4 : Horizontal Tail Drag Coefficient Due to Angle of Attack [61]	161
Figure B-5 : Vertical Tail Lift Coefficient Due to Sideslip [61]	162
Figure B-6 : Vertical Tail Lift Coefficient Due to Sideslip [61]	163
Figure B-7 : Vertical Tail Drag Coefficient Due to Sideslip [61]	164
Figure B-8 : Vertical Tail Drag Coefficient Due to Sideslip [61]	165

LIST OF TABLES

Table 2-1: Physical Properties of the Baseline Helicopter Model	29
Table 2-2: Weight and Inertia Properties of the Baseline Helicopter Model.....	30
Table 2-3: Main Rotor Control Pitch Limits	30
Table 2-4: Weight and Inertia Properties of the Generic Compound Helicopter Model.....	31
Table 2-5: Physical Properties of the Compound Helicopter Model – Wing	32
Table 2-6: Physical Properties of the Compound Helicopter Model - Propeller.....	34
Table 3-1: Parameters of Command Filter	62
Table 3-2: Controller Parameters for Error Dynamics	68
Table 4-1: Comparison of Power Required Values Operating at Nominal and Optimal RPM	100
Table 4-2: Upper and Lower Limits of Compound Control Effectors for Different Airspeeds.....	102
Table 4-3: Fuel Consumption with and without FTO at 180 knots and 200 knots.....	123
Table C-1: Lift, Drag and Pitching Moment Coefficient of the Wing with -60° Flap Deflection.....	166
Table C-2: Lift, Drag and Pitching Moment Coefficient of the Wing with -45° Flap Deflection.....	167
Table C-3: Lift, Drag and Pitching Moment Coefficient of the Wing with -30° Flap Deflection.....	168
Table C-4: Lift, Drag and Pitching Moment Coefficient of the Wing with -20° Flap Deflection.....	169
Table C-5: Lift, Drag and Pitching Moment Coefficient of the Wing with -15° Flap Deflection.....	170
Table C-6: Lift, Drag and Pitching Moment Coefficient of the Wing with -10° Flap Deflection.....	171
Table C-7: Lift, Drag and Pitching Moment Coefficient of the Wing with -5° Flap Deflection.....	172
Table C-8: Lift, Drag and Pitching Moment Coefficient of the Wing with 0° Flap Deflection.....	173

Table C-9: Lift, Drag and Pitching Moment Coefficient of the Wing with 5° Flap Deflection.....	174
Table C-10: Lift, Drag and Pitching Moment Coefficient of the Wing with 10° Flap Deflection.....	175
Table C-11: Lift, Drag and Pitching Moment Coefficient of the Wing with 15° Flap Deflection.....	176
Table C-12: Lift, Drag and Pitching Moment Coefficient of the Wing with 20° Flap Deflection.....	177
Table C-13: Lift, Drag and Pitching Moment Coefficient of the Wing with 30° Flap Deflection.....	178
Table C-14: Lift, Drag and Pitching Moment Coefficient of the Wing with 45° Flap Deflection.....	179
Table C-15: Lift, Drag and Pitching Moment Coefficient of the Wing with 60° Flap Deflection.....	180

LIST OF SYMBOLS

A, B, C	= State-Space Dynamic Matrices
u, v, w	= Body Axis Velocities
p, q, r	= Body Angular Rates
ϕ, θ, ψ	= Euler Angles
X, Y, Z	= Body Axis Forces
R, M, N	= Body Axis Moments
W	= Gross Weight
m	= Mass of the Aircraft
$\beta_0, \beta_{1c}, \beta_{1s}$	= Main Rotor Flapping Angles in Multi-Blade Coordinates
$\theta_0, \theta_{1c}, \theta_{1s}$	= Collective, Lateral and Longitudinal Cyclic Pitch Controls
H	= Main Rotor H-Force
Q	= Torque
T	= Thrust
L, D	= Lift and Drag Forces
α, β, γ	= Angle of Attack, Side-Slip Angle and Flight Path Angle
C_L, C_D	= Lift and Drag Coefficients
C_R, C_M, C_N	= Roll, Pitch and Yaw Moment Coefficients
q	= Dynamic Pressure
θ_{TR}	= Tail Rotor Collective Blade Pitch
δ_{coll}	= Collective Command
δ_{lon}	= Longitudinal Cyclic Command
δ_{lat}	= Lateral Cyclic Command
δ_{ped}	= Pedal Command

δ_{tht}	=	Throttle Command
β_P	=	Propeller Pitch Setting
δ_{FO}	=	Symmetric Flaperon Deflection
δ_{Flat}	=	Differential Flaperon Deflection
δ_e	=	Stabilator Deflection
Ω	=	Rotor Rotational Speed
V	=	Airspeed
V_z	=	Vertical Speed
h	=	Vertical Position
g	=	Gravitational Constant
e	=	Tracking Error
HP	=	Power Required
x	=	State Vector
u	=	Input Vector
y	=	Command Variable
ω_n	=	Natural Frequency
ζ	=	Damping Ratio
τ	=	Time Constant
K_P, K_I, K_D	=	Parameters of PID Error Dynamics
v	=	Pseudo Command
a_y	=	Lateral Acceleration
x_{e1}, x_{e2}, x_{e3}	=	Internal Engine States
ρ	=	Auxiliary Input for Control Law Development
ϕ	=	Golden Ratio

y_p	=	Limited Parameter
u_{lim}	=	Control Limit
I_R	=	Rotor Polar Moment of Inertia
$(L/D)_{eq}$	=	Equivalent Lift-to-Drag Ratio
$X_{u}, X_{v}, X_{\beta p}, X_{\delta col}, X_{\delta e}$	=	X Force Derivatives Normalized by Aircraft Mass
Y_u, Y_v	=	Y Force Derivatives Normalized by Aircraft Mass
$Z_w, Z_\theta, X_{\beta p}, Z_{\delta col}, Z_{\delta e}$	=	Z Force Derivatives Normalized by Aircraft Mass
W_f	=	Fuel Consumption
SFC	=	Specific Fuel Consumption

ACKNOWLEDGEMENTS

I would like to acknowledge many people who have helped me complete this dissertation. Firstly, I would like to express my deepest gratitude to my advisor Dr. Joe Horn. I am thankful for his guidance, knowledge, and opportunities throughout both my Masters and Ph.D. work. I am also very grateful to my doctoral committee members, Dr. Edward Smith, Dr. Farhan Gandhi, Dr. Kenneth Brentner, and Dr. Christopher Rahn for their insightful comments. This research was partially funded by the Government under Agreement No. W911W6-11-2-0011. I would like to thank the government technical point of contact for this research Dr. Colin Theodore of NASA Ames Research Center. Special thanks to my professors Dr. Cahit Ciray and Dr. Ilkay Yavrucuk, whom I worked with during my undergraduate studies at Middle East Technical University, for introducing me to and kindling my curiosity about rotorcraft systems.

I would like to express my thanks to my friends Ozhan Turgut, Ali Akturk, Zihni Saribay, Maryam Khoshlahjeh, Thanan Yomchinda, Mark DeAngelo, Adam Thorsen, Safakcan and Tugce Burcu Arda Tuncdemir, Emre Kultursay, Sena and Dagistan Sahin, Onur Kayiran, and Cem Topbasi for their support throughout my Ph.D. studies. I would like to thank my dearest friends for years Berk Gurakan, Volkan Aykac, Murat Torun, Gokhan Tezcan, Adnan Ozturel, Burak Ozgur, Deniz Cinalioglu, and Ayse Naz Ozpeynirci. Also special thanks to Kaya Tutuncuoglu, my oldest friend and my roommate, for his friendship throughout our graduate studies.

Most importantly I would like to thank my family for all the years of support and encouragement that led to the completion of this dissertation. Endless thanks to my mother, Senay Ozdemir, and my father, Ali Ersin Ozdemir, for their love and support that gives me the ambition and strength to achieve anything in life. Lastly, I would like to thank my fiancée, Fatma Idil Akcetin, for always being there for me. Her love and understanding helped me get through the toughest and most stressful times of my life.

Chapter 1

Introduction

1.1 Background

Although conventional helicopters are efficient air vehicles for hovering and low to moderate speed forward flight, faster and more agile configurations are necessary for increasing the capabilities of VTOL aircraft, especially in high-speed forward flight. There are certain problems related to high-speed forward flight for conventional helicopters. In forward flight, each blade of the main rotor experiences a different velocity, which is the sum of the velocity of the blade section due to the rotational velocity and the velocity of the rotorcraft. Thus, the velocity on the retreating and advancing side of the blade are different. The variation of velocity on rotor blade around the azimuth as well as the radial variation results in certain limitations. These limitations are blade stall and reverse flow on the retreating side, compressibility effects due to the high Mach number on the advancing side. Overcoming the limitations and improvements on the helicopter performance can be achieved by decreasing loading on the main rotor (lift and thrust) using auxiliary lift and thrust components and reducing rotor speed to lower the tip Mach number. A slowed rotor results in reduced power required and increased maximum speed. Variable rotor speed may have potential problems associated with complexity, vibration and rotor stability; however, modern flight control methods can resolve these issues.

Conventional helicopters are limited in the trim states achieved. Typically a given flight condition (airspeed, altitude, weight) is defined by a unique trim state (as defined by pilot controls and aircraft attitude) and the rotorcraft performance (e.g. power required) is then defined by the trim state. Compound rotorcraft and variable rotor speed provide redundancy in controls

and create an opportunity to optimize the trim state. Adjustments to redundant controls can be used to minimize power required, reduce noise, and reduce structural loads and vibration, or some hybrid objective. There are two possible approaches on how to determine optimal trim. One approach is to perform a detailed trim study and obtain trim for every possible flight condition with varying redundant controls and then determine the optimum via post-processing. Another approach is to perform optimization in flight. Various optimization methods can be applied to determine optimal redundant controls. The choice of optimization method is critical; it should be quick and stable. In-flight optimization methods require well designed flight control systems that can optimize trim while holding flight condition, since rotorcraft performance is sensitive to changes in flight condition.

1.2 Literature Review

Various compound rotorcraft configurations have been studied by researchers to increase the capabilities of conventional helicopters. In order to increase the performance of a helicopter auxiliary lift and thrust components are suggested to be used, as well as rotor speed reduction. The use of additional control effectors and variable rotor speed configurations provide redundancy in controls. Hence optimization of the redundant controls plays an important role for high performance seeking rotorcraft.

This literature review provides a summary of studies about compound rotorcraft, variable rotor speed configurations and some optimization methods applied to engineering problems which can be used for optimizing the performance of a compound rotorcraft.

1.2.1 Conventional Helicopter and Limitations

Johnson [1] describes a helicopter as an aircraft that uses rotating wings to provide lift, propulsion, and control. The main rotor, therefore, is the major source of forces and moments that drives lift, propulsion, and control of position, attitude and velocity. Particularly for translational flight, forward tilt of the rotor (propulsive force) is required. In contrast to helicopters, fixed wing aircraft have separate aerodynamic surfaces to provide lift, propulsion, and control [2, 3]. Newman [4] describes the difference between a fixed wing aircraft and a conventional helicopter by comparing sources for lift and propulsion. While lift and thrust sources are separated for a fixed wing aircraft, main rotor is the source of lift and thrust for a helicopter.

Helicopters are unique for their ability to hover. Since rotor blades observe airflow due to the rotation of main rotor, they can provide lift to overcome weight while the helicopter has no motion relative to the air. However, forward flight is challenging; with increasing translational speed, airflow observed by the individual blades start to differ. Therefore, aerodynamic behavior of air flow through rotor blades varies significantly as the helicopter transitions from hover to ever increasing forward flight speeds [1, 5, 6]. Figure 1-1 shows the relative airspeed experienced by main rotor blades during forward flight. This asymmetry of lift and variation in local velocity on the rotor becomes more pronounced with the increase of airspeed. The variation of airspeed on rotor blades results in unsteady and asymmetric distribution of aerodynamic forces and moments on rotor at forward flight.

Increasing airspeed raises the local velocity at the tip of the advancing side blade, which limits the maximum airspeed of helicopter, since airspeed at the tip approaches the speed of sound. As the Mach number reaches one, shock waves occur and also reduce the stall angle of the blade; limiting the lifting force obtained from the advancing side blade. Also high-speed flight results in fuselage/hub drag rise and this requires higher power [7, 8, 9, 10].

On the retreating side, increased longitudinal cyclic and collective pitch, due to the requirement of higher thrust from the rotor to offset increased drag, brings retreating side blades to reach their airfoil specific stall angle of attack. Stall terminates any usable lift provided by the blade. On the root region of the retreating side blade, a reverse flow region arises with a size proportional to advance ratio. This effect is shown in Figure 1-1. The reverse flow region reduces the useful area of the rotor and reduces maximum achievable lift. For this reasons, the fore and aft of the rotor have to generate more lift to compensate for the loss on the retreating side, which eventually increases the induced power [7, 8, 9, 11]. The unsteady and complex aerodynamic environment of the rotor induces high vibration levels, which leads to reduction in component life due to fatigue [8, 12, 13, 14]. Figure 1-2 shows the aerodynamic environment of main rotor in forward flight.

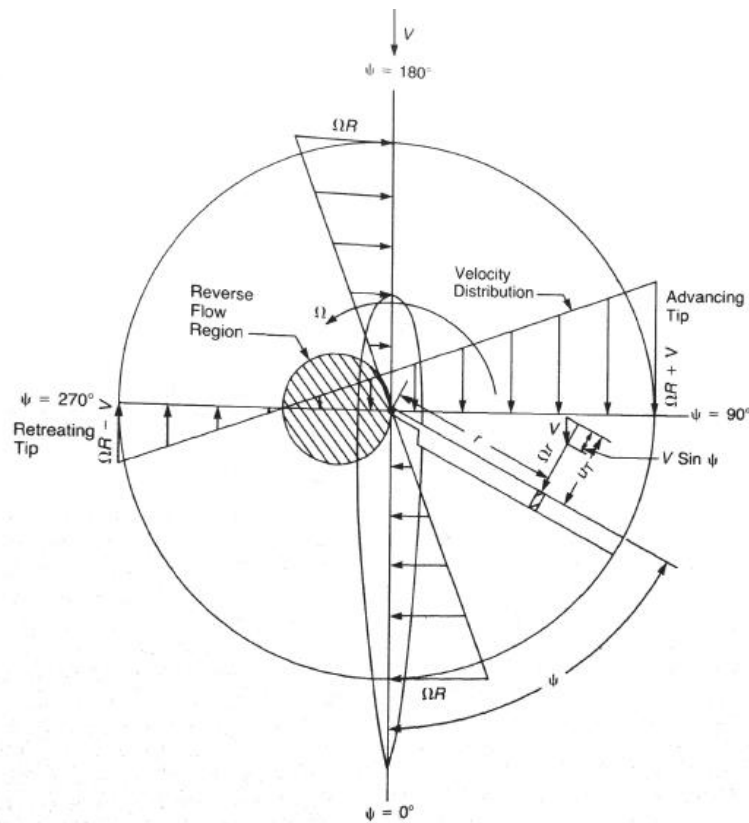


Figure 1-1: The Effect of Forward Flight Velocity on a Helicopter Main Rotor [6].

For the conventional helicopter, the only degree of freedom available to overcome issues of main rotor in forward flight is the rotor rotation speed. However, rotor speed variation cannot solve problems of advancing and retreating sides simultaneously. Although reducing rotor speed may reduce the Mach number at the advancing side and may solve compressibility issues, a larger portion of retreating side will then experience reverse flow and whole retreating side will have higher angle of attack. On the other hand, increasing rotor speed may relieve the retreating side issues with reverse flow and retreating blade stall, but advancing side Mach number increases.

As a result, these aerodynamic issues in forward flight limit conventional helicopters maximum airspeed and maneuverability. Another approach to the vehicle configuration that would be beneficial for high-speed flight is required. Helicopter compounding is a method that can be used to improve performance of existing helicopters.

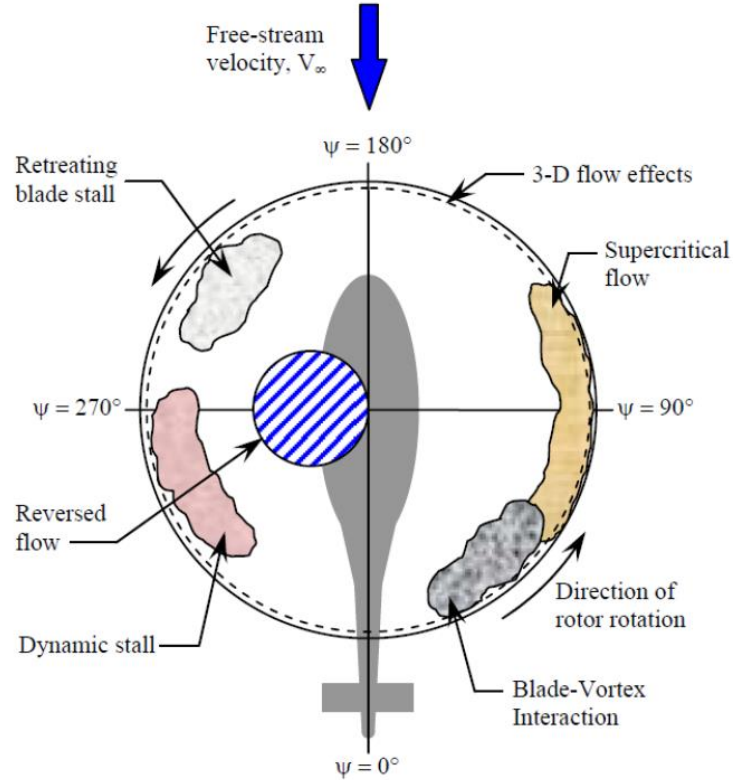


Figure 1-2: Rotary-Wing Flight Aerodynamics [15].

1.2.2 Compound Rotorcraft

A better way to solve issues of conventional helicopters in forward flight and enable higher airspeed is to use auxiliary lift and propulsion components. There are numerous examples of helicopter compounding. Compounding a helicopter with auxiliary components has to be categorized depending on how the compounding occurs. Two main categories are lift compounding and thrust compounding. A helicopter with both lift and thrust compounding is called fully compounded rotorcraft [9].

1.2.2.1 Lift Compounding

According to Sekula and Gandhi [12], lift compounding is using non-rotating lifting surfaces to provide auxiliary lift at high-speed flight; therefore, the main rotor lift requirements are reduced. Numerous studies investigated the effectiveness of lift compounding. One advantage of lift compounding is that it can reduce rotor vibrations [12, 16-19]. Since the new lift requirement is lower for main rotor, smaller blade angles of attack are needed. Therefore, advancing side compressibility effects can be reduced [16, 19] and retreating side blade stall problems can be avoided [17, 20-24]. Lynn [17] listed the results of investigations on wing-rotor combinations considered by Bell Helicopters. Addition of only wing for auxiliary lifting device gives significant efficiency gains above the speed of 120 knots. Some amount of rotor unloading is desirable for speeds 140 to 180 knots. However, above 200 knots auxiliary propulsion is required.

On the other hand, use of wings will increase the drag of overall aircraft [9], requiring main rotor to provide larger propulsive force. This requires a significant forward tilting of the main rotor thrust vector to support necessary propulsive force. Thus it leads to nose down fuselage pitch. Another disadvantage of lift compounding is the large download in hover due to the interaction with rotor downwash that decreases the hover performance [20, 25, 26]. Lift compounding can also result in an increase of main rotor sensitivity to gusts [16, 17] and a reduction in phugoid mode stability at high forward speed flight conditions [16, 27].

Capability to change wing incidence may solve rotor-wing interactions and high download in hover, but it adds complexity and additional weight to the system. A better solution is using plain flaps; they tend to have good download reduction capabilities [28]. Wing lift can be controlled using plain flaps without changing the wing pitch angle, and plain flaps can be used as ailerons when deflected differentially [7, 9, 25].

A wing used as a lift compounding component has to be designed carefully. Studies showed that high aspect ratio wing and large rotor-wing separation distance reduces power required by reducing the interference between rotor and wing [12, 25, 26]. In particular, wing area should be selected to balance vibration reductions and high-speed performance gains with hover performance reduction [16, 17]. Autorotation requirements must be considered for the design of the wing. Large wings can cause an autorotation problem that is characterized by rotor speed reduction and decrease in rotor control responsiveness [17]. A significant roll control problem can occur during autorotation because one wing can stall before the other due to the increase in descent rate, resulting in roll disturbances.

1.2.2.2 Thrust Compounding

Auxiliary thrust components reduce or eliminate the need for propulsive force from the main rotor in forward flight. Numerous studies investigated benefits of thrust compounding. Key advantages are higher forward flight speed, low to near level fuselage attitude in forward flight, reduced vibration, and increased fatigue life of the rotor [12, 29]. The main reason for these benefits is the reduction of propulsive force generated by the rotor, which leads to lower forward tilt of the rotor followed by lower fuselage tilt [16, 29]. Obtaining level fuselage in forward flight can increase passenger comfort and can be useful for military applications [30]. In addition, reduction in power applied to the rotor leads to reduced anti-torque required to stabilize rotorcraft.

Thrust compounding also has critical design tradeoffs. Use of auxiliary thrust components increase the empty weight of the rotorcraft significantly, which results in an increase in the cost and complexity in the design of the rotorcraft. Also mechanical complexities arise with thrust compounding [21, 30, 31]. Other disadvantages are blade stall problem and reverse flow at

the retreating side, and compressibility effects on the advancing side, since the rotor is the only source for lift at high-speed flight [12, 25, 29, 30, 32]. The use of the Advancing Blade Concept (ABC) or Lift Offset Concept overcomes these issues. With the use of coaxial rotors, retreating side blades are offloaded; therefore, blade stall and reverse flow problems can be minimized. At high-speed flight, rotor speed is reduced and required propulsive force is maintained by auxiliary propulsive component. Thus, the aft tilt of the rotor increases the autorotative state of rotor, reducing the main rotor power requirement [33, 34].

Various methods can be used for thrust compounding. A turbojet engine can be used as auxiliary thrust component, which has high thrust to weight ratio. However, the operating airspeed for a compound rotorcraft may reach from 200kts to 300kts, which is below the efficient operating range of a turbojet engine [26, 32]. A propeller has an operating range that better matches that of compound rotorcraft. Use of propellers, on the other hand, has some disadvantages; such as, interference from the rotor, ground personnel safety, and noise. Operating in the wake of rotor can apply significant bending moments on the propeller blades; therefore, the best place for propeller is usually chosen to be the tail, which has maximum possible separation from the rotor wake [26].

Some examples for rotorcraft with thrust compounding are the Bell 533, Lockheed XH-51, Sikorsky's XH-59A and X2 [14, 18, 24, 33- 38]. Figure 1-3 shows the XH-59A and Figure 1-4 shows the X2 thrust compounded rotorcraft. Both are coaxial and use the lift offset concept. XH-59A is compounded with a jet engine whereas X2 is compounded with a pusher propeller.



Figure 1-3: Sikorsky XH-59A [38].



Figure 1-4: Sikorsky X2 Technology™ Demonstrator [38].

1.2.2.3 Full Compounding

Fully compounded rotorcraft use both auxiliary lift and thrust components to reduce loading on the rotor for both lift and propulsion requirements at high-speed flight [4, 9, 11, 16, 25, 26, 29, 30, 32]. Thus, problems arising for conventional helicopter are resolved with the offloading of rotor. Use of both lift and thrust compounding provides significant benefits. Although auxiliary lift compounding is efficient at high-speed flight, it requires higher forward tilt of the rotor to maintain a propulsive force. Therefore, the maximum achievable speed is

limited. Similarly, auxiliary thrust compounding provides the propulsive force required at high-speed flight, but then rotor loses its lifting efficiency that limits the maximum achievable speed. On the other hand, fully compounded rotorcraft addresses both drawbacks and aircraft can reach higher speed flight [7, 26]. There are numerous studies confirming the significant increase in maximum forward velocity [16-19, 32]. One of the most significant advantages of fully compounded rotorcraft is the reduction of rotor vibration [8, 12, 14, 16-19, 24, 29, 30, 32, 39-42]. Vibration is reduced by avoiding the blade stall problems on retreating side of the rotor and compressibility effects on advancing side. Some examples of fully compounded rotorcraft are Sikorsky's NH-3A, Piasecki's X-49, Lockheed AH-56 Cheyenne, and Eurocopter's X3 [32, 43-45]. Figure 1-5 shows Eurocopter's X3.



Figure 1-5: Eurocopter's X3 [42].

The major disadvantage of using fully compounded configuration is the increased weight of the vehicle when auxiliary thrust and lift components are added [39]. Additional lift and propulsive components with the backup structures that they require can create an empty weight penalty, which is around five percent of the aircraft gross weight [21].

Another important issue is the level of structural loads supplied by the auxiliary components. It should carefully be studied to avoid any vibration problems. Any mismatch between wing-rotor loading and auxiliary propulsive force can result in vibratory loads [16]. The

location of wing and auxiliary thruster with respect to the center of gravity (CG) of the rotorcraft is an important design variable.

Redundancy in controls is achieved by the use of rotor, wing and auxiliary thruster and this can be used to optimize performance. The distribution of lift and propulsive forces for compound rotorcraft leads to non-unique trim. For a fully compounded rotorcraft this comes about through the redundant control of auxiliary thrust. Figure 1-6 shows the pitch angle of tip path plane for different compounding configurations at different airspeeds and Figure 1-7 shows the fuselage and wing pitch angles [29]. For the case with auxiliary propulsion in idle condition, main propulsive force is generated from the rotor and rotor is tilted forward followed by a nose down attitude of the fuselage, where nose down pitch attitude results in less lift from the wing. For the case with auxiliary propulsion in full power and propelling the rotorcraft, main propulsive force is generated by propellers and rotor is tilted backward followed by a nose up attitude of the fuselage that results in more lift generated by the wing [29]. For the compound flight condition, the rotor collective pitch is fixed to 40% (10 deg) and 50% (11.5 deg) of the over the speed range and auxiliary propulsion is set to the required thrust level. The wing pitch attitudes are shown in Figure 1-7 and it can be deduced that for a low rotor collective pitch value, wing pitch attitude increases to compensate the total lift required.

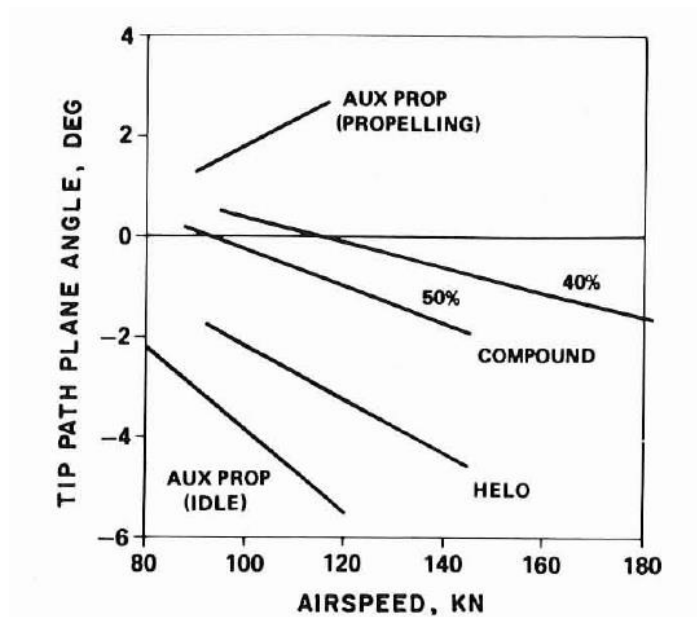


Figure 1-6: Tip Path Plane Attitudes over the Speed Range [29].

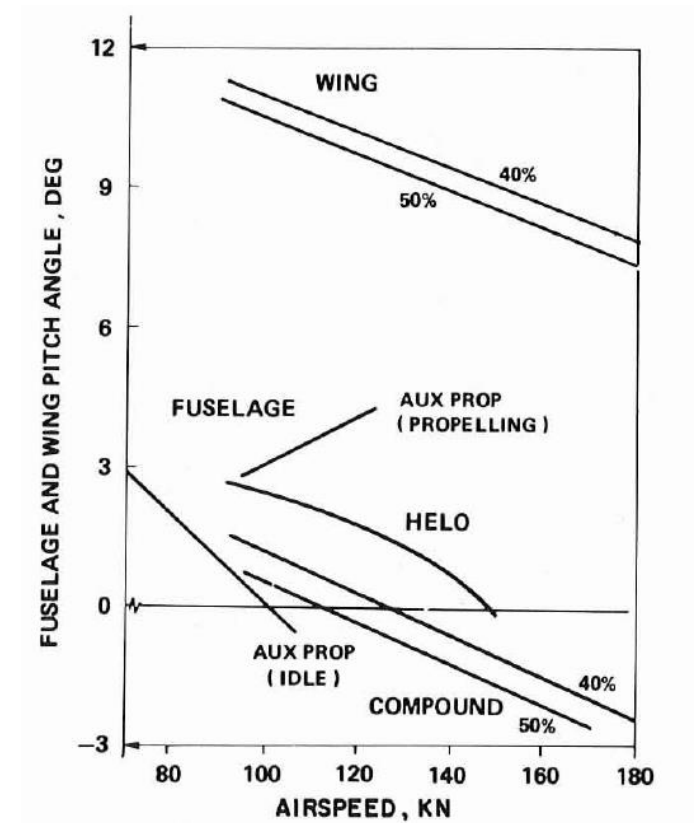


Figure 1-7: Body and Wing Pitch Attitudes over the Speed Range [29].

1.2.3 Variable Rotor Speed

Although the vast majority of helicopters are designed to operate with a constant rotor speed, variable rotor speed rotorcraft is another way of achieving redundancy in control. Variable rotor speed is achievable for both conventional and compound rotorcraft. The variations in rotor speed have potential problems associated with rotor stability and modern flight control methods such as rotor state feedback can potentially resolve these issues [46, 47]. Rotor speed reduction has been proposed for rotorcraft where advancing tip Mach number is a constraint for the maximum speed; therefore, a slowed rotor results with reduced power required and increased maximum speed. However, a reduction in rotor speed results in stall issues on retreating side of the rotor. Compound configurations [48] and Advancing Blade Concept (ABC) coaxial configuration [33, 34, 49] were proposed as methods to be applied for resolving stall issues on retreating side. A method, called Optimum Speed Rotor (OSR), proposed by Karem [50] uses large variations in rotor speed to reduce power required on a conventional rotorcraft configuration in the low to mid-speed range. The rotor speed reduction allows the rotor blades to operate at a more efficient lift to drag ratio and has been shown to improve endurance. The OSR is used on the A-160 Hummingbird unmanned helicopter.

With the aid of improved analysis tools, active control technology, advanced propulsion and drive systems, variable rotor speed could be applied to rotorcraft in order to obtain higher performance and maneuverability. Steiner and Gandhi [51] conducted a rotor speed optimization study using a comprehensive performance analysis and showed substantial potential power reductions available from reduced rotor speed. Horn and Guo [52, 53] produced similar results using a real-time simulation code and designed a flight controller to follow the optimal rotor speed schedule.

1.2.4 Trim Optimization

The concept of using control redundancy to optimize trim has been proposed for compound rotorcraft [43]. Geiger et al [44] performed a trim optimization study for a compound rotorcraft, a version of the UH-60 with lifting wing and vectored thrust ducted propeller (VTDP), called UH-60L/VTDP. Geiger [7] also proposed a flight control system to accommodate redundant control effectors with the trim conditions. In that study, the simulation model trim solver was used to generate numerous (over 300000) solutions for all permutations of trim conditions in order to minimize a combination of power required and vibration index.

The method used for determining the optimal trim by Steiner and Gandhi [51], and Horn and Guo [52, 53] had similarities to that of Geiger [7], in that it involved an extensive survey of trim solutions. The method was extended to include variations in weight as well as climb and descent maneuvers. One issue realized in the research of Guo, Steiner, and Geiger, is that the sheer volume of data required to generate an optimization database can be problematic. The required data increases exponentially with the increased number of permutations resulting from added control redundancy or variations in flight condition. The optimization process relies on trim solutions, which can be time consuming and in some cases unreliable. Furthermore, while such databases can be generated from simulation models, collecting corresponding data in flight would be prohibitively expensive.

1.2.5 Optimization Methods

There are numerous optimization methods used in engineering problems by researchers. Bodson [54] compared four control allocation methods using three simple algorithms on different models and order for the optimization problem of a C-17 fixed wing aircraft model. The study

suggested that use of a constrained optimization method with fixed number of iterations is the best and quickest way to reach optimal performance. Schultz and Zagalsky [55] used equations of motion and aircraft dynamics to optimize controls for a given performance characteristic of a fixed wing aircraft. The study suggests that the resultant control charts can either be used as a reference for the control system designer or it can be provided on the display to the pilot in real time for an optimal trajectory or control information.

Gilyard used a method originally developed for fixed-wing transport aircraft, Adaptive Performance Optimization, which applies excitation in a raised-cosine form over a period of time [56-59]. Adaptive Performance Optimization (APO) is a method of identifying unknown performance characteristics from a forced response, using a low frequency, smooth maneuver. Since the input is in low frequency, it is assumed that the aircraft is approximately in steady state trim throughout the maneuver. Gilyard achieved drag minimization by applying a low frequency sinusoidal command spanning the whole range of symmetric outboard aileron. The simulation results were compared and agreed with flight test data. The aircraft response and variation in incremental drag during the forced-excitation of symmetric outboard aileron are shown in Figure 1-8 and 1-9. The maneuver generally takes a shorter amount of time when compared to iterative methods, since it spans the whole control range.

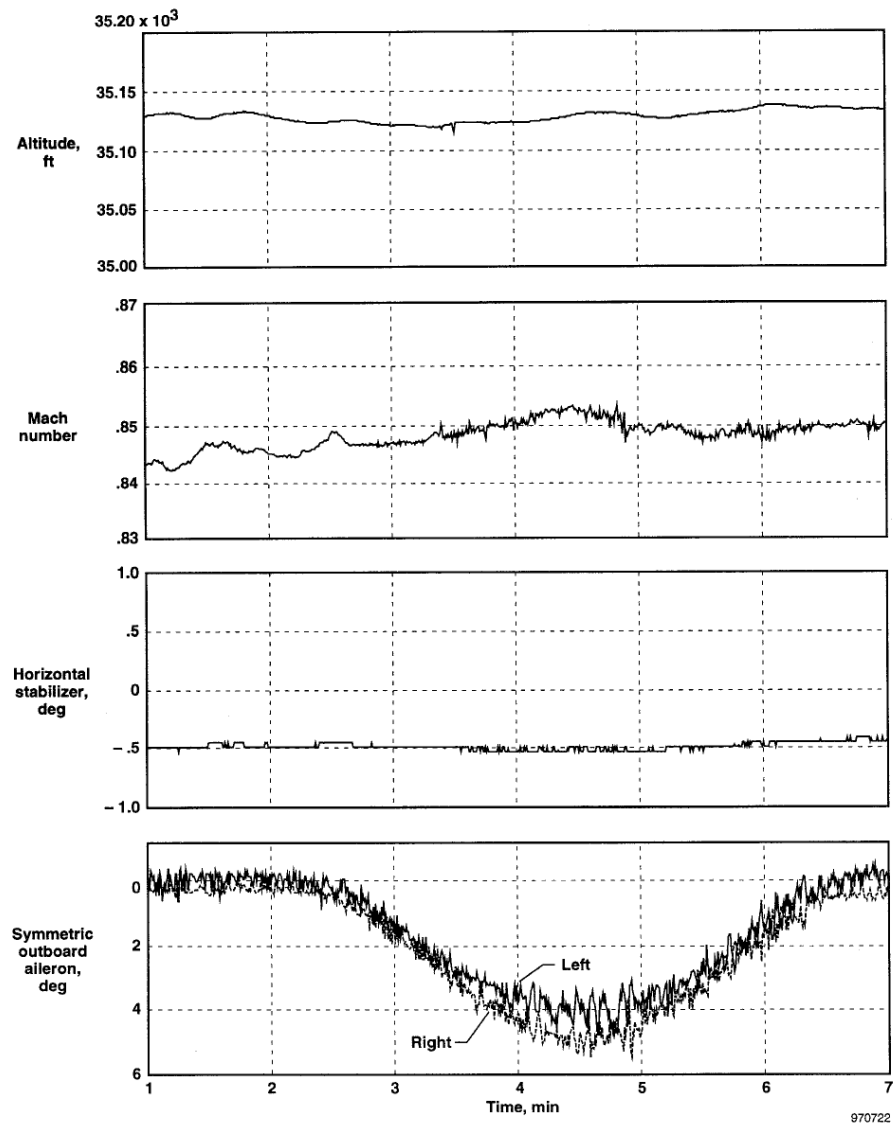


Figure 1-8: Aircraft Response to Forced-Excitation Maneuver during APO Flight Test [57]

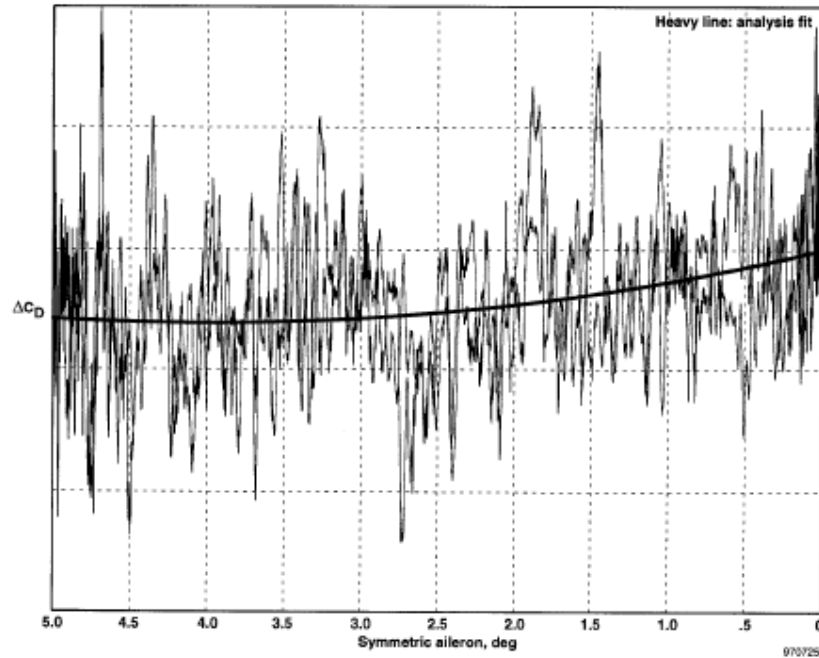


Figure 1-9: Variation of Incremental Drag with Symmetric Aileron Deflection [57]

1.3 Research Objectives

Although a significant amount of study has been done in the past on compound rotorcraft configurations and performance optimization of rotorcraft, the real-time performance optimization of compound rotorcraft has not been studied in detail. In-flight optimization techniques avoid the extensive search of trim solutions to generate optimization database which requires running a lot of simulation cases or even flight tests to collect data.

This study aims to investigate an advanced flight control system design that allows in-flight performance optimization. The concept is called “Fly to Optimal” (FTO). While maintaining trim with a stabilizing controller, perturbations are generated and performance is measured in flight. The measured response is used to drive the redundant controls and the trim state to an optimal.

In order to achieve the objective the following technical approach is proposed:

- GENHEL-PSU is the simulation tool used for this research and it is modified to model a generic compound rotorcraft with lift and thrust compounding as well as a conventional UH-60A helicopter model.
- Basic understanding of the rotorcraft trim theory helps identifying the use of redundant control effectors. Since there is not a unique trim state for a compound rotorcraft, it is crucial to know and define different trim states for the same flight condition. This will later allow choosing the trim method desired for different flight conditions. For example, at high-speed forward flight trim, collective control can be set to a constant and trim can be performed for auxiliary thrust.
- Integrated flight control system design is an important part of this study. The control system should be designed to avoid any changes in the flight condition during optimization process, because performance measurements are sensitive to the changes in flight condition. Also the control system should use the compound rotorcraft controls in addition to conventional rotorcraft controls and variable rotor speed as redundant control effectors.
- Various optimization methods are studied and implemented using the integrated flight control system. Comparisons between different optimization methods help choose the faster and more accurate method. Steepest Descent, Golden Section and Adaptive Performance Optimization methods are chosen to be investigated in this study.
- Comprehensive sweeps of trim solutions of the rotorcraft are performed using the simulation model. The aim of this analysis is to provide confirmation of in-flight optimization results. Also the trim analysis help explore the constraints of the model using redundant control effectors.

This study features differences from the previous research, including:

- This study uses a high fidelity simulation model of UH-60A helicopter with conventional configuration of main rotor and tail rotor. The model is modified to accommodate auxiliary lift and thrust components to develop a generic compound rotorcraft with variable rotor speed.
- Two different compound rotorcraft models are used in this study. One model has a wing and a vectored-thrust-ducted-propeller (VTDP) without a tail rotor (similar configuration to X-49 compound rotorcraft design) and the other model has a wing and a pusher propeller with tail rotor.
- The Adaptive Performance Optimization (APO) method is applied to a rotorcraft in this study and optimization of two control effectors performed simultaneously using the APO method to optimize the power required and the specific range of generic compound rotorcraft.
- The flight control system is designed to control the rotorcraft and the rotor speed actively, while performing optimization using model following and dynamic inversion controller.
- The proposed flight control system design is performed at different flight speeds and rotor speeds with different optimization methods.

Chapter 2

Aircraft Dynamic Model

This chapter presents the aircraft model and the simulation program used in this study. Sikorsky's UH-60A Black Hawk is used as the baseline configuration and the non-linear mathematical model of the aircraft model was developed, which is based on Sikorsky General Helicopter (GENHEL) Flight Dynamics Simulation. GENHEL is a well-established Fortran-based simulation code that represents the flight dynamics and has been verified with flight test data. GENHEL is a suitable tool for performance and control design studies.

2.1 GENHEL Model Background

The aircraft model is developed with Penn State version of Sikorsky General Helicopter Flight Dynamics Simulation (GENHEL) program called GENHEL-PSU. GENHEL-PSU is based on the U.S. Army/NASA Ames GENHEL model [7, 60-63] of the UH-60A Black Hawk, which is a well-established Fortran-based simulation code. The GENHEL model is a non-linear, blade element flight dynamics model of a UH-60A helicopter whose accuracy is adequate for handling qualities evaluation and flight control design. The GENHEL simulation program models forces and moments in six degree of freedom without using small angle assumptions. In addition to rigid body degrees of freedom, four rotor flapping, four rotor lagging, one rotor rotational and additional degrees of freedom and dynamic states due to inflow, engine dynamics, actuators are modeled. The simulation program is structured in a modular fashion, with both primary and supporting modules and subroutines. The primary modules and subroutines model the major aircraft components such as, the main rotor, tail rotor, fuselage, horizontal and vertical tails, and the engine. The supporting modules and subroutines approximate aerodynamic forces and

moments, and flight conditions such as takeoff and landing. The relationship of subroutines is shown in Figure 2-1.

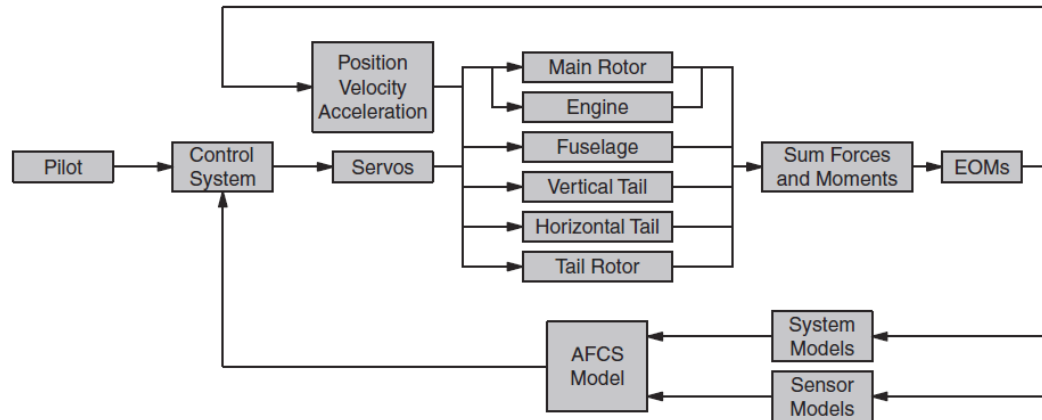


Figure 2-1: Structure of GENHEL [62]

GENHEL-PSU was developed and used at the Penn State Multi-Disciplinary Rotorcraft Simulation Facility (MDSRF) [60] and now on Penn State VLRCOE Rotorcraft Simulation Facility. The facility, as shown in Figure 2-2 , includes a fixed-base cab with electronic control loaders, a 180 degrees field of view on an 11-ft high by 15-ft diameter cylindrical screen, and flat screen instrument panels. The cockpit also includes programmable switches.



Figure 2-2: The VLRCOE Rotorcraft Simulation Facility

Several modifications were made to improve and add new features to GENHEL. Some of the modifications made prior to this study are described as followed:

- There is a network interface with real-time simulation environment to transmit data from the flight dynamics model to the external flight simulation software FlightGear. As required by this interface code developed in C++, the GENHEL-PSU code is compiled and executed with Intel Fortran Compiler 9.1 and Microsoft Visual Studio 2005 under 32-bit or 64-bit versions of Windows XP operating system, which not only provides debugging features but also allows easy compilation of mixed-language code.
- An interface with the MATLAB software environment provides a straightforward interface to perform the simulation and data analysis. MATLAB scripts can be used to specify the operation points and perform a large number of trim, linearization, and numerical simulations. Therefore, all the trim results, linearized models, and the simulation time history data can be managed, analyzed, and displayed with MATLAB tools.
- High order linearized models can be generated using a perturbation method. The 28-state vector includes 8 rigid body fuselage states (3 velocities and 3 angular rates in body axes, pitch and roll Euler angles), 12 rotor states (flapping and lagging dynamics in multi-blade coordinates), 3 inflow states (Pitt-Peters model), and 5 engine states (rotor speed, gas generator speed, turbine temperature, fuel flow, and Hydro-Mechanics Unit (HMU) load demand spindle). The input vector consists of the lateral and longitudinal cyclic pitches, collective pitch, pedal, and the RPM governor input to the engine's HMU.

- GENHEL-PSU can disable independent channels of the existing UH-60A Mechanical Control System, Stability Augmentation System (SAS) and Flight Path Stabilization System (FPS) and interface with modified, user-defined flight control laws. The flight control modules are completely decoupled from the flight dynamics model. Hence the new flight control design could be implemented fast and integrated seamlessly.
- Modified control laws can be designed in Simulink and transitioned directly to the simulation software using Real-Time Workshop, providing an efficient “pictures-to-code” development environment.

2.1.1 Modifications on GENHEL-PSU for Variable Rotor Speed

In the study by Guo, the rotor speed variation was implemented by changing the engine’s power turbine speed [63]. Rotor speed control on UH-60A is achieved by using the Electrical Control Unit (ECU) and the HMU [64]. The engine and fuel control system in GENHEL-PSU was modified and a rotor speed controller was developed to replace the ECU. The proposed rotor speed range is between 80% and 120% of nominal rotor speed of 27 rad/sec.

2.1.2 Modifications on GENHEL-PSU for Compound Helicopter Model

In the present study, two different compound rotorcraft models have been studied. Initial analyses have been performed for UH-60L/VTDP compound rotorcraft, which is a similar configuration of Piasecki’s X-49 SpeedHawk design with a wing and a vectored thrust ducted propeller (VTDP). Further analyses have been performed for a generic compound rotorcraft model of the baseline UH-60A helicopter with a wing and a pusher propeller. The first

configuration of VTDP compound rotorcraft used in the simulation in references [7, 43, 62] is based upon the UH-60L/VTDP (Vectored Thrust Ducted Propeller) compound helicopter, as shown in Figure 2-3. This configuration includes normal helicopter components along with wings and a ducted fan whose thrust vector can be controlled. The wing features both flap and aileron controls and mounted in a high position. The VTDP replaces the tail rotor, horizontal tail and the vertical tail of the baseline helicopter model. The basic flight dynamics model of the UH-60 had not been significantly modified from the original GENHEL model. However, a model of a compound version of the UH-60 with a wing and a vectored thrust ducted propeller (the configuration is similar to the X-49A compound rotorcraft design, as shown in Figure 2-4) was included in GENHEL-PSU.

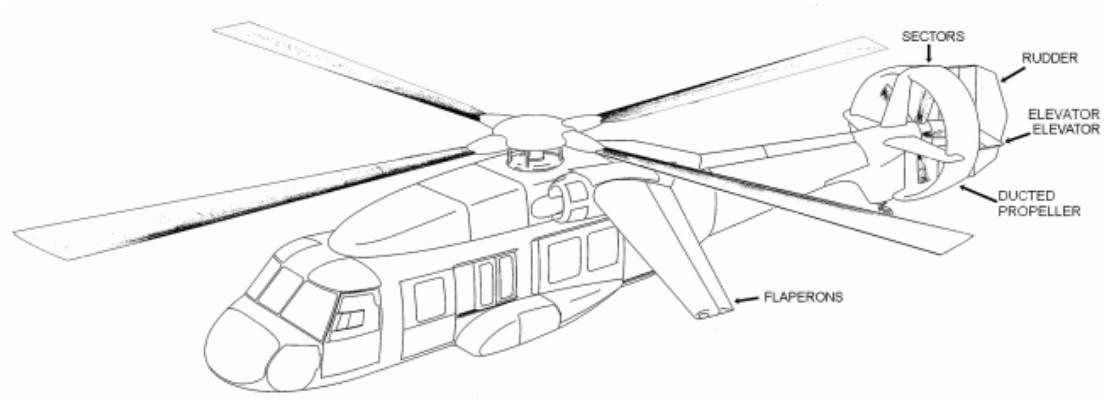


Figure 2-3: The UH-60L/VTDP Aircraft Model



Figure 2-4: Piasecki X-49A SpeedHawk VTDP Technology Demonstrator

The GENHEL simulation program is structured in a modular fashion as shown in Figure 2-1. The primary subroutines that define the major aircraft components were modified to account for helicopter compounding. An auxiliary thruster model replaced the tail and tail rotor and a wing model was also added. The compound helicopter configuration is shown in Figure 2-5. Details of the aircraft model and vehicle dynamics are given in Section 2.2.

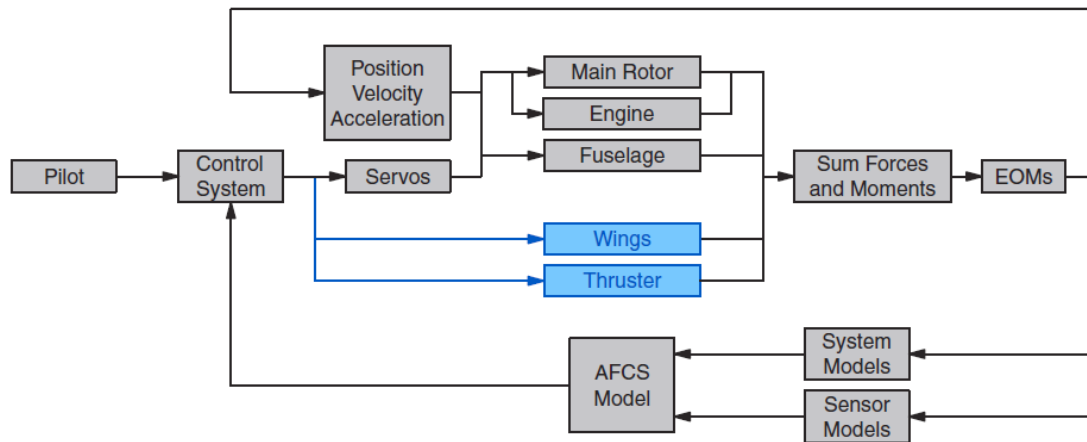


Figure 2-5: Structure of Compound-Modified GENHEL [62]

The second compound rotorcraft model is a generic compound rotorcraft with a baseline UH-60A helicopter compounded with a wing and a pusher propeller as shown in Figure 2-6. A wing and a rear-mounted pusher propeller model were developed and added to the GENHEL-PSU software. The tail rotor position of the compound model matches that of the UH-60A, whereas the stabilator is moved forward to avoid interference effects to the inflow into the propeller. The wing model developed for the UH-60L/VTDP compound rotorcraft model is used for the generic compound rotorcraft model as well. A propeller model is developed to be implemented in the model using blade element/vortex theory. The generic compound helicopter configuration is shown in Figure 2-7.



Figure 2-6: The Generic Compound Rotorcraft Configuration

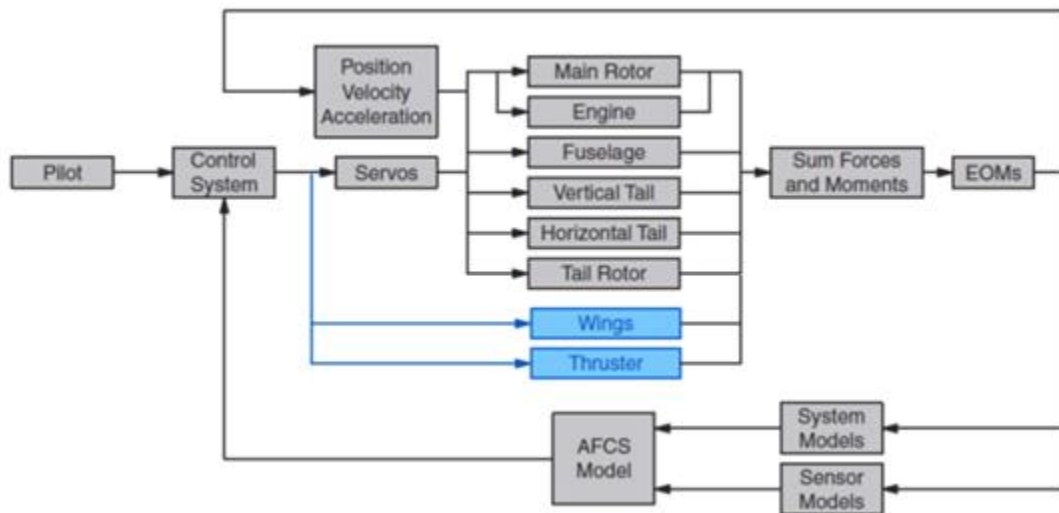


Figure 2-7: Structure of Generic Compound Rotorcraft –Modified GENHEL [62]

2.1.3 Recent Modifications on GENHEL-PSU

In addition to the previous modifications and added features, in this study several updates and modification were made to improve the simulation program. Several modifications that were made are described as follows:

- The code has been modified to use a different syntax for calling global variable for Intel FORTRAN Compiler 9.1. Module programming units are used to have an easier to understand code.
- Both variable rotor speed control modifications and compound helicopter configuration modifications were synchronized to have a compound helicopter configuration with rotor speed control.
- For high-speed flight with compound rotorcraft model, the trim algorithm is altered. As the collective control authority diminishes rapidly at high speeds, vertical force becomes less sensitive to collective. So auxiliary thrust component is used to trim longitudinal acceleration, while pitch attitude trims vertical acceleration by effectively changing aircraft angle of attack.

2.2 Vehicle Properties

The rotorcraft models used in this study are the UH-60A helicopter model, the compound version of the UH-60A helicopter, called UH-60L/VTDP, with a wing and a vectored thrust ducted propeller instead of a tail rotor and a tail, and the generic compound rotorcraft version of the UH-60A helicopter with a wing and a pusher propeller. Throughout the remainder of this thesis, ‘baseline’ term will mean a configuration based on the conventional UH-60A. The term ‘compound’ will mean a configuration based on the UH-60L/VTDP and the term ‘generic

compound' will mean a configuration based on the compound rotorcraft with wings and a pusher propeller. A list of physical characteristics of baseline helicopter configuration is given on Table 2-1 and the weight and inertia properties are given on Table 2-2.

Table 2-1: Physical Properties of the Baseline Helicopter Model

Module	Value	Module	Value
<i>Main Rotor</i>	Radius (ft): 26.83 Blades: 4 Chord(0.75R)(ft): 1.73 100% RPM: 258 Airfoil: SC 1095 Blade Area (ft ²): 186.8 Solidity: 0.0826 Tip Sweep (deg): 20 Shaft Angle (deg): 3 – fwd	<i>Vertical Stabilator</i>	Span (ft): 8.167 Area (ft ²): 32.3 Root Chord (ft): 6 Tip Chord (ft): 2.83 Sweep (c/4) (deg): 41 Aspect Ratio: 1.92 Airfoil: NACA 0021 Position with respect to Main Rotor Hub Fuselage Station (in): -353.8 Waterline (in): -68.0 Buttline (in): 0.0
<i>Tail Rotor</i>	Radius (ft): 5.5 Blades: 4 Chord (ft): 0.81 Angular Speed (rad/s): 124.62 Airfoil: SC 1095 Blade Area (ft ²): 17.82 Solidity: 0.1875 Cant Angle (deg): 20 Position with respect to Main Rotor Hub Fuselage Station (in): -390.8 Waterline (in): 9.0 Buttline (in): 14.0	<i>Horizontal Stabilator</i>	Span (ft): 14.38 Area (ft ²): 45 Root Chord (ft): 3.67 Tip Chord (ft): 2.54 Sweep (c/4) (deg): 0 Aspect Ratio: 4.6 Airfoil: NACA 0014 Incidence/Dihedral: Calculated in the Control System Position with respect to Main Rotor Hub Fuselage Station (in): -348.8 Waterline (in): -71.0 Buttline (in): 0.0
<i>General</i>	Overall Length (ft): 64.83 Fuselage Length (ft): 50.06 Wheel Tread (ft): 8.86 Wheel Base (ft): 28.93		

The relative positions of the components are given on Table 2-1. For fuselage station positive means forward, for waterline positive means higher, and for buttline positive is towards right. The estimated lift, drag and moment coefficients of fuselage, horizontal tail and vertical tail

are used to calculate aerodynamic forces and moments. These tabulated values are presented graphically in Appendix A and B. The tail rotor forces and moments are calculated by a simplified, closed form Bailey solution as described in detail by Ref. 61.

The wake of the main rotor on the each component is calculated using lookup tables provided, that generated from experimental data. Rotor wake is a function of longitudinal flapping and rotor wake skew angle, which is the angle between longitudinal shaft velocity and normal rotor inflow velocity [61]. For the compound rotorcraft models, rotor wake on the wing is taken to be the same as rotor wake on the fuselage. Similarly, the propeller rotor wake is taken to be the same as the rotor wake on the horizontal tail. GENHEL has control limits defined for the main rotor pitch angles and these limits are given on Table 2-3.

Table 2-2: Weight and Inertia Properties of the Baseline Helicopter Model

Weight (lbs)	16830.9
Center of Gravity Position with respect to Main Rotor Hub	
Fuselage Station (in)	-25.1
Waterline (in)	-71.2
Buttline (in)	0.0
I_{xx} (slug-ft)	4659.0
I_{yy} (slug-ft)	38512.0
I_{zz} (slug-ft)	36769.0
I_{xz} (slug-ft)	1882.0

Table 2-3: Main Rotor Control Pitch Limits

	Upper Limit (deg)	Lower Limit (deg)
Longitudinal Pitch	16.3	-12.5
Lateral Pitch	8.0	-8.0
Collective Pitch	25.9	9.9

Both the VTDP compound and the generic compound rotorcraft have a wing as the auxiliary lift source. The VTDP compound rotorcraft uses the VTDP as the auxiliary thruster and the generic compound rotorcraft uses an open pusher propeller as the auxiliary thruster. The weight and inertia properties of both the VTDP compound and the generic compound rotorcraft

configurations are same and given on Table 2-4. In this study the installed power for the generic compound rotorcraft is chosen to be 4500 hp. Specific engine power available is not critical to the analysis, as we are seeking ways to optimize power required

Table 2-4: Weight and Inertia Properties of the Generic Compound Helicopter Model

Weight (lbs)	20000.0
I_{xx} (slug-ft)	6176.0
I_{yy} (slug-ft)	34244.0
I_{zz} (slug-ft)	31596.0
I_{xz} (slug-ft)	1839.0
Center of Gravity Position with respect to Main Rotor Hub	
Fuselage Station (in)	-5.8
Waterline (in)	-67.0
Buttline (in)	0.0

2.3.1 Wing Model – Lift Compounding

The wing is designed to achieve balance between minimal power/max velocity capabilities and minimal vibrations and maximum maneuverability. An effective wing area to disk area ratio of 10% was selected as a design point, which is more favorable for low vibrations and high maneuverability [25]. The use of flaperons and variable rotor speed will be the main measures to extend the maximum velocity capabilities. Each flaperon spans approximately 90% of each wing, with a chord one-fifth of that of the wing mean aerodynamic chord such that the location of the flap hinge is at 80% chord. A relatively high wing placement was chosen and promotes a favorable lift distribution on the rotor and is advantageous from an operational standpoint for egress and ingress [65]. The wing is located approximately 5 ft below the main rotor, with its center of pressure directly above the center of gravity of the helicopter. The NACA 63-412 airfoil was selected for its favorable lift and low minimum drag capabilities with an emphasis on minimizing power required due to drag [66]. The span and aspect ratio were selected

from a basic structural mindset to meet the wing area constraint set by the 10% wing area to disk area ratio. The wing planform is linearly tapered with an aspect ratio of 9.00 and in total spans approximately 51 ft when mounted on the existing fuselage. The basic wing properties are listed in Table 2-5.

Lookup tables for the wing lift, drag, and pitching moment coefficients were created based a design cruise speed of 180 knots, while induced drag based on an Oswald efficiency factor, derived from zero-lift drag characteristics and the taper ratio of the wing, is included to account for finite wing effects [66]. For high angles of attack, quasi-steady lift, drag, and pitching moment coefficient models were developed at the design Reynolds number. In order to develop these models, data used from a NACA airfoil which was tested through 360 degrees and a trigonometric function was developed to estimate the post-stall behavior. Rotor wake on the wing is also taken into consideration for the wing force and moment calculations. The placement of the wing plays a key role on the performance of the helicopter. High rotor-wing interference increases main rotor power requirements and decrease autorotational performance [62]. The tabulated values of lift, drag and pitching moment coefficients are presented in Appendix C.

Table 2-5: Physical Properties of the Compound Helicopter Model – Wing

<i>Wing</i>	
Span (ft):	45.0
Total Effective Wing Area (ft ²):	226.0
Root Chord (ft):	5.5
Tip Chord (ft):	4.5
Taper Ratio:	1.22
Mean Aerodynamic Chord (ft):	5.02
Aspect Ratio:	9.00
Airfoil:	NACA 63-412
Design Reynolds Number at Mean Aerodynamic Chord:	9,331,000
Design Mach Number:	0.27
Position with respect to Main Rotor Hub	
Fuselage Station (in):	-5.8
Waterline (in):	-61.0
Buttline (in):	97.0

2.3.2 Propeller Model – Thrust Compounding

The VTDP compound rotorcraft has the VTDP for the auxiliary thrust component and the details of the VTDP configuration can be found in References [7, 62]. The generic compound rotorcraft has a pusher propeller as the auxiliary thrust component. GENHEL-PSU uses look-up tables for calculation of forces and moments for components of the rotorcraft such as the tail rotor and tails. However, in this study the propeller is modeled with a blade element/vortex theory [66].

Blade element theory was combined with Goldstein's classical vortex theory in order to create a refined model of the pusher propeller [67]. Blade element theory cannot comprehensively model a propeller, especially at low speeds. Blade stall for certain ranges of relatively high pitch inputs at low enough speeds also creates issues. Vortex Theory was introduced and incorporated into a baseline blade element model for a more accurate determination of inflow and sectional angles of attack [66]. The main inputs necessary for the model include: radial chord, pitch, and thickness variations, along with the propeller diameter, number of blades, RPM, spinner diameter, and airfoil properties. The propeller model was validated using wind tunnel results from NACA Technical Report 594 [68]. The wind tunnel results were also extrapolated to negative thrust conditions to validate the reverse thrust results generated by the blade element vortex theory model. The main propeller properties are listed in Table 2-6 and an efficiency map of the propeller used in the compound analysis is shown in Figure 2-8. The thrust and power calculations of the propeller are presented in Appendix D. The performance and thrust of the propeller can be highly sensitive to both airspeed and the propeller pitch, where the range of reasonable propeller pitch settings changes significantly with forward speed. Thus, a schedule of propeller pitch versus airspeed was established that results in reasonable thrust and efficiencies, as shown in Figure 2-9. This helps avoid putting the propeller in a stalled condition, reverse thrust condition, or any other inefficient setting. The propeller is engaged at 130 knots to avoid

operation in low efficiency regions. The propeller is scheduled with airspeed up to 220 knots at a constant collective pitch around its maximum efficiency region. However, only the schedule up until approximately 180 knots is needed when the high-speed flight trim algorithm is used. Rotor wake on the propeller is also taken into consideration. Rotor wake exerts significant bending moments on the propeller blades [7]. For the calculations, the interference factors used are the same as those for the horizontal tail.

Table 2-6: Physical Properties of the Compound Helicopter Model - Propeller

<i>Propeller</i>	
Diameter (ft):	8
Number of Blades:	7
Solidity:	0.34
RPM:	2160
Tip Twist (deg):	34.6
Root Twist (deg):	83.8
Chord (0.75R)(ft):	0.88
Pitch (0.75R)(ft):	42.4
Airfoil:	Clark-Y
Position with respect to Main Rotor Hub	
Fuselage Station (in):	-428.8
Waterline (in):	-79.0
Buttline (in):	0.0

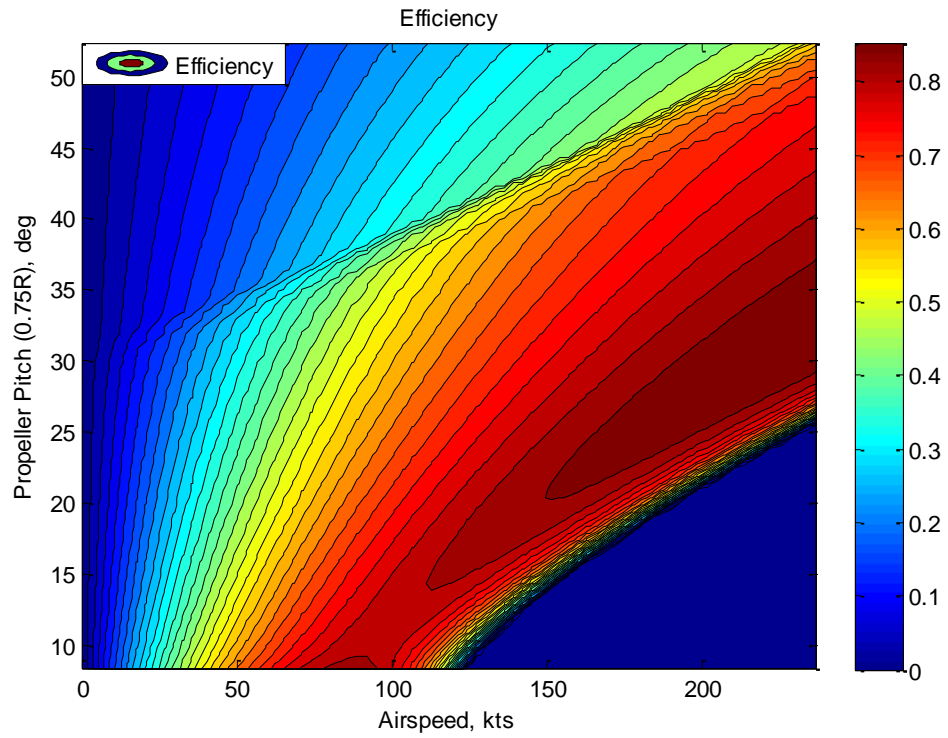


Figure 2-8: Propeller Efficiency Map

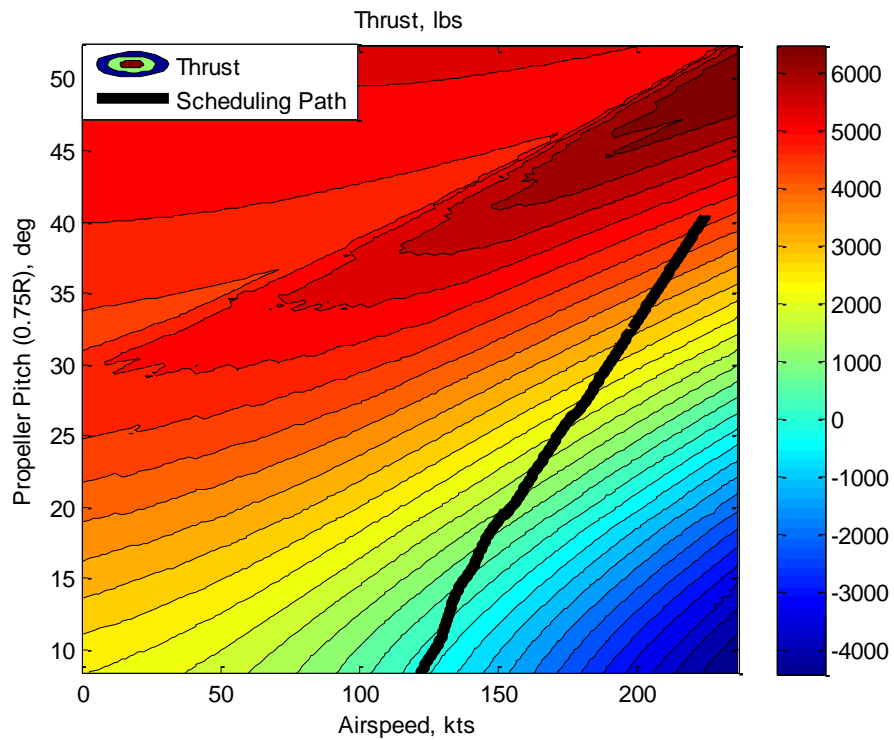


Figure 2-9: Propeller Thrust Map and Propeller Pitch Schedule with Airspeed

2.3 Basic Theory on Trim

The trim problem concerns the control positions required to hold the helicopter in equilibrium [69]. Trimmed flight condition for a baseline helicopter configuration is defined as an unaccelerated flight condition that is achieved by the application of a unique combination of the four pilot controls and attitude without any acceleration. There are six equations of motion used to describe the forces and moments acting on the aircraft in three-dimensional space and these forces and moments are assumed to be functions of the four pilot controls and the translational and rotational velocities. GENHEL-PSU numerically solves for the combination of controls and aircraft attitude to achieve equilibrium in flight condition by driving all accelerations to zero.

The trim problem for the VTDP compound rotorcraft configuration is similar to the trim problem for the baseline helicopter configuration. The forces added by the auxiliary thruster and acting on the wings and thruster duct are the major difference in the trim problem. Similarly the generic compound rotorcraft configuration adds the forces and moments from the wings and the propeller to the trim problem. GENHEL-PSU includes the added forces to the six equations of motion and seeks the zero acceleration solution to find combination of fuselage attitude and pilot controls for each different redundant compound controls setting. For the compound rotorcraft configurations the trim problem does not yield a unique solution; hence a trimmed flight condition can be achieved by different combinations of fuselage attitude, pilot controls and compound controls.

2.3.1 Force and Moment Equilibrium

The forces and moments of the generic compound rotorcraft configuration are portrayed in Figures 2-10, 2-11 and 2-12, and referred to a system of body-fixed axes centered at center of

gravity of the rotorcraft. The equations of motion for fuselage degrees of freedom are derived from applying Newton's laws of motion by of motion derived for the six degrees of freedom are shown in equations 2.1 to 2.6 relating the applied forces and moments to the resulting translational and angular accelerations [3].

$$\dot{u} = -(wq - vr) + \frac{X}{M_A} - g \sin \theta \quad (2.1)$$

$$\dot{v} = -(ur - wp) + \frac{Y}{M_A} - g \cos \theta \sin \phi \quad (2.2)$$

$$\dot{w} = -(vp - uq) + \frac{Z}{M_A} - g \cos \theta \cos \phi \quad (2.3)$$

$$I_{xx} \dot{p} = (I_{yy} - I_{zz})qr + I_{xz}(\dot{r} + pq) + R \quad (2.4)$$

$$I_{yy} \dot{q} = (I_{zz} - I_{xx})rp + I_{xz}(r^2 - p^2) + M \quad (2.5)$$

$$I_{zz} \dot{r} = (I_{xx} - I_{yy})pq + I_{xz}(\dot{p} - qr) + N \quad (2.6)$$

Equations 2.1, 2.2 and 2.3 are the force equations and equations 2.4, 2.5 and 2.6 are the moment equations, where u , v , and w are the body translational velocities, p , q and r are the body angular rates, and θ and ϕ are the Euler angles defining the orientation of the fuselage. I_{xx} , I_{yy} , I_{zz} are the fuselage moments of inertia, I_{xz} is the product of inertia, M_A is the mass of the aircraft and g is the gravitational constant. The external forces and moments are defined as X , Y , Z , R , M and N by the summation of contributions from different aircraft components. In order to avoid any confusion between roll moment and lift force, roll moment is called R and lift is called L . For example, the pitching moment, M , can be defined as shown in equation 2.7, where the subscripts stand for: main rotor, MR; tail rotor, TR; fuselage, F; horizontal tail, HT; vertical tail, VT; wings, W; and propeller P.

$$M = M_{MR} + M_{TR} + M_F + M_{HT} + M_{VT} + M_W + M_P \quad (2.7)$$

In a trimmed flight, total forces and moments on the aircraft are equal to zero. The six equations of equilibrium are defined in equations 2.8 to 2.13

$$X_{MR} + X_P + X_F + X_W + X_{HT} + X_{VT} - W \sin(\theta) = 0 \quad (2.8)$$

$$Y_{MR} + Y_{TR} + Y_F + Y_{VT} + W \cos(\theta) \sin(\phi) = 0 \quad (2.9)$$

$$Z_{MR} + Z_{HT} + Z_F + Z_W + W \cos(\theta) \cos(\phi) = 0 \quad (2.10)$$

$$\begin{aligned} R_{MR} + R_F + R_P + Z_{MR} y_{off} + Y_{MR} h_{MR} + Y_F h_F + Z_F y_{off} + Y_{VT} h_{VT} + Y_{TR} h_{TR} \\ + Z_{Wsb} y_{Wsb} - Z_{Wpo} y_{Wpo} + Z_{HTsb} y_{HTsb} - Z_{HTpo} y_{HTpo} = 0 \end{aligned} \quad (2.11)$$

$$\begin{aligned} M_{MR} + M_F + M_{TR} + M_W + Z_{MR} l_{MR} - X_{MR} h_{MR} + Z_F l_F - X_F h_F \\ - X_P h_P + Z_W l_W - X_W h_W + Z_{HT} l_{HT} - X_{HT} h_{HT} - X_{VT} h_{VT} = 0 \end{aligned} \quad (2.12)$$

$$\begin{aligned} N_{MR} + N_F - X_{MR} y_{off} - Y_{MR} l_{MR} - X_F y_{off} - Y_F l_F - X_P y_P - Y_{TR} l_{TR} - X_{Wsb} y_{Wsb} \\ + X_{Wpo} y_{Wpo} - X_{HTsb} y_{HTsb} + X_{HTpo} y_{HTpo} - X_{VT} y_{off} - Y_{VT} l_{TR} = 0 \end{aligned} \quad (2.13)$$

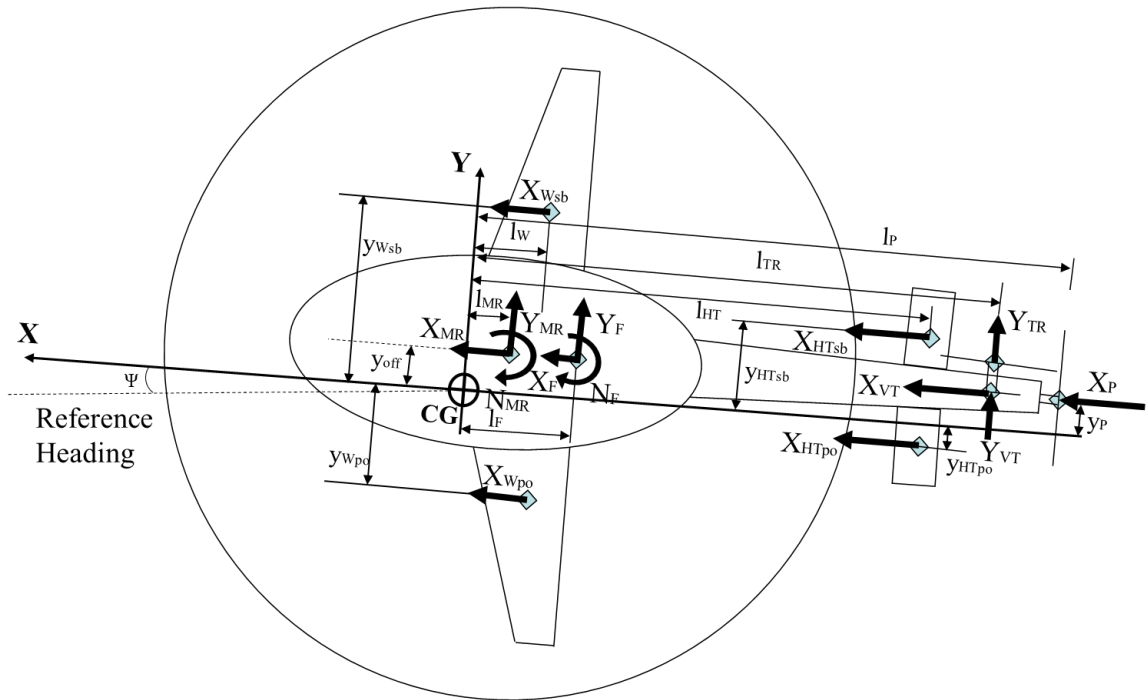


Figure 2-10: Free Body Diagram of The Generic Compound Rotorcraft Configuration-Top View

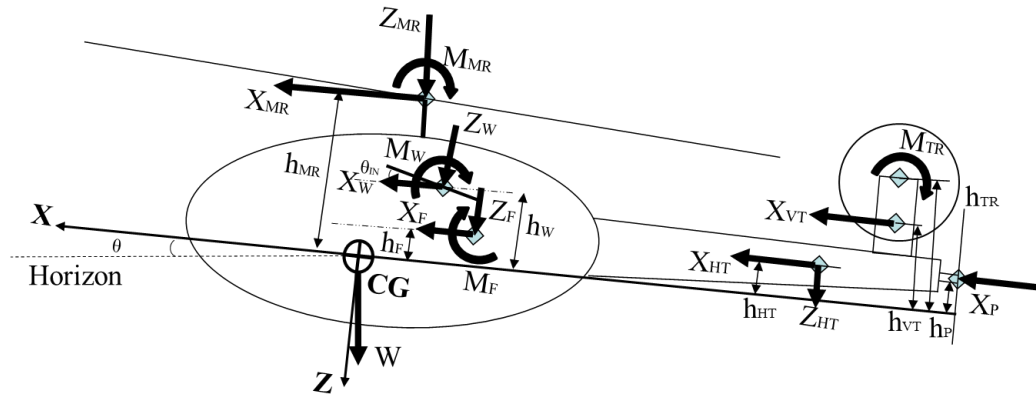


Figure 2-11: Free Body Diagram of The Generic Compound Rotorcraft Configuration-Side View

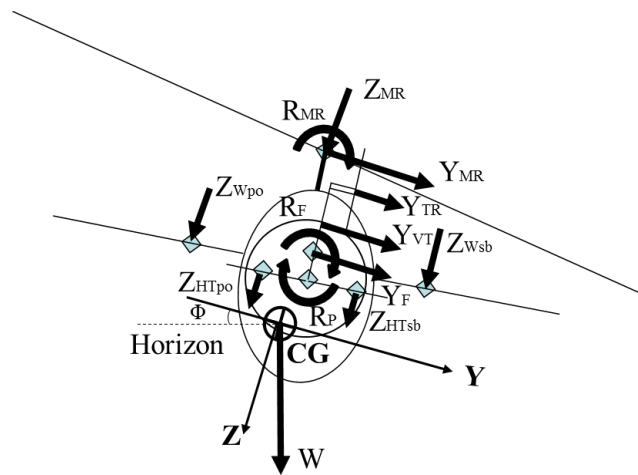


Figure 2-12: Free Body Diagram of The Generic Compound Rotorcraft Configuration-Rear View

The forces experienced by the wings and the horizontal tail are defined by the location of the force. The wing and the horizontal tail on the right hand side are called “Starboard” and the subscript “sb” is used, and the ones on the left hand side are called “Port” and the subscript “po” is used. However, for the ease of deriving the force and moment balance equations, the total forces by the wings and the horizontal tail are used as the summation of forces from starboard and port side wings. The forces and moments from each component are investigated in the following sections in detail.

2.3.1.1 Main Rotor

The main rotor as the source of forces and moments on the helicopter is shown in Figure 2-13 and is described by the equations 2.14 to 2.19, where T_{MR} is the main rotor thrust, β_{1s} , β_{1c} are the lateral and longitudinal flapping angles, β is the sideslip angle, H_{MR} is the rotor H-force, Q_{MR}

is the rotor torque, and $\left(\frac{dR_{MR}}{d\beta_{1s}}\right)$ and $\left(\frac{dR_{MR}}{d\beta_{1c}}\right)$ are the hub rolling and pitching moment stiffness values.

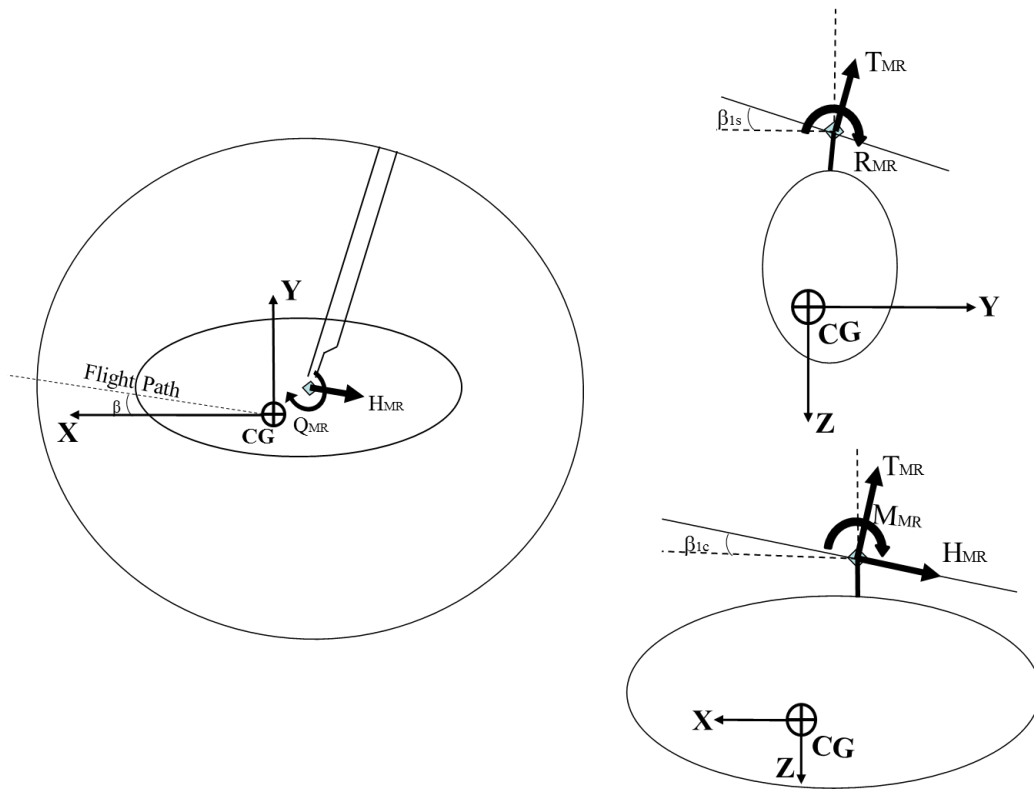


Figure 2.13: The Main Rotor Forces and Moments

$$X_{MR} = -H_{MR} \cos(\beta_{1c}) - T_{MR} \sin(\beta_{1c}) \quad (2.14)$$

$$Y_{MR} = T_{MR} \sin(\beta_{1s}) - H_{MR} \sin(\beta) \quad (2.15)$$

$$Z_{MR} = -T_{MR} \cos(\beta_{1c}) \quad (2.16)$$

$$R_{MR} = \left(\frac{dR_{MR}}{d\beta_{1s}} \right) \beta_{1s} + Q_{MR} \sin(\beta_{1c}) \quad (2.17)$$

$$M_{MR} = \left(\frac{dM_{MR}}{d\beta_{1c}} \right) \beta_{1c} - Q_{MR} \sin(\beta_{1s}) \quad (2.18)$$

$$N_{MR} = Q_{MR} \cos(\beta_{1c}) \sin(\beta_{1s}) \quad (2.19)$$

2.3.1.2 Tail Rotor

The tail rotor is assumed to be generating only a normal force to the rotor and a torque due to the rotation of the tail rotor. The force and moment generated by the tail rotor are shown in equations 2-20 and 2-21, where T_{TR} is the tail rotor thrust and Q_{TR} is the tail rotor torque.

$$Y_{TR} = T_{TR} \quad (2.20)$$

$$M_{TR} = Q_{TR} \quad (2.21)$$

2.3.1.3 Fuselage

The forces and moments that fuselage experiences are shown in Figure 2-14 and are described in equations 2.22 to 2.25, where L_F and D_F are the lift and drag forces, SF_F is the side force produced by the fuselage, C_{Rf} , C_{Mf} and C_{Nf} are the roll, pitch and yaw moment coefficients, γ is the angle of climb, α is the angle of attack that fuselage observes during forward flight, θ is the body pitch attitude ($\alpha = \theta - \gamma$), q is the dynamic pressure, and V_∞ is the freestream velocity. The fuselage will produce side forces, rolling and yawing moments as a function of sideslip angle.

$$X_F = -D_F \cos(\alpha) + L_F \sin(\alpha) \quad (2.22)$$

$$Y_F = SF_F \cos(\beta) - D_F \sin(\beta) \quad (2.23)$$

$$Z_F = -L_F \cos(\alpha) - D_F \sin(\alpha) \quad (2.24)$$

$$R_F = C_{Rf} q, \quad M_F = C_{Mf} q, \quad N_F = C_{Nf} q \quad (2.25)$$

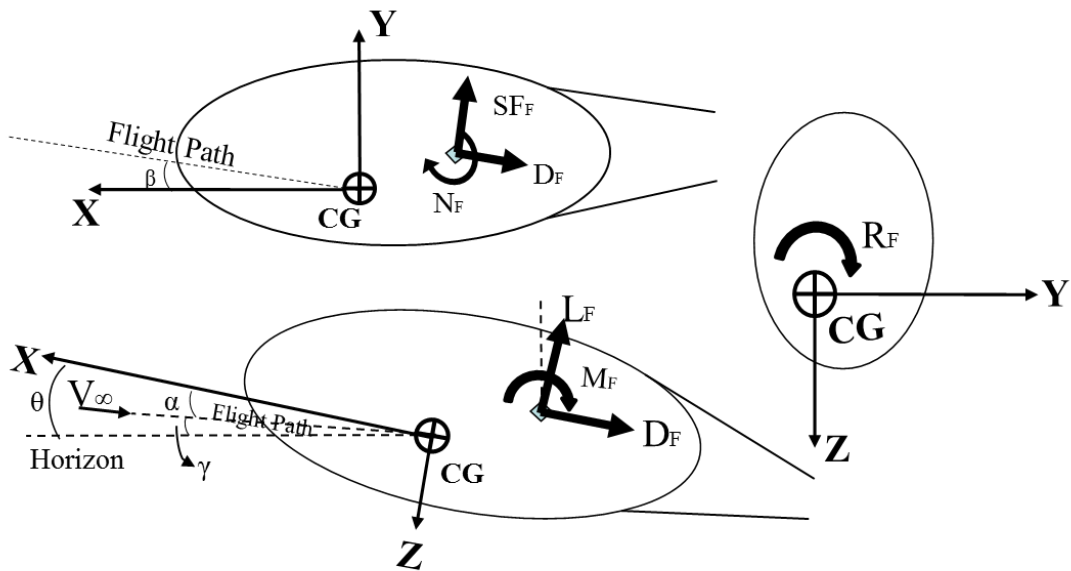


Figure 2.14: The Fuselage Forces and Moments

2.3.1.4 Propeller

The propeller is assumed to be the source of only thrust force and a torque due to the rotation of the propeller. The other forces and moments are assumed to be negligible when compared with the thrust and torque of the rotor. Equations 2-26 and 2-27 show the force and moment generated by the propeller, where T_P is the propeller thrust and Q_P is the propeller torque.

$$X_P = T_P \quad (2.26)$$

$$R_P = Q_P \quad (2.27)$$

Although in this basic trim theory study the UH-60L/VTDP compound rotorcraft model has not been used, it is worthwhile to discuss how VTDP is generating forces and moments. The VTDP compound rotorcraft has different flight modes for low and high-speed forward flight. The VTDP configuration allows aircraft to generate a side force to overcome the torque developed by the main rotor. At low speeds, the extendable duct allows air flow to deflect at right angle and therefore change the direction of the thrust vector from the propeller. At high speeds, a simple rudder deflection generates enough force to overcome the torque by the main rotor.

2.3.1.5 Wings

The forces and moments that wings experience are described in equations 2.28 to 2.30, where L_W and D_W are the lift and drag forces produced by the wings and are functions of angle of attack and wing incidence angle. Changing the wing incidence during flight or using flaperons control the lift force produced by the wings. Differential use of flaperons between starboard and port sides produces a rolling and a yawing moment on the aircraft.

$$X_W = L_W \sin(\alpha - \theta_{in}) - D_W \cos(\alpha - \theta_{in}) \quad (2.28)$$

$$Z_W = -L_W \cos(\alpha - \theta_{in}) - D_W \sin(\alpha - \theta_{in}) \quad (2.29)$$

$$M_W = C_{Mw} q \quad (2.30)$$

2.3.1.6 Horizontal/Vertical Tail

The lift and drag forces of the horizontal and vertical tails are important components of trim calculations. Equations 2.31 to 2.34 show the forces generated by the horizontal and vertical

tails, where L_{HT} , D_{HT} , L_{VT} and D_{VT} are the lift and drag forces produced by the horizontal and vertical tails and are functions of angle of attack and sideslip angle respectively, α is the angle of attack that fuselage observes during forward flight, θ_{HTin} is the horizontal tail incidence angle that is controllable by the flight control system and β is the sideslip angle that fuselage observes during forward flight.

$$X_{HT} = L_{HT} \sin(\alpha - \theta_{HTin}) - D_{HT} \cos(\alpha - \theta_{HTin}) \quad (2.31)$$

$$Z_{HT} = -L_{HT} \cos(\alpha - \theta_{HTin}) - D_{HT} \sin(\alpha - \theta_{HTin}) \quad (2.32)$$

$$X_{VT} = -D_{VT} \cos(\beta) - L_{VT} \sin(\beta) \quad (2.33)$$

$$Y_{VT} = L_{VT} \cos(\beta) - D_{VT} \sin(\beta) \quad (2.34)$$

2.3.2 Change in Trim with Redundant Controls

Baseline helicopter configuration has four standard control variables: main rotor collective blade pitch, θ_0 , main rotor longitudinal cyclic blade pitch, θ_{1s} , main rotor lateral cyclic blade pitch, θ_{1c} , and tail rotor collective blade pitch, θ_{TR} . These four control variables can only have one unique combination in trimmed flight. However, a compound rotorcraft has nine control variables: main rotor blade pitch angles, θ_0 , θ_{1c} , θ_{1s} , tail rotor collective blade pitch θ_{TR} , thrust of the propeller controlled by the propeller blade pitch, β_p , symmetric and differential flaperon deflection angles, δ_{F0} , δ_{Flat} , horizontal stabilator deflection angle, δ_e , and rotor speed for variable rotor speed configuration, Ω . Compound rotorcraft has four additional control variables when compared to baseline configuration, as well as the variable rotor speed which creates an additional redundancy in controls. The redundancy allows the compound helicopter to achieve trim at a flight condition with various control combinations.

Pitch attitude and airspeed are coupled for the baseline helicopter configuration. To increase the airspeed, the propulsive component of main rotor thrust must be increased by tilting the thrust force and tip path plane forward while keeping the lift component constant, which requires increasing the magnitude of the main rotor thrust. Pitch attitude can also vary with the tilting of tip path plane depending on the configuration of the helicopter. A configuration with a single main rotor and a single tail rotor has the pitch attitude tightly coupled with airspeed. For a configuration with horizontal stabilizers the pitch attitude of the aircraft can be reduced at trim with changing airspeed. The control of horizontal stabilizers also allows using a combination of pitch attitude and tip path plane tilt. Figure 2-15 illustrates how an increase in airspeed changes the trim state of the aircraft pitch attitude for a single main rotor and a single tail rotor configuration. In order to accelerate, the main rotor thrust is tilted forward by tilting the tip path plane forward, which induces a forward pitch attitude.

For a compound rotorcraft a trim condition for forward flight can be achieved by various combinations of thrust from main rotor, auxiliary propulsive force from propeller, lift from the wings and pitch attitude. By looking at the equations 2.8, 2.10 and 2.12 for forward and vertical force, and pitching moment balance and substituting the forces and moments of each component, the relationship between aircraft attitude and lift/thrust distribution can be identified. Equations 2.35 to 2.37 shows the force and moment balance defined by equations 2.8, 2.10 and 2.12 in detail with force and moment terms of each component during forward flight.

$$\begin{aligned}
 & -H_{MR} \cos(\beta_{1c}) - T_{MR} \sin(\beta_{1c}) + T_P - D_F \cos(\alpha) + L_F \sin(\alpha) \\
 & + L_W \sin(\alpha - \theta_{in}) - D_W \cos(\alpha - \theta_{in}) + L_{HT} \sin(\alpha - \theta_{HTin}) \\
 & - D_{HT} \cos(\alpha - \theta_{HTin}) - D_{VT} \cos(\beta) - L_{VT} \sin(\beta) - W \sin(\theta) = 0
 \end{aligned} \tag{2.35}$$

$$\begin{aligned}
 & -T_{MR} \cos(\beta_{1c}) - L_F \cos(\alpha) - D_F \sin(\alpha) - L_W \cos(\alpha - \theta_{in}) \\
 & - D_W \sin(\alpha - \theta_{in}) - L_{HT} \cos(\alpha - \theta_{HTin}) \\
 & - D_{HT} \sin(\alpha - \theta_{HTin}) + W \cos(\Theta) \cos(\phi) = 0
 \end{aligned} \tag{2.36}$$

$$\begin{aligned}
& \left(\frac{dM_{MR}}{d\beta_{1c}} \right) \beta_{1c} - Q_{MR} \sin(\beta_{1s}) + C_{Mf} q + Q_{TR} + C_{Mw} q - T_{MR} \cos(\beta_{1c}) l_{MR} \\
& + (H_{MR} \cos(\beta_{1c}) + T_{MR} \sin(\beta_{1c})) h_{MR} - (L_F \cos(\alpha) + D_F \sin(\alpha)) l_F \\
& + (D_F \cos(\alpha) - L_F \sin(\alpha)) h_F - T_P h_P - (L_W \cos(\alpha - \theta_{in}) + D_W \sin(\alpha - \theta_{in})) l_W \\
& - (L_W \sin(\alpha - \theta_{in}) - D_W \cos(\alpha - \theta_{in})) h_W - (L_{HT} \cos(\alpha - \theta_{HTin}) + D_{HT} \sin(\alpha - \theta_{HTin})) l_{HT} \\
& - (L_{HT} \sin(\alpha - \theta_{HTin}) - D_{HT} \cos(\alpha - \theta_{HTin})) h_{HT} - (D_{VT} \cos(\beta) - L_{VT} \sin(\beta)) h_{VT} = 0
\end{aligned} \tag{2.37}$$

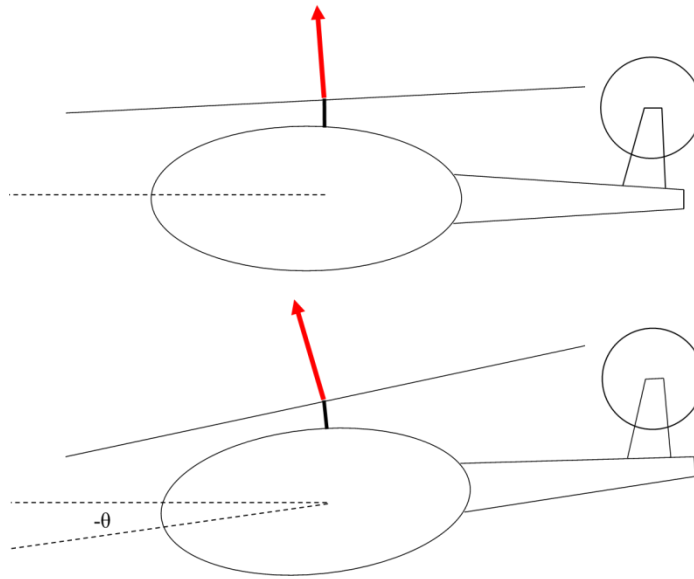


Figure 2-15: Acceleration in a Baseline Helicopter Configuration

In order to study equations 2.35, 2.36 and 2.37 to understand the effects of auxiliary components on rotorcraft trim, the following assumptions were made and equations 2.38 to 2.40 were obtained:

- Small angles are used for rotor flapping, aircraft pitch and roll attitude,
- Wings, fuselage and horizontal and vertical tail lift and drag forces are proportional to the angle of attack of the aircraft,
- Main rotor H force is assumed to be too small compared to rotor thrust
- For vertical force balance the drag force compared to lift force from wings and the fuselage are assumed to be too small,

- Component of main rotor torque on pitching moment is assumed to be too small compared to the main rotor hub moment due to main rotor stiffness.

These assumptions are only made to study the auxiliary component effects. The simulation model uses the non-linear equations of motions and do not include any of the assumptions made above.

$$-T_{MR}\beta_{1c} + T_P + L_W(\alpha - \theta_{in}) - D_F - D_W - D_{HT} - D_{VT} - W\theta = 0 \quad (2.38)$$

$$-T_{MR} - L_{HT} - L_F - L_W + W = 0 \quad (2.39)$$

$$\begin{aligned} \left(\frac{dM_{MR}}{d\beta_{1c}} \right) \beta_{1c} + C_{Mf}q + Q_{TR} + C_{Mw}q - T_{MR}l_{MR} + T_{MR}\beta_{1c}h_{MR} \\ - L_F l_F + D_F h_F - T_P h_P - L_W l_W - (L_W(\alpha - \theta_{in}) - D_W)h_W \\ - L_{HT} l_{HT} - (L_{HT}(\alpha - \theta_{HTin}) - D_{HT})h_{HT} - D_{VT} h_{VT} = 0 \end{aligned} \quad (2.40)$$

The fuselage, wing and tail lift and drag forces are proportional to the angle of attack and the sideslip angle of the aircraft. The wing and stabilator forces are also functions of symmetric and differential flaperons and stabilator deflection angles that are commanded by the flight control system. Auxiliary propulsive force is controlled by the flight control system as well as the main rotor thrust. In order to further simplify the forward force balance equation, drag forces of fuselage, wing, horizontal tail and vertical tail are grouped and called total body drag force, D_{body} . For the pitching moment balance equation, moments due to fuselage, wings, tail rotor, vertical tail and moment of horizontal tail due to forward directional force are grouped and called total body pitch moment, M_{body} . Thus, the forward and vertical force balance can be represented as shown in equations 2.41 and 2.42, and pitching moment balance in equation 2.43.

$$T_P - T_{MR}\beta_{1c} + L_W(\alpha - \theta_{in}) - D_{Body} = W\theta \quad (2.41)$$

$$T_{MR} + L_W + L_{HT} + L_F = W \quad (2.42)$$

$$\left(\frac{dM_{MR}}{d\beta_{1c}} \right) \beta_{1c} - T_{MR}l_{MR} + T_{MR}\beta_{1c}h_{MR} - T_P h_P - L_{HT}l_{HT} - M_{Body} = 0 \quad (2.43)$$

Equation 2.42 states the relationship between the main rotor thrust force and the wing lift force, while assuming the fuselage and horizontal tail lift forces are negligible when compared to the main rotor thrust and the wing lift. The total lift force required to hold the aircraft in trim is shared between main rotor and wing. Equations 2.41 and 2.43 show the relationship between the auxiliary thrust force, the main rotor flapping angle and aircraft pitch attitude. Increasing auxiliary thrust will induce a pitching moment and to reach trim either rotor flapping can be increased or main rotor thrust can be decreased, which leads to an increase on the lift by the wings due to the vertical force balance. Following to the pitching moment equilibrium, in order to reach equilibrium in forward force balance, aircraft attitude has to change as well. Figure 2-16 illustrates how an increase in the auxiliary thrust changes the trim state of the compound rotorcraft.

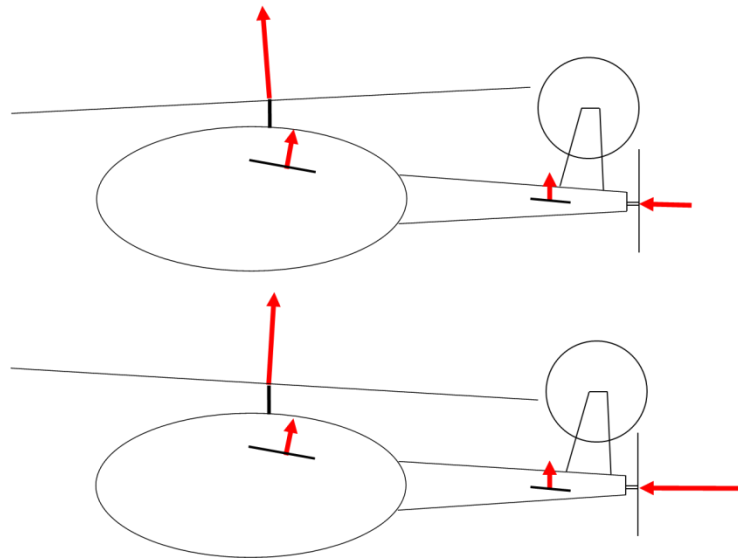


Figure 2-16: Acceleration in a Compound Helicopter Configuration

High advance ratios can lead to reduction in the collective effectiveness of the main rotor, due to the growing reverse flow region on the retreating side blades [70]. The total negative lift from the reverse flow region matches the total lift of the main rotor at high advance ratios and at

even higher advance ratios the total lift of the overall main rotor becomes negative. As these high advance ratios, the collective control authority diminishes rapidly to the point of reversal and beyond. Figure 2-17 shows the rotor lift derivative of collective pitch response to the advance ratio for various rotors [70]. In addition to experimental data, predictions from a simple blade element theory with uniform inflow and CAMRAD II analysis with non-uniform inflow are presented. The collective control authority reduction occurs and collective response reversal occurs at around a critical advance ratio of 0.95.

The similar trend in the collective response observed for the generic compound rotorcraft model. GENHEL-PSU uses the blade element theory for rotor force and moment calculations. Lift and drag characteristics are provided for the range of 360 degrees by applying simple sweep theory and making corrections at high Mach numbers to avoid discontinuities in blade lift and drag data [61]. Fully coverage of angle of attack allows definition of aerodynamic characteristics on the retreating side of the rotor where reverse flow occurs. Figure 2-18 presents the collective effectiveness for increasing airspeed and the lift response derivative for collective pitch is shown to be decreasing with increasing airspeed. Therefore, for high-speed flight (i.e. airspeeds above the maximum speed capabilities of the baseline helicopter), the trim algorithm is altered.

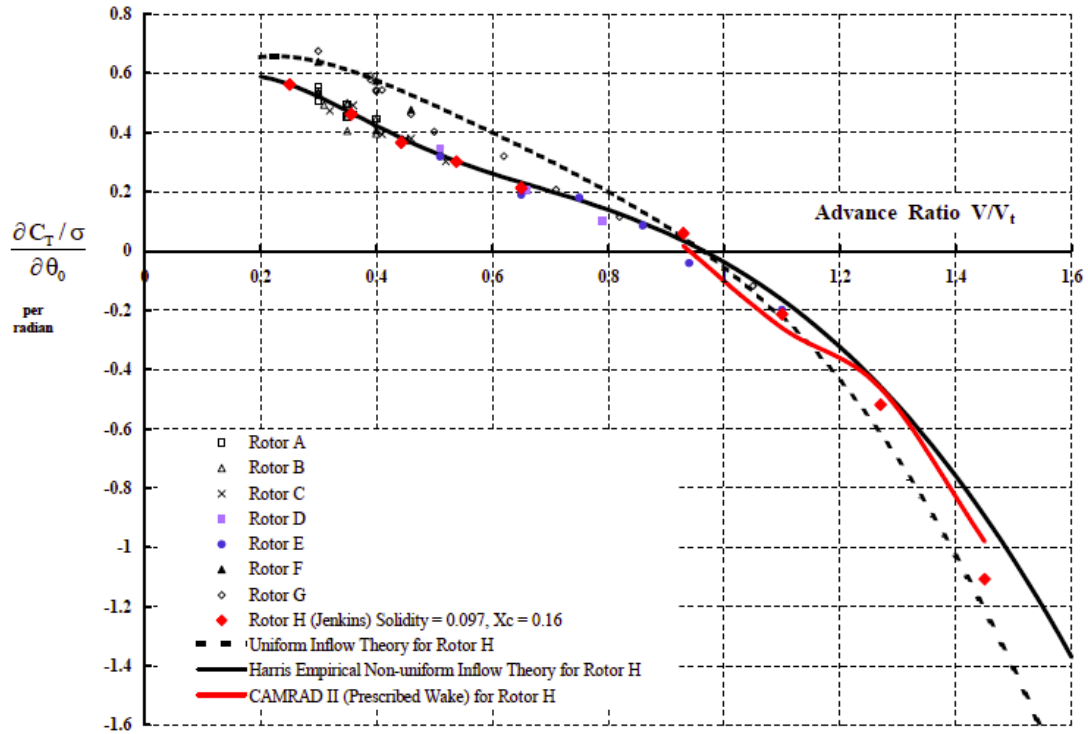


Figure 2-17: Rotor Lift Response Derivative for Collective Pitch [70]

For the sake of a point of reference, high-speed flight will be characterized as level flight trim above 180 knots. In the standard helicopter trim algorithm, collective is adjusted to trim vertical acceleration and thus maintain level flight, the pitch attitude is adjusted to trim longitudinal acceleration, and the propeller pitch is held at some user-prescribed value. At speeds approaching and exceeding 200 knots, the collective becomes a much less effective control effector for trimming the aircraft. Vertical force is less sensitive to the collective, causing it to become saturated in an attempt to trim vertical acceleration. At the same time small changes in collective can cause large variations in power required (and probably vibrations as well). The GENHEL-PSU trim algorithm was modified for high-speed trim. The propeller longitudinal force capabilities are used to trim longitudinal acceleration, while pitch attitude trims vertical

acceleration by effectively changing aircraft angle of attack. The collective is then used as a redundant control effector. This control strategy is also used in the high-speed control law.

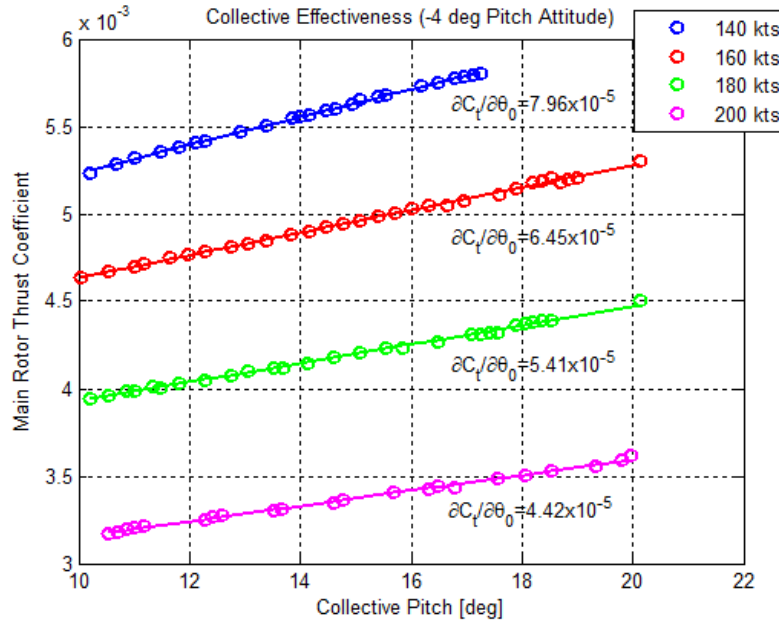


Figure 2-18: Rotor Lift Response Derivative for Collective Pitch of the Generic Compound Rotorcraft Model

2.3.3 Trim Analysis with the Nonlinear Simulation

A trim analysis study was conducted for a level flight condition at 160 knots airspeed and 1000 ft altitude for the generic compound rotorcraft model of GENHEL-PSU. In this analysis, trim procedure is performed for different propeller pitch angle values. Figure 2-19 shows the change in the auxiliary thrust and the main rotor propulsive force with propeller pitch angle at 75% of the propeller radius. Higher propeller thrust reduces the propulsive force component of the main rotor thrust by tilting the tip path plane aft as shown in Figure 2-20. Therefore, the rotorcraft experiences a nose up pitching moment and that corresponds to higher lift force from the wings. Figure 2-21 shows the variation of main rotor thrust lift component and the wing lift

force. Figure 2-22 shows the trim collective control stick position for different propeller blade pitch angles and it is observed that collective is reduced for increasing propeller thrust.

The wing and the main rotor shares the most of the load required to balance the weight of the generic compound rotorcraft. The trim analysis of the nonlinear simulation supports the trim theory for compound rotorcraft shown in the previous section. The auxiliary lift and thrust components reduce the load on the main rotor and this can be used to solve the limitations due to the loading on main rotor at high forward speed flight conditions.

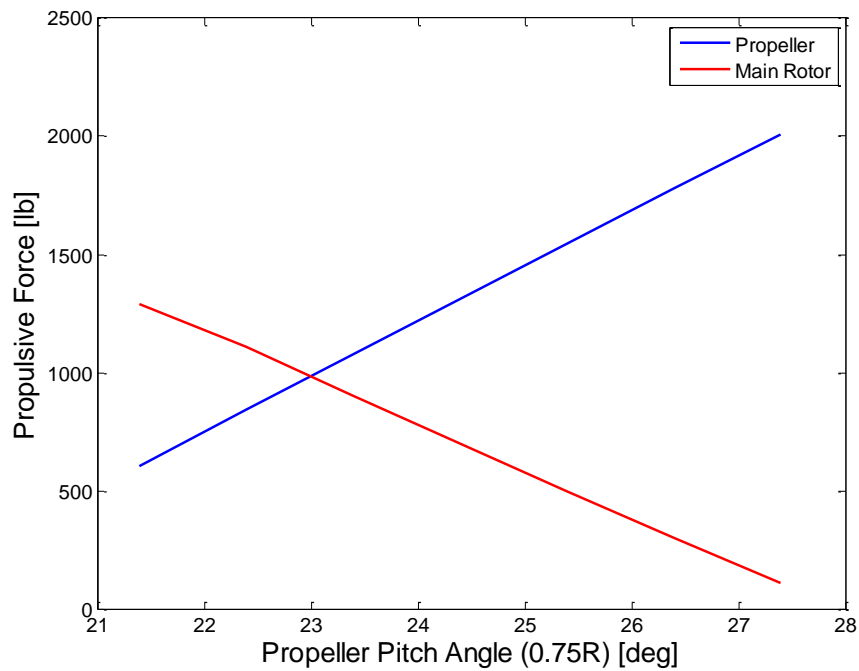


Figure 2-19: Propulsive Forces at Different Propeller Pitch Angles at 160 kts Level Flight

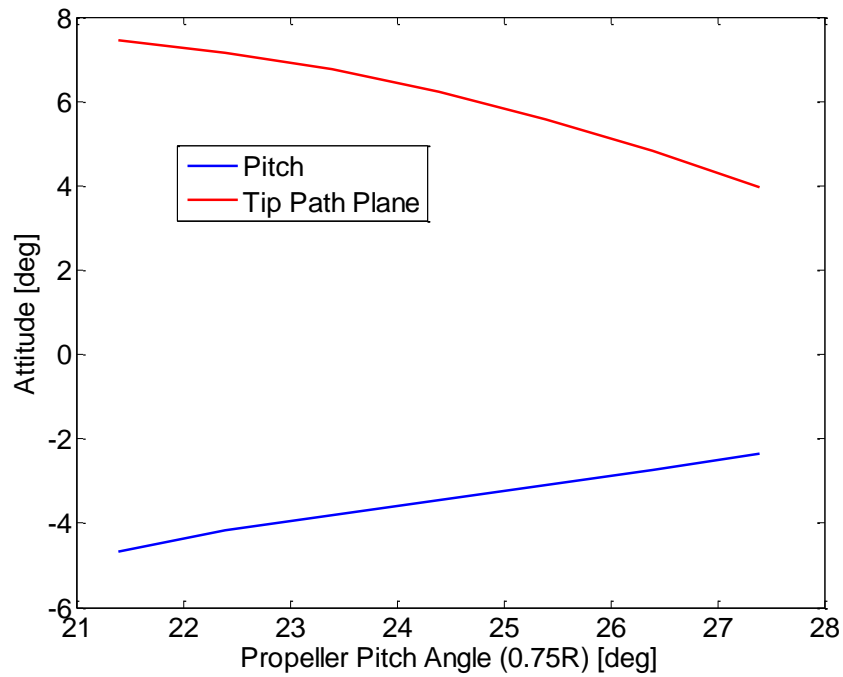


Figure 2-20: Pitch Attitude and TPP Deflection at Different Propeller Pitch Angles

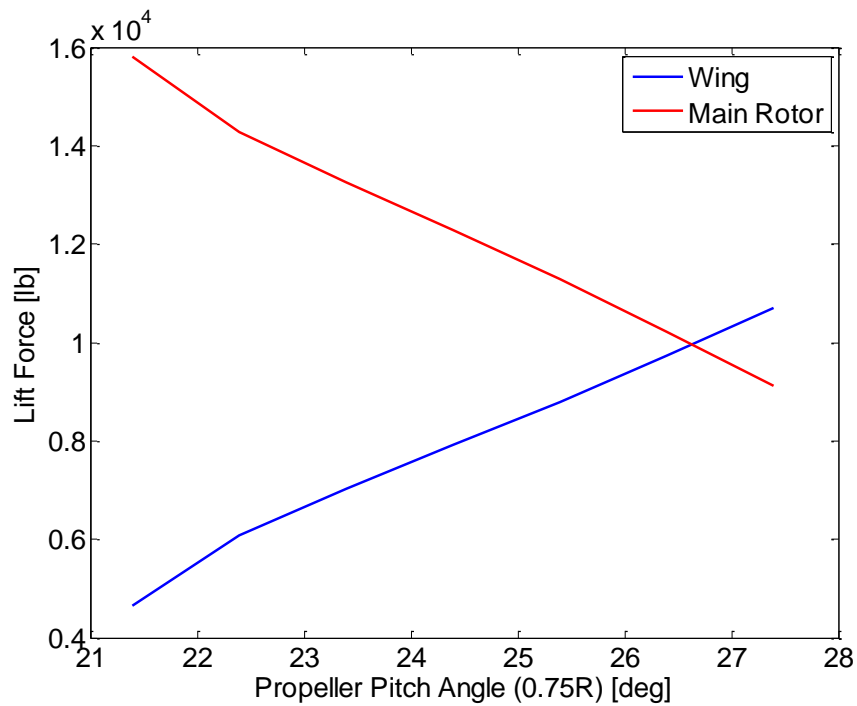


Figure 2-21: Lift Forces at Different Propeller Pitch Angles at 160 kts Level Flight

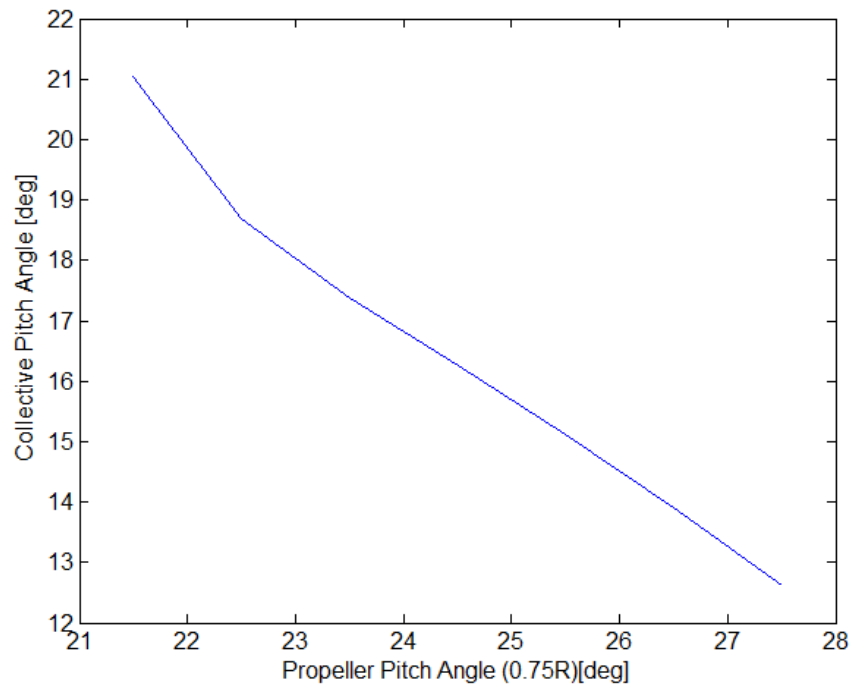


Figure 2-22: Collective Pitch at Blade Root with Different Propeller Pitch Angles at 160 kts Level Flight

Chapter 3

Integrated Flight Control System Design

This chapter presents the development of an integrated flight control system design for a generic compound rotorcraft with variable rotor speed that can also perform an in-flight performance optimization. The flight dynamics model and control system design are based on the modified GENHEL-PSU as described in Chapter 2. The control system architecture should perform flight control, rotor speed control and govern the redundant controls of generic compound rotorcraft to improve performance characteristics. In a steady level flight, the integrated flight control system will optimize rotorcraft performance and hold the trimmed flight condition. Once the optimization process is initiated, the control system will adjust the rotorcraft controls to hold the aircraft in steady state, which is essential for performance measurements.

The flight control system architecture consists of an inner loop, a dynamic inversion control of roll, pitch, yaw, heave and rotor RPM axes, and an outer loop, which can have different modes depending on flight condition. At low airspeeds, which are from hover to 60 knots, a translational rate command (TRC) controller was designed. Forward and sideward translational rate commands are tracked by controlling the pitch and roll attitude commands, which are sent to the inner loop to track corresponding pitch and roll attitudes. For velocities up to 180 knots, the outer loop regulates the forward velocity using pitch attitude commands sent to the inner loop. This is called Cruise Speed Flight (CSF) mode. In this mode, vertical speed is regulated with collective pitch in the inner loop control law, and the propeller pitch is a redundant control effector that can be optimized. The outer loop acts as an airspeed hold type of controller and the lateral input is directly sent to the inner loop as the roll attitude command. For velocities higher than 180 knots, the main rotor collective pitch is no longer an effective control for forward

propulsive force and lift, as discussed with regard to the trim algorithms. Auxiliary thrust, via propeller blade pitch, is used to regulate airspeed and pitch attitude of the rotorcraft is used to control vertical velocity. This is called the High-Speed Flight (HSF) mode. In this mode the collective pitch is a redundant control effector which can be optimized. All of the outer loop controllers use a dynamic inversion type of control scheme based on linearized models of the rotorcraft scheduled with airspeed. For TRC and CSF mode controllers, vertical velocity is controlled by collective pitch in the inner loop and for HSF mode the collective pitch is used as a redundant control effector. Figures 3-1 to 3-3 show the general layout of the integrated flight control system architecture for different flight speed modes.

The following sections discuss the details about the control system design, where the control law development and analysis are shown in detail. Rotor State Feedback (RSF) module of the controller was developed [46] to mitigate rotor instability and high vibratory loads occurring at reduced rotor speeds. The RSF controller was developed for baseline helicopter configuration and is applicable to the compound configurations.

3.1 Control System Design

The control law design uses 28th order linearized models extracted from the GENHEL-PSU simulation model using a perturbation method. The state vector includes 8 rigid body fuselage states (3 velocities, 3 angular rates, pitch and roll Euler angles), 12 rotor states (flapping and lagging dynamics in multi-blade coordinates), 3 inflow states (Pitt-Peters model), and 5 engine states (rotor speed and turbine engine states). The input vector consists of the lateral, longitudinal, collective, and yaw inputs to the UH-60A control mixer, and the RPM governor input.

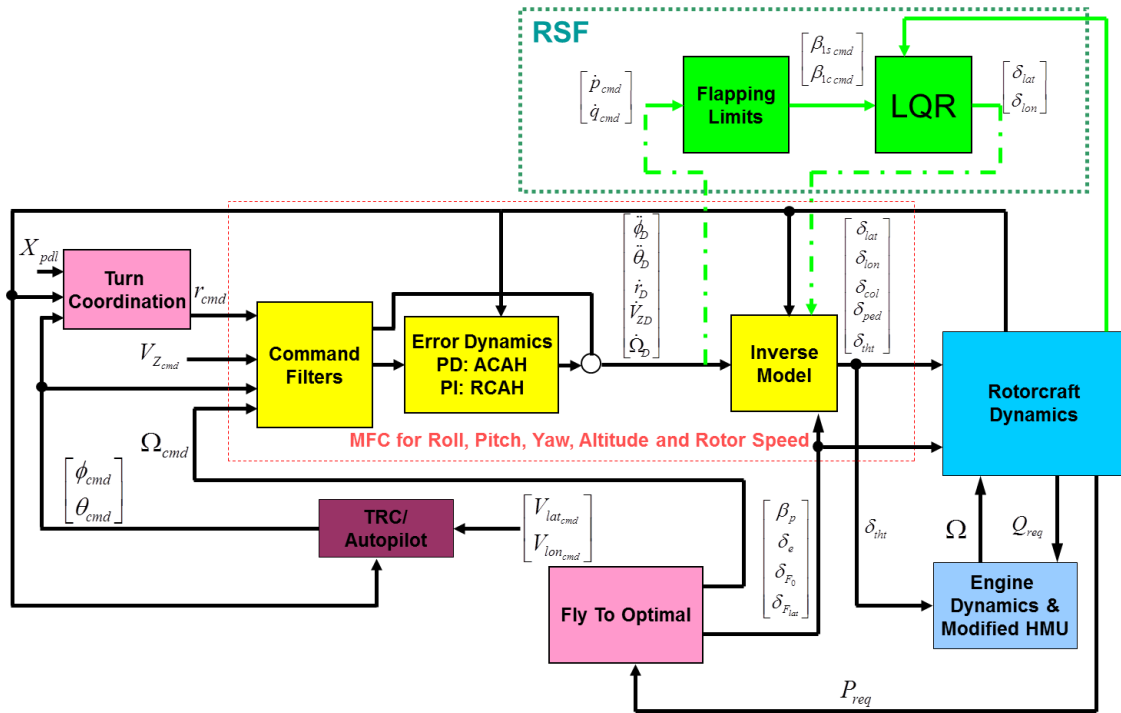


Figure 3-1: General Layout of the Integrated Flight Control System for Low Speed Flight

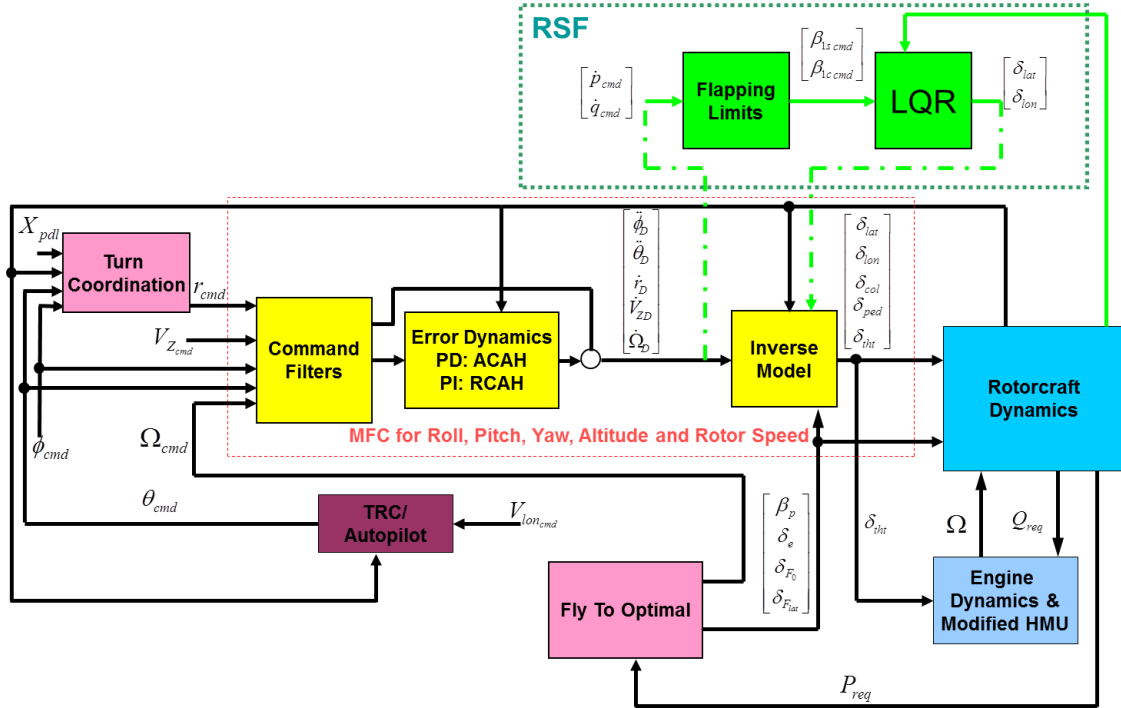


Figure 3-2: General Layout of the Integrated Flight Control System for Cruise Speed Flight

coordination component of the controller to generate yaw rate commands to regulate lateral acceleration; and the “Fly to Optimal” (FTO) tool designed to command rotor speed, rotorcraft controls and compound controls and drive them to an optimal by using optimization methods. As stated in the previous section, the control system has three different designs for low, cruise and high-speed forward flight. The differences in the outer loop for the control of airspeed drives required modifications in the inner loop as well. Especially for HSF controller, the vertical velocity is regulated by pitch attitude commands sent from the outer loop. Therefore, the inner loop governs only four states; pitch attitude, roll attitude, yaw rate and rotor speed and excluding heave axis, which makes the collective pitch a redundant control effector. The next section will discuss the control system design for TRC and CSF controllers with inner loop controlling pitch attitude, roll attitude, yaw rate, rotor speed and vertical velocity. Also HSF controller with inner loop regulating roll, pitch, yaw and rotor speed axes. In-flight optimization methods and FTO tool will be discussed in Chapter 4. The following subsections will introduce dynamic inversion controller and outer loop controller modes. The control laws also include a Rotor State Feedback (RSF) controller, which provides an additive signal to the cyclic inputs to mitigate rotor instability that can occur at reduced rotor speeds. Discussion about the RSF control law can be found in the study by Guo [63].

3.1.1 Inner Loop Control Law

The inner loop control law design is based on the model following and dynamic inversion control design. The dynamic inversion controller does not require gain scheduling since it takes the nonlinearities of the aircraft into account. Therefore, the controller is suitable for a wide range of flight conditions [3]. Although dynamic inversion is a powerful tool for nonlinear systems, in this study the dynamic inversion controller is designed using linearized models of the nonlinear

rotorcraft model. However, since the model is linearized at different airspeeds and linear models are scheduled with airspeed, this induces the nonlinearity in the control system design.

The aim of this control law is to let aircraft respond to the pilot command as a first or second order linear system. The inner loop controller is designed to achieve Attitude Command Attitude Hold (ACAH) response in the roll and pitch axes, rotor speed command rotor speed hold in the rotor RPM axis, Rate Command Attitude Hold (RCAH) response in the yaw axis, and vertical speed command in the heave axis. The ACAH response type controller and rotor speed command type controller is illustrated in Figure 3-4 and the RCAH response type controller and vertical speed command type controller is illustrated in Figure 3-5. The commanded states are shown in Equation 3.1. Commanded states are passed through a command filter that represents the ideal dynamic response characteristics, to yield the desired states, and first and second time derivatives of the states, as shown in equation 3.2.

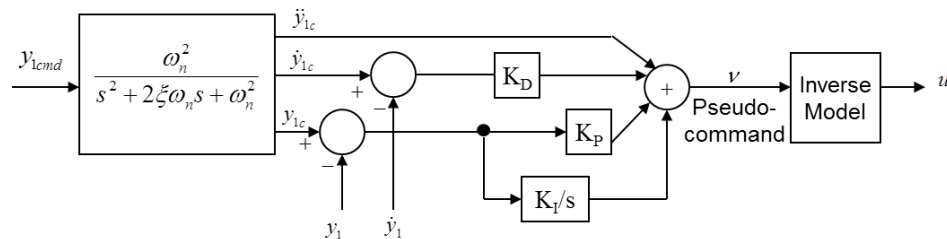


Figure 3-4: Model Following and Dynamic Inversion Control for ACAH

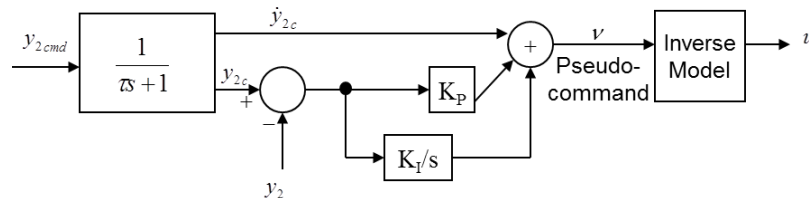


Figure 3-5: Model Following and Dynamic Inversion Control for RCAH

$$y_{cmd} = \begin{bmatrix} \phi_{cmd} \\ \theta_{cmd} \\ \Omega_{cmd} \\ r_{cmd} \\ V_{Z_{cmd}} \end{bmatrix} \quad (3.1)$$

$$y_c = \begin{bmatrix} \phi_c \\ \theta_c \\ \Omega_c \\ \int r_c \\ \int V_{Z_c} \end{bmatrix} \quad \dot{y}_c = \begin{bmatrix} \dot{\phi}_c \\ \dot{\theta}_c \\ \dot{\Omega}_c \\ r_c \\ V_{Z_c} \end{bmatrix} \quad \ddot{y}_c = \begin{bmatrix} \ddot{\phi}_c \\ \ddot{\theta}_c \\ \ddot{\Omega}_c \\ \dot{r}_c \\ \dot{V}_{Z_c} \end{bmatrix} \quad (3.2)$$

The yaw axis transitions to a turn coordination mode between 40 and 60 knots. Turn coordination uses a computed yaw rate approach, where the pilot inceptor (pedals) is proportional to commanded lateral acceleration, and the yaw rate command is then calculated as:

$$r_{cmd} = \frac{g(a_{y_{cmd}} + \sin \phi \cos \theta)}{V} \quad (3.3)$$

Second-order command filter is used for the roll and pitch attitude control, and rotor speed control. A first-order command filter is used for the yaw and heave axes.

$$\ddot{\phi}_c + 2\xi_\phi \omega_\phi \dot{\phi}_c + \omega_\phi^2 (\phi_c - \phi_{cmd}) = 0 \quad (3.4)$$

$$\ddot{\theta}_c + 2\xi_\theta \omega_\theta \dot{\theta}_c + \omega_\theta^2 (\theta_c - \theta_{cmd}) = 0 \quad (3.5)$$

$$\ddot{\Omega}_c + 2\xi_\Omega \omega_\Omega \dot{\Omega}_c + \omega_\Omega^2 (\Omega_c - \Omega_{cmd}) = 0 \quad (3.6)$$

$$\tau_r \dot{r}_c + (r_c - r_{cmd}) = 0 \quad (3.7)$$

$$\tau_{V_z} \dot{V}_{Z_c} + (V_{Z_c} - V_{Z_{cmd}}) = 0 \quad (3.8)$$

The parameters of the command filter are selected to meet desired handling qualities specifications. In this study, the parameters were selected to meet Level 1 specifications as designated by ADS-33E for small-amplitude response (bandwidth) in roll, pitch and yaw. The

natural frequency, damping ratios, and time constants for command filters are given in Table 3-1. The filtered states and state derivatives are compared to measured outputs of plant described in equation 3.9, where state and input vectors are defined in equation 3.10, and tracking error for each axis is defined as shown in equation 3.11.

Table 3-1: Parameters of Command Filter

Command Filter	Natural Frequency (ω_n) (rad/sec)	Damping Ratio (ξ)	Time Constant (τ) (sec)
Roll Attitude	2.5	0.8	-
Pitch Attitude	2.5	0.8	-
Rotor Speed	5.0	0.8	-
Yaw Rate	-	-	0.4
Vertical Velocity	-	-	2.0

A dynamic inversion model is implemented in the controller, where the inversion model is based on a 12th-order linear model; 8 rigid body fuselage states and 4 engine states. This is reduced from the full 28th order linear model extracted from GENHEL. The linear model includes five inputs; four pilot inputs of lateral cyclic, longitudinal cyclic, pedal and collective input; and an engine throttle input. There are four additional inputs for the compound configuration that is set by the FTO tool and assumed to be known for the dynamic inversion calculations. The state space model is shown in equation 3.9. The A matrix is 12 by 12, the B₁ matrix is 12 by 5, the B₂ matrix is 12 by 4, and the C matrix is 5 by 12. The output, y , has the same dimension with input vector, which makes this a square system. For a square system, desired response can be achieved by tracking a reference command.

In dynamic inversion, the input-output feedback linearization technique is used by differentiating the output, y , until the controls appear in the expression for the derivative [3]. By taking the first derivative of the output, y , equation 3.12 is obtained. The output, u , appears in equation 3.12 if the matrix CB_1 is not equal to zero. If CB_1 is equal to zero or singular, then the differentiation has to be performed again. Equation 3.13 is the second derivative of the output and

CAB_1 is the term that appears with the input. If CAB_1 is singular too, differentiation should continue until the coefficient of input, u_1 , is not zero.

$$\begin{aligned}\dot{x} &= Ax + B_1u_1 + B_2u_2 \\ y &= Cx\end{aligned}\quad (3.9)$$

$$\begin{aligned}x &= [u \quad v \quad w \quad p \quad q \quad r \quad \phi \quad \theta \quad \Omega \quad x_{e_1} \quad x_{e_2} \quad x_{e_3}]^T \\ u_1 &= [\delta_{lat} \quad \delta_{lon} \quad \delta_{hti} \quad \delta_{ped} \quad \delta_{coll}]^T \\ u_2 &= [\beta_p \quad \delta_e \quad \delta_{F_0} \quad \delta_{F_{ur}}]^T\end{aligned}\quad (3.10)$$

$$e = y_c - y, \quad \dot{e} = \dot{y}_c - \dot{y}\quad (3.11)$$

$$\dot{y} = C\dot{x} = CAx + CB_1u_1 + CB_2u_2\quad (3.12)$$

$$\begin{aligned}\ddot{y} &= C\ddot{x} = CA\dot{x} + CB_1\dot{u}_1 + CB_2\dot{u}_2 \\ &= CA\dot{x} = CA^2x + CAB_1u_1 + CAB_2u_2\end{aligned}\quad (3.13)$$

For the control system design in this study, single differentiation of the output does not guarantee the input to appear in the first derivative of the output. The matrix CB_1 is singular for roll attitude; pitch attitude, and rotor speed; therefore, the output for those three has to be differentiated twice and the equation 3.13 should be used for the control design. However, CB_1 matrix is nonsingular for yaw rate and vertical speed. Thus, single differentiation of the output, as shown in equation 3.12, for those two can be used for the control design.

It must be noted that the heave axis controller is designed to achieve vertical speed command altitude hold type response. Unlike the other control axes, the output variable controlled is not identical to a state. The vertical body velocity w was converted to the inertial vertical velocity V_Z . The conversion is shown in equation 3.14, where V is the trim airspeed. According to this conversion, C matrix is set as shown in equation 3.15.

$$\begin{aligned}w &= -V_Z + V\theta \\ V_Z &= -w + V\theta\end{aligned}\quad (3.14)$$

$$C = \begin{bmatrix} 0 & 0 & 0 & 0 & 0 & 0 & 1 & 0 & 0 & 0 & 0 & 0 \\ 0 & 0 & 0 & 0 & 0 & 0 & 0 & 1 & 0 & 0 & 0 & 0 \\ 0 & 0 & 0 & 0 & 0 & 0 & 0 & 0 & 1 & 0 & 0 & 0 \\ 0 & 0 & 0 & 0 & 0 & 1 & 0 & 0 & 0 & 0 & 0 & 0 \\ 0 & 0 & -1 & 0 & 0 & 0 & 0 & V & 0 & 0 & 0 & 0 \end{bmatrix} \quad (3.15)$$

The difference in the number of differentiations of the output for each axis complicates the way how the controller is designed. The output vector and matrix can then be partitioned to separate variables that require two or one differentiations of the output equation. In addition the control vector can be partitioned, such that the control axes match the differentiation scheme for their corresponding output variables. There will be two components of the output vector: y_1 and y_2 , as shown in equation 3.16. Also the partitioned output matrix components are shown in equations 3.17 and 3.18.

$$\begin{bmatrix} y_1 \\ y_2 \end{bmatrix} = \begin{bmatrix} C_1 \\ C_2 \end{bmatrix} x, \quad u_1 = \begin{bmatrix} u_{1_1} \\ u_{2_3} \end{bmatrix} \quad (3.16)$$

$$y_1 = \begin{bmatrix} \phi_{cmd} \\ \theta_{cmd} \\ \Omega_{cmd} \end{bmatrix}, \quad y_2 = \begin{bmatrix} r_{cmd} \\ V_{zcmd} \end{bmatrix}, \quad u_{1_1} = \begin{bmatrix} \delta_{lat} \\ \delta_{lon} \\ \delta_{tht} \end{bmatrix}, \quad u_{1_2} = \begin{bmatrix} \delta_{coll} \\ \delta_{pdl} \end{bmatrix}$$

$$C_1 = \begin{bmatrix} 0 & 0 & 0 & 0 & 0 & 0 & 1 & 0 & 0 & 0 & 0 & 0 \\ 0 & 0 & 0 & 0 & 0 & 0 & 0 & 1 & 0 & 0 & 0 & 0 \\ 0 & 0 & 0 & 0 & 0 & 0 & 0 & 0 & 1 & 0 & 0 & 0 \end{bmatrix} \quad (3.17)$$

$$C_2 = \begin{bmatrix} 0 & 0 & 0 & 0 & 0 & 1 & 0 & 0 & 0 & 0 & 0 & 0 \\ 0 & 0 & -1 & 0 & 0 & 0 & 0 & V & 0 & 0 & 0 & 0 \end{bmatrix} \quad (3.18)$$

Roll, pitch, and RPM reside in the first partition of the output vector, which indicates the output variables that require two differentiations for input-output feedback linearization. Lateral cyclic, longitudinal cyclic, and the throttle input reside in the first partition of the input. Vertical speed, yaw rate, collective pitch, and pedal inputs reside in the second partitions, which indicate that the output variables vertical speed and yaw rate require one differentiation for input-output

feedback linearization. As the input-output feedback linearization is performed, the output equation in equation 3.9 can be expressed as follows:

$$\begin{bmatrix} \ddot{y}_1 \\ \dot{y}_2 \end{bmatrix} = \begin{bmatrix} C_1 A^2 \\ C_2 A \end{bmatrix} x + \begin{bmatrix} C_1 A B_1 \\ C_2 B_1 \end{bmatrix} \begin{bmatrix} u_{1_1} \\ u_{1_2} \end{bmatrix} + \begin{bmatrix} C_1 A B_2 \\ C_2 B_2 \end{bmatrix} u_2 \quad (3.19)$$

An auxiliary input is defined as shown in equation 3.20, so the input can be defined as in equation 3.21, where $\begin{bmatrix} C_1 A B_1 \\ C_2 B_1 \end{bmatrix}$ is an invertible matrix. Substituting the expression of input, u_1 ,

into the equation 3.19 yields to the pseudo command as defined in equation 3.22.

$$\begin{bmatrix} \rho_1 \\ \rho_2 \end{bmatrix} = \begin{bmatrix} C_1 A^2 \\ C_2 A \end{bmatrix} x + \begin{bmatrix} C_1 A B_1 \\ C_2 B_1 \end{bmatrix} \begin{bmatrix} u_{1_1} \\ u_{1_2} \end{bmatrix} + \begin{bmatrix} C_1 A B_2 \\ C_2 B_2 \end{bmatrix} u_2 - \begin{bmatrix} \ddot{y}_{1c} \\ \dot{y}_{2c} \end{bmatrix} \quad (3.20)$$

$$\begin{bmatrix} u_{1_1} \\ u_{1_2} \end{bmatrix} = \begin{bmatrix} C_1 A B_1 \\ C_2 B_1 \end{bmatrix}^{-1} \left(\begin{bmatrix} \ddot{y}_{1c} \\ \dot{y}_{2c} \end{bmatrix} - \begin{bmatrix} C_1 A^2 \\ C_2 A \end{bmatrix} x - \begin{bmatrix} C_1 A B_2 \\ C_2 B_2 \end{bmatrix} u_2 + \begin{bmatrix} \rho_1 \\ \rho_2 \end{bmatrix} \right) \quad (3.21)$$

$$\begin{aligned} \begin{bmatrix} \ddot{y}_1 \\ \dot{y}_2 \end{bmatrix} &= \begin{bmatrix} C_1 A^2 \\ C_2 A \end{bmatrix} x + \begin{bmatrix} C_1 A B_2 \\ C_2 B_2 \end{bmatrix} u_2 + \begin{bmatrix} C_1 A B_1 \\ C_2 B_1 \end{bmatrix} \left(\begin{bmatrix} C_1 A B_1 \\ C_2 B_1 \end{bmatrix}^{-1} \left(\begin{bmatrix} \ddot{y}_{1c} \\ \dot{y}_{2c} \end{bmatrix} - \begin{bmatrix} C_1 A^2 \\ C_2 A \end{bmatrix} x - \begin{bmatrix} C_1 A B_2 \\ C_2 B_2 \end{bmatrix} u_2 + \begin{bmatrix} \rho_1 \\ \rho_2 \end{bmatrix} \right) \right) \\ &= \begin{bmatrix} C_1 A^2 \\ C_2 A \end{bmatrix} x + \begin{bmatrix} C_1 A B_2 \\ C_2 B_2 \end{bmatrix} u_2 + \begin{bmatrix} \ddot{y}_{1c} \\ \dot{y}_{2c} \end{bmatrix} - \begin{bmatrix} C_1 A^2 \\ C_2 A \end{bmatrix} x - \begin{bmatrix} C_1 A B_2 \\ C_2 B_2 \end{bmatrix} u_2 + \begin{bmatrix} \rho_1 \\ \rho_2 \end{bmatrix} \\ &= \begin{bmatrix} \ddot{y}_{1c} \\ \dot{y}_{2c} \end{bmatrix} + \begin{bmatrix} \rho_1 \\ \rho_2 \end{bmatrix} = \begin{bmatrix} v_1 \\ v_2 \end{bmatrix} \\ \begin{bmatrix} \ddot{y}_1 \\ \dot{y}_2 \end{bmatrix} &= \begin{bmatrix} v_1 \\ v_2 \end{bmatrix} \end{aligned} \quad (3.22)$$

The pseudo commands, v , represent the desired accelerations (angular, RPM, and vertical speed) of the vehicle and passed through an inverse model of aircraft dynamics to get the control inputs. The selection of p defines the error dynamics of the control design. The pseudo command is defined as shown in equation 3.23. K_p , K_I and K_D are diagonal gain matrices, as shown in equation 3.24, representing proportional, integral and derivative (PID & PI) compensation on the

tracking error signals shown in equation 3.25. The PID compensator is used to minimize the tracking error for the roll and pitch attitudes to achieve ACAH type of response, and to minimize rotor speed to achieve rotor speed command rotor speed hold type of response. The PI compensator is used to minimize the tracking error for the yaw rate to achieve RCAH type of response and to minimize vertical speed to achieve vertical speed command type of response.

$$\begin{bmatrix} v_1 \\ v_2 \end{bmatrix} = \begin{bmatrix} \ddot{y}_{1c} \\ \dot{y}_{2c} \end{bmatrix} + \begin{bmatrix} K_P & K_D & K_I \end{bmatrix} \begin{bmatrix} e \\ \dot{e} \\ \int e dt \end{bmatrix} \quad (3.23)$$

$$\begin{aligned} K_P &= \begin{bmatrix} K_{P\phi} & 0 & 0 & 0 & 0 \\ 0 & K_{P\theta} & 0 & 0 & 0 \\ 0 & 0 & K_{P\Omega} & 0 & 0 \\ 0 & 0 & 0 & K_{Pr} & 0 \\ 0 & 0 & 0 & 0 & K_{PV_z} \end{bmatrix} \\ K_D &= \begin{bmatrix} K_{D\phi} & 0 & 0 & 0 & 0 \\ 0 & K_{D\theta} & 0 & 0 & 0 \\ 0 & 0 & K_{D\Omega} & 0 & 0 \\ 0 & 0 & 0 & 0 & 0 \\ 0 & 0 & 0 & 0 & 0 \end{bmatrix} \\ K_I &= \begin{bmatrix} K_{I\phi} & 0 & 0 & 0 & 0 \\ 0 & K_{I\theta} & 0 & 0 & 0 \\ 0 & 0 & K_{I\Omega} & 0 & 0 \\ 0 & 0 & 0 & K_{Ir} & 0 \\ 0 & 0 & 0 & 0 & K_{IV_z} \end{bmatrix} \end{aligned} \quad (3.24)$$

$$e = \begin{bmatrix} e_1 \\ e_2 \end{bmatrix} = \begin{bmatrix} y_{1c} \\ y_{2c} \end{bmatrix} - \begin{bmatrix} y_1 \\ y_2 \end{bmatrix} \quad (3.25)$$

Assuming a perfect representation of the flight dynamics, the tracking error dynamics for output variables would be governed by the differential equation shown in equation 3.26, where the gains K_P , K_D , and K_I can be selected to make sure that tracking error dynamics are stable and

well damped. A typical choice for the compensator gains is that the error dynamics match the ideal response model. In practice we use a very simplified linear model of the aircraft flight dynamics. However, judicious choice of the gains ensures the closed loop system is stable, and tracking errors due to disturbances or modeling error are well regulated.

$$\begin{bmatrix} \ddot{e}_1 \\ \dot{e}_2 \end{bmatrix} + K_D \begin{bmatrix} \dot{e}_1 \\ 0 \end{bmatrix} + K_P \begin{bmatrix} e_1 \\ e_2 \end{bmatrix} + K_I \begin{bmatrix} \int e_1 dt \\ \int e_2 dt \end{bmatrix} = \begin{bmatrix} 0 \\ 0 \end{bmatrix} \quad (3.26)$$

The characteristic equation of the error dynamics can be described in equation 3.27 for ACAH and rotor speed command rotor speed hold response type. The feedback gains of the PID compensator are determined by assigning the controller parameters, natural frequency, damping ratio and a real pole, for each axis. Compensator gains are defined in terms of controller parameters as shown in equation 3.27. The characteristic equation of the error dynamics can be described in equation 3.28 for RCAH and vertical speed command type. The feedback gains of the PI compensator are determined by assigning the controller parameters, natural frequency and damping ratio, for each axis. Compensator gains are defined in terms of controller parameters as shown in equation 3.28. The natural frequency, damping ratio and real pole for the PID compensator gains of roll, pitch, and rotor speed axes and the natural frequency and damping ratio for the PI compensator gains of yaw and heave axes are given in Table 3-2. The overall dynamic inversion control input is given by equation 3.29.

$$\begin{aligned} s^3 + K_D s^2 + K_P s + K_I &= 0 \\ (s^2 + 2\xi\omega_n s + \omega_n^2)(s + p) &= 0 \\ K_P = 2\xi\omega_n p + \omega_n^2 \quad K_I = \omega_n^2 p \quad K_D = 2\xi\omega_n + p \end{aligned} \quad (3.27)$$

$$\begin{aligned} s^2 + K_P s + K_I &= 0 \\ s^2 + 2\xi\omega_n s + \omega_n^2 &= 0 \\ K_P = 2\xi\omega_n \quad K_I = \omega_n^2 \end{aligned} \quad (3.28)$$

$$\begin{bmatrix} u_{1_1} \\ u_{1_2} \end{bmatrix} = \begin{bmatrix} C_1AB_1 \\ C_2B_1 \end{bmatrix}^{-1} \left(\begin{bmatrix} \ddot{y}_{1c} \\ \dot{y}_{2c} \end{bmatrix} + \begin{bmatrix} K_P & K_D & K_I \end{bmatrix} \begin{bmatrix} e \\ \dot{e} \\ \int e dt \end{bmatrix} - \begin{bmatrix} C_1A^2 \\ C_2A \end{bmatrix} x - \begin{bmatrix} C_1AB_2 \\ C_2B_2 \end{bmatrix} u_2 \right) \quad (3.29)$$

Table 3-2: Controller Parameters for Error Dynamics

Control Axis	Natural Frequency (ω_n) (rad/sec)	Damping Ratio (ζ)	Real Pole (p)
Roll Attitude	3.5	1.0	0.75
Pitch Attitude	3.5	1.0	0.75
Rotor Speed	5.0	1.0	0.75
Yaw Rate	2.5	1.0	-
Vertical Velocity	0.5	1.0	-

The control scheme given by this control law is shown in Figures 3.6 and 3.7. In Figure 3.6, v_2 is the pseudo command for the yaw and heave axes control law and in Figure 3.7, v_1 is the pseudo command for the roll, pitch and rotor speed axes control law.

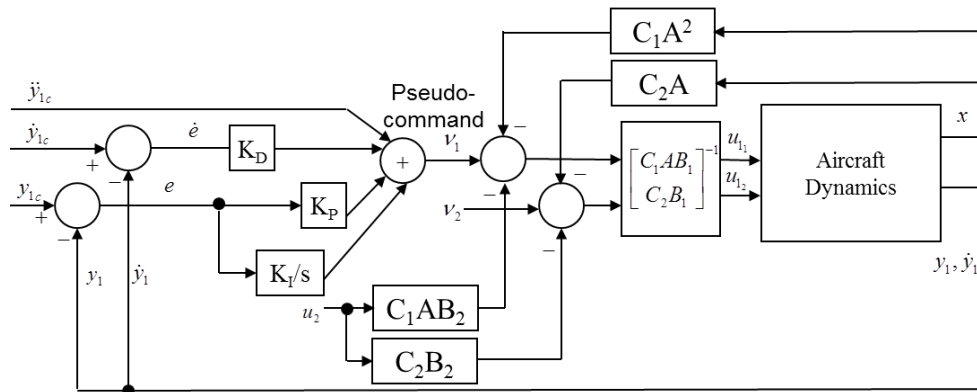


Figure 3.6: Dynamic Inversion Control Scheme for Roll, Pitch and Rotor Speed Axes

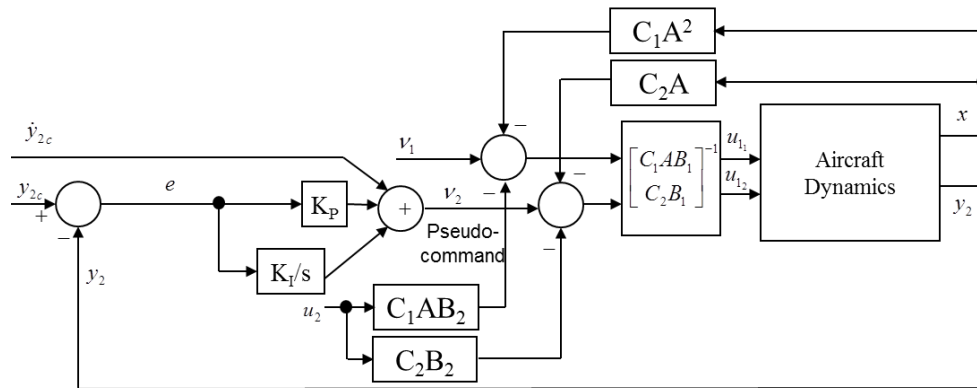


Figure 3.7: Dynamic Inversion Control Scheme for Yaw and Heave Axes

The control system has three different designs for low, cruise and high-speed forward flight. The differences in the outer loop for the control of airspeed drives required modifications in the inner loop as well. Especially for high-speed flight controller, the vertical speed is controlled in the outer loop. Therefore, the inner loop governs only four states; pitch attitude, roll attitude, yaw rate and rotor speed and excludes heave axis. The design of the control law is similar to the one shown above; the heave axis is removed from the equations and collective becomes a redundant control.

In order to let the control law provide desired response and disturbance rejection properties for most flight conditions, linear models in the model inversion are scheduled with flight condition. A simple scheduling approach was used to vary the inverse model with airspeed, while the command filters and compensator gains remain constant.

3.1.2 Outer Loop Control Law

It is important to keep airspeed and altitude as close to the desired set point as possible during an in-flight optimization process. Keeping trimmed flight with constant forward and vertical speed is essential for getting an accurate measurement of power required. Therefore, an

outer loop autopilot is designed to regulate trimmed forward, sideward and vertical speeds during the optimization maneuvers. The controller has three modes scheduled to the airspeed and the following sections discuss these modes.

3.1.2.1 Low Speed Mode – Translational Rate Command Control Law

For the low speed mode controller, where airspeed is below 60 knots, the controller regulates lateral and longitudinal velocities by commanding roll and pitch attitudes sent to the inner loop. Vertical speed is controlled by the inner loop by the dynamic inversion controller.

For the low speed mode of the controller, a model following and model inversion schemed controller used for controlling translational rates as shown in Figure 3-8 with lateral velocity axis. A first order command filter with a time constant of 2.0 sec yields desired state and derivative of lateral velocity. A second-order linear model extracted from the higher-order linear model of the helicopter, as shown in equation 3.30, where the attitude dynamics are assumed faster than translational dynamics, thus roll and pitch attitudes are treated as inputs to the linear model. A PI compensator is added to minimize the tracking error, defined in equation 3.31. The tracking error passes through the PI compensator and added to the desired response of the state derivative to obtain the pseudo command. The pseudo command is passed through the inverse model of the aircraft dynamics to get the roll and pitch command inputs to the inner loop, as shown in equation 3.32. If the inverse model is exact, the aircraft model and inverse model will behave as a simple integrator. The pseudo command is defined in equation 3.33 and the error dynamics are governed as shown in equation 3.34. The PI compensator gains are defined in terms of controller parameters as shown in equation 3.35. The natural frequency and the damping ratio of the error dynamics are set to be 1.0 rad/sec and 0.9. A similar scheduling used in inner loop is

also used for linear models in TRC, to ensure desired response and disturbance rejection properties provided.

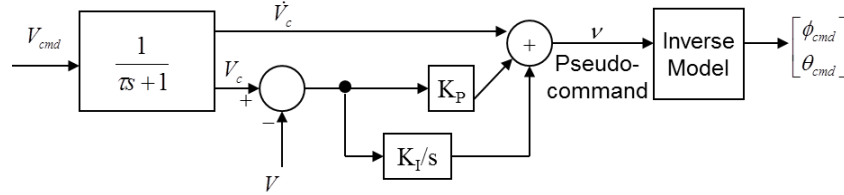


Figure 3-8: Model Following and Model Inversion Control for Translational Rate Command Controller – Low Speed Mode

$$\begin{bmatrix} \dot{V}_{lat} \\ \dot{V}_{lon} \end{bmatrix} = \begin{bmatrix} Y_v & Y_u \\ X_v & X_u \end{bmatrix} \begin{bmatrix} V_{lat} \\ V_{lon} \end{bmatrix} + \begin{bmatrix} g & 0 \\ 0 & -g \end{bmatrix} \begin{bmatrix} \phi_{cmd} \\ \theta_{cmd} \end{bmatrix} = [A_{TRC}] \begin{bmatrix} V_{lat} \\ V_{lon} \end{bmatrix} + [B_{TRC}] \begin{bmatrix} \phi_{cmd} \\ \theta_{cmd} \end{bmatrix} \quad (3.30)$$

$$e = V_c - V \quad (3.31)$$

$$\begin{bmatrix} \phi_{cmd} \\ \theta_{cmd} \end{bmatrix} = [B_{TRC}]^{-1} \left(v - [A_{TRC}] \begin{bmatrix} V_{lat} \\ V_{lon} \end{bmatrix} \right) \quad (3.32)$$

$$v = \dot{V}_c + K_P e + K_I \int e dt \quad (3.33)$$

$$\dot{e} + K_P e + K_I \int e = 0 \quad (3.34)$$

$$K_P = 2\xi\omega_n \quad K_I = \omega_n^2 \quad (3.35)$$

3.1.2.2 Cruise Speed Mode Control Law

The cruise speed mode of the controller regulates airspeed by commanding pitch attitude and holds roll attitude. Vertical speed is controlled by the inner loop with the dynamic inversion controller similar to the low speed mode controller.

The cruise speed mode of the controller is schemed similar to the low speed mode for longitudinal velocity control. Forward speed control achieved by a model following and model

inversion control of longitudinal translational aircraft dynamics and outputs pitch attitude command to the inner loop, as shown in equation 3.38. If the inverse model is exact, the aircraft model and inverse model will behave as a simple integrator. The pseudo command is defined in equation 3.39 and the error dynamics are governed as shown in equation 3.40. The PI compensator gains are defined in terms of controller parameters as shown in equation 3.41. The natural frequency and the damping ratio of the error dynamics are set to be 1.0 rad/sec and 0.9.

$$\dot{V}_{lon} = X_u V_{lon} - g \theta_{cmd} \quad (3.36)$$

$$e = V_{lon_c} - V_{lon} \quad (3.37)$$

$$\theta_{cmd} = \frac{1}{g} (-v + X_u V_{lon}) \quad (3.38)$$

$$v = \dot{V}_{lon_c} + K_p e + K_I \int e dt \quad (3.39)$$

$$\dot{e} + K_p e + K_I \int e = 0 \quad (3.40)$$

$$K_p = 2\xi\omega_n \quad K_I = \omega_n^2 \quad (3.41)$$

The lateral axis command bypasses the TRC and feeds into the inner loop directly as the roll attitude command.

3.1.2.3 High-Speed Mode Control Law

The high-speed controller regulates airspeed and altitude by commanding auxiliary thruster and pitch attitude. Similar to cruise mode control law, the controller holds the roll attitude. However, in this controller the auxiliary thruster command regulates airspeed and the pitch attitude command regulates altitude. The collective pitch becomes a redundant control effector which can be optimized.

The high-speed mode of the outer loop controller, a model following and model inversion schemed controller is used for controlling airspeed and altitude. A first order command filter with a time constant of 2.0 sec is designed for airspeed model follower that yields desired state and derivative of longitudinal velocity, as shown in Figure 3-9. For the altitude control a second order command filter with 0.5 rad/sec natural frequency and damping ratio of 0.9 is designed to yield desired altitude, vertical velocity and vertical acceleration, as shown in Figure 3-10. A second-order linear model extracted from the higher-order linear model of the helicopter, as shown in equation 3.42, where the pitch attitude and propeller pitch are the primary input variables. Collective and stabilator deflections are treated as redundant control effectors and kept in the linear model to account for their perturbation on the primary control axes. A PI compensator is added to minimize the tracking error for airspeed control, defined in equation 3.43 and a PID compensator to minimize the tracking error for altitude control. The tracking error passes through the compensators and added to the desired response of the state derivative to obtain the pseudo command. The pseudo command is passed through the inverse model of the aircraft dynamics to get the pitch attitude command input to the inner loop and propeller pitch angle command input to the inner loop dynamic inversion controller, as shown in equation 3.44. If the inverse model is exact, the aircraft model and inverse model will behave as a simple integrator. The pseudo command is defined in equation 3.45 and the error dynamics are governed as shown in equation 3.46. The PI and PID compensator gains are defined in terms of controller parameters as shown in equation 3.47 and 3.48 respectively. The natural frequency and the damping ratio of the error dynamics are set to be 0.5 rad/sec and 0.9 for both axes. A real pole is defined as 0.75 for the PID compensator of altitude hold controller.

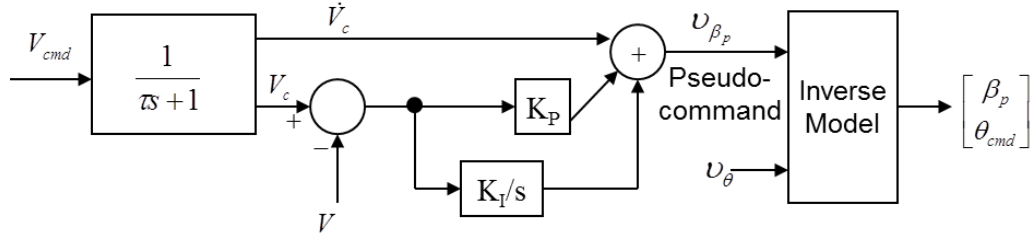


Figure 3-9: Model Following and Model Inversion Control for Airspeed Axis of High-Speed Mode Outer Loop Controller

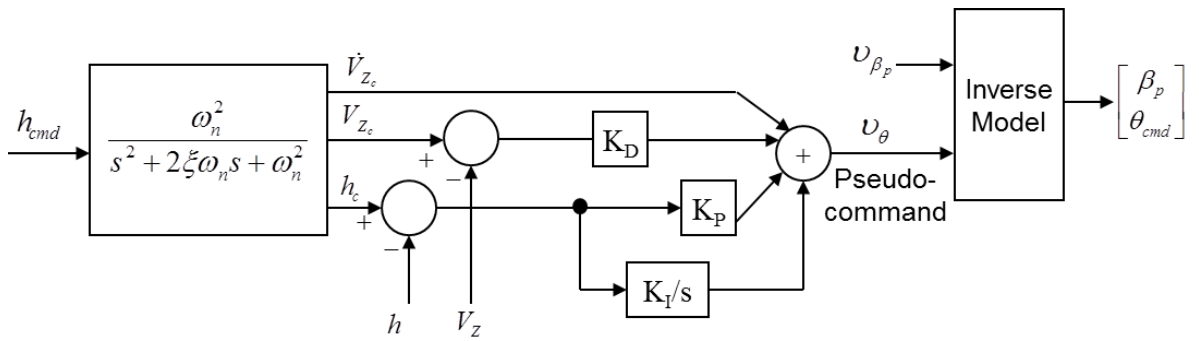


Figure 3-10: Model Following and Model Inversion Control for Heave Axis of High Speed Mode Outer Loop Controller

$$\begin{bmatrix} \dot{V}_{lon} \\ \dot{V}_Z \end{bmatrix} = \begin{bmatrix} X_u & 0 \\ 0 & Z_w \end{bmatrix} \begin{bmatrix} V_{lon} \\ V_Z \end{bmatrix} + \begin{bmatrix} X_{\beta_p} & -g \\ -Z_{\beta_p} & -(Z_w V + Z_\theta) \end{bmatrix} \begin{bmatrix} \beta_p \\ \theta_{cmd} \end{bmatrix} + \begin{bmatrix} X_{\delta_{col}} & X_{\delta_e} \\ -Z_{\delta_{col}} & -Z_{\delta_e} \end{bmatrix} \begin{bmatrix} \delta_{col} \\ \delta_e \end{bmatrix} \quad (3.42)$$

$$\begin{bmatrix} \dot{V}_{lon} \\ \dot{V}_Z \end{bmatrix} = [A_{HSFC}] \begin{bmatrix} V_{lon} \\ V_Z \end{bmatrix} + [B_{1HSFC}] \begin{bmatrix} \beta_p \\ \theta_{cmd} \end{bmatrix} + [B_{2HSFC}] \begin{bmatrix} \delta_{col} \\ \delta_e \end{bmatrix}$$

$$e_v = V_c - V \quad e_h = h_c - h \quad (3.43)$$

$$\begin{bmatrix} \beta_p \\ \theta_{cmd} \end{bmatrix} = [B_{1HSFC}]^{-1} \left(v - [A_{HSFC}] \begin{bmatrix} V_{lon} \\ V_Z \end{bmatrix} + [B_{2HSFC}] \begin{bmatrix} \delta_{col} \\ \delta_e \end{bmatrix} \right) \quad (3.44)$$

$$\begin{aligned} v_{\beta_p} &= \dot{V}_c + K_P e_v + K_I \int e_v dt \\ v_\theta &= \dot{V}_{Z_c} + K_P e_h + K_D \dot{e}_h + K_I \int e_h dt \end{aligned} \quad (3.45)$$

$$\begin{aligned} \dot{e}_V + K_P e_V + K_I \int e_V &= 0 \\ \ddot{e}_h + K_D \dot{e}_h + K_P e_h + K_I \int e_h &= 0 \end{aligned} \quad (3.46)$$

$$K_P = 2\xi\omega_n \quad K_I = \omega_n^2 \quad (3.47)$$

$$K_P = 2\xi\omega_n p + \omega_n^2 \quad K_I = \omega_n^2 p \quad K_D = 2\xi\omega_n + p \quad (3.48)$$

3.2 Control System Evaluation with Nonlinear Simulation

The integrated flight control system designed in the previous section is implemented in the nonlinear model of the generic compound rotorcraft, GENHEL-PSU. The existing stability and augmentation systems of UH-60A were turned off and the control system was simulated.

3.2.1 Longitudinal Axis Evaluation

All three modes of the outer loop controller are evaluated with different airspeeds and a step input is introduced in longitudinal axis. Figures 3-11, 3-12 and 3-13 show the time history results for simulation response of the generic compound rotorcraft at 20, 100 and 200 knots level flight. For all three modes of the controller, the command is tracked successfully as the model following dynamic inversion controller works well on the non-linear simulation model.

The low speed and the cruise speed flight control laws are designed to hold roll and pitch attitudes and the responses in Figures 3-11 and 3-12 show that controllers are successfully holding the attitude. A slight variation in the altitude is observed; however the controllers for those modes are designed to hold vertical velocity instead of altitude. For the high-speed flight control law simulation as shown in Figure 3-13, altitude is held within the range of 10 feet, which is an acceptable variation from the trimmed state at high-speed forward flight. The high-speed

mode of the controller is designed to hold altitude and the outer loop is designed to command the pitch attitude for the control of vertical speed and altitude. The controller is designed to control airspeed by commanding the propeller pitch.

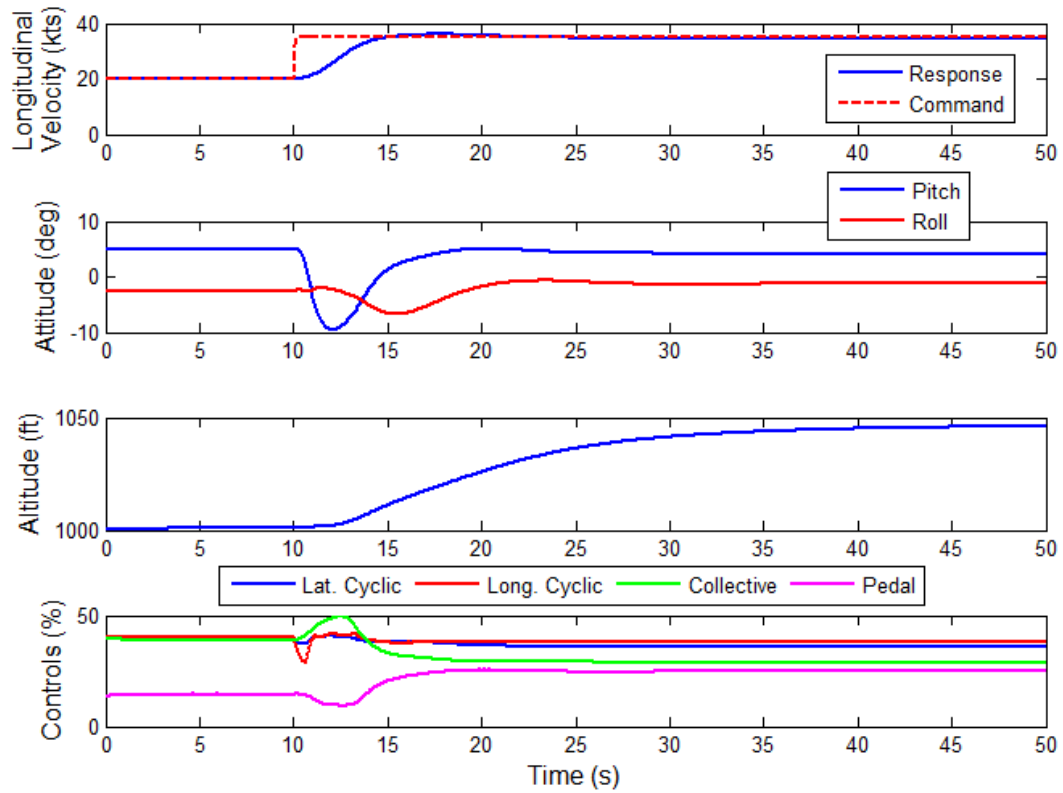


Figure 3-11: GENHEL-PSU Simulation at Nominal RPM, $V=20$ kts, Airspeed Command = 15 knots

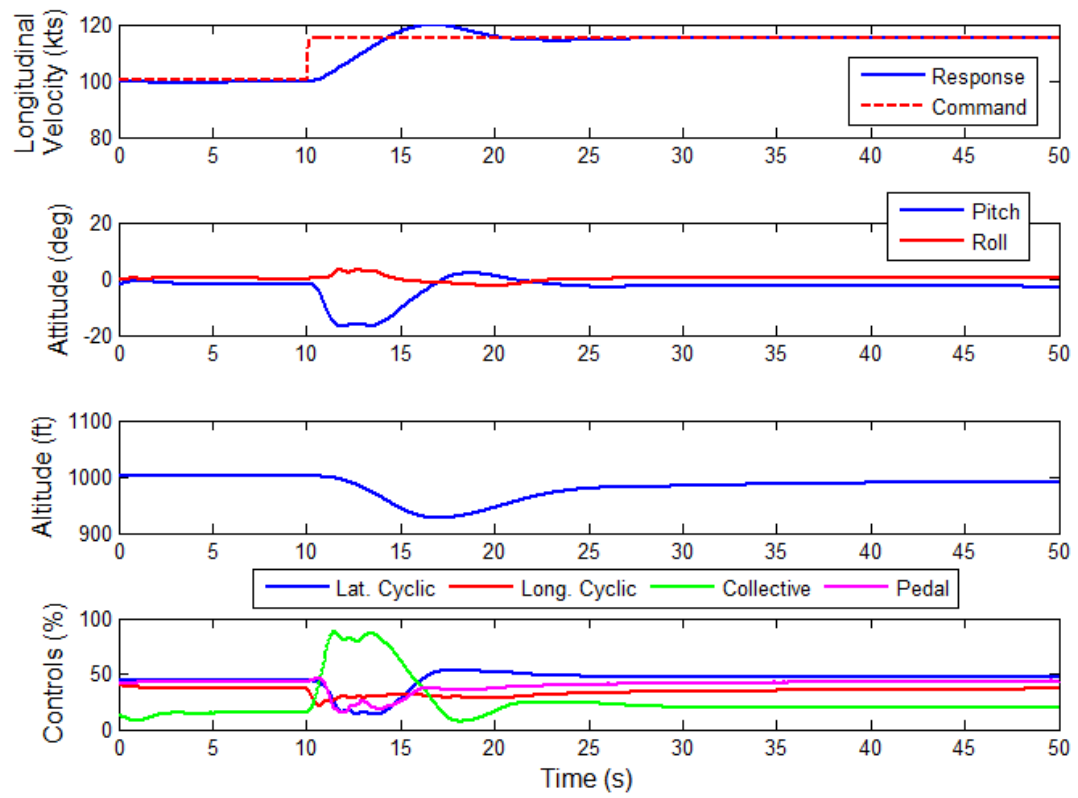


Figure 3-12: GENHEL-PSU Simulation at Nominal RPM, $V=100$ kts, Airspeed Command = 15 knots

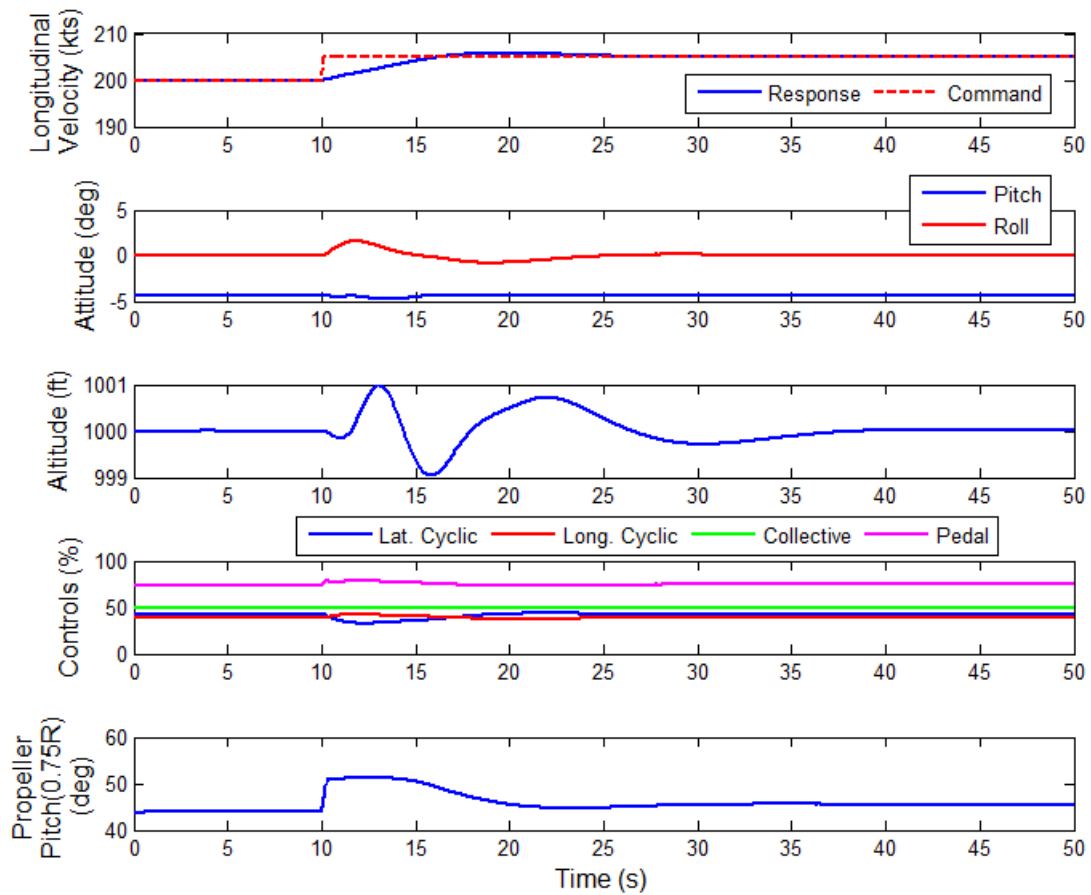


Figure 3-13: GENHEL-PSU Simulation at 80% of Nominal RPM, $V=200$ kts, Airspeed Command = 5 knots

3.2.2 Lateral Axis Evaluation

All three modes of the outer loop controller are evaluated with different airspeeds by introducing a doublet command in lateral axis. Lateral axis command tracks the lateral velocity in the low speed mode of the controller, whereas for the cruise and the high-speed mode of the controller lateral axis command tracks the roll attitude. Figures 3-14 to 3-19 show the time history results for simulation response of the generic compound rotorcraft at 20, 100 and 200 knots level

flight. For all three modes of the controller, the command is tracked successfully as the model following dynamic inversion controller works well on the non-linear simulation model without significant off-axis response.

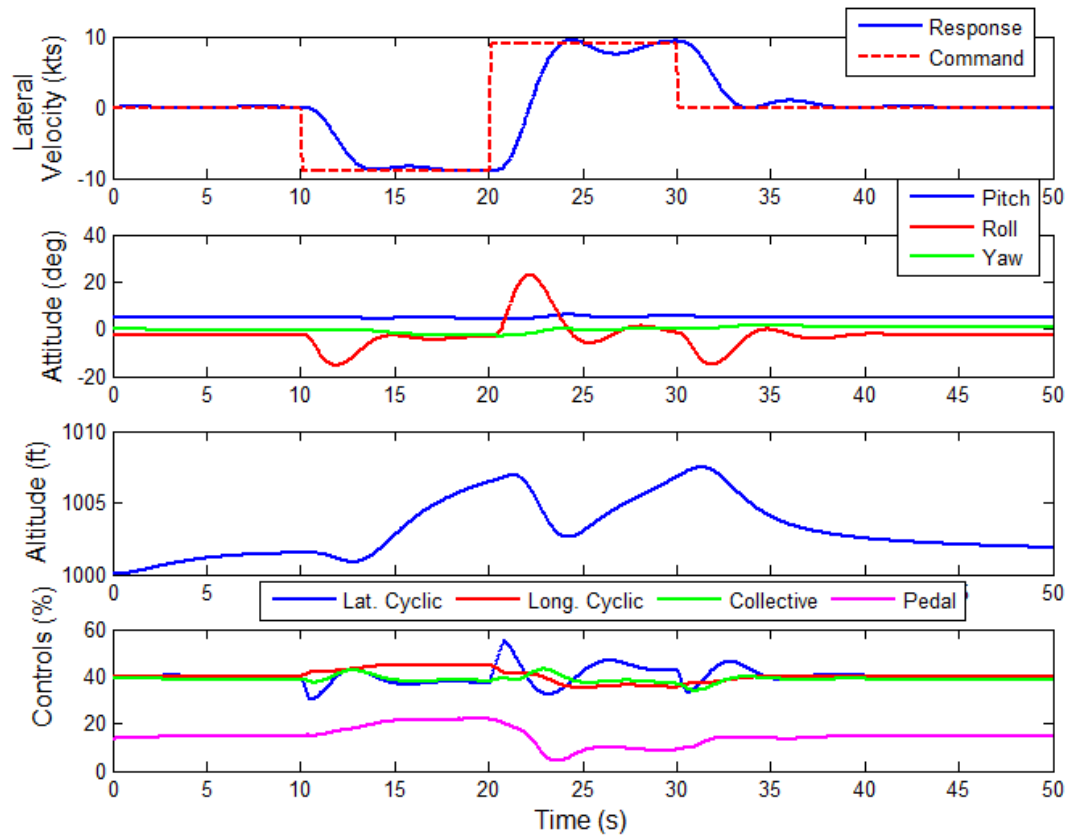


Figure 3-14: GENHEL-PSU Simulation at Nominal RPM, V=20 kts, Lateral Velocity Doublet = ± 9 knots

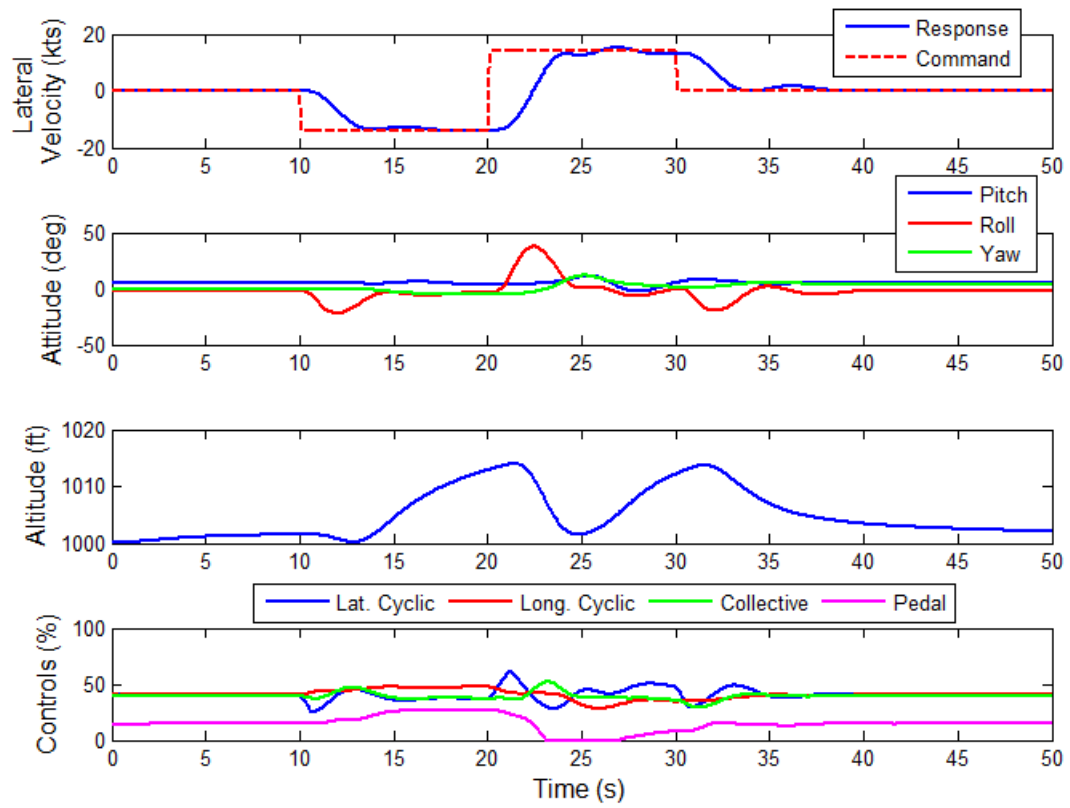


Figure 3-15: GENHEL-PSU Simulation at Nominal RPM, $V=20$ kts, Lateral Velocity Doublet = ± 18 knots

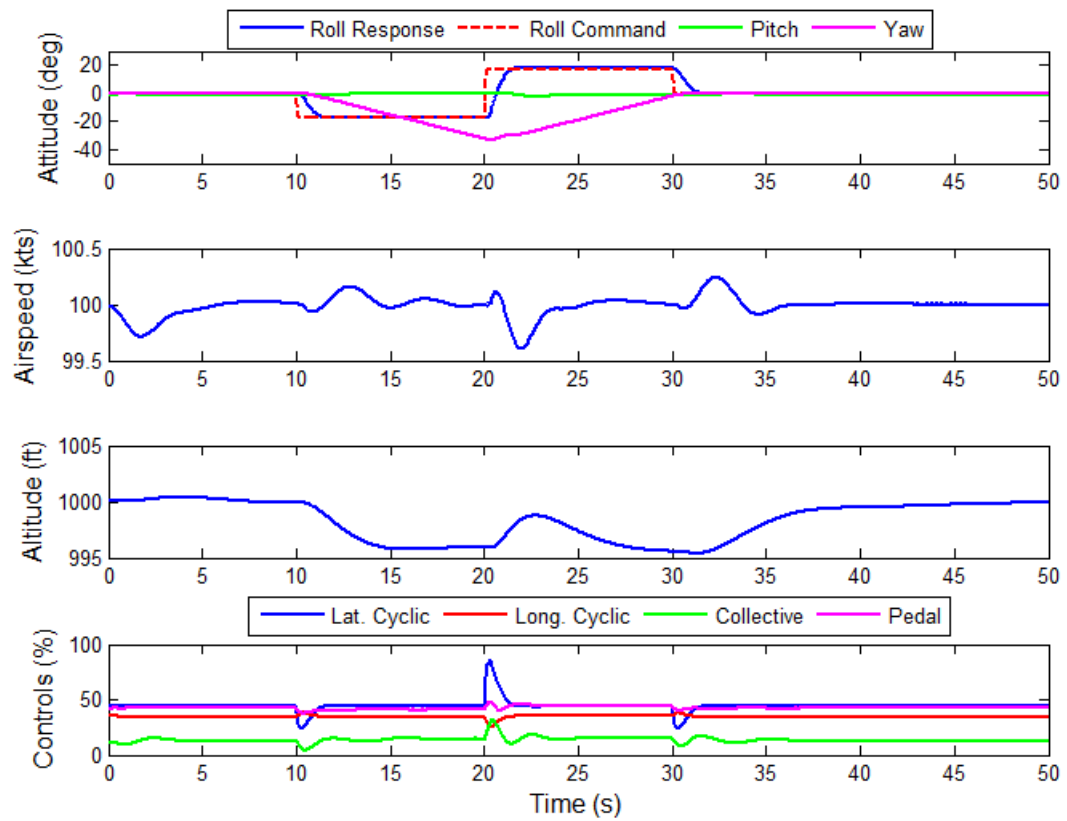


Figure 3-16: GENHEL-PSU Simulation at Nominal RPM, $V=100$ kts, Roll Command= ± 18 degrees

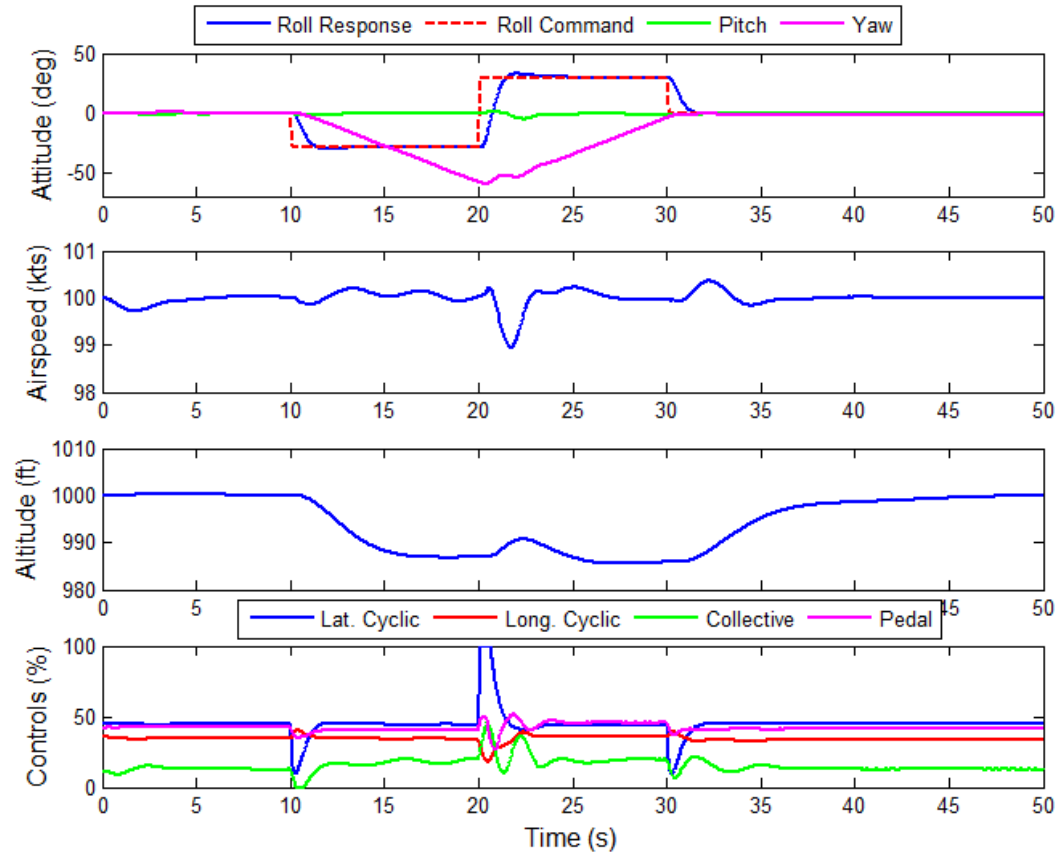


Figure 3-17: GENHEL-PSU Simulation at Nominal RPM, V=100 kts, Roll Command= ± 30 degrees

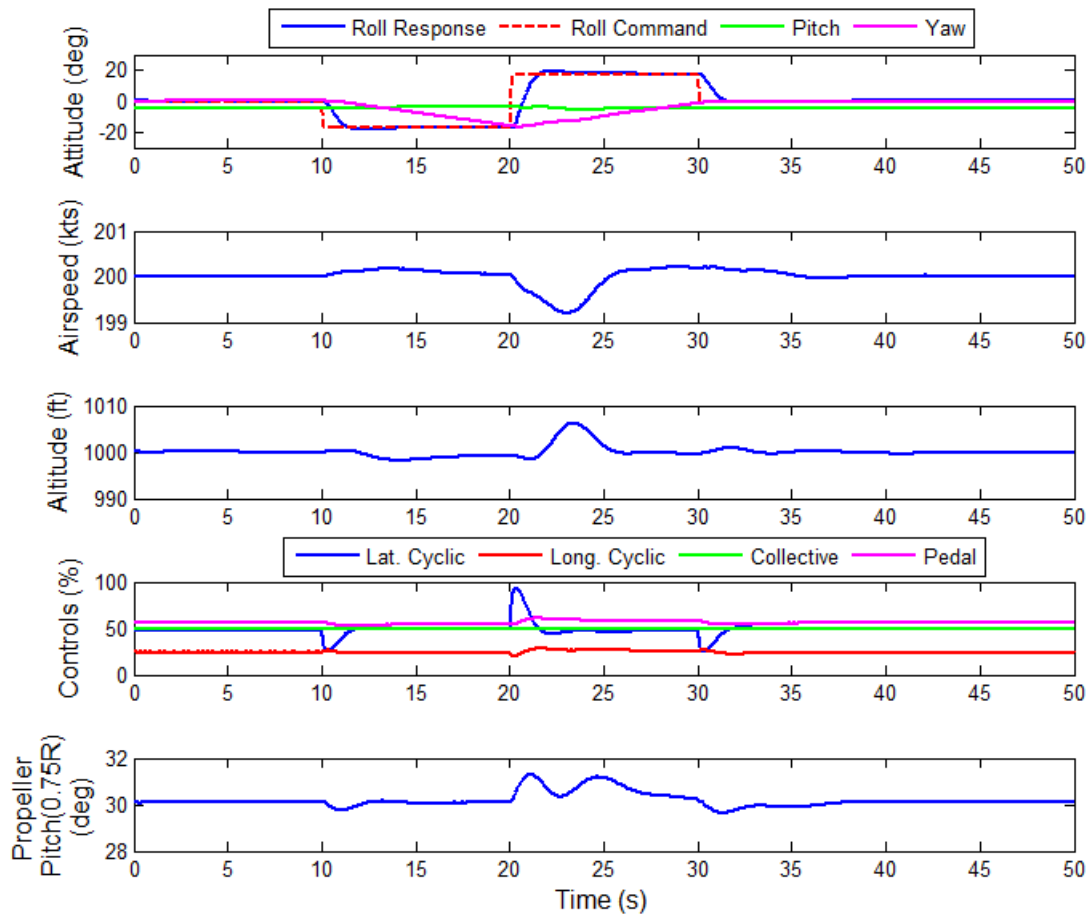


Figure 3-18: GENHEL-PSU Simulation at Nominal RPM, $V=200$ kts, Roll Command= ± 18 degrees

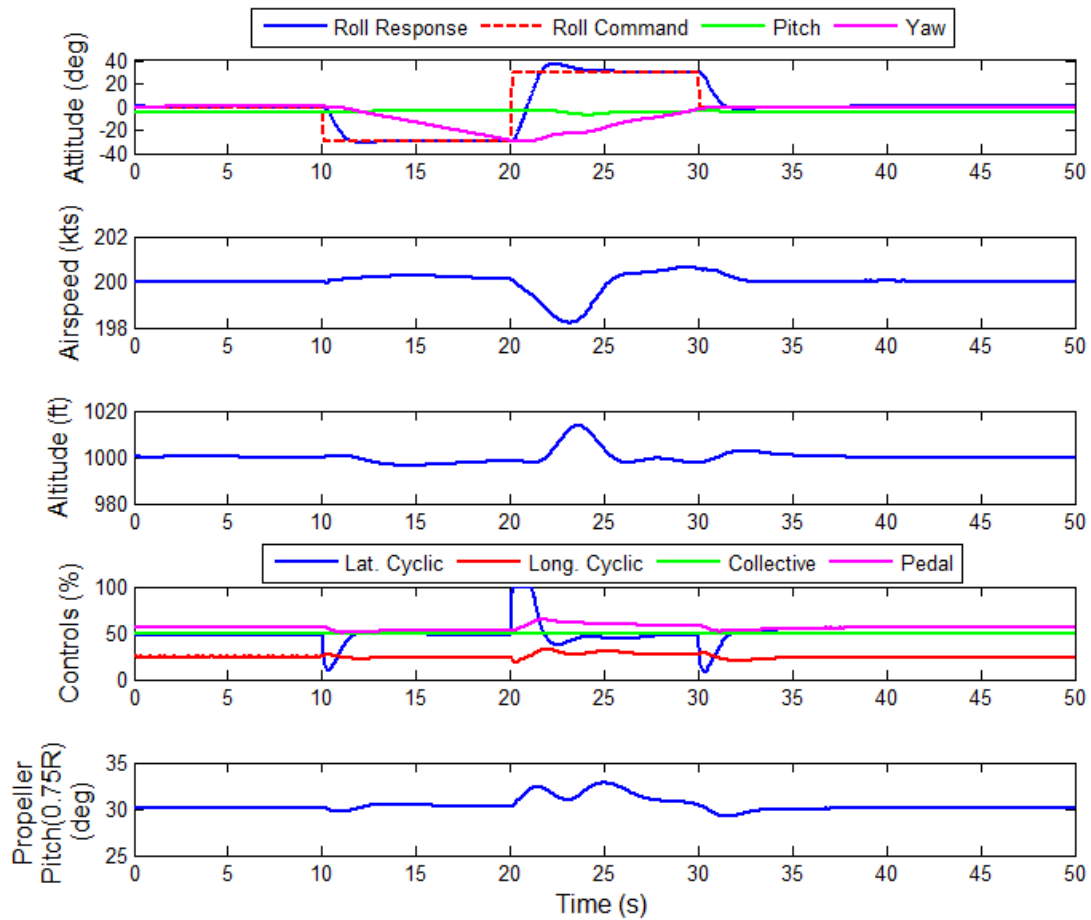


Figure 3-19: GENHEL-PSU Simulation at Nominal RPM, $V=200$ kts, Roll Command= ± 30 degrees

3.2.3 Heave Axis Evaluation

All three modes of the outer loop controller are evaluated with different airspeeds by introducing a step command in heave axis. Low and cruise speed mode controllers track vertical speed commands, while high-speed controller tracks the altitude by regulating the vertical speed with pitch attitude command and holds airspeed by commanding the propeller pitch. Figures 3-20 to 3-22 show the time history results for simulation response of the generic compound rotorcraft

at 20, 100 and 200 knots. For all three modes of the controller, the command is tracked successfully as the model following dynamic inversion controller works well on the non-linear simulation model without significant off-axis response.

The collective pitch is used for climbing for the low and cruise speed mode controller and the maximum rate of climb is limited by the collective control limit. Figures 3-20 and 3-21 show the change in collective control in order to gain vertical speed. The high-speed flight mode of the controller has the pitch attitude to control altitude. Figure 3-22 shows that outer loop controller successfully commands pitch attitude to control altitude and compared to low and cruise speed flight modes of the controller, higher rates of climb can be achieved by this configuration. However, this introduces a delay in the tracking of altitude command.

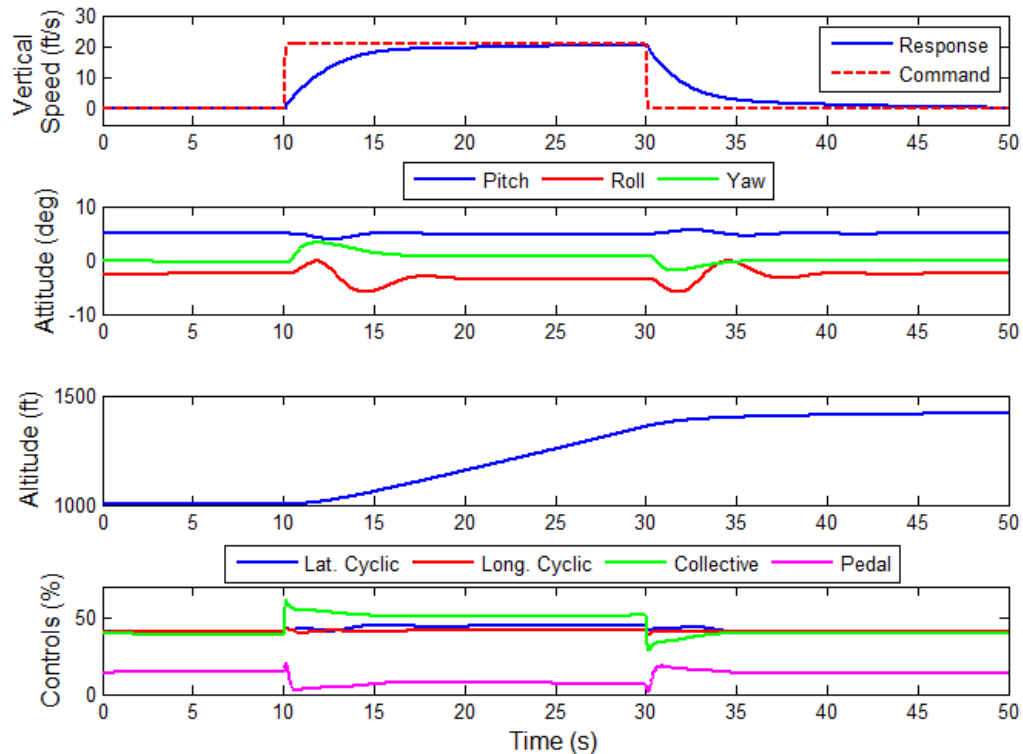


Figure 3-20: GENHEL-PSU Simulation at Nominal RPM, V=20 kts, Vertical Speed Command=21 ft/s

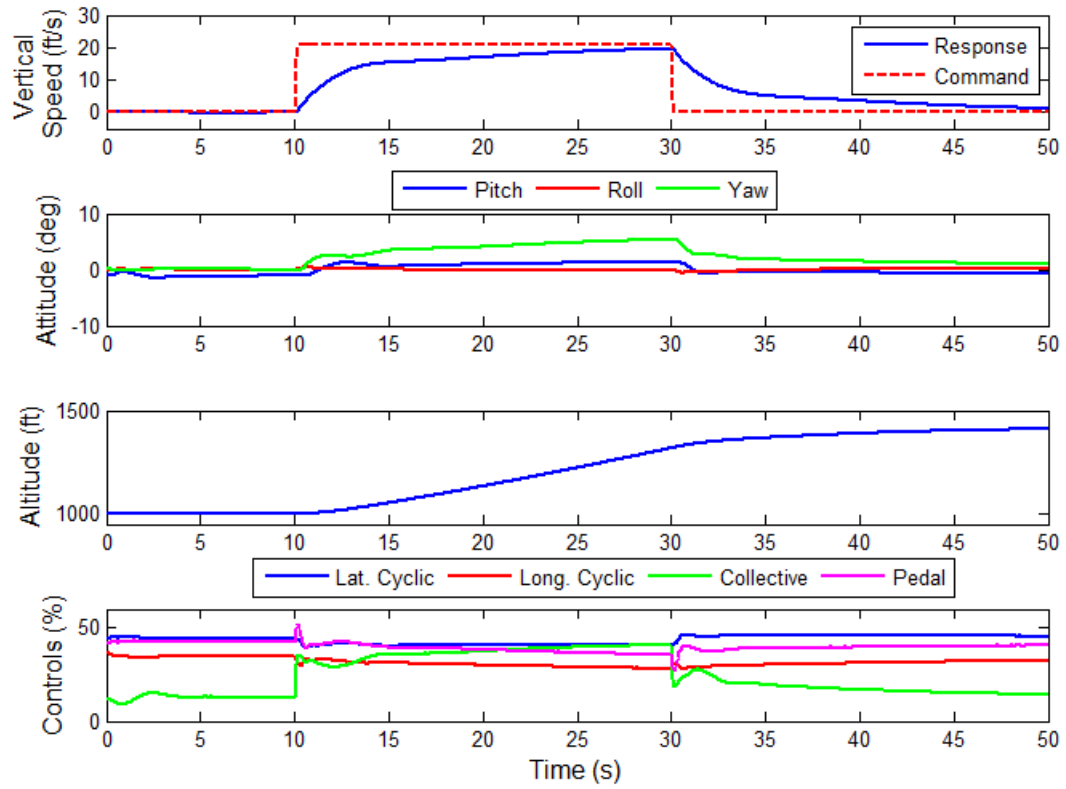


Figure 3-21: GENHEL-PSU Simulation at Nominal RPM, V=100 kts, Vertical Speed Command=21 ft/s

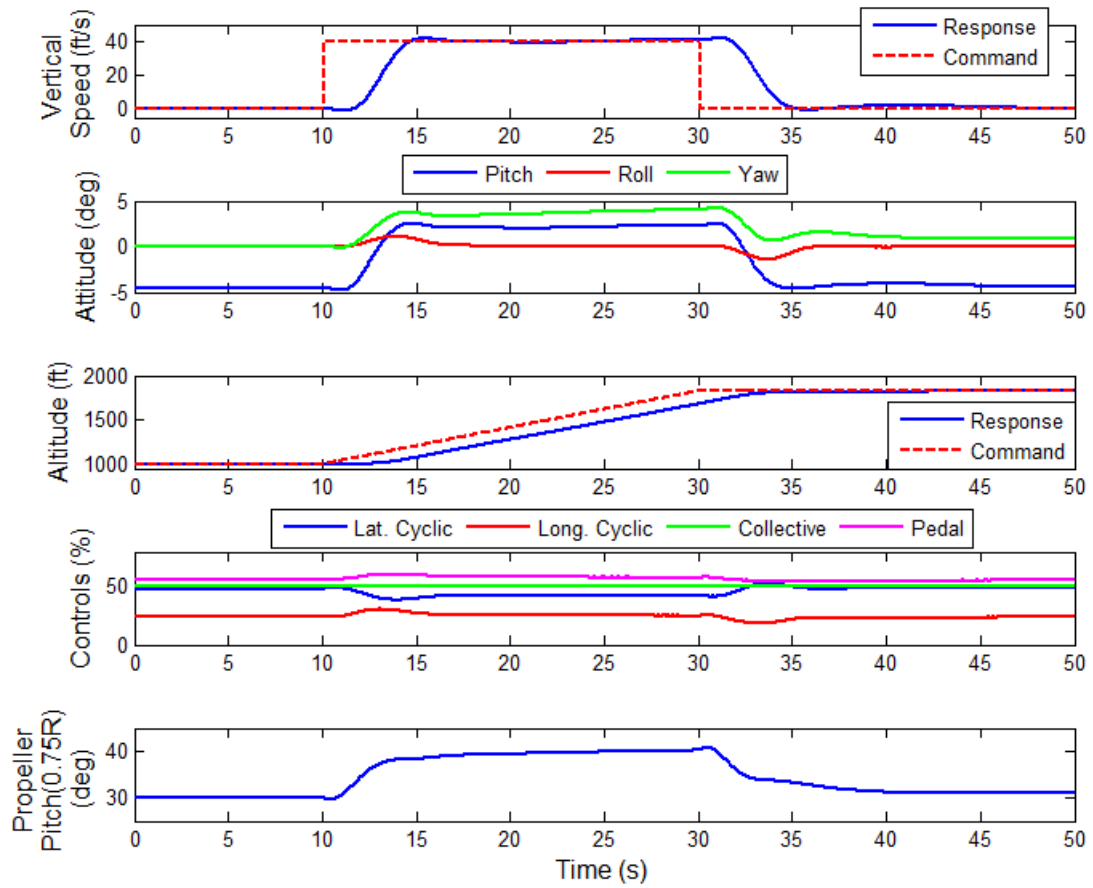


Figure 3-22: GENHEL-PSU Simulation at Nominal RPM, V=200 kts, Vertical Speed Command=40 ft/s

Chapter 4

In-Flight Optimization Algorithm

This chapter presents the development and implementation of an advanced flight control system that allows in-flight performance optimization. The concept is called “Fly to Optimal” (FTO). While maintaining trim with a stabilizing controller, as demonstrated in Chapter 3, perturbations are generated and performance is measured in flight. The measured response is used to drive the redundant controls (those control effectors not used in the primary control) and the trim state to some optimal. Several optimization methods were applied to make a comparison between different methods. As shown in Figures 3-1, 3-2 and 3-3, Fly-to-Optimal system is integrated with the integrated flight control laws and could be engaged or disengaged as needed by the pilot. Fly-to-optimal can be applied for baseline helicopter, compound rotorcraft and generic compound rotorcraft configurations. For the baseline helicopter, FTO performs a rotor speed optimization, for the compound rotorcraft, FTO performs optimization for rotor speed and compound controls together, and for the generic compound rotorcraft, FTO can perform either power minimization or range maximization. Minimizing power for a given flight condition has significant effect on performance parameters, such as endurance, rate of climb or ceiling. These performance parameters define the operational capabilities of the rotorcraft. Better performance can be achieved by reducing the power required. Therefore, optimizing power will simultaneously optimize the operational capabilities [1].

4.1 Optimization Method Study

A comprehensive study of the stability and speed of various optimization methods was conducted. The steepest descent, golden section, and the adaptive performance optimization

(APO) methods were evaluated to identify which method resulted in the quickest and most accurate optimization.

4.1.1 Steepest Descent Method

The Steepest descent method was implemented in the Fly to Optimal control law to optimize rotor speed on baseline helicopter configuration. The nominal rotor speed (100%) is selected as the starting point for the optimization and positive and negative perturbations on RPM command are applied. The perturbations are chosen to be 1% of the nominal rotor speed. The gradient on power required is calculated and the direction of the optimization is determined. The new rotor speed is calculated by applying the selected step size in the optimization direction. This method continued until the gradient of power required is below a limit value. However, the method proved to be somewhat sensitive to the complex and non-linear variations in aircraft performance with main rotor RPM. High frequency oscillations in the measured power required were also problematic for this method. These issues would often result in large gradient calculations that would drive the optimization solution to extreme values and miss the true optimal solution.

4.1.2 Golden Section Method

The golden section method is an interval reduction strategy. In this approach, rotor speed is allowed to vary between 120% and 80% of the nominal rotor speed, 27 rad/sec. Figure 4-1 illustrates a single iteration step in the golden section method. Initial boundaries of the interval are shown as points 1 and 4 with the length of I_1 . A third point, 2, is selected inside the interval, where I_3/I_2 is equal to the golden ratio, ϕ , as shown in equation 4.1. The function values at these

points are assumed to be known. Since f_2 is smaller than f_1 and f_4 , it is clear that a minimum lies inside the interval, assuming the function is unimodal.

$$\varphi = \frac{\sqrt{5}-1}{2} \quad (4.1)$$

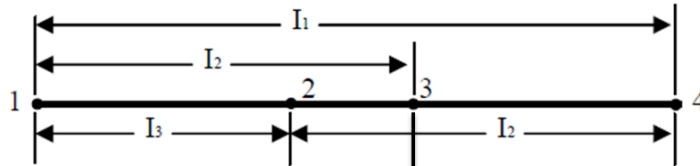


Figure 4-1: Golden Section Method Iteration Step Diagram

The next step is to determine a new point, 3, inside the interval and evaluate its function value. The golden section method requires that the length of intervals between 1 and 3, and 2 and 4 are equal. The function value f_3 has two possibilities: f_3 is larger than f_2 or f_2 is larger than f_3 . In the first case, it is clear that a minimum lies between 1 and 3, and the new interval becomes 1 to 3. In the other case, a minimum lies between 2 and 4, and the new interval becomes 2 to 4. As a result, for both cases, a new narrower interval is obtained with a minimum value inside the interval.

The initial size of the rotor speed interval is 40% and the optimization method desires to reduce this value to below 0.5%, which requires 11 interval reductions. Since this method requires fixed number of iterations and rotor RPM command range reduces in each iteration step, golden section method is superior to steepest descent method in terms of stability and speed. In this study the Golden Section Method is applied only to the baseline helicopter configuration for rotor speed optimization.

4.1.3 Adaptive Performance Optimization

Adaptive Performance Optimization (APO) is a method of identifying unknown performance characteristics from a forced response, using a low frequency, smooth maneuver [56-59]. In the case of rotor speed optimization, the controller is set to apply a low frequency sinusoidal command spanning the whole range of RPMs. Since the input is in low frequency, it is assumed that the aircraft is approximately in steady state trim throughout the maneuver. Then, rotor speed is set to the optimal performance as measured during the course of the maneuver. The maneuver generally takes a shorter amount of time when compared to the iterative methods described before. Therefore, APO appears to be superior to both steepest descent and golden section methods in terms of stability and speed.

This optimization method will also be investigated for the optimization of compound control effectors of the compound rotorcraft model, in which there are more than one parameter to optimize. Initially, successive applications of the APO maneuver applied to each control effector, where each application of APO is considered as a single parameter optimization. The order of control effectors optimized is important. In this study the order is determined by the level of impact of individual variable. The compound helicopter configuration includes four redundant control effectors in addition to main rotor RPM. These include propeller pitch (which changes auxiliary thrust and power), stabilator (which changes the pitch attitude trim), symmetric flaperons (which change the wing lift), and differential flaperons (which change the roll moment produced by the wing).

Theoretically, infinite number of variables can be simultaneously optimized by forcing to an out-of-phase or different frequency sinusoidal responses. In this study, performance optimization of the generic compound rotorcraft with two variables is performed and those

control effectors are forced to an out-of-phase sine wave with the same frequency. Performance measurements are made during the maneuver and the optimal state of the controls is determined.

4.2 Fly-to-Optimal Controller Design

The general layout of the integrated flight control system is shown Figures 3-1, 3-2 and 3-3. The Fly-to-Optimal (FTO) component is designed to generate commands to perform optimization maneuver and inputs rotorcraft states and performance measurements to calculate the optimal trim state. However, as the airspeed increases the range of controls resulting in aircraft can trim gets smaller. So, sweeping controls for performance optimization outside of trim forces the aircraft into a transient dynamic response. Therefore, a method is used to predict the values of limited parameters as a function of controls and flight conditions to estimate the control margins. Limited parameters in this study are chosen as the longitudinal control stick position and power required. Collective stick position is used as a limited parameter for the cruise speed controller.

The FTO controller applies low frequency inputs on the optimization variables, so it is assumed that the aircraft is approximately in steady state trim throughout the maneuver. A similar concept called dynamic trim estimation was applied to find envelope constraints on pilot controls during quasi-steady maneuvers [71]. The current problem is similar in that the aircraft is in an approximate trim condition throughout the FTO maneuver. Variations in a limited parameter can be represented as shown in equation 4.2, where y_p is the limited parameter and u is the 2-component vector of optimization variables:

$$y_p = y_{p_0} + \frac{\partial y_p}{\partial u_1} \Delta u_1 + \frac{\partial y_p}{\partial u_2} \Delta u_2 \quad (4.2)$$

$$\Delta y_p = \begin{bmatrix} \frac{\partial y_p}{\partial u_1} & \frac{\partial y_p}{\partial u_2} \end{bmatrix} \begin{bmatrix} \Delta u_1 \\ \Delta u_2 \end{bmatrix}$$

where Δy_p represents the difference between the current value of the limited parameter and the limit boundary. The vector Δu is the control margin, which is the difference between the current control position and the control position that will allow the aircraft to reach the limit boundary. The partial derivative terms are the sensitivities of the limited parameter to each control input. The sensitivities are calculated during the optimization maneuver using simple finite difference approximations as shown in equation 4.3 where the perturbations are applied to the optimization variables and are measured at various points during the spiral search pattern used in FTO. The control margin vector defines the shortest vector from the current control position to the limit boundary and it is calculated as shown in equation 4.4 by taking the pseudo-inverse of the sensitive row vector. For simplicity, in this study the control margins are calculated one control at a time as shown equation 4.5. So 1-D limit estimation is performed instead of 2-D limit estimation as shown in equation 4.4. The aircraft might have multiple limit boundaries, in that case different sets of control margins are calculated and a control axis might end up having an upper and a lower bound. Figure 4-2 shows the schematic of the control margin approach and dashed lines are the upper and lower limits of the controls calculated by equations 4.2 and 4.5. Since the actual system is non-linear, the calculated sensitivities are the linear approximation of the actual system and they get close to the exact value as the limited boundary is approached. The limit boundaries are updated periodically throughout the maneuver; therefore the range of the optimization search for control positions change depending on the control limits.

$$\frac{\partial y_p}{\partial u_1} = \frac{y_{p_1} - y_{p_0}}{u_{1_1} - u_{1_0}} \quad (4.3)$$

$$\begin{bmatrix} \Delta u_1 \\ \Delta u_2 \end{bmatrix} = \begin{bmatrix} \frac{\partial y_p}{\partial u_1} \\ \left(\frac{\partial y_p}{\partial u_1} \right)^2 + \left(\frac{\partial y_p}{\partial u_2} \right)^2 \\ \frac{\partial y_p}{\partial u_2} \\ \left(\frac{\partial y_p}{\partial u_1} \right)^2 + \left(\frac{\partial y_p}{\partial u_2} \right)^2 \end{bmatrix} \Delta y_p \quad (4.4)$$

$$\Delta u = u_{\text{lim}} - u_0 = \frac{1}{\frac{\partial y_p}{\partial u}} \Delta y_p \quad (4.5)$$

Figure 4-3 shows the layout of the FTO component of the controller: y_p is the limited parameter that defines the limits on the optimization controls. The optimization method chosen generates the commands while considering the operational limits on the optimization parameters. The control limits are calculated using the Control Limit Calculation by using the current state of the controls and values of the limited parameter, y_p , such as power required, torque or control margins. Throughout the optimization maneuver, “optimal status check” searches for optimal performance and control. Any of the optimization methods discussed in the previous section can be implemented in the Optimization Method / Command Generator block. The Control Limit Calculation tool is only used for multi variable optimization using adaptive performance optimization method.

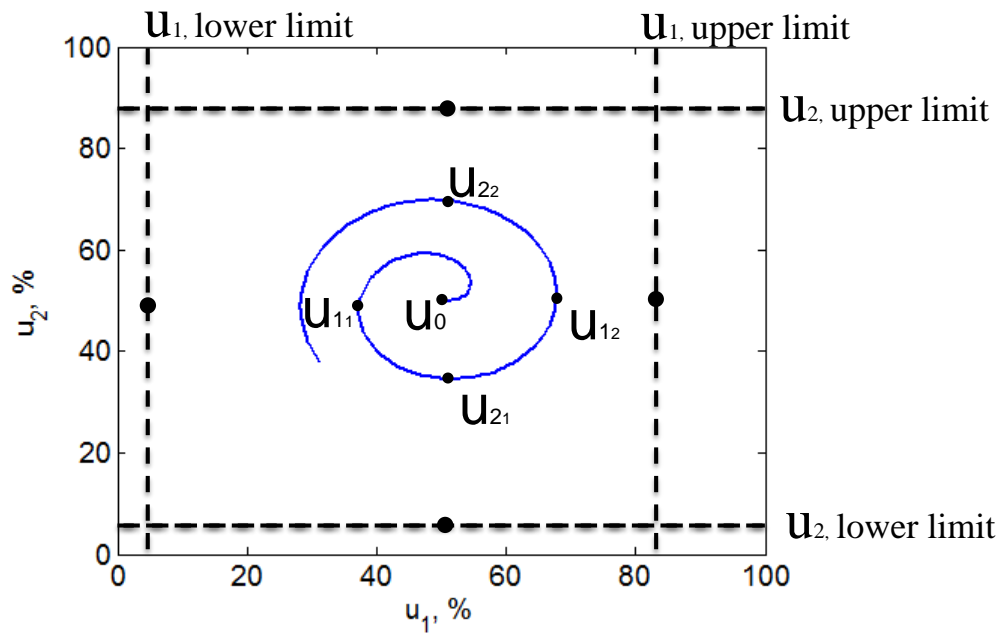


Figure 4-2: Schematic of Control Margin Approach

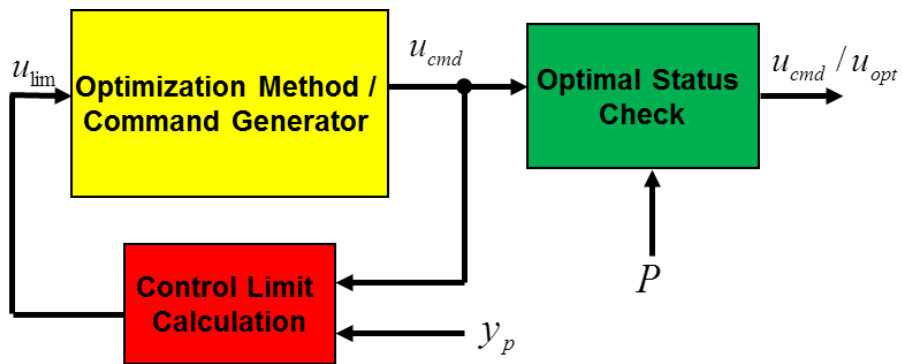


Figure 4-3: Layout of the Fly-to-Optimal Component of the Controller

4.3 Nonlinear Simulation Results

4.3.1 Single Parameter Optimization using Golden Section Method

The flight control architecture with golden section method optimization discussed in the previous section was implemented in the nonlinear model of the baseline helicopter model, UH-60A Black Hawk, using GENHEL-PSU. Figures 4-4 and 4-5 show rotor speed optimization results at 40 knots level flight, Figures 4-6 and 4-7 show similar results at 80 knots, and Figures 4-8 and 4-9 show results at 120 knots.

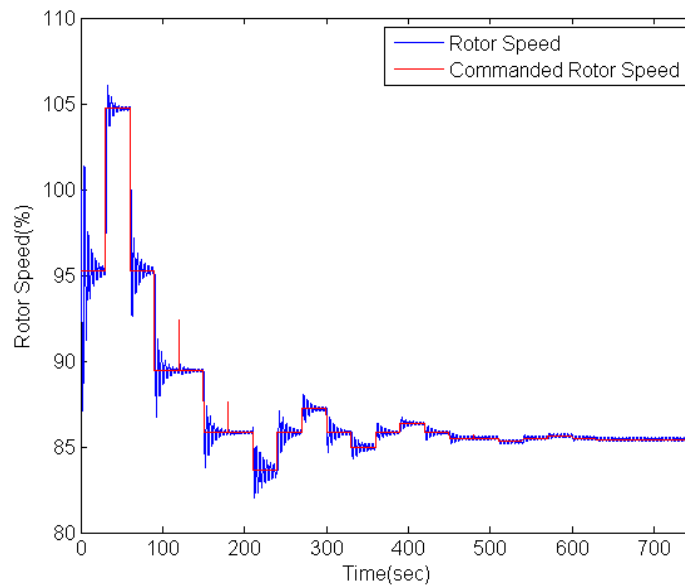


Figure 4-4: Rotor Speed Optimization at 40 knots using Golden Section Method

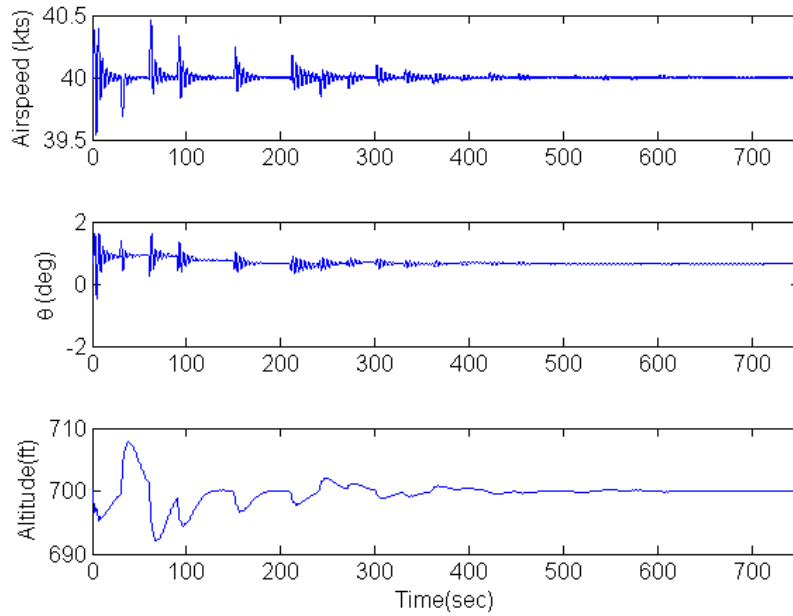


Figure 4-5: Longitudinal Response at 40 knots during Golden Section Method

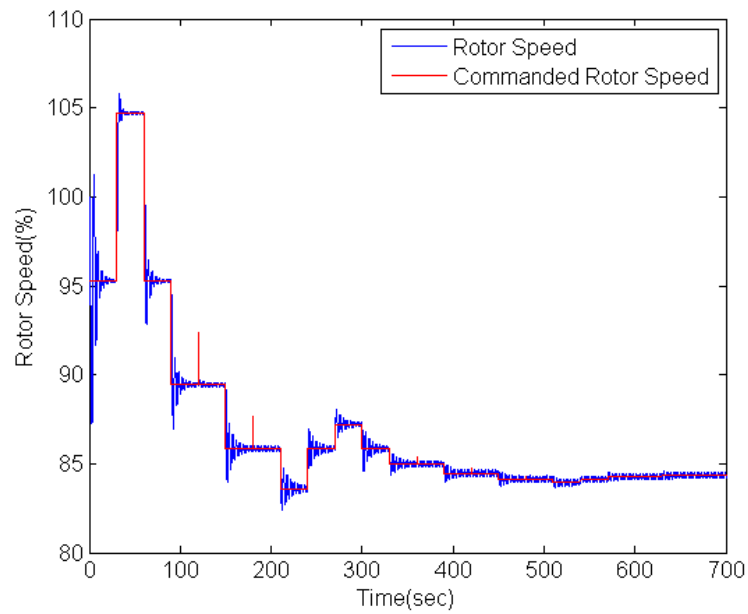


Figure 4-6: Rotor Speed Optimization at 80 knots using Golden Section Method

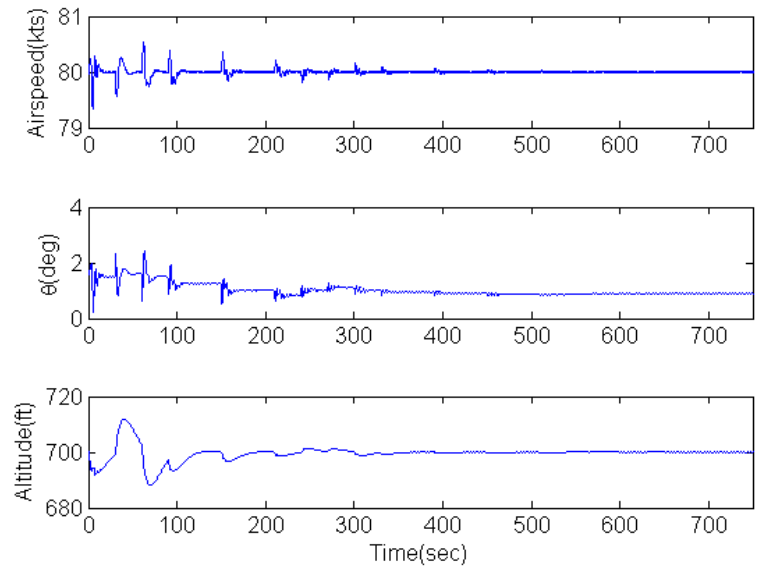


Figure 4-7: Longitudinal Response at 80 knots during Golden Section Method

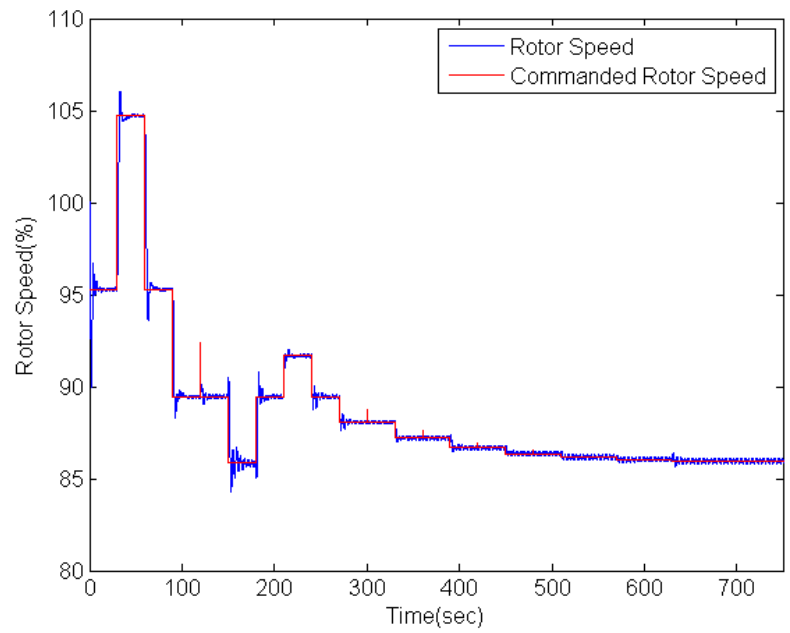


Figure 4-8: Rotor Speed Optimization at 120 knots using Golden Section Method

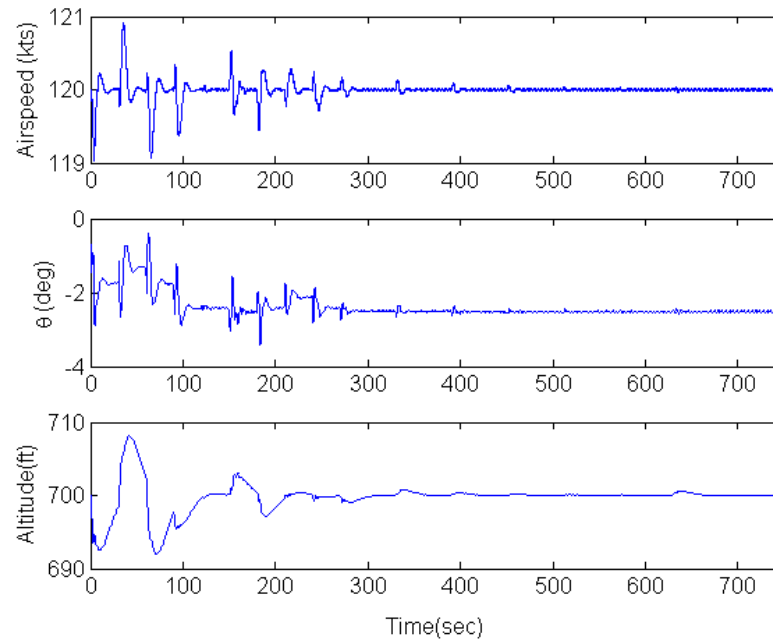


Figure 4-9: Longitudinal Response at 120 knots during Golden Section Method

In all three cases the optimal rotor speed is found to be around 85% of nominal rotor speed. For all three optimization processes, there are spikes observed at the commanded rotor speed. These spikes are generated between the two iterations of interval reduction. If the new interval has a new upper boundary, the commanded rotor speed will be limited to the latest rotor speed command. But the rotor speed command follows the former upper boundary before the new boundary is determined. Therefore, the commanded rotor speed increases for an instant and returns back to the new upper limit, which causes spikes in the rotor speed command. During the optimization process, airspeed was successfully held within ± 1 knot range and altitude was held ± 10 ft. Figure 4-10 shows the variation of power required during the optimization process for all three cases compared to the power required with nominal RPM. Table 4-1 shows the comparison of initial power required percentage value operating at nominal RPM to power required percentage value operating at optimal RPM and the percentage reduction in power required for each case. For the power required calculations 100% is accepted to be 3400 hp.

In order to check the accuracy of the golden section method, series of trims at different rotor speeds were calculated and compared to the optimized rotor speeds by FTO. For all three cases minimum power required obtained from trim study stayed within $\pm 1\%$ region.

Table 4-1: Comparison of Power Required Values Operating at Nominal and Optimal RPM

Airspeed (kts)	Power Required at Nominal RPM (%)	Power Required at Optimal RPM (%)	Percentage Reduction in Power Required (%)
40	37.61	33.24	4.37
80	31.02	25.29	5.73
120	44.28	37.65	6.63

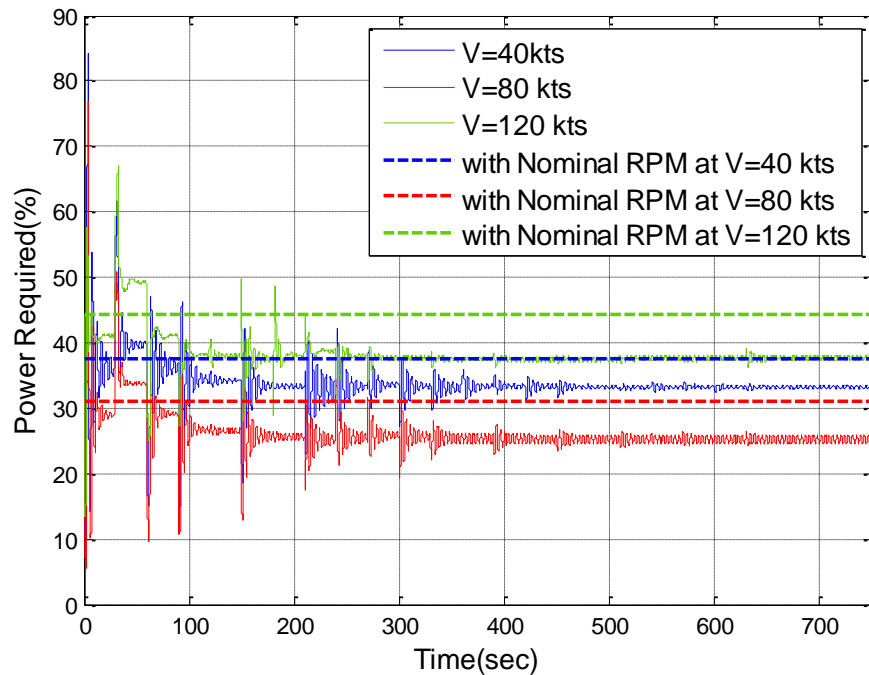


Figure 4-10: Power Required for Different Airspeed using Golden Section Method for FTO

4.3.2 Single Parameter Optimization of Multiple Control Effectors using Adaptive Performance Optimization Method

The flight control architecture with adaptive performance optimization method shown in the Chapter 3 implemented in the nonlinear model of the compound rotorcraft. Figure 4-11 shows

rotor speed and compound control effector maneuvers, and power required value during the whole optimization process at 150 knots level flight. Figure 4-12 shows the response of the rotorcraft throughout the optimization process at the same flight condition.

In the simulation, all five control effectors are forced to a low-frequency sinusoidal input in sequence. After the sinusoidal input the control effectors set to the value where minimum power required obtained before optimal search begins for the next control effector. Therefore, five individual optimizations take place in order, by applying the resultant condition of the previous one. The order of the optimization is important due to the change in trimmed controls after the optimization of the control effector. A different order of optimization may lead to a different set of controls by the end of optimization sequence, thus in this study the order of optimization is determined by the level of impact of each control effector. The rotor speed is chosen to be optimized first, because rotor speed is observed to affect rotorcraft performance more than other compound controls. The rest of the sequence is determined by comparing the effects of compound control effectors on rotorcraft performance. Therefore, rotor speed optimization is followed by propeller pitch angle, elevator deflection, symmetric flaperon deflection and differential flaperon deflection. The compound controls were initialized at some arbitrary condition. Optimization results later compared with the values obtained from the optimization study by Geiger [7].

The compound helicopter configuration includes four redundant control effectors in addition to main rotor RPM. These include propeller pitch (which changes auxiliary thrust and power), elevator (which changes the trimmed pitch attitude), symmetric flaperons (which change the wing lift), and differential flaperons (which change the roll moment produced by the wing). Table 4-2 shows the upper limits (UL) and lower limits (LL) for the compound control effectors at different airspeeds determined in the study by Geiger [7].

Table 4-2: Upper and Lower Limits of Compound Control Effectors for Different Airspeeds

Airspeed (kts)	0 to 40		50 to 70		80 to 200	
	LL	UL	LL	UL	LL	UL
Prop. Pitch (deg)	10	44	10	44	10	44
Elev. Trim (deg)	-10	10	-10	10	-10	10
Sym. Flap (deg)	62	62	-10	62	-10	10
Diff. Flap (deg)	0	0	-5	5	-5	5

Figure 4-13 shows the variation of rotor speed and power required during APO for rotor speed only at 150 knots level flight. Rotor speed is set to the minimum obtained by APO right after the optimization search is complete. Figure 4-14 shows power required with respect to rotor speed for the same flight condition. Figures 4-15 and 4-16 show similar APO results for propeller pitch with power required variation. Figures 4-17 and 4-18 show results for elevator, figures 4-19 and 4-20 show results for symmetric flap deflection, and figures 4-21 and 4-22 show results for differential flap deflection. Figure 4-23 shows the control stick positions and engine throttle position during the adaptive performance optimization routine at 150 knots.

From these results, optimal values of each control effectors can be determined and these values are stored to set the aircraft fly at an optimal state, once the optimization routine completed. If desired, the process could then be repeated starting at the new trim positions of the redundant controls. Significant reductions in power required appear to be achievable through adjustments in rotor speed, propeller pitch, elevator and differential flaps. Symmetric flap deflection remained close to their optimal trim value (0 degrees) as obtained by Geiger [7]. Rotor speed optimization results in more than 10% reduction in power required. Following that propeller pitch, elevator and differential flap optimizations each result in almost 1% reduction in power required.

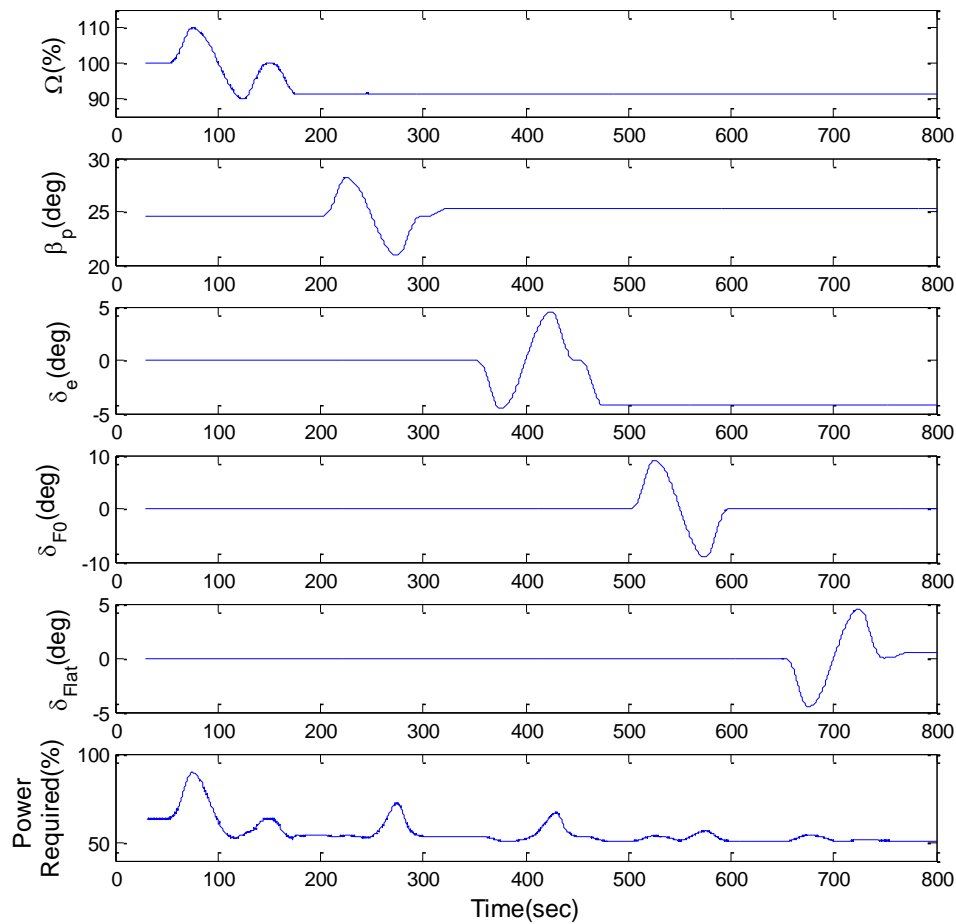


Figure 4-11: Adaptive Performance Optimization Results at 150 knots

As discussed earlier, it is desirable to apply slow varying changes to the optimization variables so the aircraft is near trim throughout the maneuver. However, the aircraft cannot maintain perfect trim during the optimization, and it is sought to perform the optimization maneuver within a reasonable time span. Therefore, power required adjustments were used to account for power used for a small amount of acceleration, climb/descent, and rotor speed variations during the maneuver. These adjustments are shown in equations 4.6, 4.7, and 4.8. The adjusted power required is shown in equation 4.9.

$$\Delta HP_{accel} = \frac{mV\dot{V}}{550} \quad (4.6)$$

$$\Delta HP_{climb} = \frac{mgh}{550} \quad (4.7)$$

$$\Delta HP_{RPM} = \frac{I_R \Omega \dot{\Omega}}{550} \quad (4.8)$$

$$HP_{adjusted} = HP_{measured} - \Delta HP_{accel} - \Delta HP_{climb} - \Delta HP_{RPM} \quad (4.9)$$

In the equations above, m is the rotorcraft mass, V is the equivalent airspeed, h is the altitude, I_R is the main rotor moment of inertia and Ω is the main rotor speed. The adjustments help reduce the hysteresis effect observed in Figures 4-14, 4-16, 4-18, 4-20, and 4-22 although it did not eliminate it completely. The hysteresis effect is the main factor determining the length of the APO maneuver (shortening the APO maneuver results in larger hysteresis and makes estimating optimal more difficult). However, the overall APO maneuver took almost the same time as golden section method optimization. Considering the five different redundant controls that are optimized during this maneuver, it is clear that APO is superior to golden section method in terms of speed. Optimization results were compared with the optimization study performed by Geiger [7]. All four compound controls stayed in the margin of ± 2 degrees.

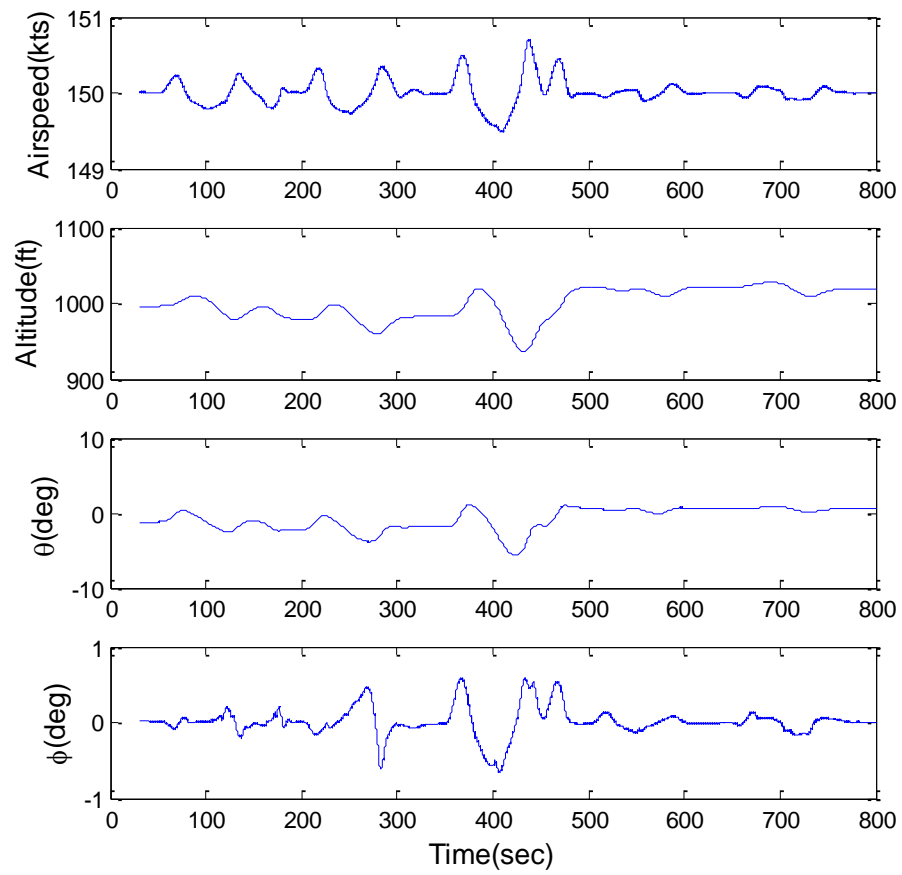


Figure 4-12: Aircraft Response during APO at 150 knots

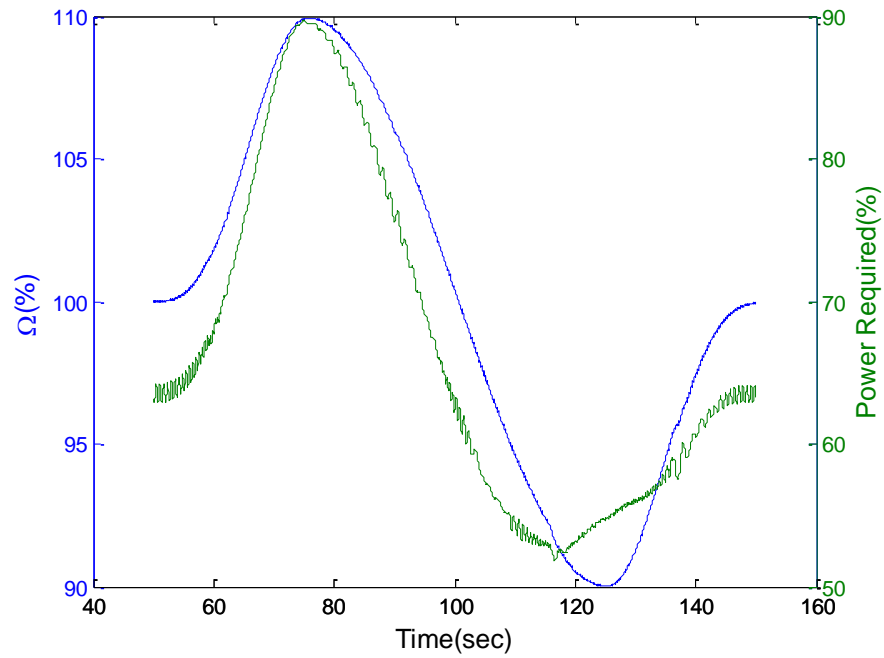


Figure 4-13: Adaptive Performance Optimization Results for Rotor Speed at 150 knots

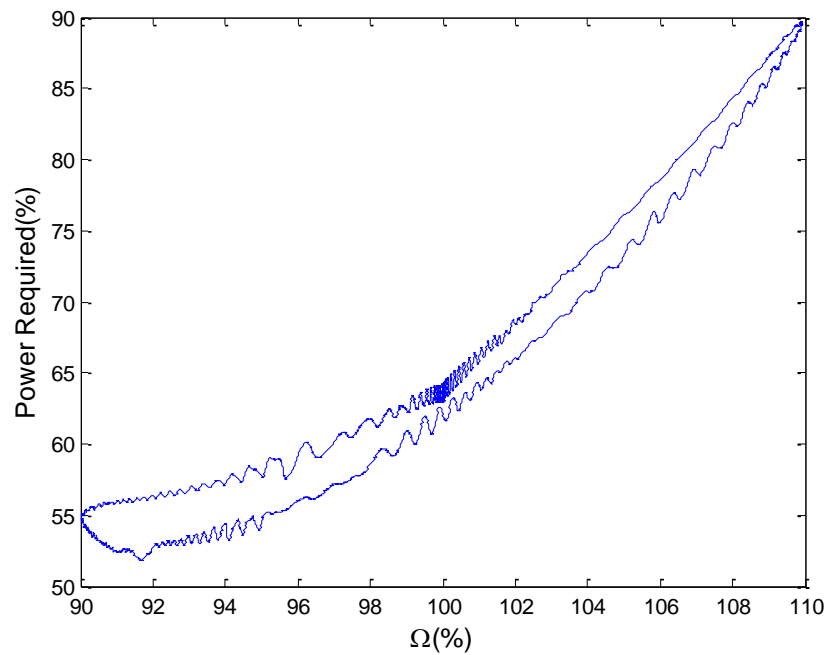


Figure 4-14: Power Required vs. Rotor Speed at 150 knots during APO

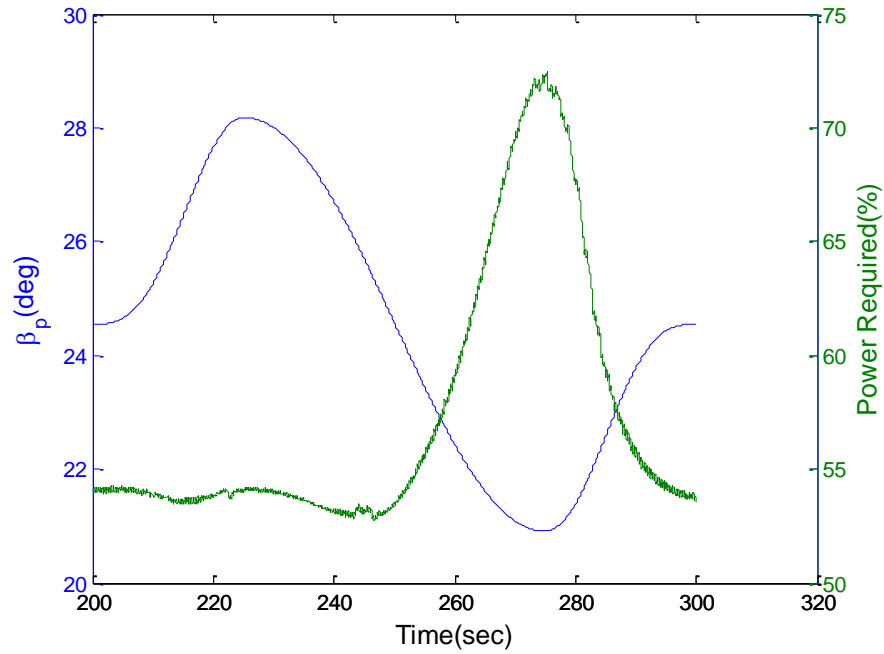


Figure 4-15: Adaptive Performance Optimization Results for Propeller Pitch at 150 knots

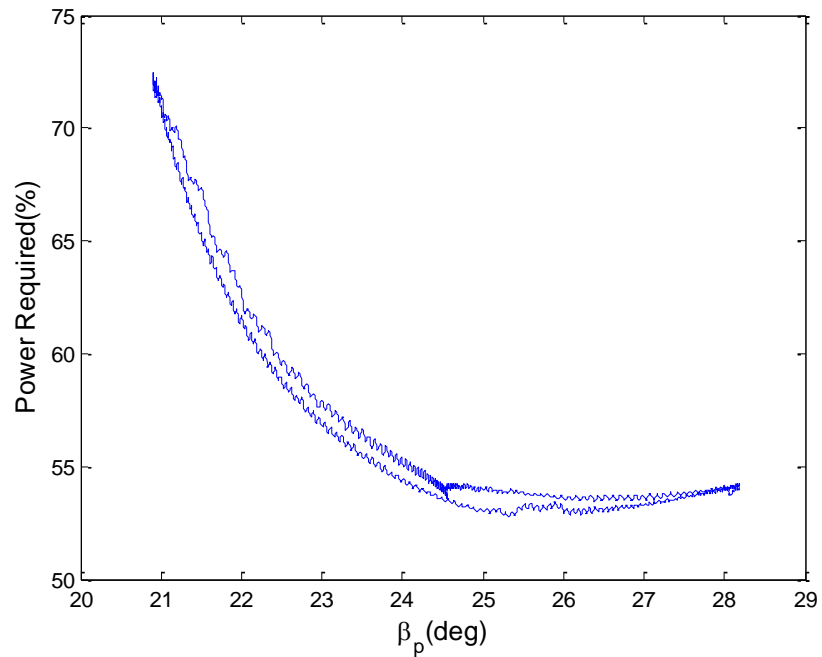


Figure 4-16: Power Required vs. Propeller Pitch at 150 knots during APO

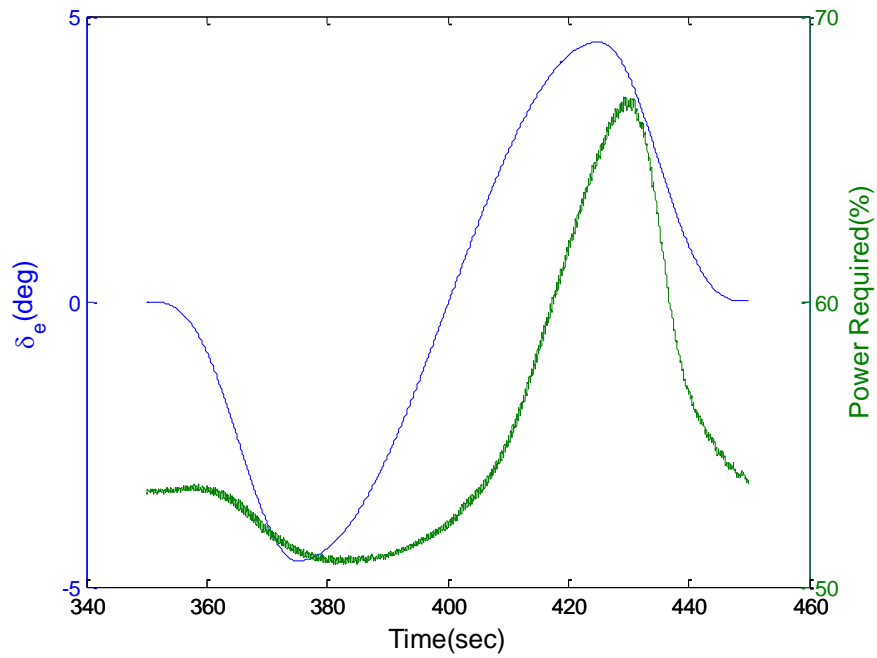


Figure 4-17: Adaptive Performance Optimization Results for Elevator Deflection at 150 knots

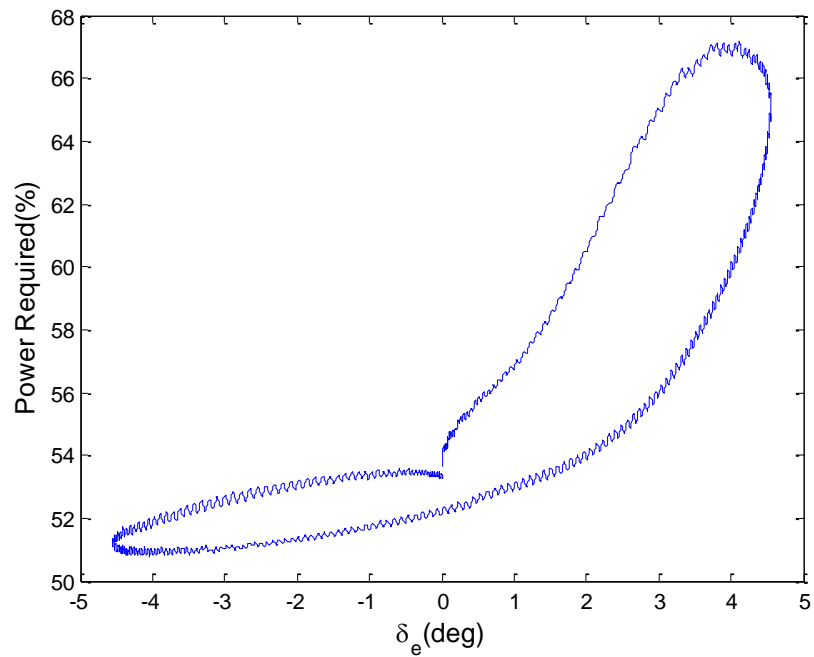


Figure 4-18: Power Required vs. Elevator Deflection at 150 knots during APO

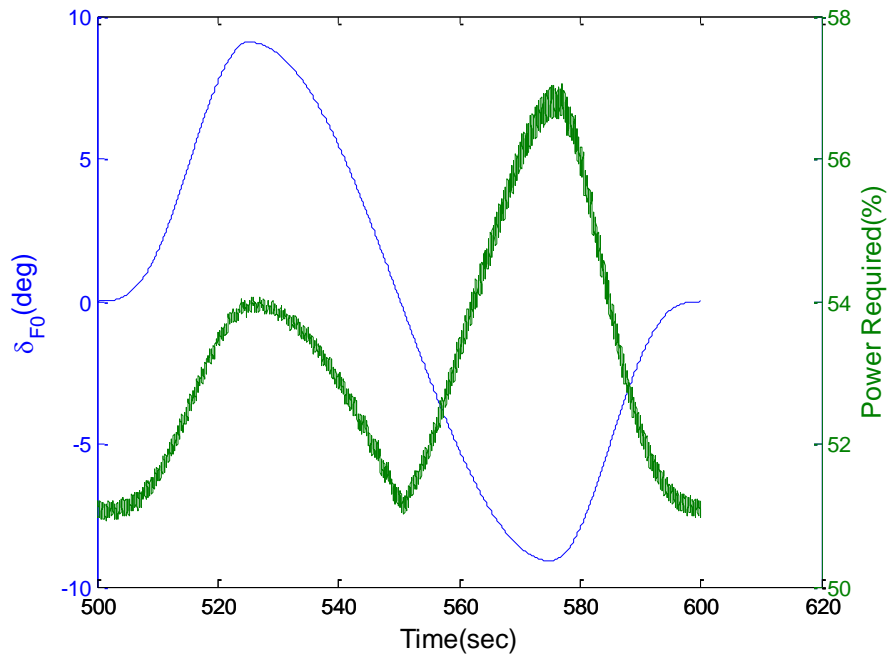


Figure 4-19: Adaptive Performance Optimization Results for Symmetric Flaperon at 150 knots

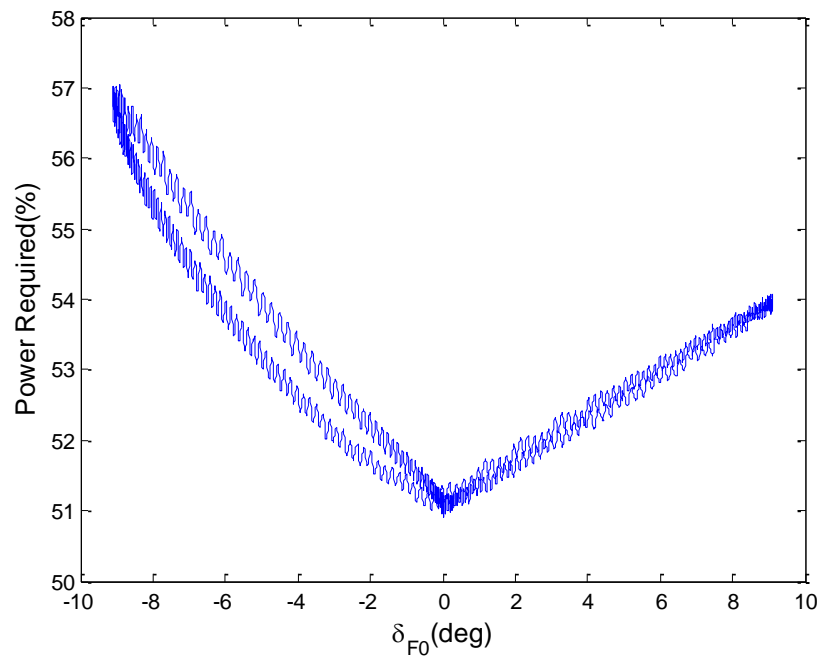


Figure 4-20: Power Required vs. Symmetric Flaperon at 150 knots during APO

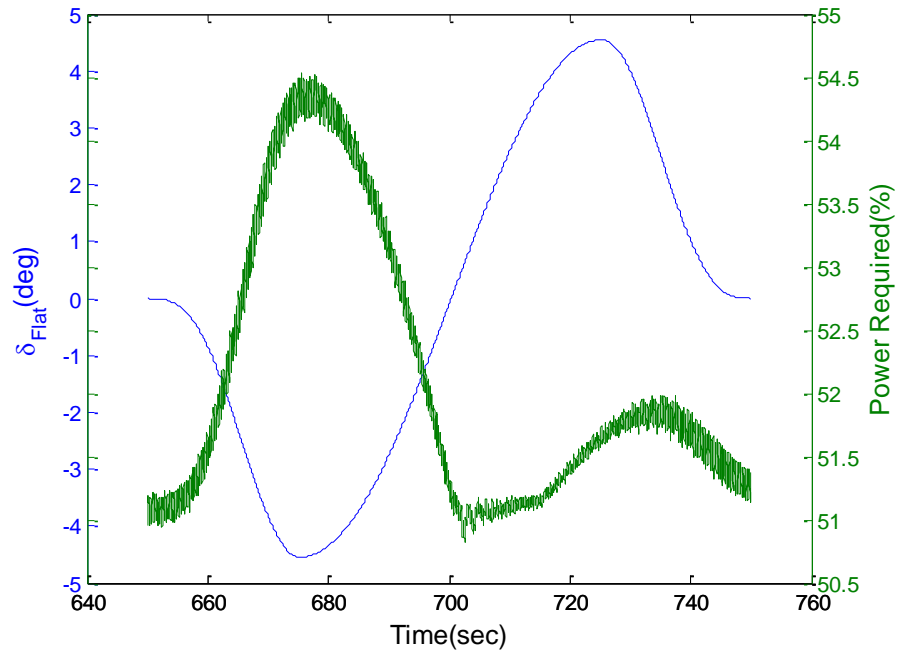


Figure 4-21: Adaptive Performance Optimization Results for Differential Flaperon at 150 knots

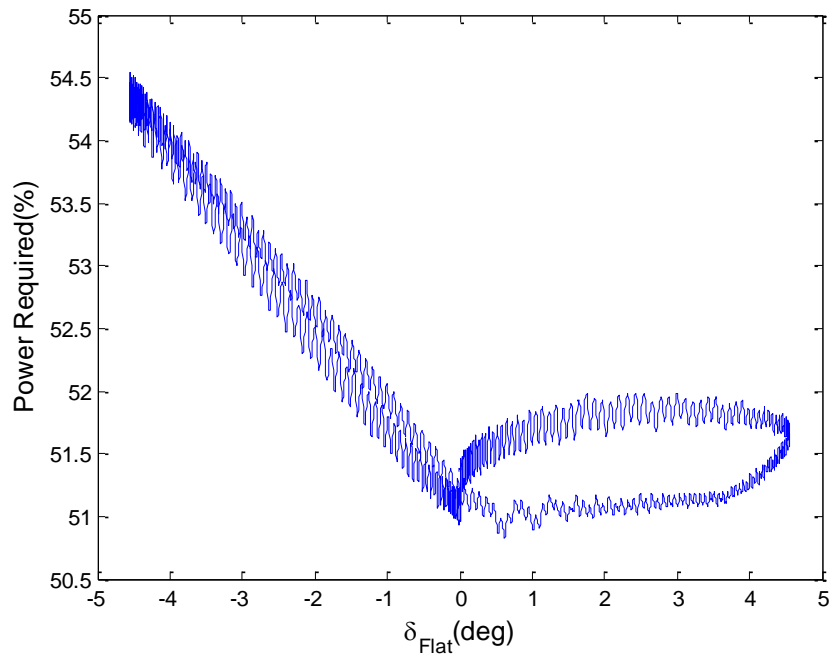


Figure 4-22: Power Required vs. Differential Flaperon at 150 knots during APO

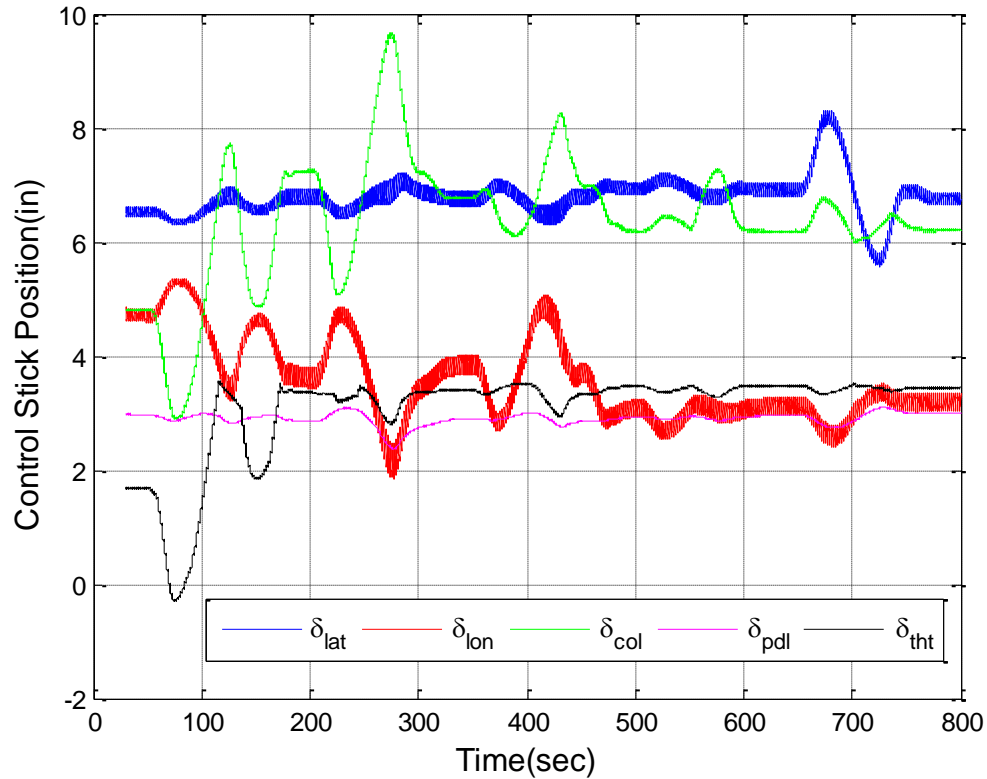


Figure 4-23: Control Stick Positions and Engine Throttle Position during APO at 150 knots

4.3.3 Multiple Parameter Optimization of Multiple Control Effectors Using Adaptive Performance Optimization Method

In this section two performance characteristics are optimized separately, range and power. In order to maximize the range of the aircraft, airspeed and stabilator are used as optimization variables to maximize the equivalent L/D of the aircraft. To minimize power at high speeds, collective and stabilator deflection are optimized. The focus is on optimization of two control variables to investigate a new multi-variable approach to adaptive performance optimization. However, for the high-speed mode of the controller, the trim variables change and the optimization variables change as well. Also, in the study for multiple parameter optimization of multiple control effectors the RPM control axis was disabled, as the results were generated

using a fixed rotor RPM in the simulation model. This study focuses on the simultaneous optimization of two control variables to investigate a new multi-variable approach to performance optimization.

Typically, the airspeed at which the range is maximized can be obtained from the power required curve of a rotorcraft where the ratio of power over velocity is minimized. This is equivalent to maximizing the effective lift-to-drag ratio. Equation 4.10 shows how the equivalent lift-to-drag ratio is calculated. Thus, maximum range is a function of the airspeed operating point as well as the aircraft configuration.

$$\left(\frac{L}{D}\right)_{eq} = \frac{WV_{\infty}}{HP} \quad (4.10)$$

In range optimization study, the airspeed set point and stabilator deflection were chosen as the optimization variables. The two variables are perturbed simultaneously using out of phase sinusoidal commands with varying amplitude. This is done in a way that spans a wide range of possible trims. The airspeed sweep is performed between 80 knots and 150 knots and the stabilator sweep is varied between -15 degrees to 5. The CSF control law with FTO tool is used for this optimization maneuver.

The minimum power optimization for the generic compound helicopter at constant airspeed is performed by the excitation of collective and stabilator deflection using a simultaneous perturbation. Real time measurement of power required of the helicopter is used as the performance characteristic to be optimized. Similar to range maximization, collective and stabilator deflection aim to span the whole range of possible trims and search for minimum power. Due to the high airspeed, the range of controls that the aircraft can trim is reduced compared to lower or cruise speed flights. Therefore, the range of the sweeps for controls is limited using the Control Limit Calculation tool of the FTO component of the controller, as described in section 4.2.

4.3.3.1 Maximum Range Optimization

Figure 4-24 shows the trim analysis for the maximum range optimization. Symmetric stabilator deflection and airspeed sweeps are used in this analysis. The trim values are used to check the results of the FTO maneuver. For this configuration it was found that best L/D is achieved using only lift compounding, where the propeller is put in a low power state and the main rotor is used for forward propulsion. However, the wing offloads some of the rotor lift requirements. The stabilator sweep effectively optimizes the trim angle of attack to achieve the best wing / rotor lift distribution for maximum range while the speed set point sweep simultaneously finds the best airspeed. Figures 4-25 and 4-26 show commanded values of the optimization variables during the range optimization and the equivalent lift-to-drag ratio variation with optimization controls. The airspeed and symmetric stabilator deflection are forced to out-of-phase low-frequency sinusoidal inputs; therefore, the full range of controls can be searched for the optimal trim through a spiraling pattern. In figure 4-25, the maneuver starts with level flight at 120 knots and with 0 degree symmetric stabilator deflection and lasts for 25 minutes. Figure 4-27 shows the response of the aircraft during the maneuver. Figures 4-26 and 4-28 show the range optimization maneuver that starts from 100 knots and 0 degree symmetric stabilator deflection.

From these results, optimal values for each control effector can be determined and these values are stored to set the aircraft to fly at an optimal state once the optimization routine has completed. The range of the compound helicopter can be maximized by defining the new trim state at the high values of equivalent lift-to-drag ratio. For the first maneuver, at the initial trim state, the equivalent lift-to-drag ratio is 4.99, and throughout the optimization search equivalent lift-to-drag ratio increases up to 5.18. The optimization drives the controls to the optimal state, which is level flight at 107.5 knots and a stabilator deflection of -6.13 degrees. For the second maneuver, at the initial trim state, the equivalent lift-to-drag ratio is 4.89, and throughout the

optimization search equivalent lift-to-drag ratio increases up to 5.17. The optimization drives the controls to the optimal state, which is level flight at 108.1 knots and a stabilator deflection of -5.33 degrees. The trim results show that maximum range occurs at 111.4 knots when stabilator deflection is -6.4 degrees and the equivalent lift-to-drag ratio is 5.28. According to these results, the FTO reached within 1.89% of the optimal lift-to-drag ratio for the first maneuver and 2.08% of the optimal lift-to-drag ratio for the second maneuver as found through an extensive search of trim solutions. The controls that reach the optimal lift-to-drag ratio lies within a flat surface in the control space as shown in figure 4-24. The FTO maneuvers end up at slightly different control positions, but the lift-to-drag ratio is close to the optimal value. However, aircraft response indicates during the optimization maneuver, the altitude shows variation from the trim altitude. The controller has trouble holding the altitude with the variation of stabilator and airspeed. This drives the aircraft into a transient state. Although corrections for transient effects included in the optimization calculations, the transient in the lift-to-drag ratio can be observed in figures 4-25 and 4-26. This effect is visibly observed at high stabilator deflection values.

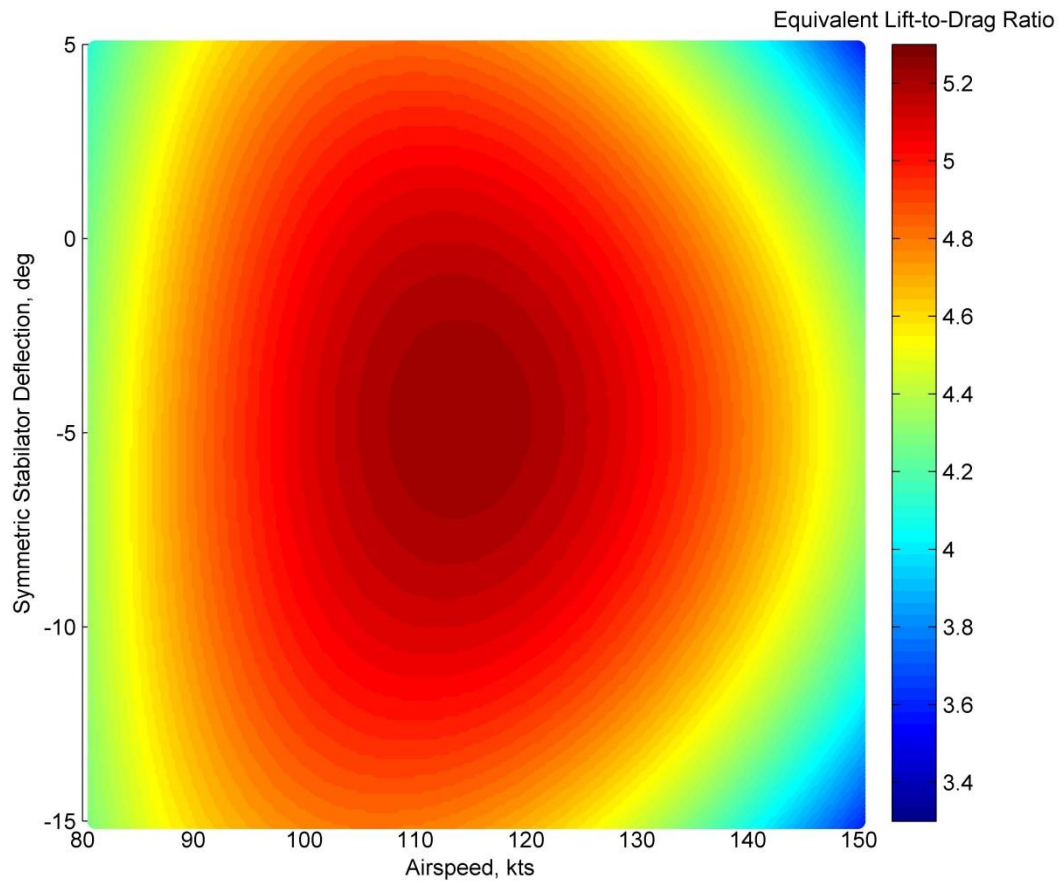


Figure 4-24: Trim Analysis for the Maximum Range Search

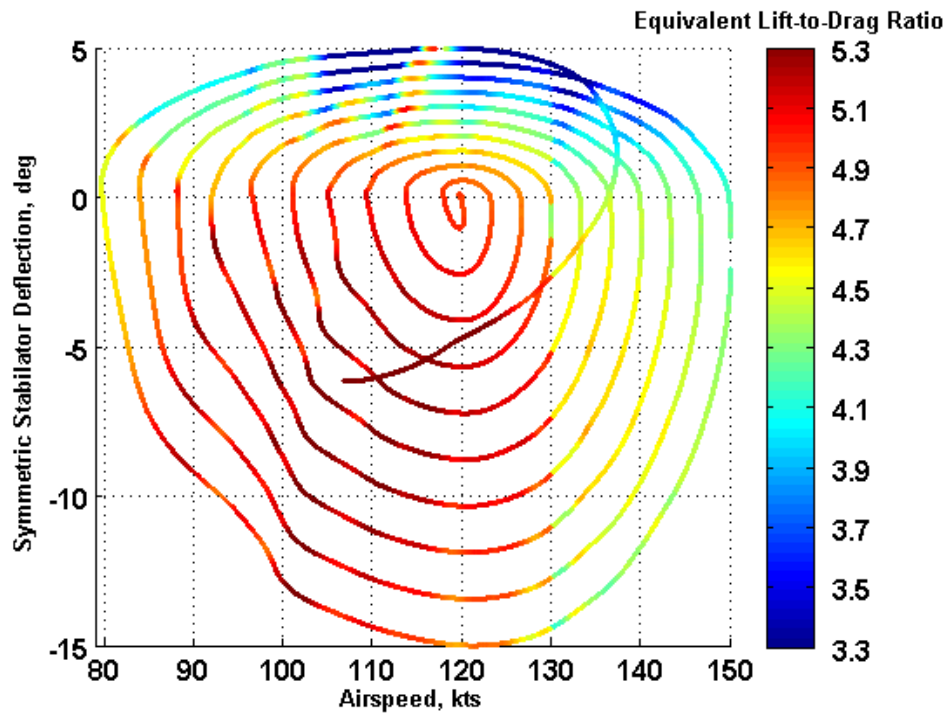


Figure 4-25: Range Optimization Maneuver starting at 120 knots

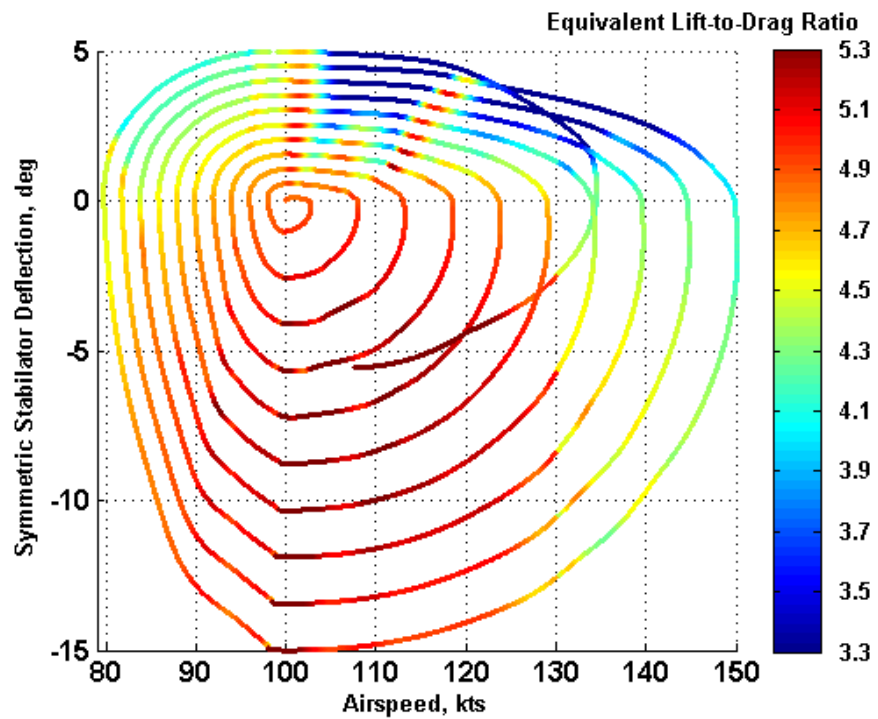


Figure 4-26: Range Optimization Maneuver starting at 100 knots

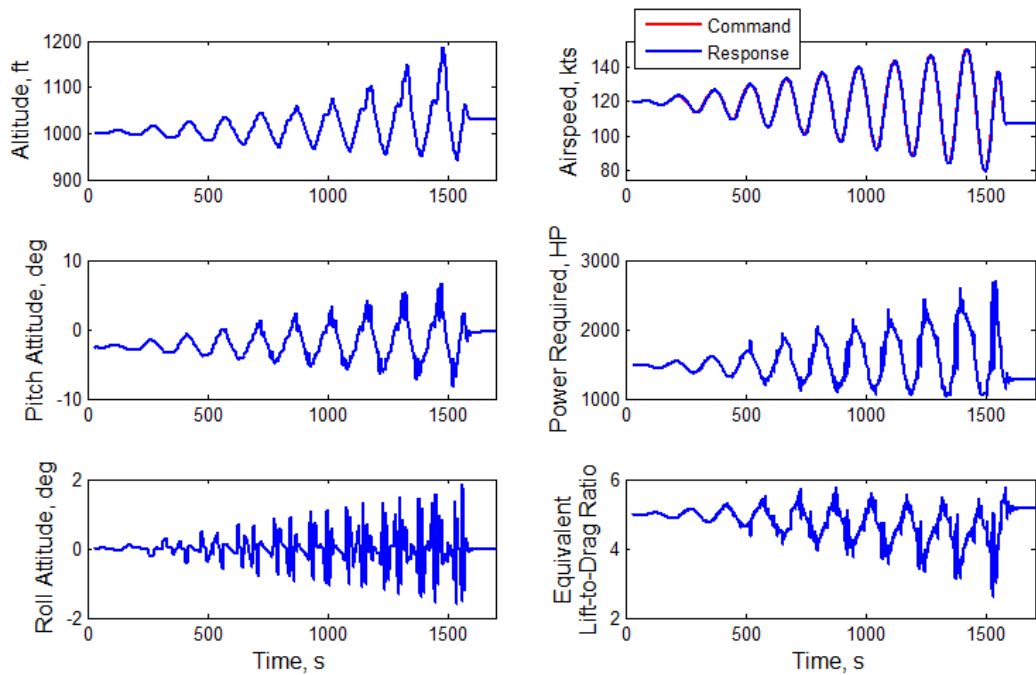


Figure 4-27: Response of the Aircraft during Range Optimization Maneuver starting at 120 knots

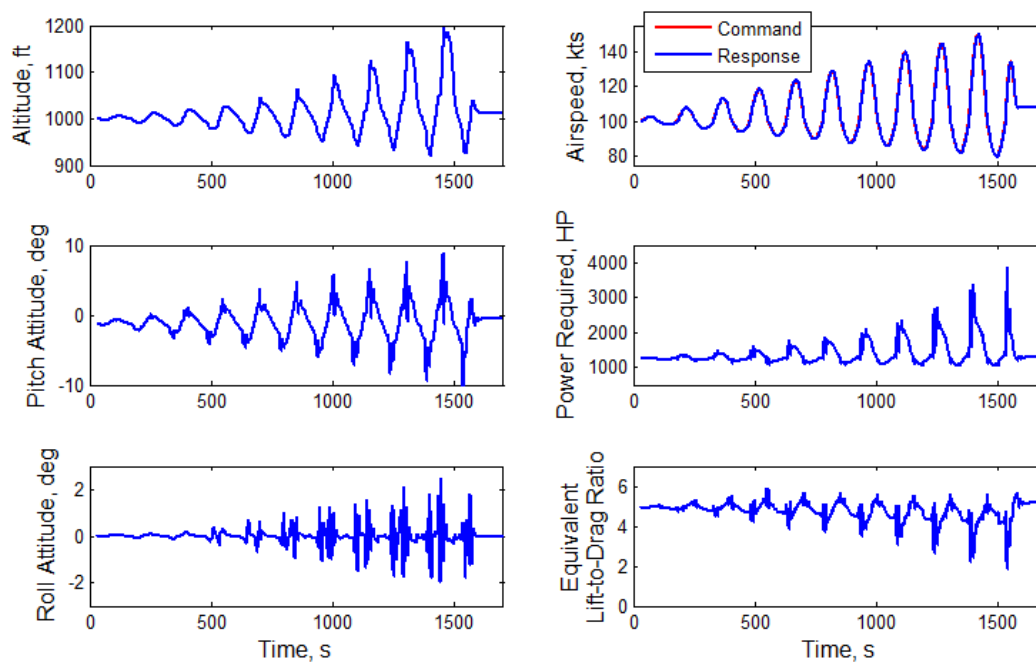


Figure 4-28: Response of the Aircraft during Range Optimization Maneuver starting at 100 knots

4.3.3.2 Minimum Power Optimization

A power optimization maneuver is performed for two different flight conditions: 180 knots and 200 knots. The main rotor and propeller rotation speeds are reduced to 90% of the nominal RPM in order to avoid compressibility effects due to the high main rotor tip speed for the 180 knots case and to 85% of the nominal RPM for the 200 knots case. Figures 4-29 and 4-37 show the trim analysis for the minimum power optimization for 180 and 200 knots cases, respectively. Figures 4-30 and 4-38 show higher resolution trim analysis for the minimum power required with collective pitch and stabilator deflection for a focused region of controls. Figures 4-31 and 4-39 show the power required variation with collective pitch and stabilator deflection. Collective pitch and stabilator deflection angles are forced to out-of-phase low-frequency sinusoidal inputs. Figures 4-32 and 4-40 show the responses of the aircraft during the optimization maneuvers. Figures 4-33 and 4-41 show the lift and thrust sharing between main rotor and auxiliary components, wing and propeller during the optimization maneuvers. For both maneuvers, at optimal wing is the main source of the lift, off-loading main rotor. Figures 4-34 and 4-42 show the main rotor flapping angles and main rotor controls during the optimization maneuvers. Main rotor controls stayed within the control limits, as given in Table 2-3, during the optimization maneuvers. Main rotor flapping angles are stayed within ± 5 degrees during 180 knots optimization and ± 7 degrees during 200 knots optimization. Figures 4-35 and 4-43 show the lift distribution over the rotor disk before and after the optimization maneuvers and for both maneuvers reductions in lift can be observed due to the off-loading of the rotor disk. Similarly, figures 4-36 and 4-44 show the inflow distribution over the rotor disk before and after the optimization maneuver. Reduction in the inflow is observed for both optimization maneuvers.

The boundaries of the trim regions shown in figures 4-29 and 4-37, in general, are constrained by propeller stall, longitudinal cyclic saturation, and collective travel limits. At high

negative stabilator deflections and low collective, main rotor lift drops below zero and drives up wing lift. As main rotor lift becomes more negative and wing lift increases, wing induced drag begins to rise rapidly. Eventually, the demand from the propeller to trim forward acceleration causes the maximum allowable propeller pitch to be approached and the propeller stalls. At high positive stabilator deflection, beyond the maximum power limit, the main rotor drag rises rapidly partly due to a consistent large nose down pitch attitude and continues to increase with increased collective pitch. A high enough positive stabilator deflection at high collective tends to push the trim region into an increasing propeller pitch and increasing collective pitch direction. The in-plane main rotor drag force (H-force) then rises at a much faster rate than the rotor thrust increase from increasing collective, and this causes the propeller thrust to increase to compensate for overall increased rotor drag. The in-plane rotor drag force is highly sensitive to the main rotor thrust coefficient at high speeds. Once again, the demand from the propeller to trim forward acceleration causes propeller stall to eventually occur; but this is well beyond the maximum power limit. Beyond the propeller stall limit for increasing positive stabilator deflection and increasing collective pitch would be the stabilator and negative angle of attack wing stall limits. High stabilator download combined with longitudinal cyclic saturation at high negative stabilator deflections and low collective further constrains the trim region as both the pitching moment and vertical force equilibrium equations are unable to be satisfied. The range of feasible trim conditions gets smaller at high airspeeds, and the optimization maneuver starts to operate very close to control margins. In-flight optimization maneuver searches a wide range of collective pitch and stabilizer positions, but some of the points in this range are not feasible trim conditions. In order to avoid the optimization to search those points dynamic trim concept is used. Dynamic trim method predicts the limits on the controls and the FTO maneuver is modified accordingly; this is the reason for the distorted shape of the search area. The upper and lower limits on the controls are updated periodically during the maneuver.

The 180 knots optimization of the rotorcraft is trimmed at power required value of 2948 hp and throughout the optimization search the power required drops to 2691 hp, 8.7% reduction in power required, where the collective pitch is 17.76 degrees and stabilator deflection is -3.85 degrees. The trim analysis shows that for 180 knots level flight, minimum power is 2662 hp and the collective pitch is 15.38 degrees and stabilator is 0 degrees.

The 200 knots optimization is trimmed at power required value of 3605 hp, and after the optimization search, the power required drops to 3455 hp, 4.1% reduction in power required, where the collective pitch is 17.81 degrees and the stabilator deflection is -0.59 degrees. The trim analysis shows that for 200 knots level flight, minimum power is 3410 hp with the collective pitch is 14.30 degrees and the stabilator is 2.1 degrees.

The FTO reached within 1.09% of the optimal power value for the optimization at 180 knots and 1.32% of the optimal power for the 200 knots optimization as found through an extensive search of trim solutions. Similar to the maximum range optimization trim analysis, the controls that reach the optimal power lies within a flat surface in the control space as shown in figures 4-30 and 4-38. The FTO maneuvers end up at slightly different control positions, but the power values are close to the optimal.

Although a significant reduction in power required is obtained by FTO maneuvers for both 180 and 200 knots, figures 4-31 and 4-39 show drastic increases in power during the FTO maneuver, especially for the region with high collective pitch and high symmetric stabilator deflection. Searching for the optimal at the controls that has higher power required values than the trim power is obviously a waste of time and fuel. Therefore, the power can be limited to a lower value than the available power during the FTO maneuver. With the lower power limit, the time it takes to complete the optimization maneuver can be lowered 21 minutes, instead of 25 minutes. Figures 4-45 and 4-51 show the FTO maneuver for minimum power search at 180 knots and 200 knots with maximum power limited to 5% higher of the initial trimmed power value. The

search method is avoiding the search of region with high power values, so in addition to shortening the search time, the waste of fuel in searching regions with very high power is avoided. Figures 4-46 and 4-52 show the responses of the aircraft during the optimization maneuvers. Figures 4-47 and 4-53 show the lift and thrust sharing between main rotor and auxiliary components; wing and propeller, during the optimization maneuvers. Figures 4-48 and 4-54 show the main rotor flapping angles and main rotor controls during the optimization maneuvers. Main rotor controls stayed within the control limits, as given in Table 2-3. Main rotor flapping angles are stayed within ± 6 degrees during both 180 knots and 200 knots optimizations. Figures 4-49 and 4-55 show the lift distribution over the rotor disk before and after the optimization maneuvers. A reduction in lift is observed due to the off-loading of the rotor disk. Similarly, figures 4-50 and 4-56 show the inflow distribution over the rotor disk before and after the optimization maneuver. Reduction in the inflow is also observed for both optimization maneuvers.

With the low power limit, the 180 knots optimization of the rotorcraft is trimmed at power required value of 2948 hp and throughout the optimization search the power required drops to 2698 hp, 8.4% reduction in power required, where the collective pitch is 17.98 degrees and stabilator deflection is -4.17 degrees. The trim analysis shows that for 180 knots level flight, minimum power is 2662 hp, where the collective pitch is 15.38 degrees and stabilator is 0 degrees. The FTO with low power limit reached within 1.35% of the optimal power value for the optimization at 180 knots as found through an extensive search of trim solutions. A good indicator of the effect of FTO is to compare the fuel consumption between a flight scenario with and without FTO maneuver over a given time. The fuel consumption, W_f , over a given time, t , can be calculated using equation 4.11, where SFC is the specific fuel consumption and HP is the power required. The specific fuel consumption at 180 knots is 0.2228 lb/hp/hr. Without the FTO maneuver, for 2 hours of flight the rotorcraft consumes 1313.63 lb of fuel at 2948 hp trimmed

power and 229.88 lb of fuel is consumed for the first 21 minutes. With the FTO maneuver, first 21 minutes of the flight time is used for the optimization maneuver and 222.51 lb of fuel consumed, which is 7.37 lb less than the nominal flight condition. The remaining flight time (1 hour and 40 minutes) is performed at the optimal flight condition determined by the optimization maneuver, which has the power required value of 2698 hp, and 991.84 lb of fuel is consumed during this portion of the flight. So the total fuel consumption of 2 hours flight at 180 knots with FTO maneuver is 1238.17 lb, which is 99.28 lb less than the nominal flight condition. Table 4-3 tabulates the fuel consumptions for flights with and without FTO at 180 knots.

$$W_f = SFC \times HP \times t \quad (4.11)$$

Similarly, with the low power limit, the 200 knots optimization is trimmed at power required value of 3605 hp, and after the optimization search, the power required drops to 3460 hp, 4.0% reduction in power required, where the collective pitch is 17.88 degrees and the stabilator deflection is -0.76 degrees. The trim analysis shows that for 200 knots level flight, minimum power is 3410 hp, where the collective pitch is 14.30 degrees and the stabilator is 2.1 degrees. The FTO with low power limit reached within 1.47% of the optimal power for the 200 knots optimization as found through an extensive search of trim solutions. The specific fuel consumption at 200 knots is 0.2150 lb/hp/hr. Without performing the FTO maneuver, for 2 hours of flight the rotorcraft consumes 1550.15 lb of fuel at 3605 hp trimmed power and 271.28 lb of fuel is consumed for the first 21 minutes. With the FTO maneuver, first 21 minutes of the flight time is used for the optimization maneuver and 268.63 lb of fuel consumed, which is 2.65 lb less than the nominal flight condition. The remaining flight time (1 hour and 40 minutes) is performed at optimal flight condition determined by the optimization maneuver, which has a power required value of 3460 hp, and 1227.43 lb of fuel is consumed during this portion of the flight. So the total fuel consumption of 2 hours flight at 200 knots with FTO maneuver is 1496.06 lb, which is 54.09

lb less than the nominal flight condition. Table 4-3 tabulates the fuel consumptions for flights with and without FTO at 200 knots.

Table 4-3: Fuel Consumption with and without FTO at 180 knots and 200 knots

Flight	Fuel Consumption 0-21 minutes (lb)	Fuel Consumption 21-120 minutes (lb)	Total Fuel Consumption (lb)
180 kts without FTO	229.88	1083.75	1313.63
180 kts with FTO	222.51	991.84	1214.35
200 kts without FTO	271.28	1278.87	1550.15
200 kts with FTO	268.63	1227.43	1496.06

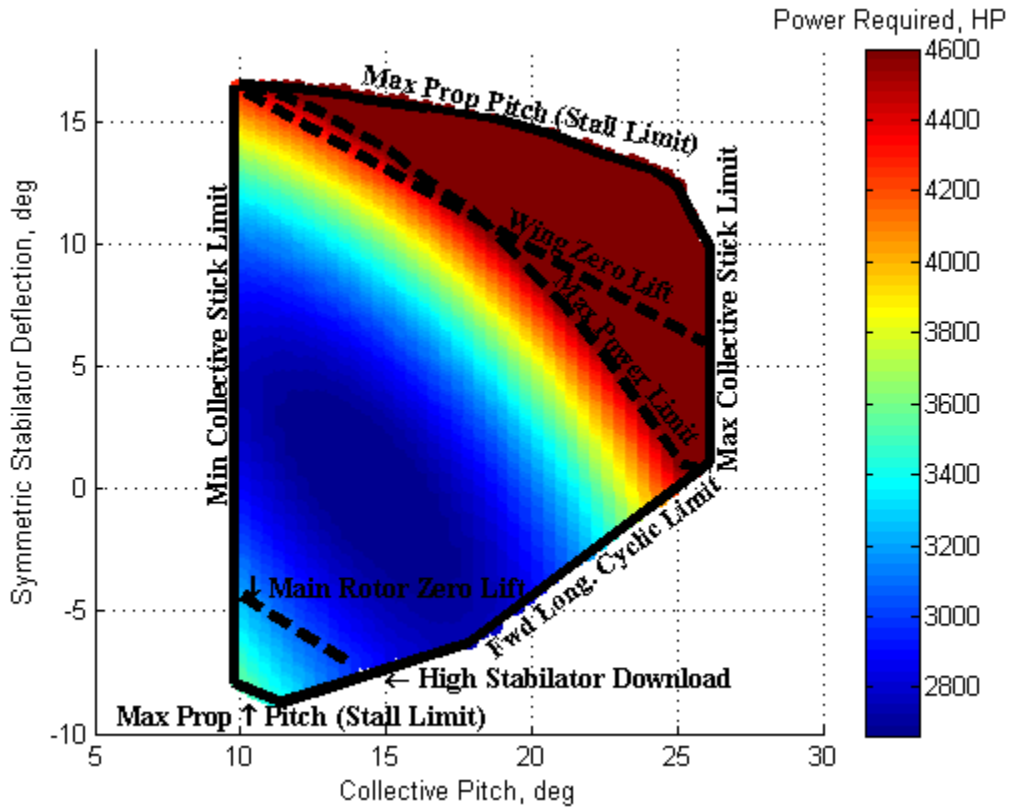


Figure 4-29: Trim Analysis for the Minimum Power Search at 180 knots with Trim Boundaries

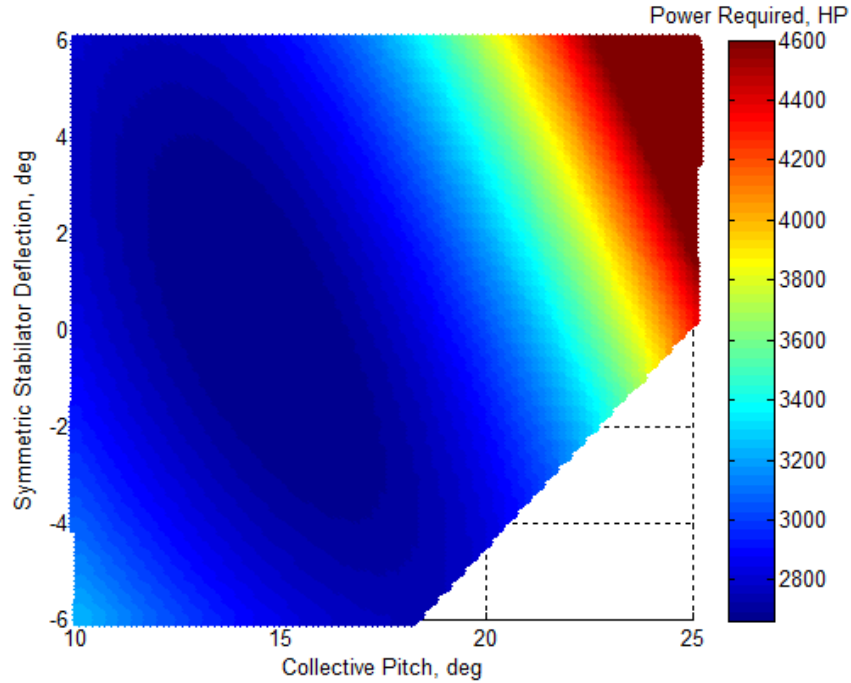


Figure 4-30: Trim Analysis for the Minimum Power Search at 180 knots

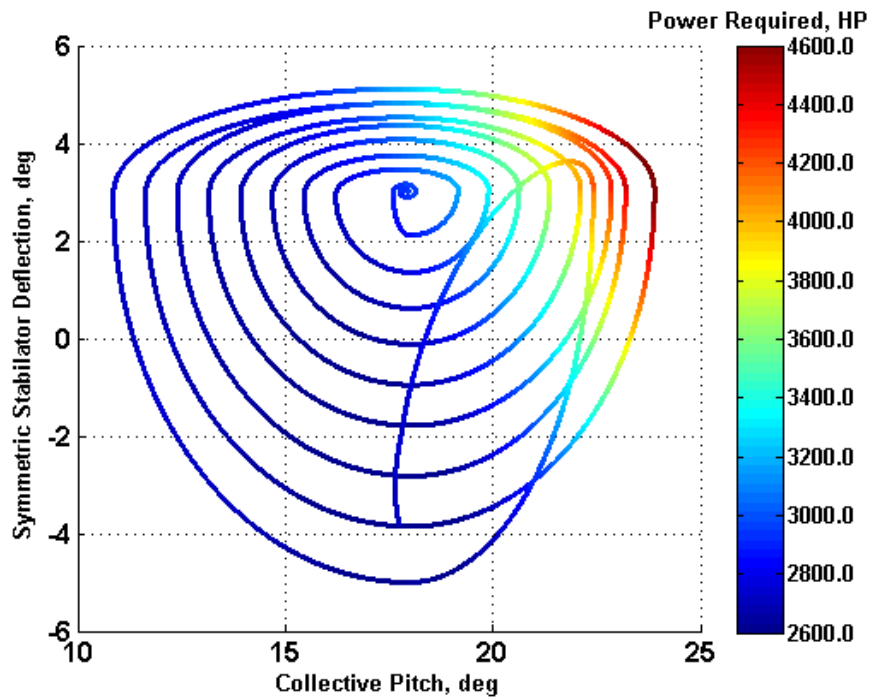


Figure 4-31: Optimization with Collective Pitch and Stabilator Deflection for Minimum Power Required at 180 knots

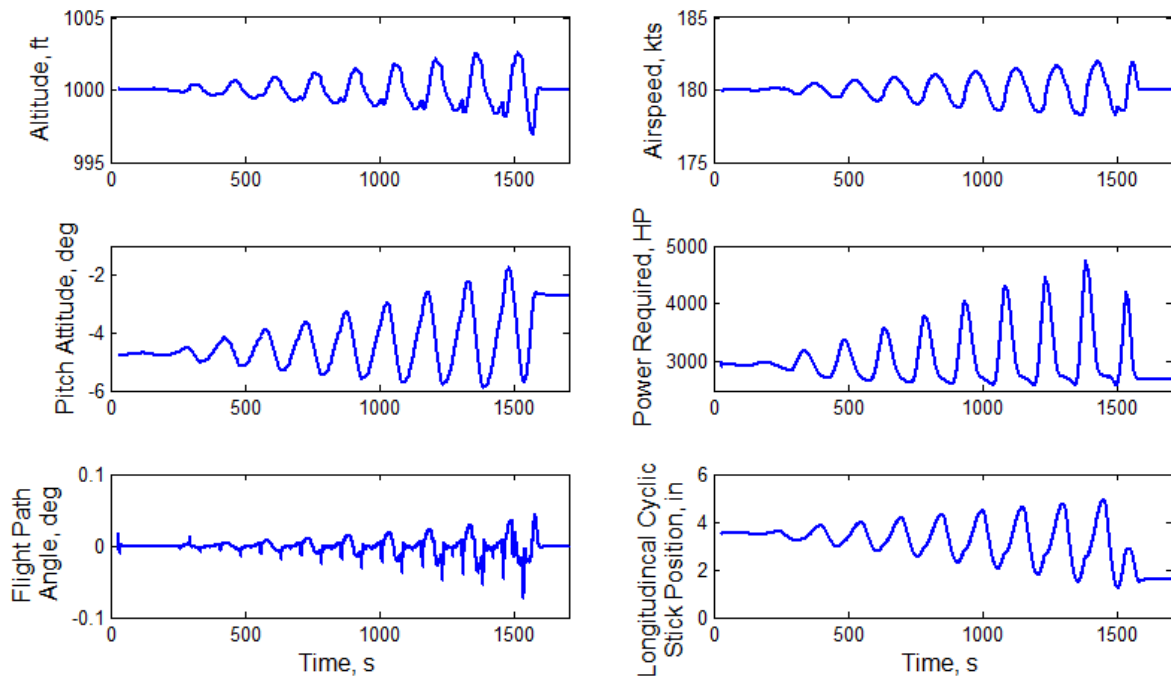


Figure 4-32: Response of the Aircraft during Power Optimization Maneuver at 180 knots

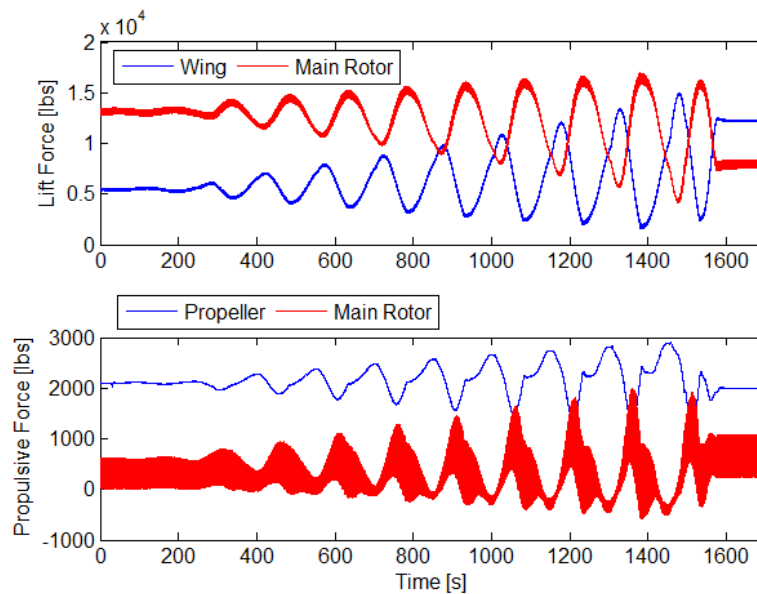


Figure 4-33: Lift and Thrust Sharing between Main Rotor, Wing and Propeller during Power Optimization Maneuver at 180 knots

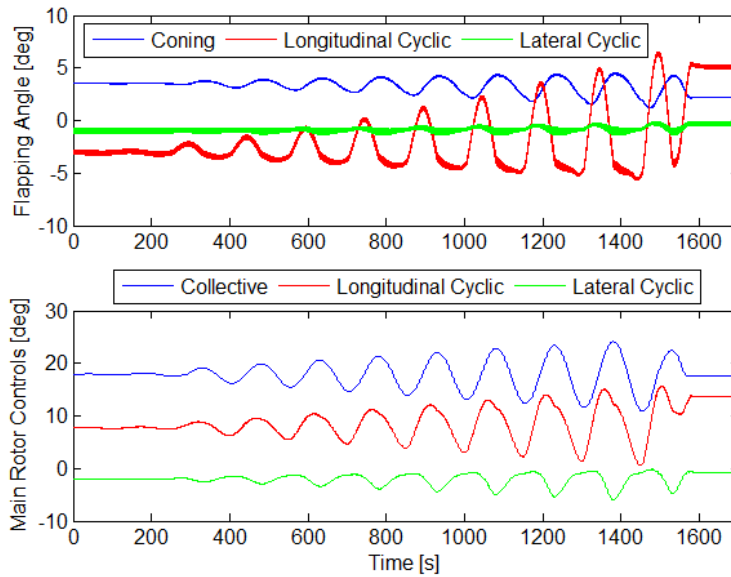


Figure 4-34: Flapping of the Rotor and Main Rotor Controls during Power Optimization Maneuver at 180 knots

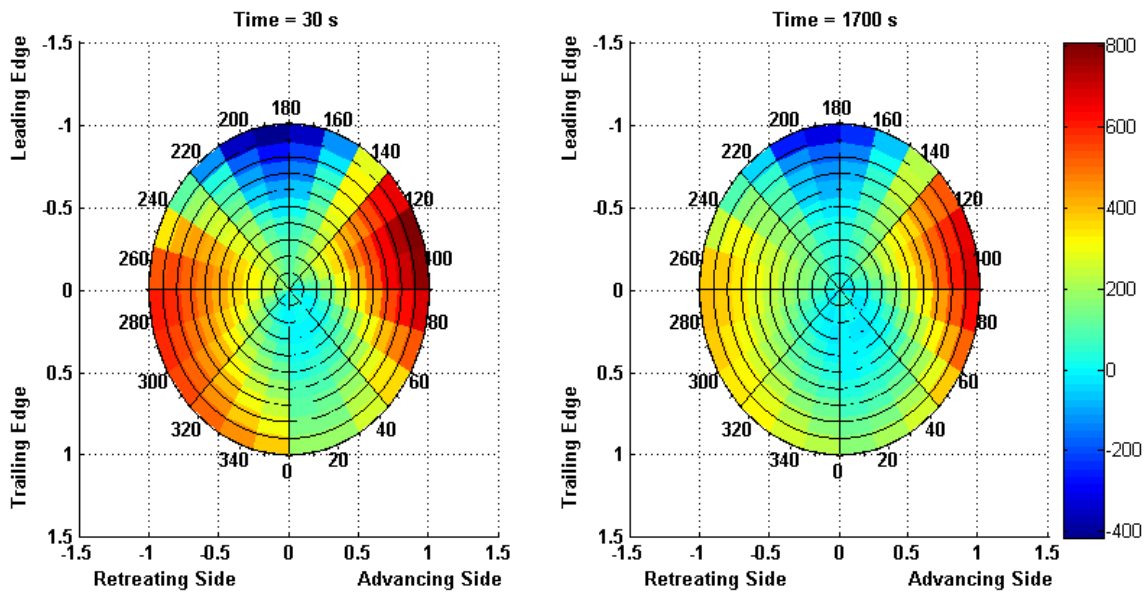


Figure 4-35: Lift Distribution over the Main Rotor Disk before and after the Power Optimization Maneuver at 180 knots [lbs]

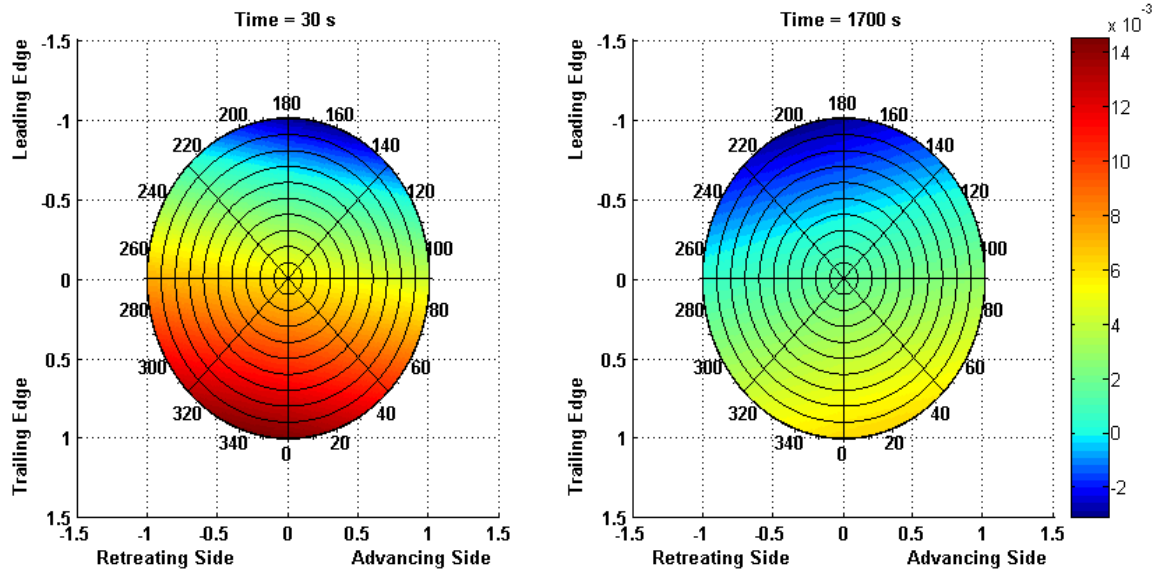


Figure 4-36: Inflow Distribution over the Main Rotor Disk before and after the Power Optimization Maneuver at 180 knots

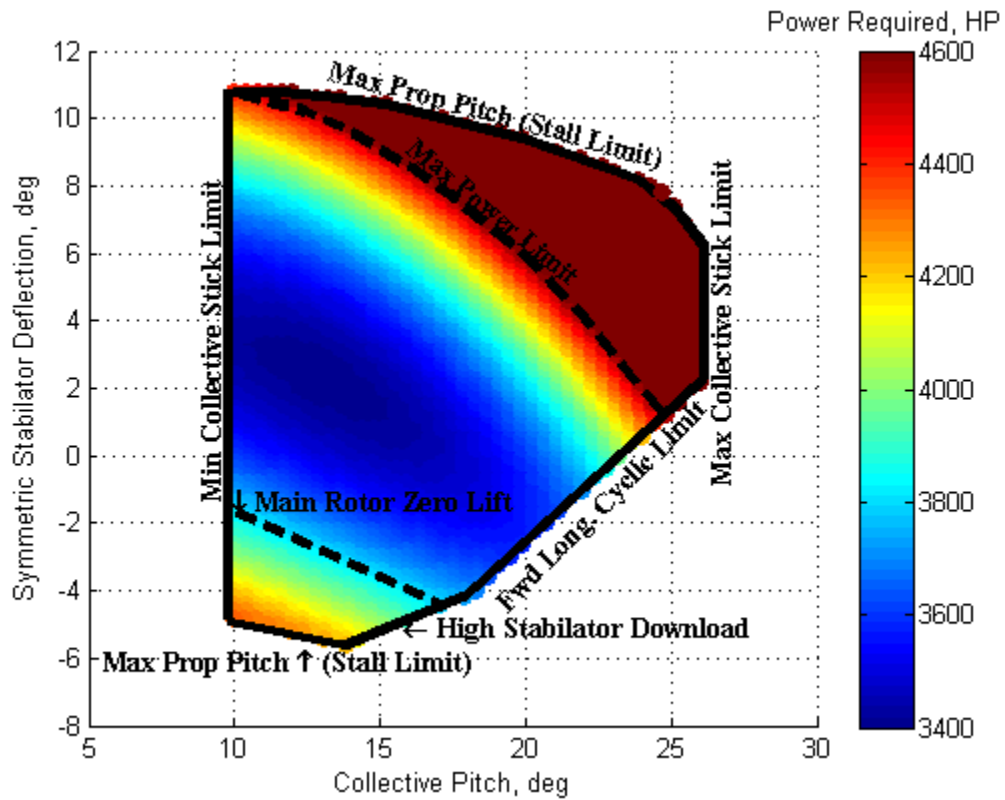


Figure 4-37: Trim Analysis for the Minimum Power Search at 200 knots with Trim Boundaries

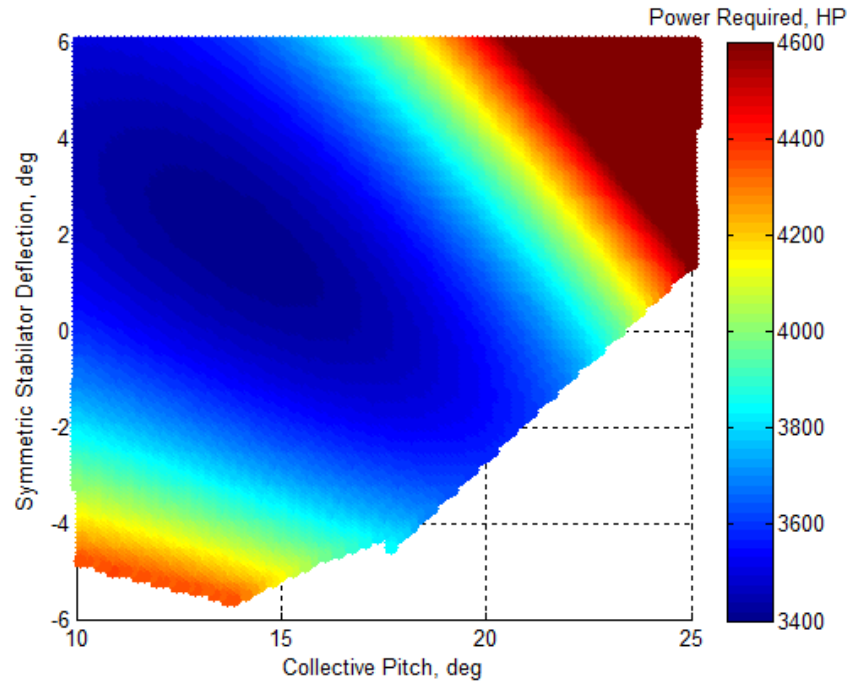


Figure 4-38: Trim Analysis for the Minimum Power Search at 200 knots

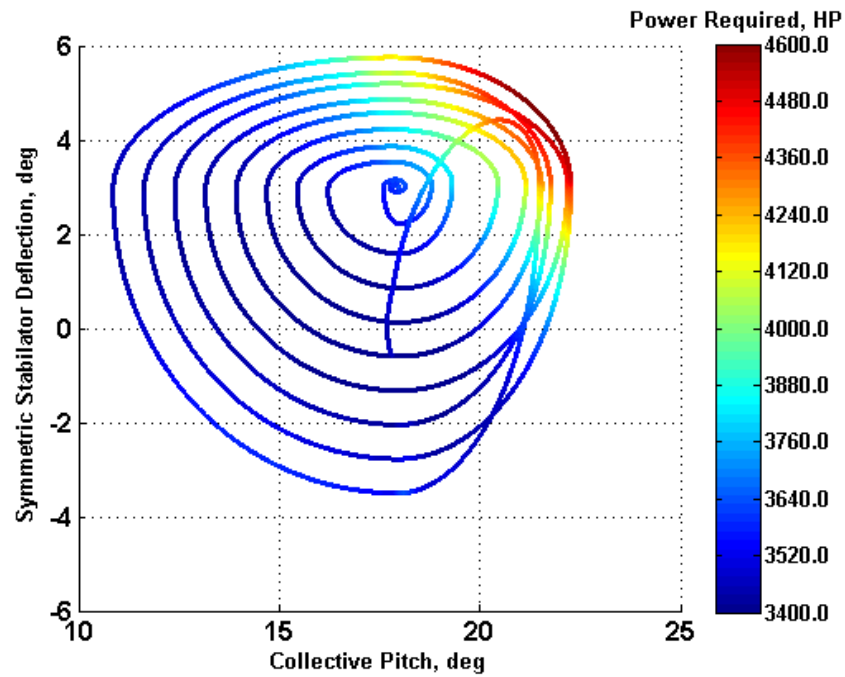


Figure 4-39: Optimization with Collective Pitch and Stabilator Deflection for Minimum Power Required at 200 knots

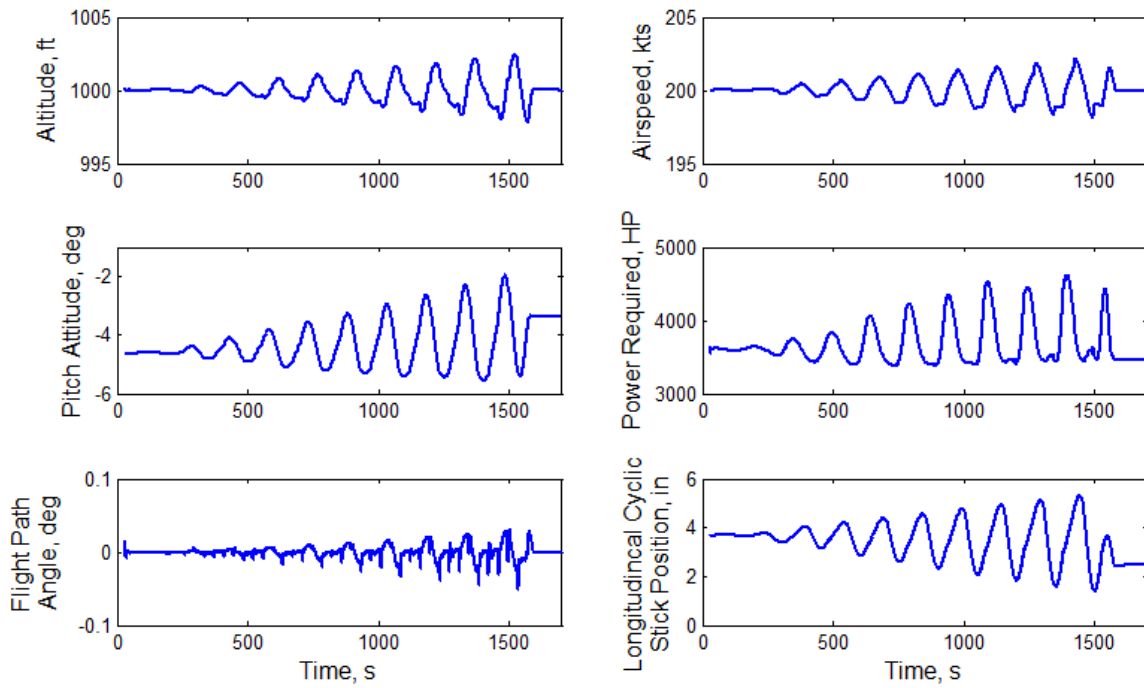


Figure 4-40: Response of the Aircraft during Power Optimization Maneuver at 200 knots

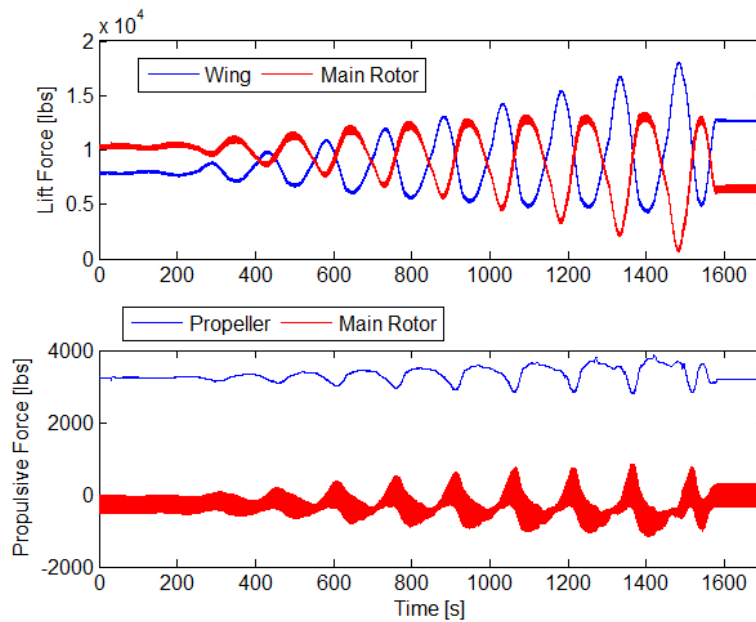


Figure 4-41: Lift and Thrust Sharing between Main Rotor, Wing and Propeller during Power Optimization Maneuver at 200 knots

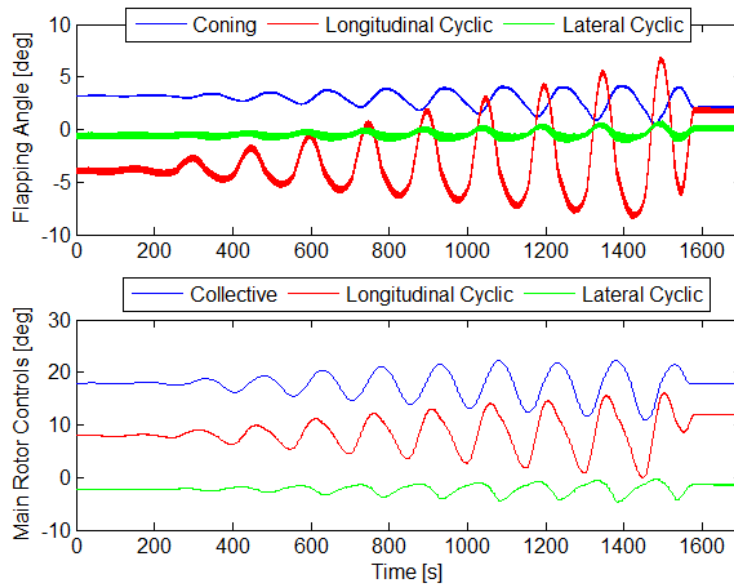


Figure 4-42: Flapping of the Rotor and Main Rotor Controls during Power Optimization Maneuver at 200 knots

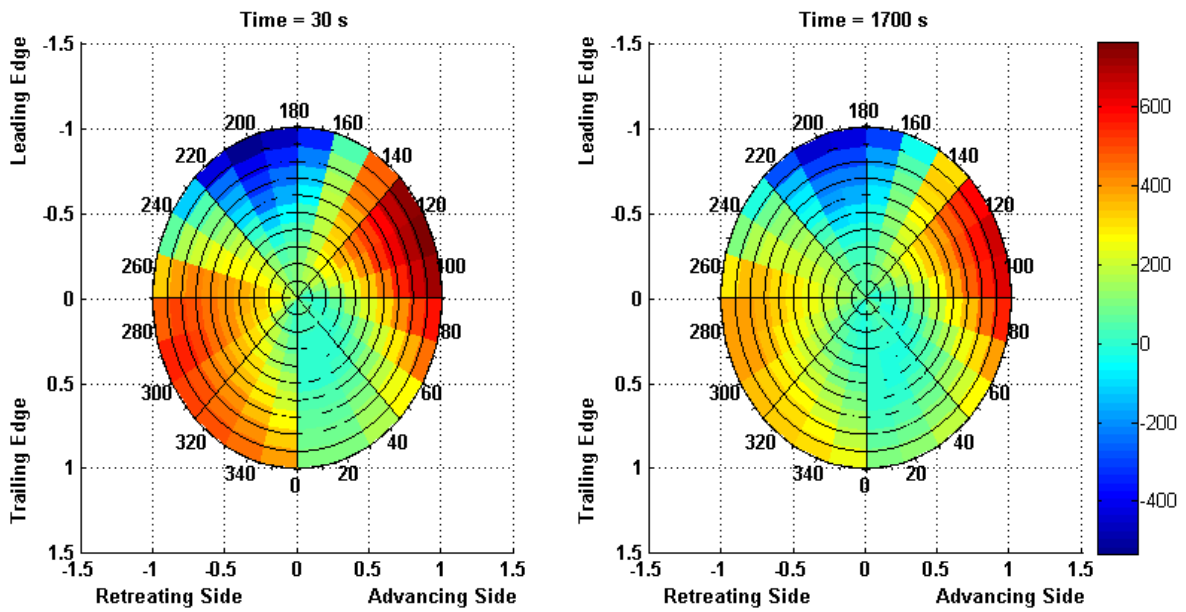


Figure 4-43: Lift Distribution over the Main Rotor Disk before and after the Power Optimization Maneuver at 200 knots

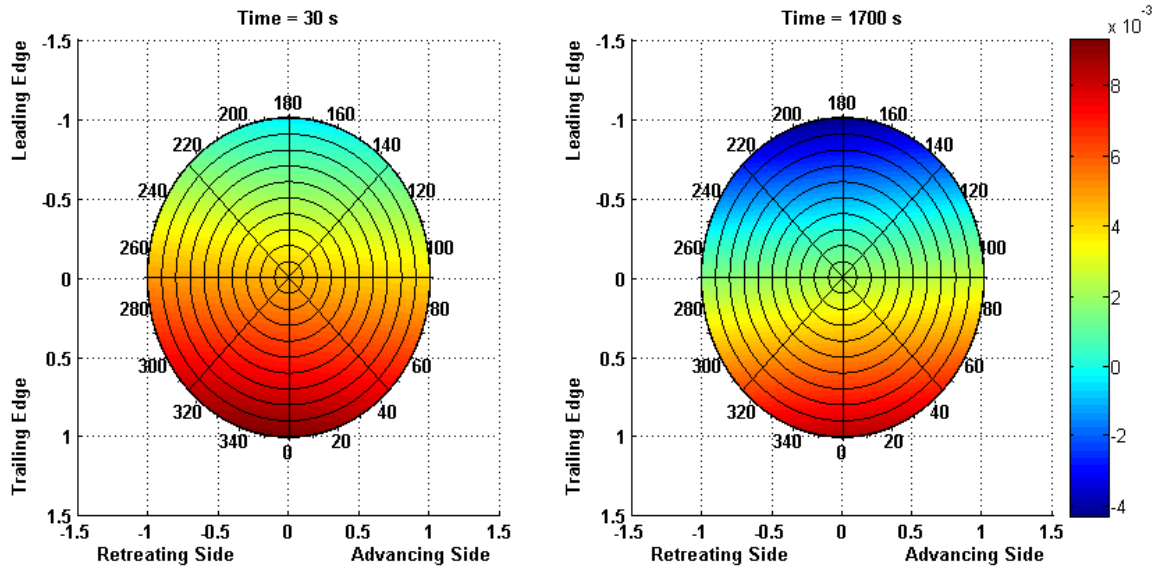


Figure 4-44: Inflow Distribution over the Main Rotor Disk before and after the Power Optimization Maneuver at 200 knots

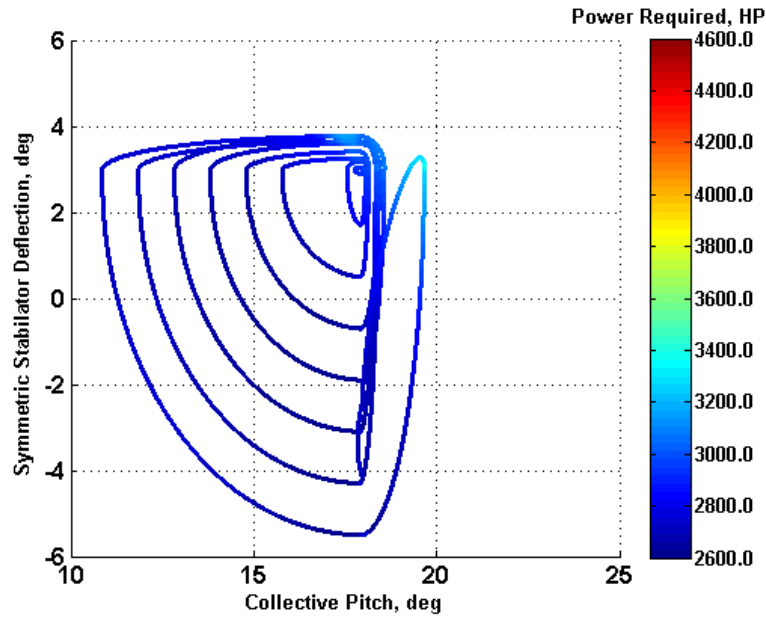


Figure 4-45: Optimization with Collective Pitch and Stabilator Deflection for Minimum Power Required at 180 knots with Low Power Limit

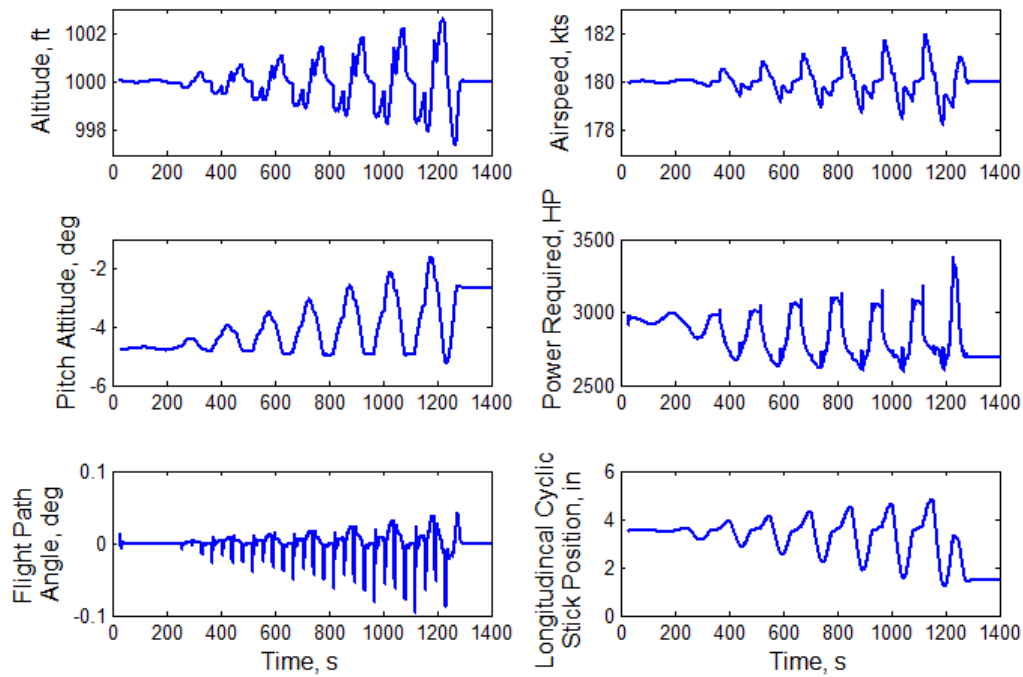


Figure 4-46: Response of the Aircraft during Power Optimization Maneuver at 180 knots with Low Power Limit

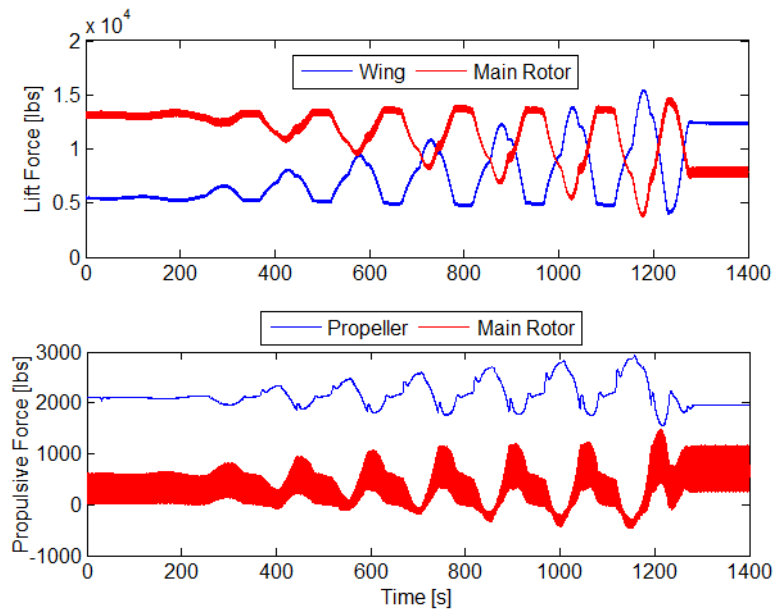


Figure 4-47: Lift and Thrust Sharing between Main Rotor, Wing and Propeller during Power Optimization Maneuver at 180 knots with Low Power Limit

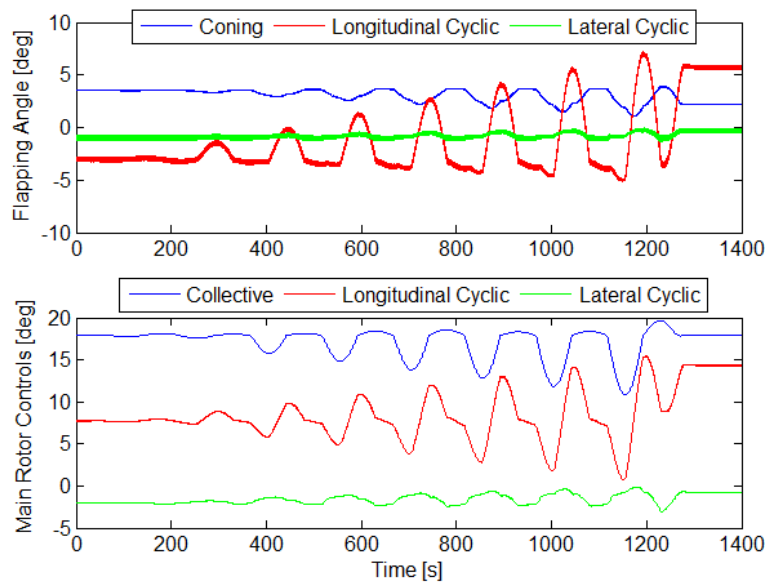


Figure 4-48: Flapping of the Rotor and Main Rotor Controls during Power Optimization Maneuver at 180 knots with Low Power Limit

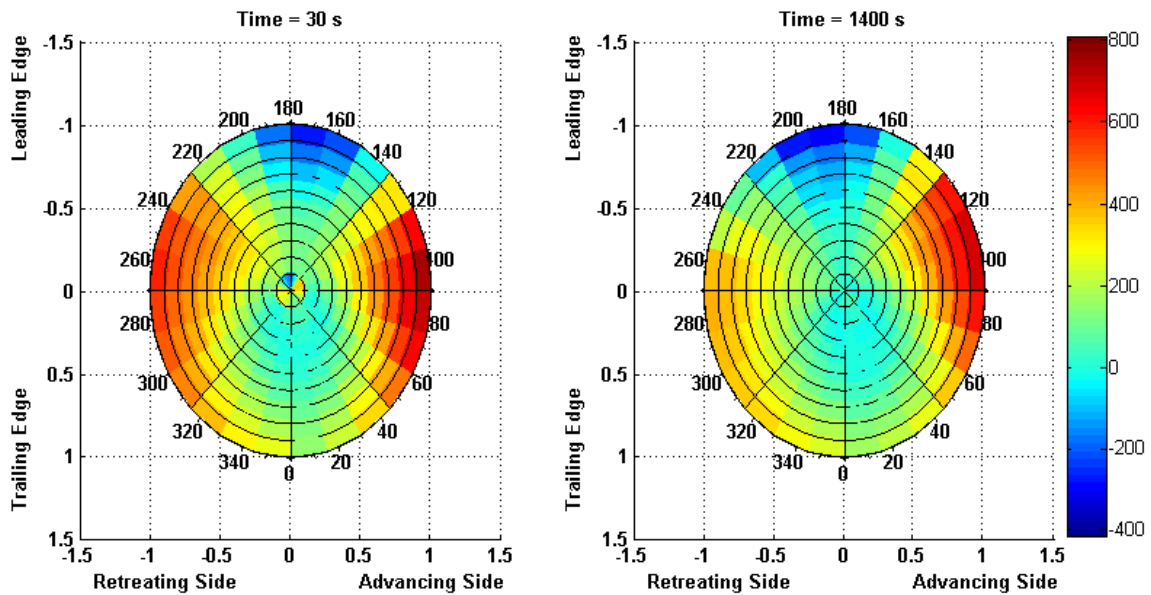


Figure 4-49: Lift Distribution over the Main Rotor Disk before and after the Power Optimization Maneuver at 180 knots with Low Power Limit [lbs]

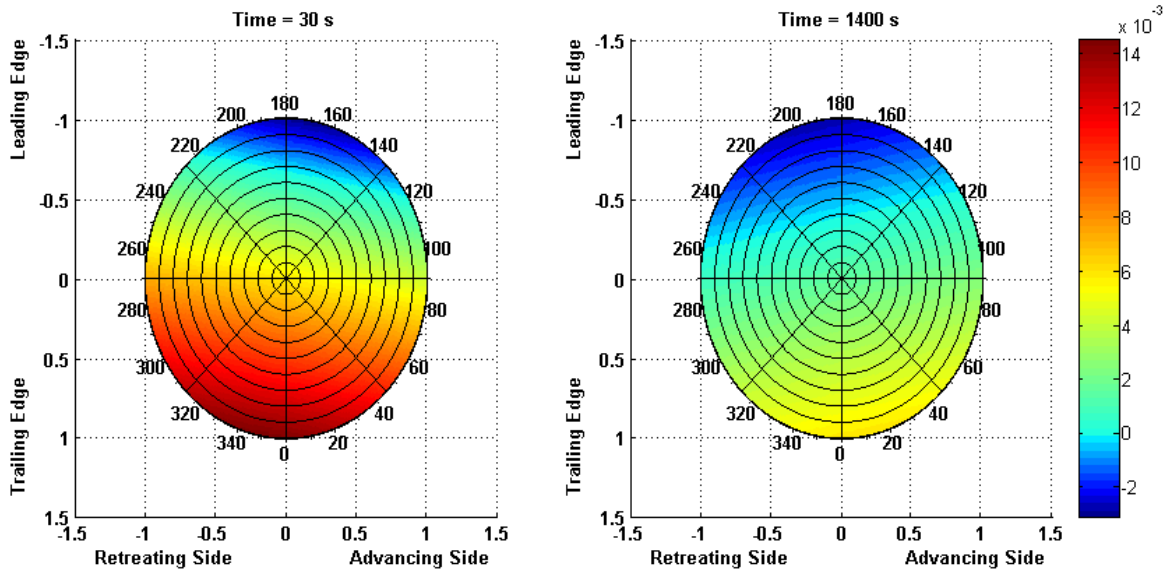


Figure 4-50: Inflow Distribution over the Main Rotor Disk before and after the Power Optimization Maneuver at 180 knots with Low Power Limit

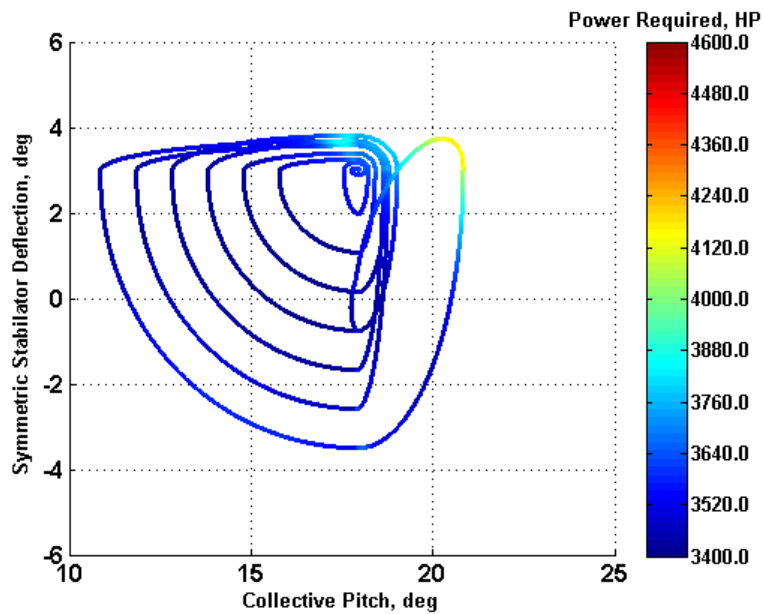


Figure 4-51: Optimization with Collective Pitch and Stabilator Deflection for Minimum Power Required at 200 knots with Low Power Limit

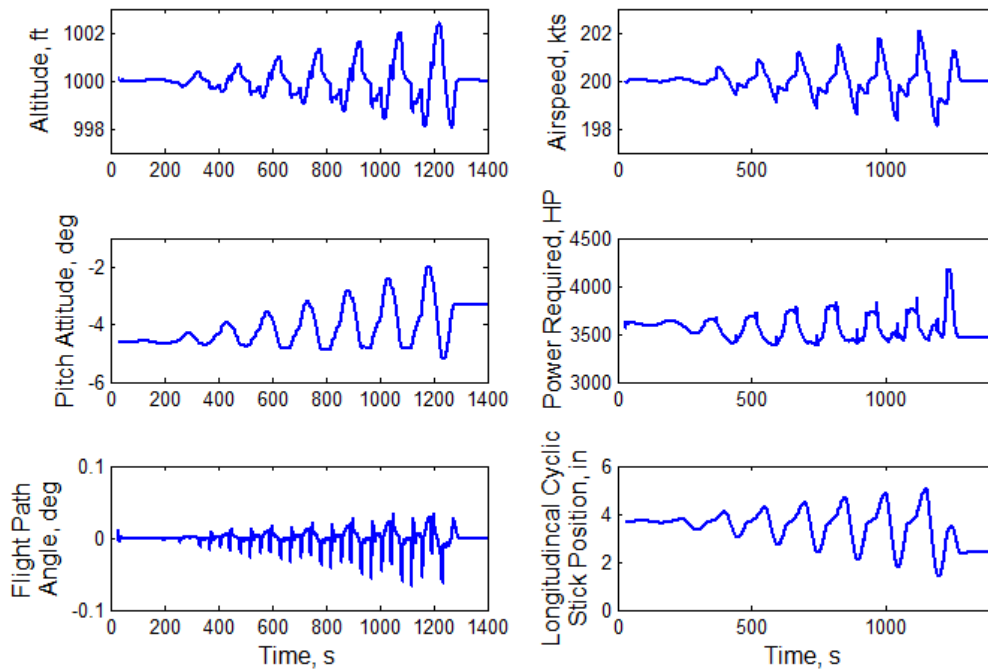


Figure 4-52: Response of the Aircraft during Power Optimization Maneuver at 200 knots with Low Power Limit

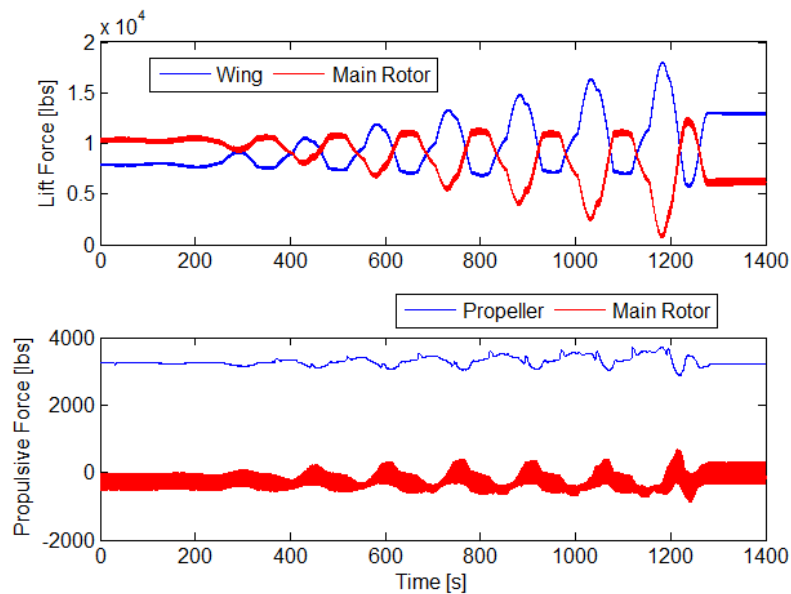


Figure 4-53: Lift and Thrust Sharing between Main Rotor, Wing and Propeller during Power Optimization Maneuver at 200 knots with Low Power Limit

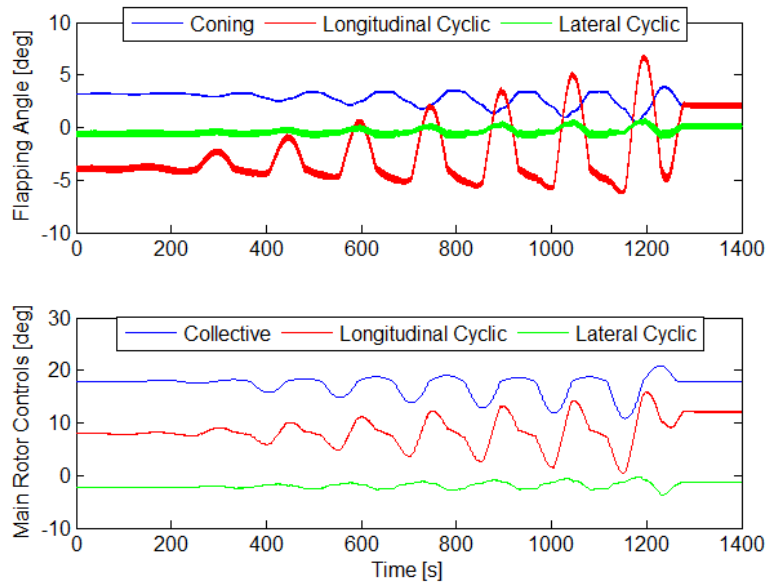


Figure 4-54: Flapping of the Rotor and Main Rotor Controls during Power Optimization Maneuver at 200 knots with Low Power Limit

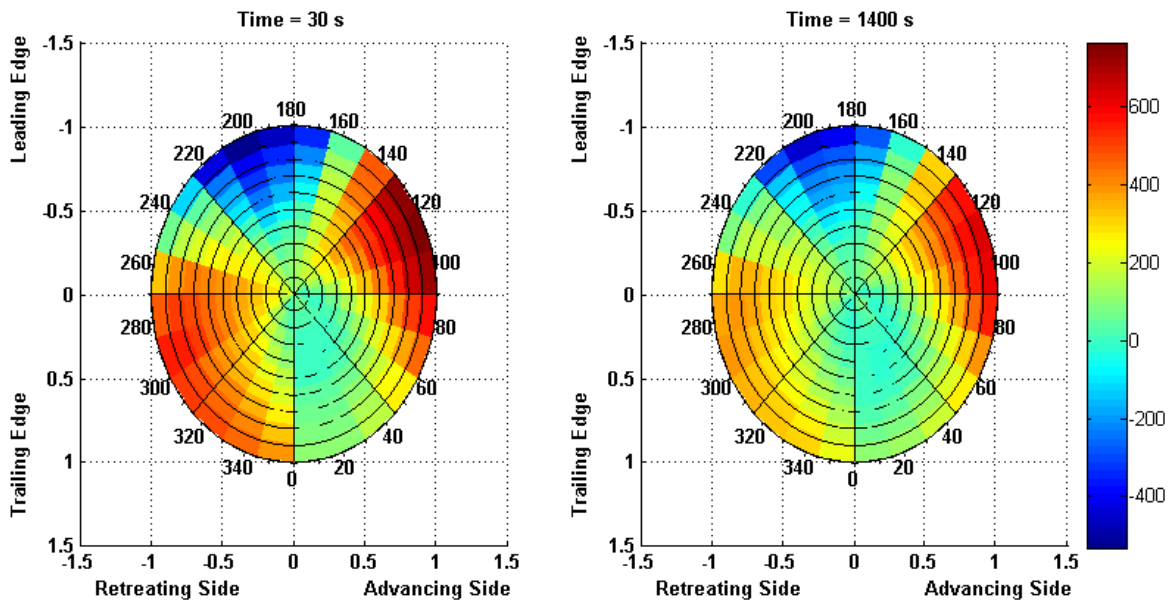


Figure 4-55: Lift Distribution over the Main Rotor Disk before and after the Power Optimization Maneuver at 200 knots with Low Power Limit [lbs]

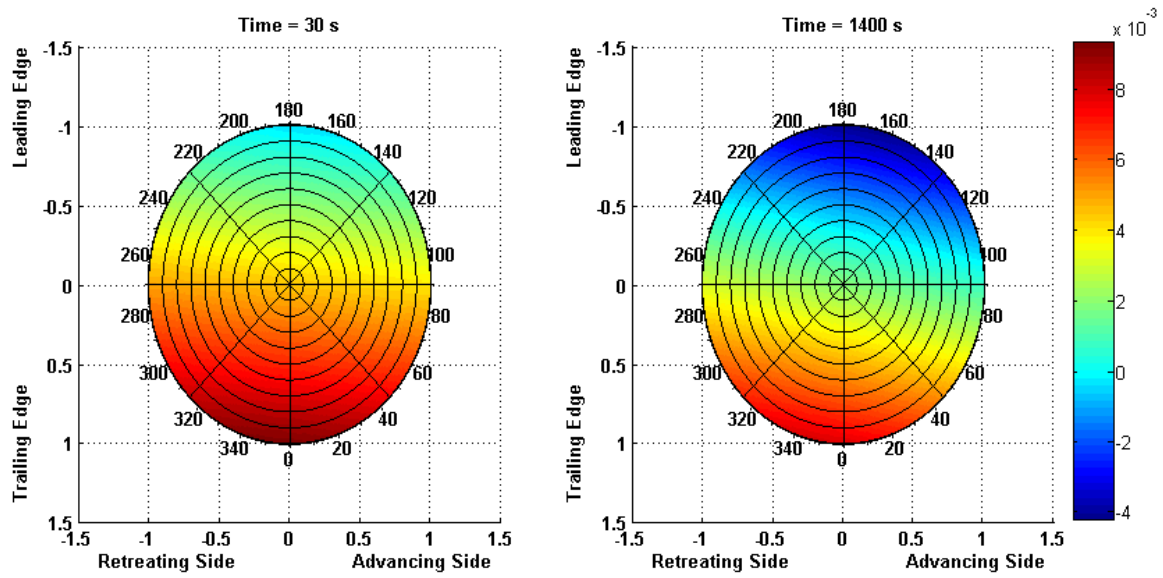


Figure 4-56: Inflow Distribution over the Main Rotor Disk before and after the Power Optimization Maneuver at 200 knots with Low Power Limit

Chapter 5

Conclusion and Future Work

5.1 Conclusion

The objective of this study is to design a flight control system that optimizes redundant control effectors for conventional and compound helicopter during flight. The control system builds off of the golden section method and adaptive performance optimization methods and extends it to a multi-variable optimization approach. To achieve this, a model following and dynamic inversion controller is expanded to include the heave and rotor RPM axes to closely regulate the trimmed flight condition throughout the optimization maneuver. The design methods are implemented and tested using the GENHEL model of the UH-60A and a compound version of the UH-60A with lifting wing and propeller, and evaluated using the GENHEL-PSU software. The following conclusions can be drawn from the results of this simulation study:

- 1) It is critical to have an accurate and well-designed flight control law to maintain trimmed flight conditions during the in-flight optimization process. The controller designed to act as an autopilot, so pilot can fly the helicopter hands-off throughout the optimization maneuver.

- 2) Rotor speed optimization studies showed that golden section method optimization can be performed during flight with very small disturbances in flight condition.

- 3) Initial results show that the FTO optimization method is effective and reliable in reaching a power required optimum, but with the current iteration steps the optimization with golden section method takes almost 10 minutes of simulated flight to be completed. This does not result in long computation times since the simulation model runs faster than real time. However;

use of adaptive performance optimization requires almost similar time to complete optimization of five different redundant controllers.

4) Adaptive Performance Optimization method is used to optimize performance using multiple redundant control effectors both using a single variable and multi variable optimization. Although sequential optimization of controls results in significant performance enhancement, the resultant state might not be the optimal condition.

5) Comparisons of simulation results using the FTO optimization and comprehensive sweeps of trim solutions in the simulation model show that the FTO optimization is effective and reliable in reaching a power required and range close to optimal (when optimizing up to two redundant controls). The current method performs a two-variable optimization using low frequency out-of-phase sinusoidal commands to the two optimization variables. The method should be extended to search a control space of three or more dimensions. However, still performing a multi-dimensional optimization over such a complex dynamic system and estimating the optimal very close to the actual optimal trim state is a satisfying result of this research.

6) Control margins in high-speed flight can become critical when performing in-flight optimization. Control Limit calculation is crucial to avoid aircraft controls to saturate by driving an optimization variable to an extreme. Although it is assumed that the aircraft stays in steady-state trim during the optimization maneuver, the control law is not perfect and this results in transient effects. This can be reduced through basic power adjustments for acceleration, climb, and rotor speed, but not eliminated. This is the main challenge of the APO method.

7) The optimization takes almost 25 minutes of simulated flight to be completed and 21 minutes for maneuvers with low power limit. This does not result in long computation times since the simulation model runs faster than real time. However, even 21 minutes of flight for optimization can be significant, depending on the flight mission. For long distance cruise

missions, this optimization maneuver can be performed at the very beginning of the flight. But for rather shorter distance missions, performing this maneuver for about 21 minutes might not be desirable. The issue with time required to complete the optimization maneuver is the least satisfying result of this research.

8) The optimization can be performed by only a single helicopter in the fleet for once and the optimization results can be transferred to the rest of the fleet. Another application of this method can be a flight test program, where optimal trim states for various flight conditions can be determined and recorded during flight tests for performance evaluation. Considering the total flight test hours for only performance and handling qualities testing of Lockheed AH-56 Cheyenne, which has a similar configuration to the generic compound rotorcraft model of this study, is 42 hours, performing 21 minutes of optimization maneuvers can be performed for various performance evaluations of rotorcraft with redundant controls at different flight conditions. [72, 73].

5.2 Future Work

The previous section summarized the study on a flight control law for a compound rotorcraft with in-flight performance optimization. The experiences and lessons learned from this study will give directions for future studies.

In compound rotorcraft study, the following topic could be studied:

- Optimization routine is specified for the compound configuration given in this study and making changes in the aircraft model requires effort.
- The propeller model should be refined and validated for low speed flight where the propeller might operate at very low to negative thrust regions.

- The wing model currently uses lookup tables for lift, drag and moment coefficients, a wing and a flap model should be developed and validated to be included in the compound rotorcraft model, therefore, various wing models can be used without the need to modify lookup tables.
- The APO search method should be improved to search for three or more control effectors simultaneously. Also alternative optimization methods can be investigated to improve the performance of the optimization by reducing the time needed to complete optimization. Peak-Seeking Control and Extremum-Seeking Control are examples of alternative optimization methods that can be studied.
- Piloted simulations should be performed to observe pilot reactions and comfort during the optimization maneuvers.

Appendix A

Figures for Lift, Drag and Moment Coefficients of the Fuselage

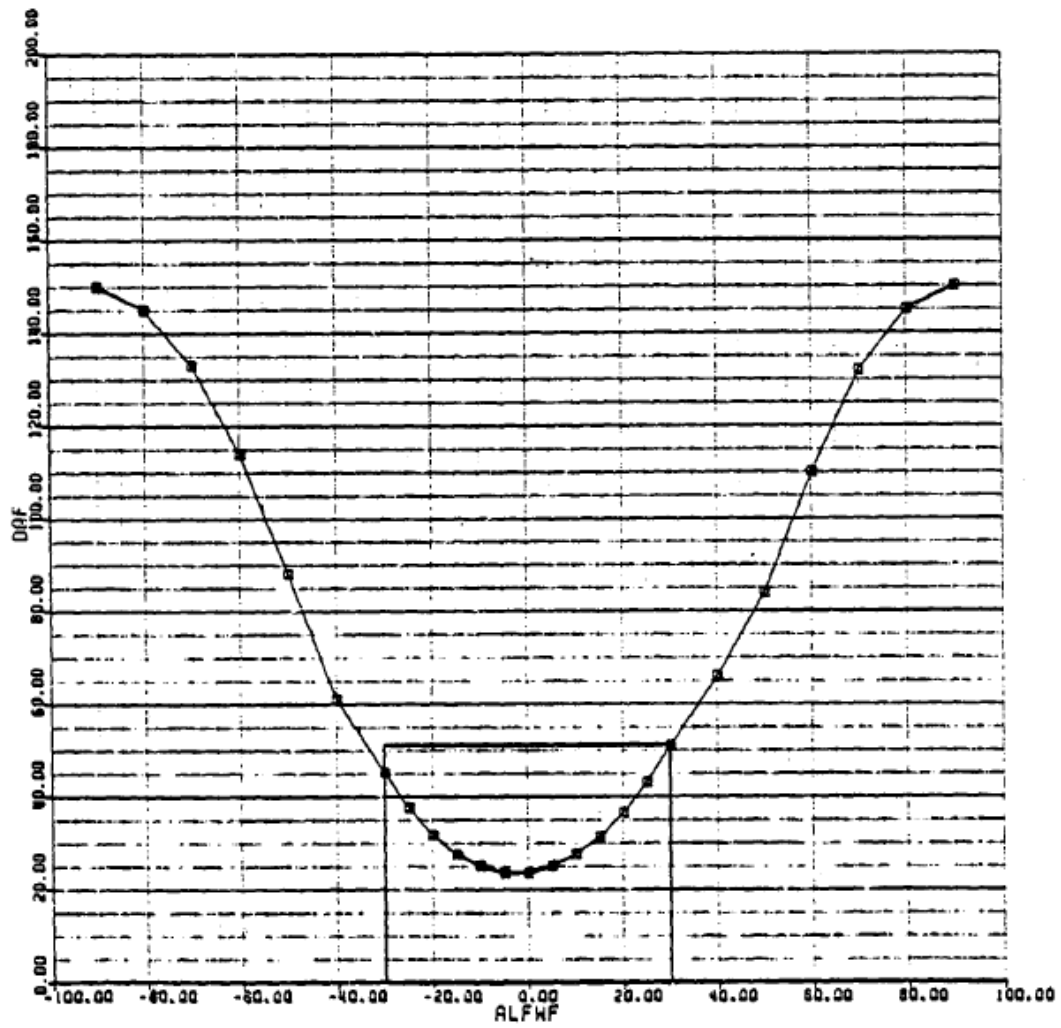


Figure A-1: Fuselage Drag Coefficient Due to Angle of Attack [61]

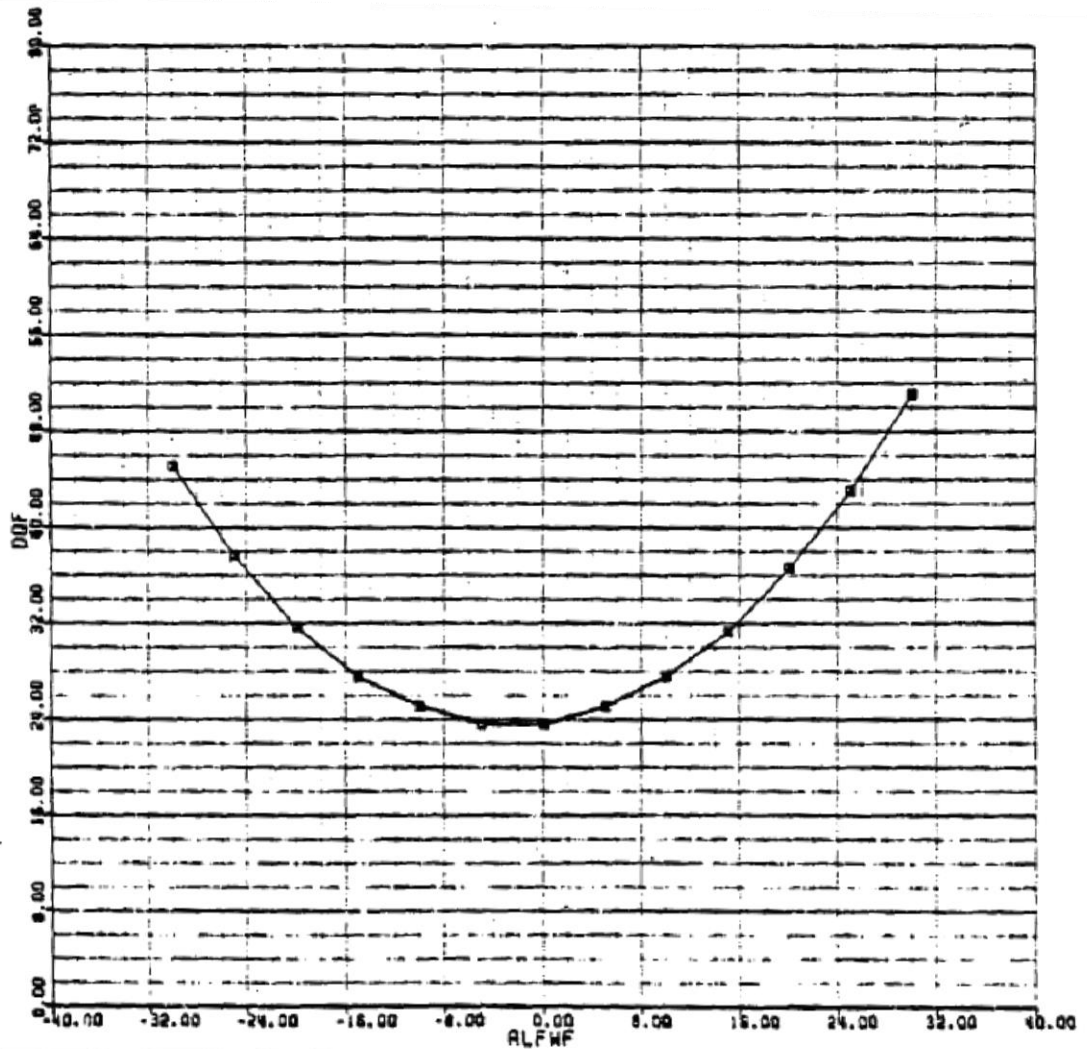


Figure A-2: Fuselage Drag Coefficient Due to Angle of Attack [61]

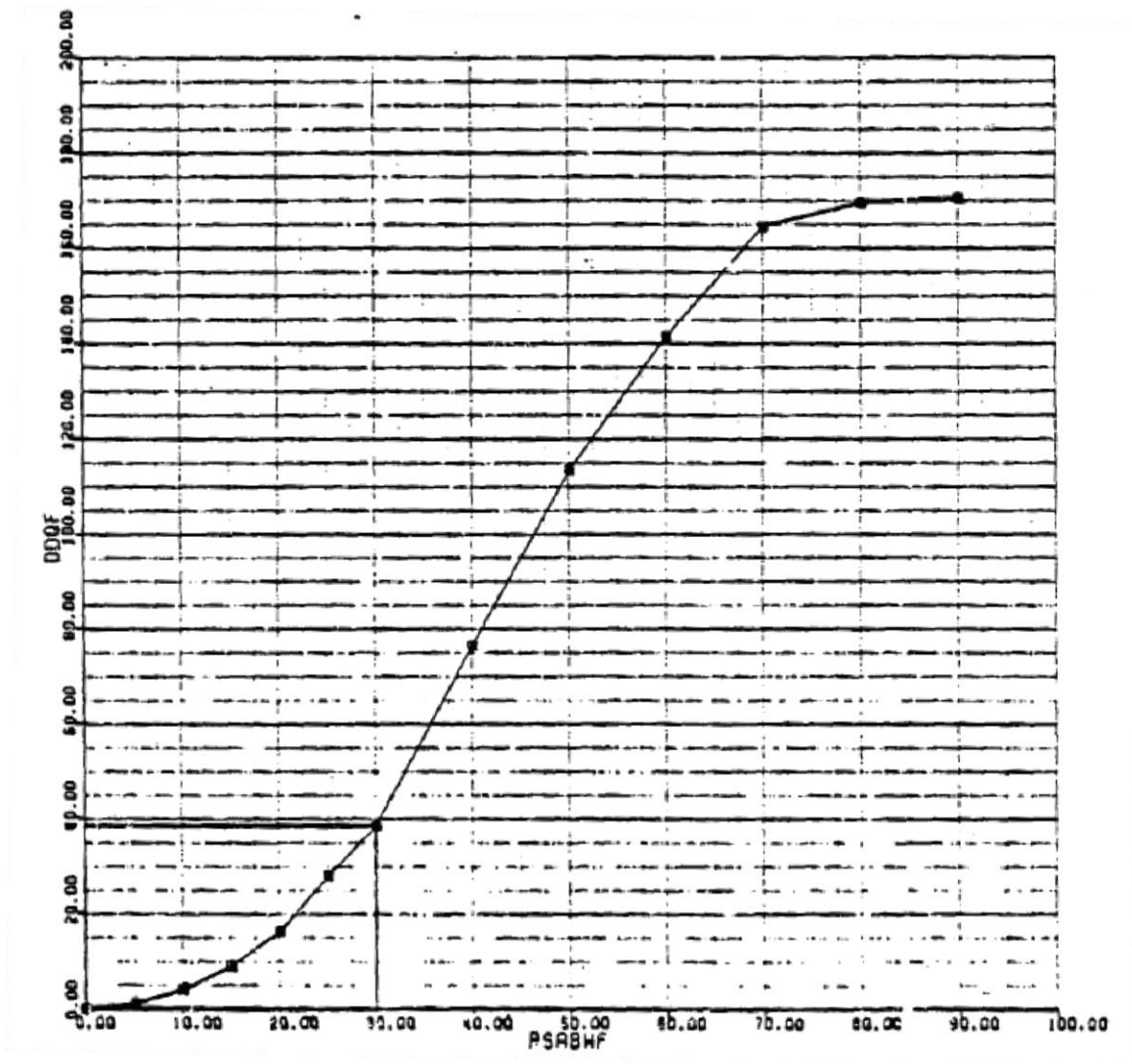


Figure A-3: Incremental Fuselage Drag Coefficient Due to Sideslip [61]

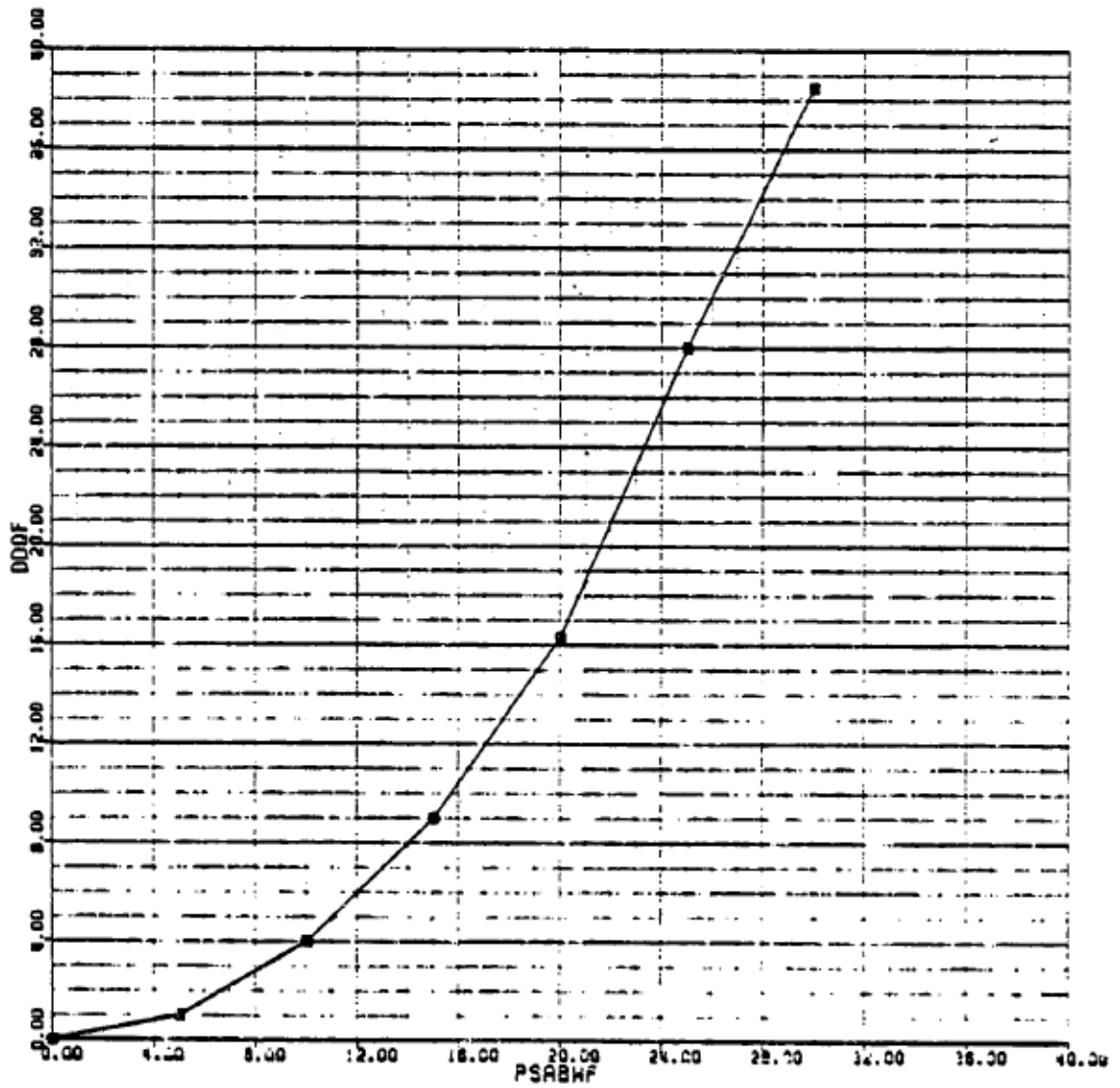


Figure A-4: Incremental Fuselage Drag Coefficient Due to Sideslip [61]

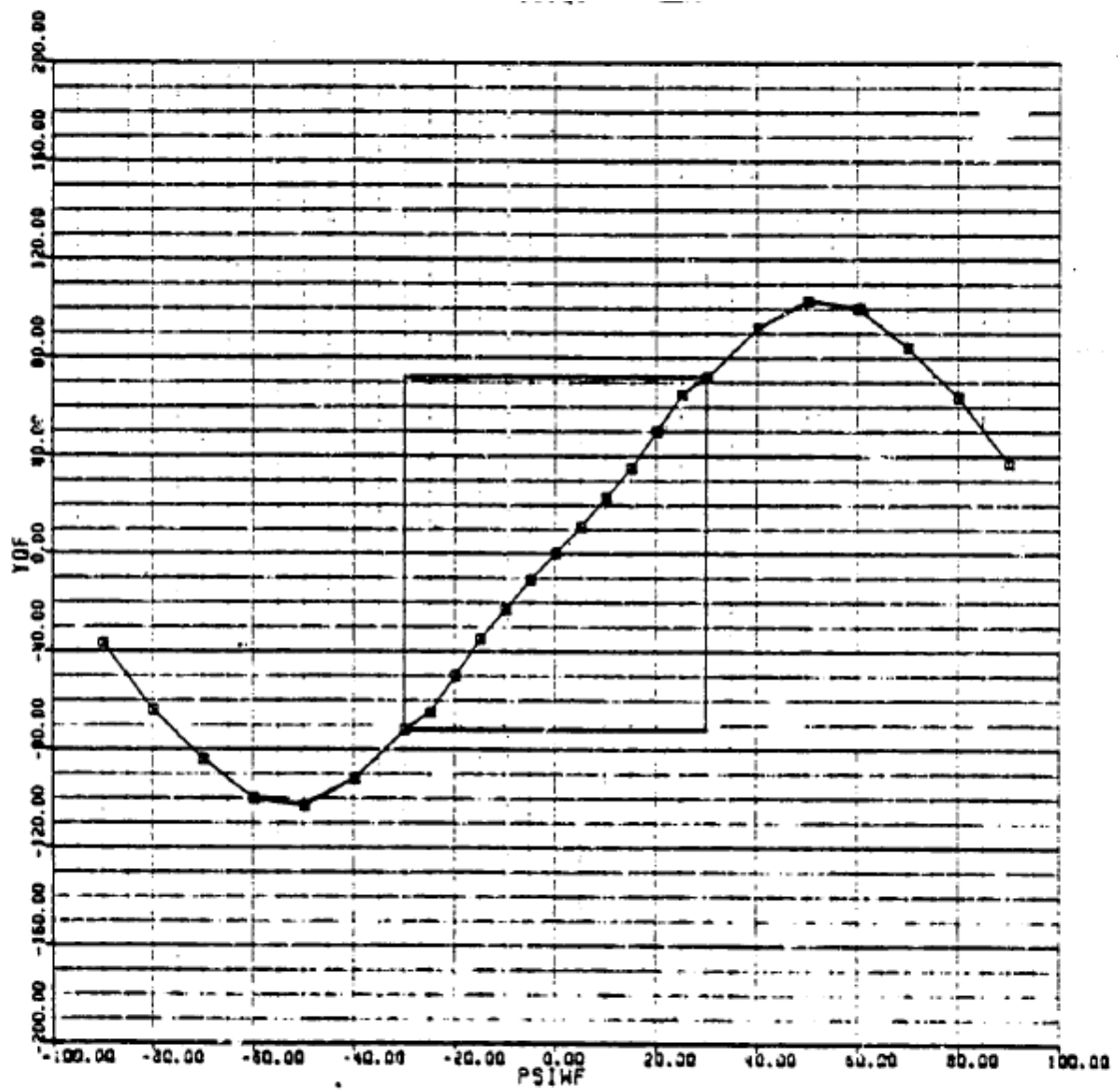


Figure A-5: Fuselage Sideforce Coefficient Due to Sideslip [61]

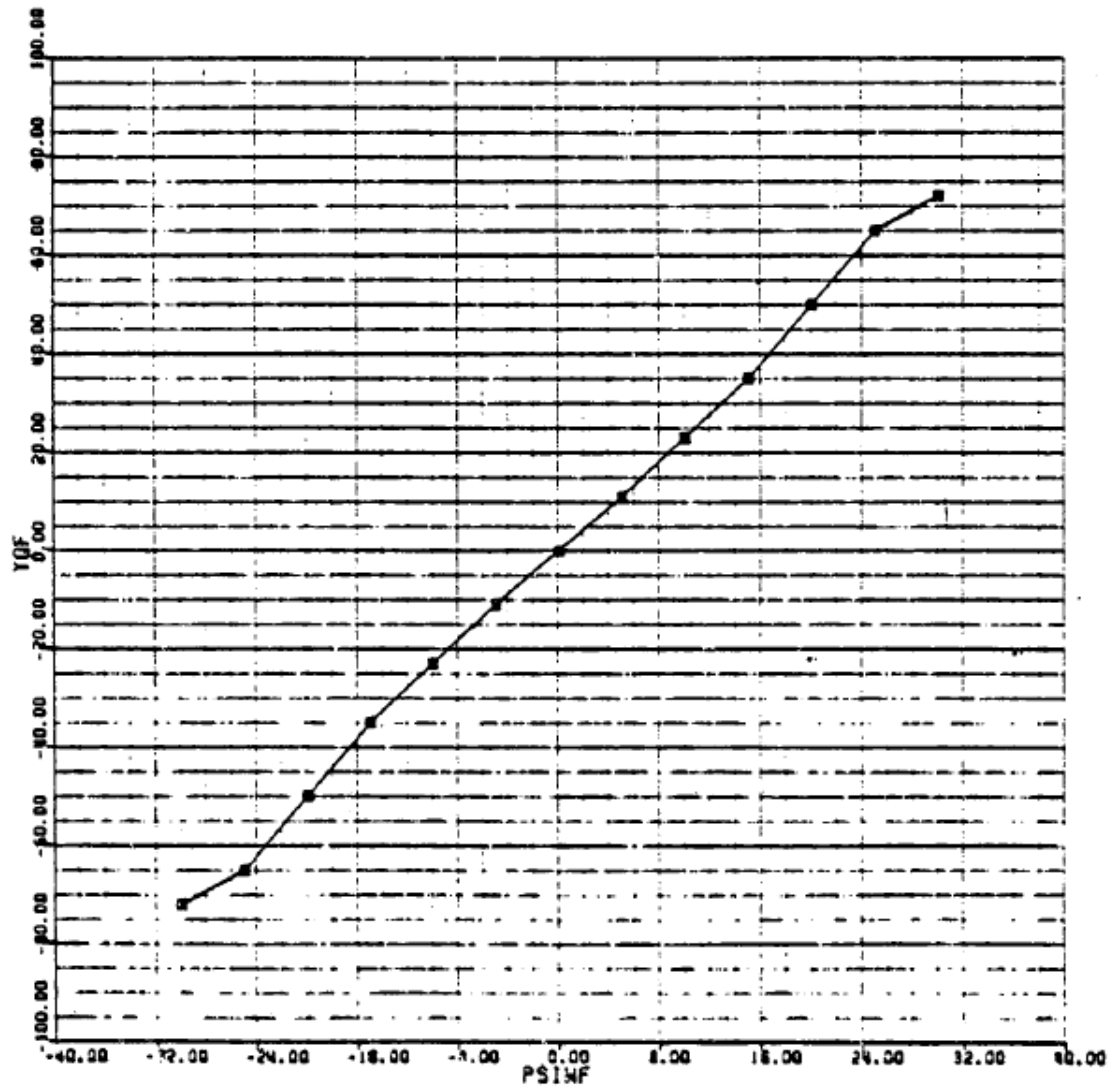


Figure A-6: Fuselage Sideforce Coefficient Due to Sideslip [61]

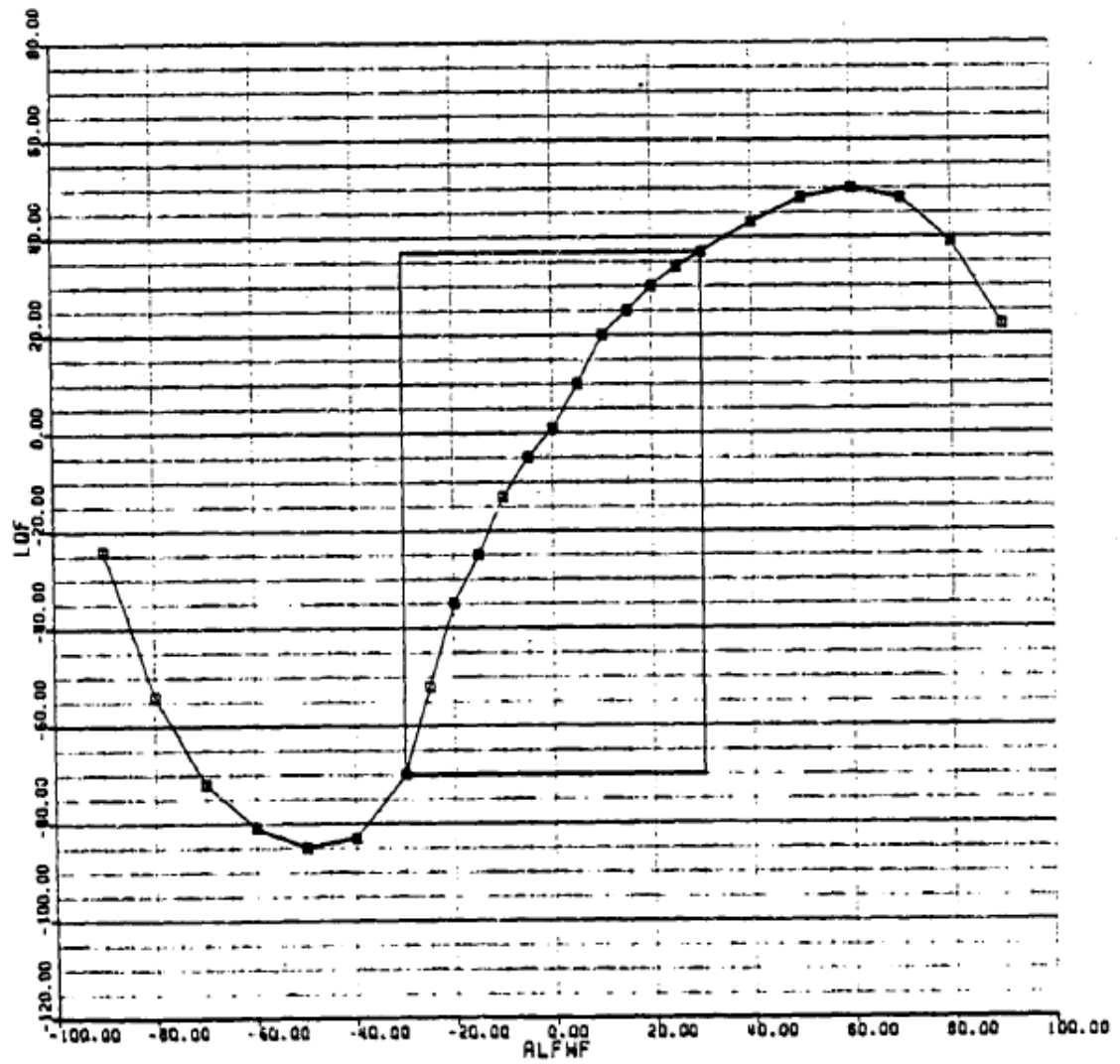


Figure A-7: Fuselage Lift Coefficient Due to Angle of Attack [61]

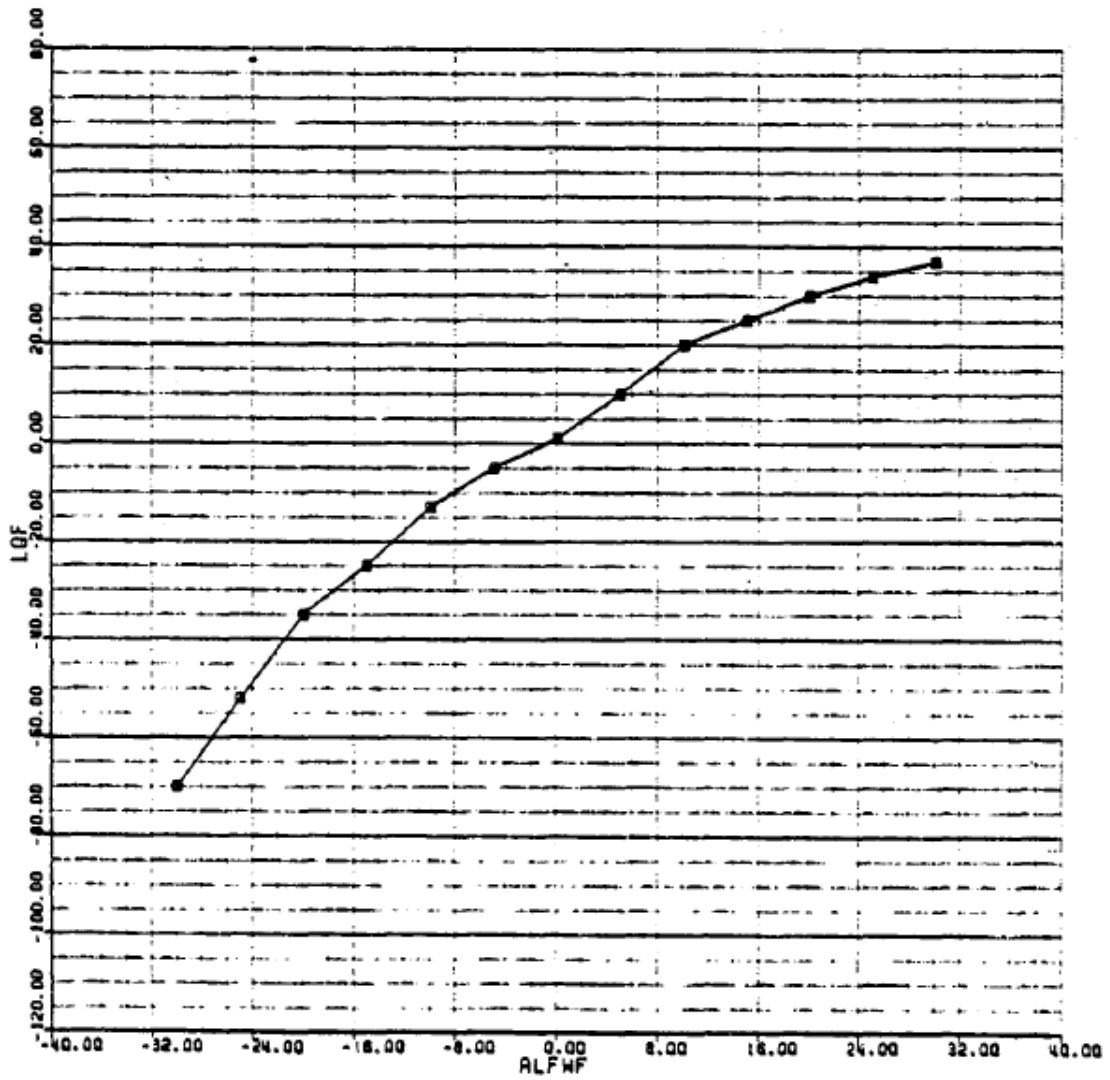


Figure A-8: Fuselage Lift Coefficient Due to Angle of Attack [61]

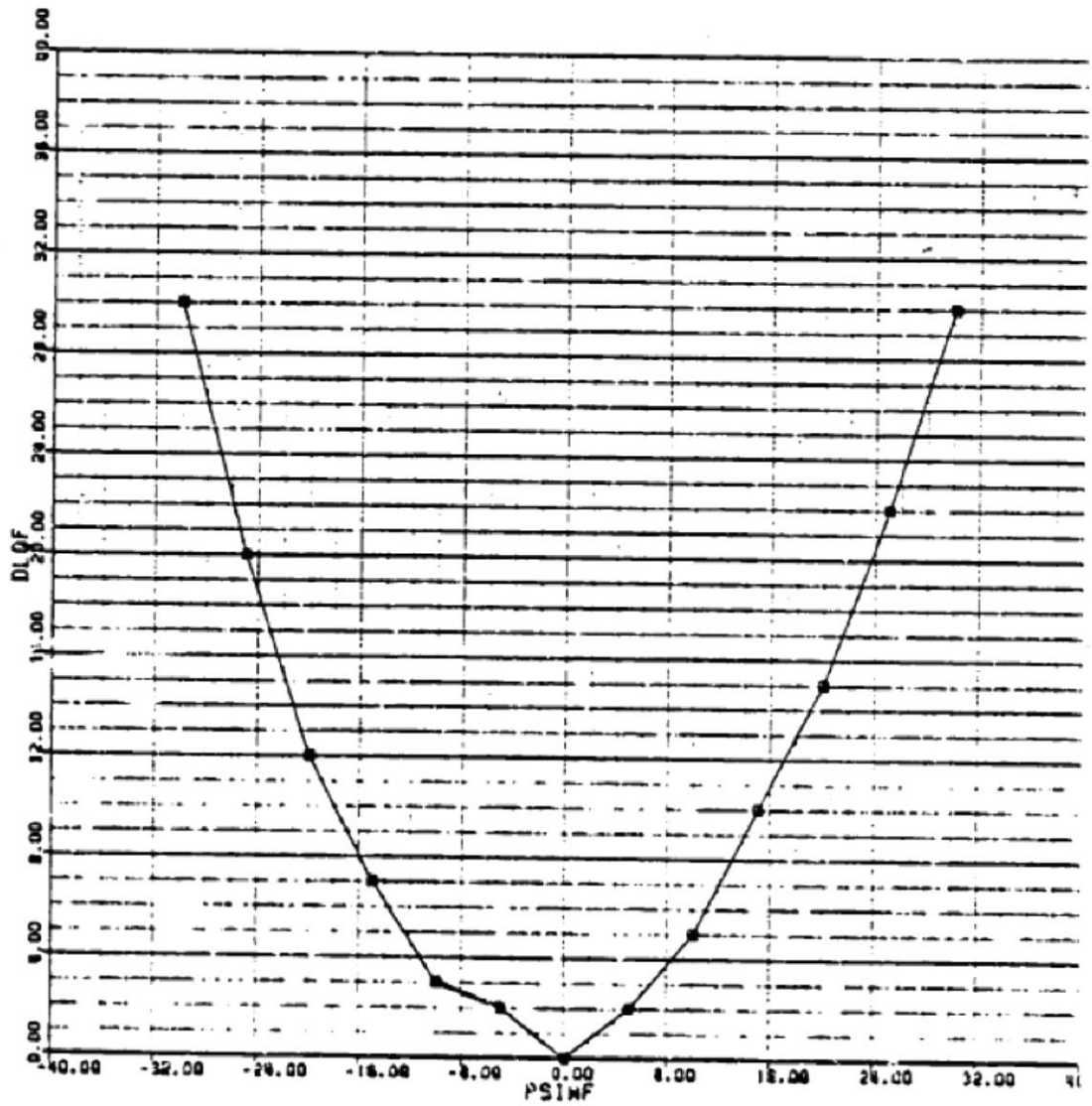


Figure A-9: Incremental Fuselage Lift Coefficient Due to Sideslip [61]

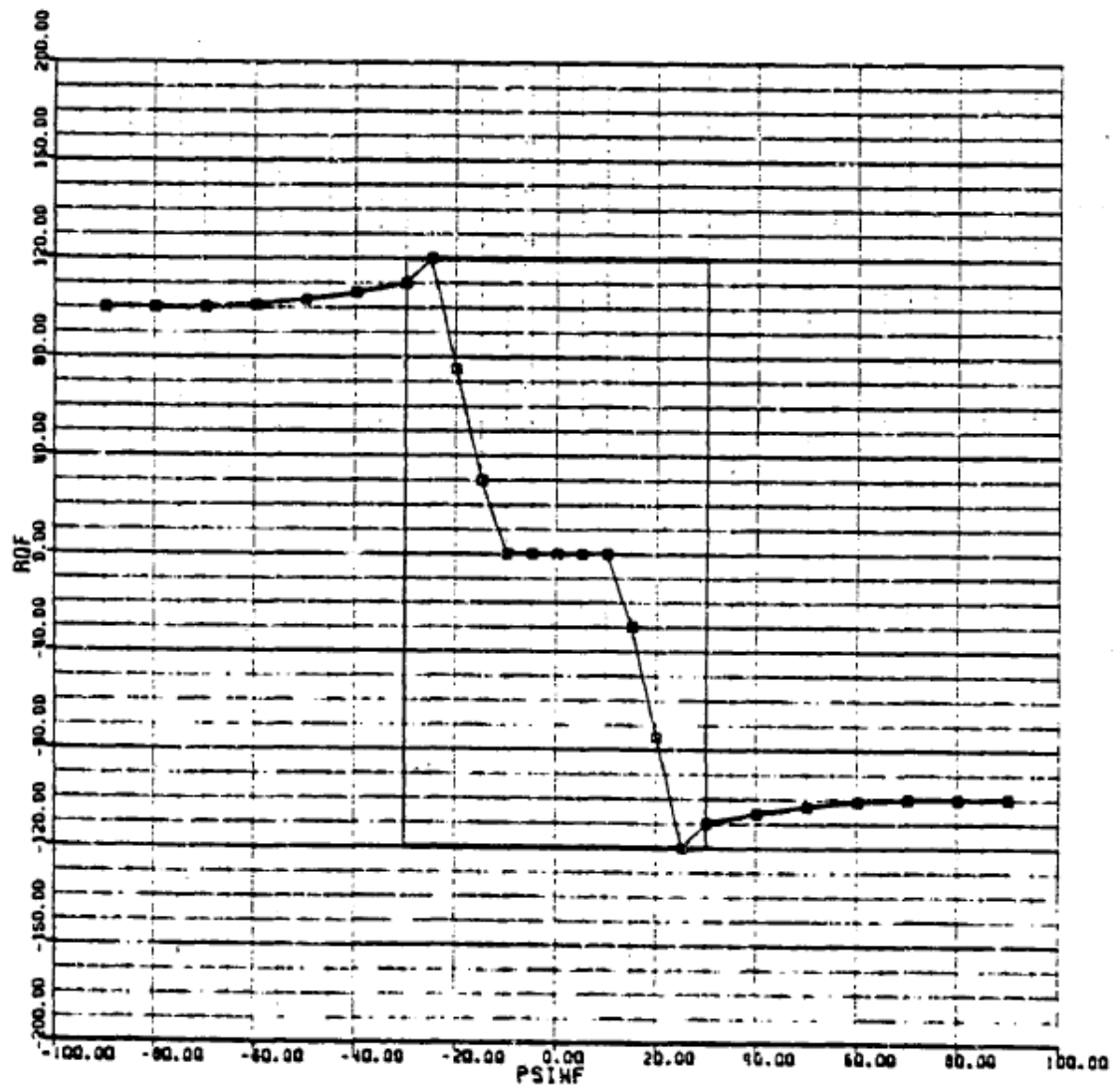


Figure A-10: Fuselage Rolling Moment Coefficient Due to Sideslip [61]

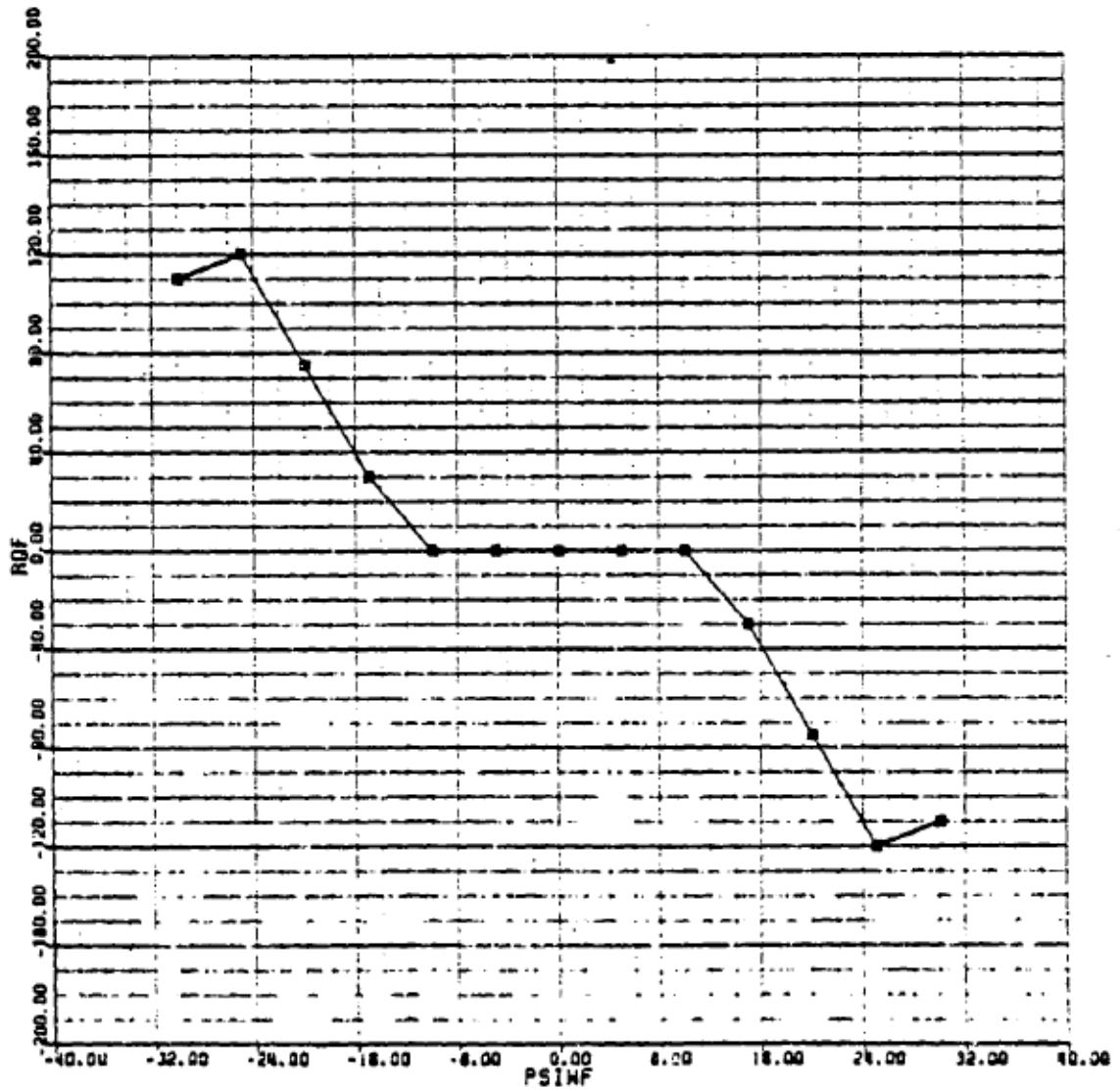


Figure A-11: Fuselage Rolling Moment Coefficient Due to Sideslip [61]

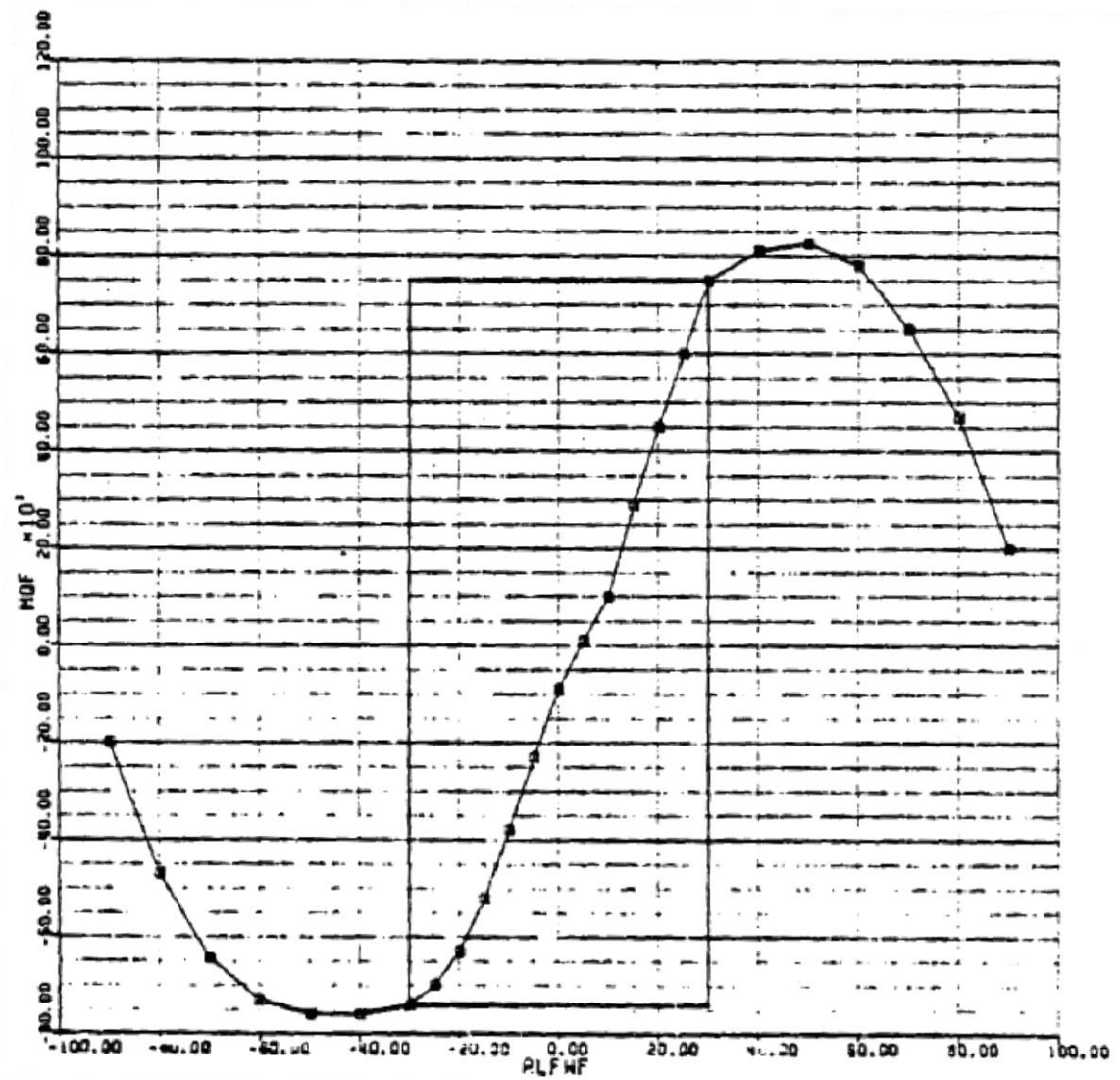


Figure A-12: Fuselage Pitching Moment Coefficient Due to Angle of Attack [61]

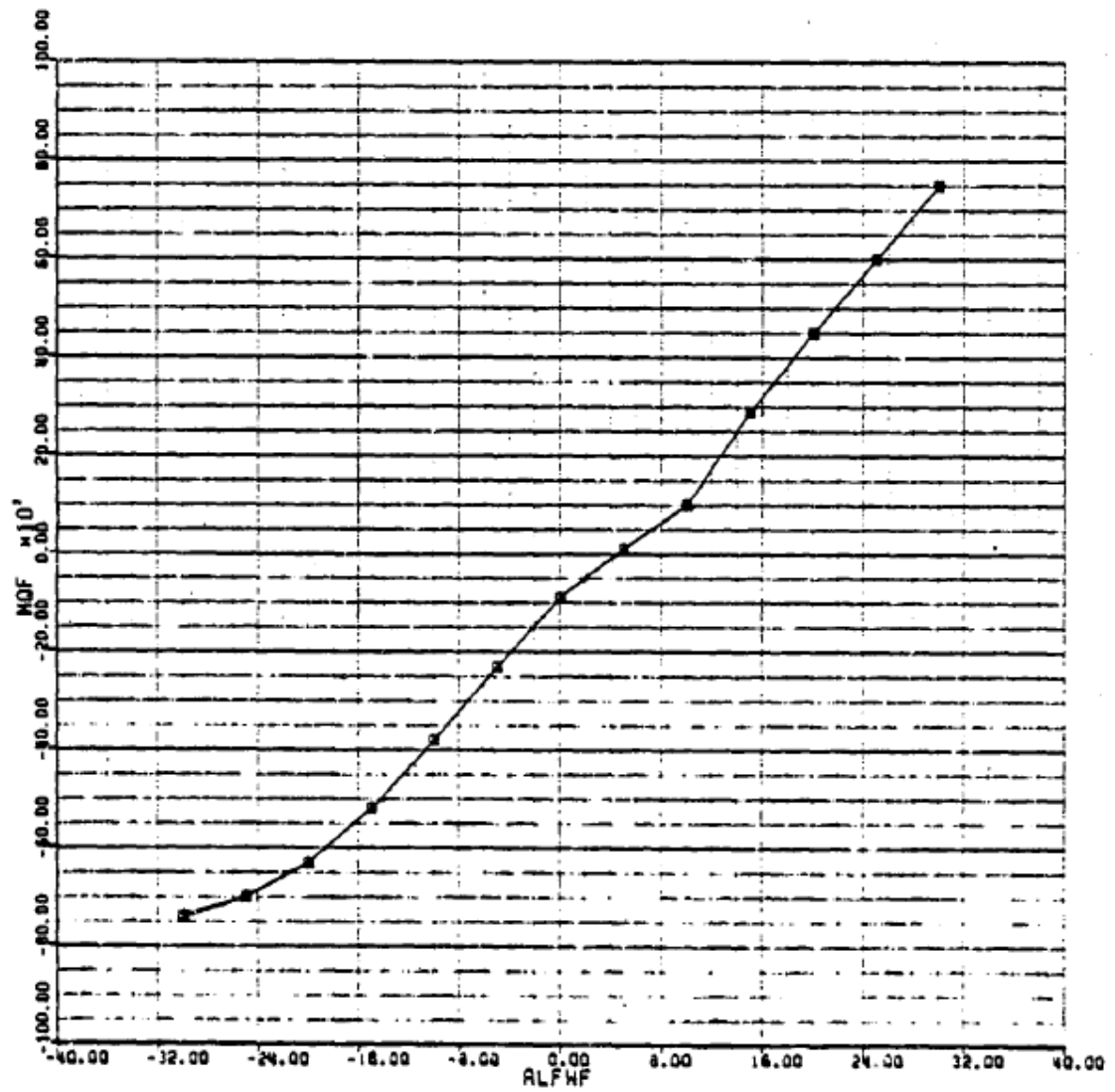


Figure A-13: Fuselage Pitching Moment Coefficient Due to Angle of Attack [61]

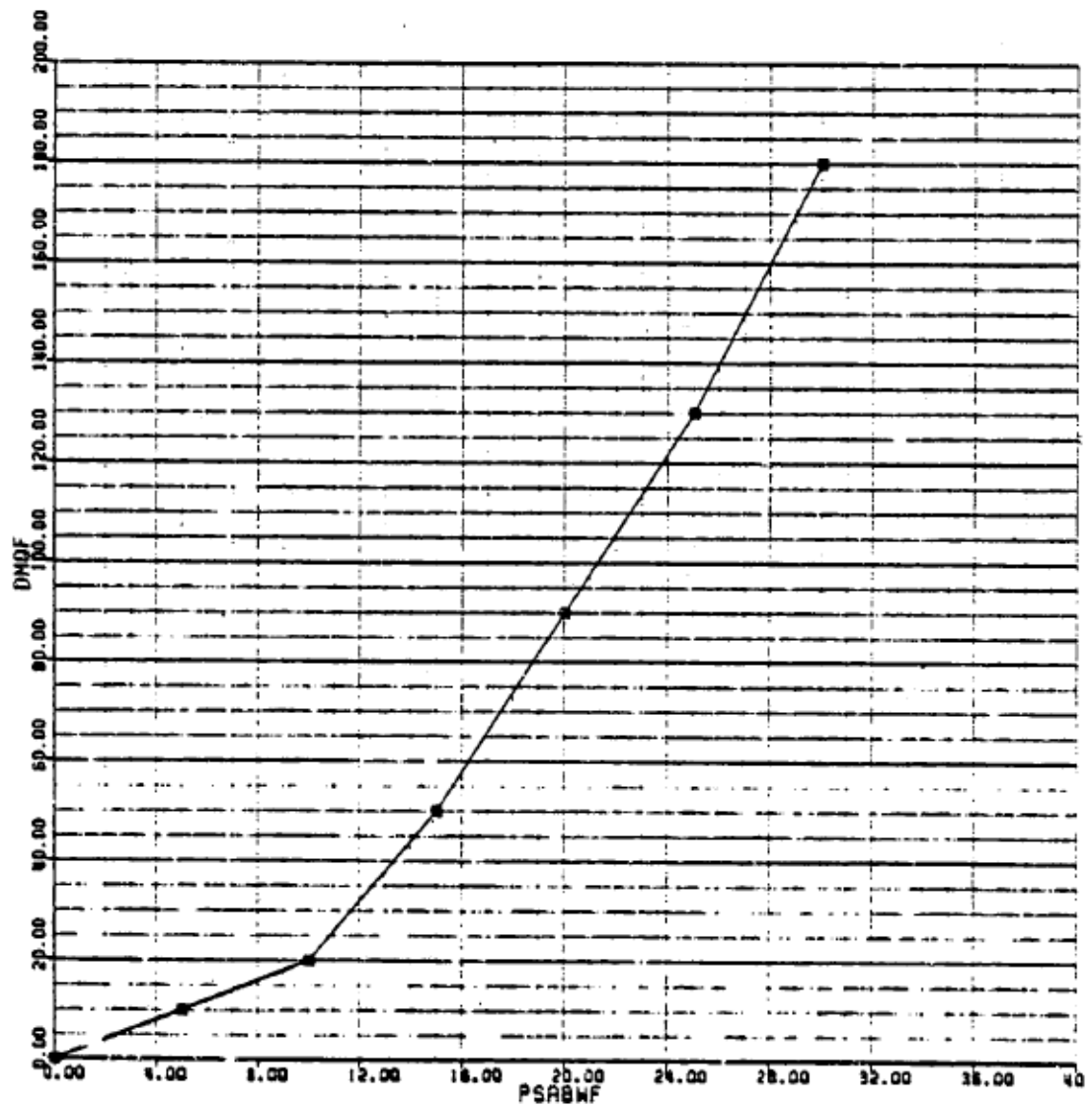


Figure A-14: Incremental Fuselage Pitching Moment Coefficient Due to Sideslip [61]

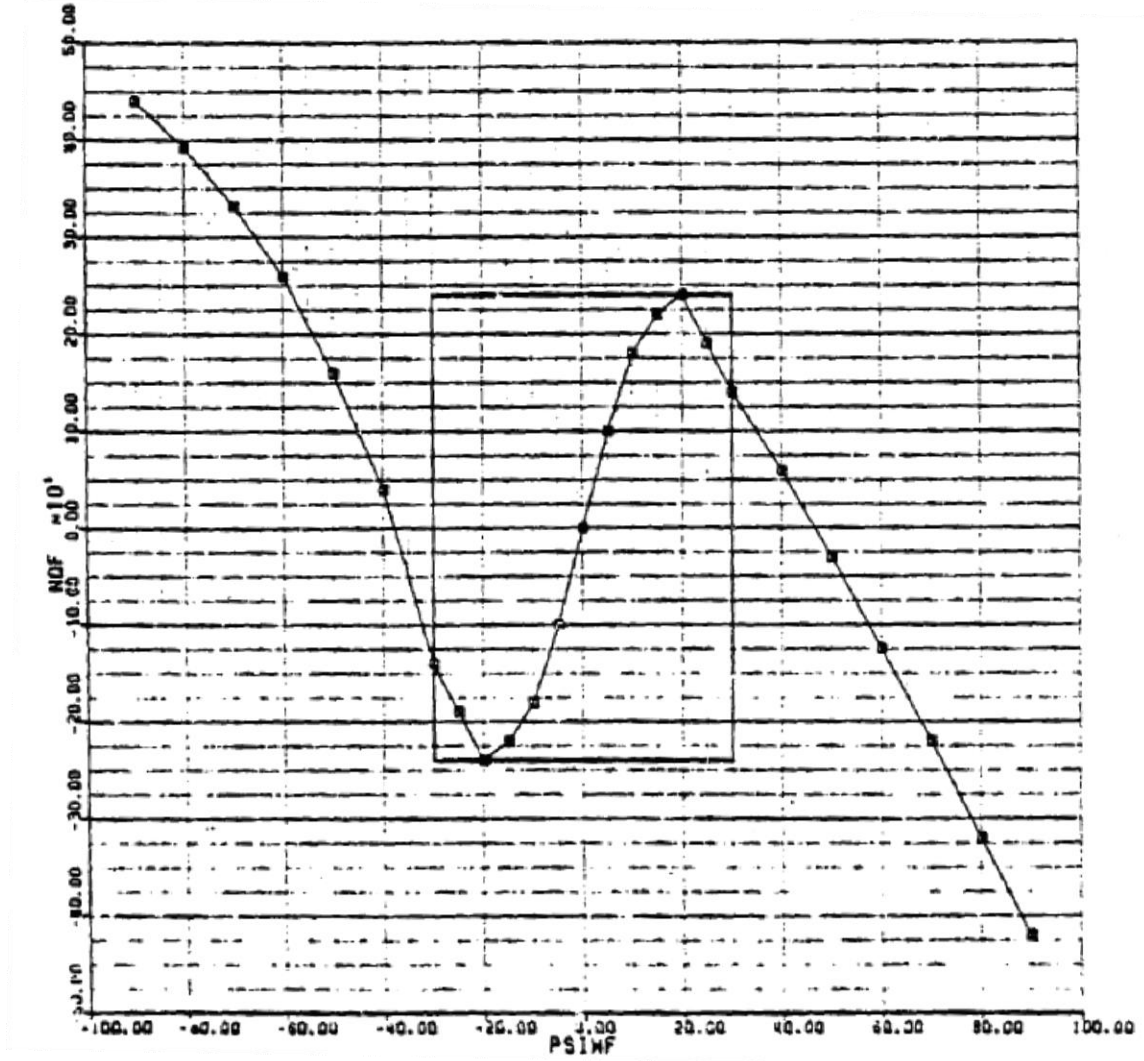


Figure A-15: Fuselage Yawing Moment Coefficient Due to Sideslip [61]

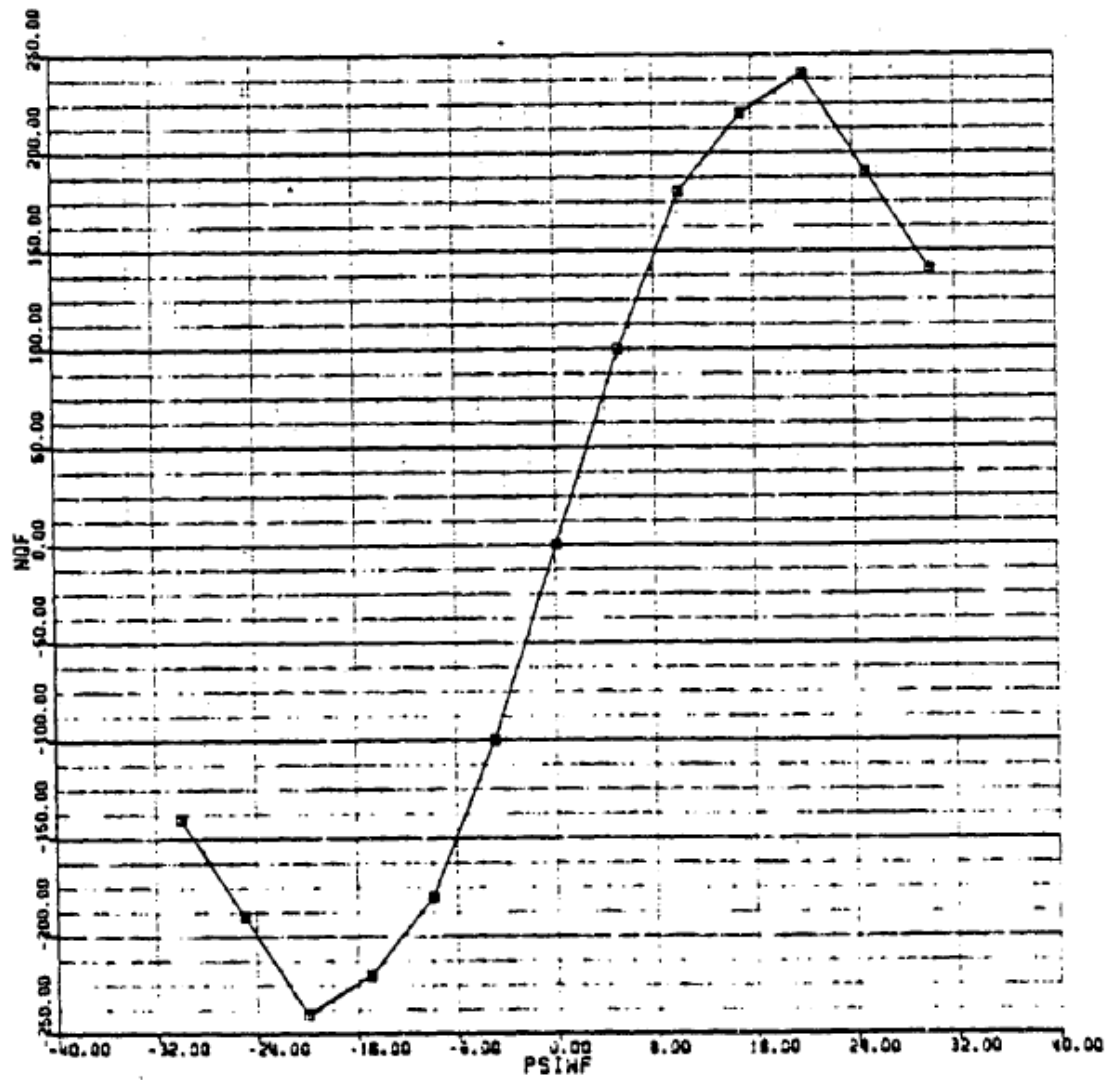


Figure A-16: Fuselage Yawing Moment Coefficient Due to Sideslip [61]

Appendix B

Figures for Lift and Drag Coefficients of the Horizontal and Vertical Tails

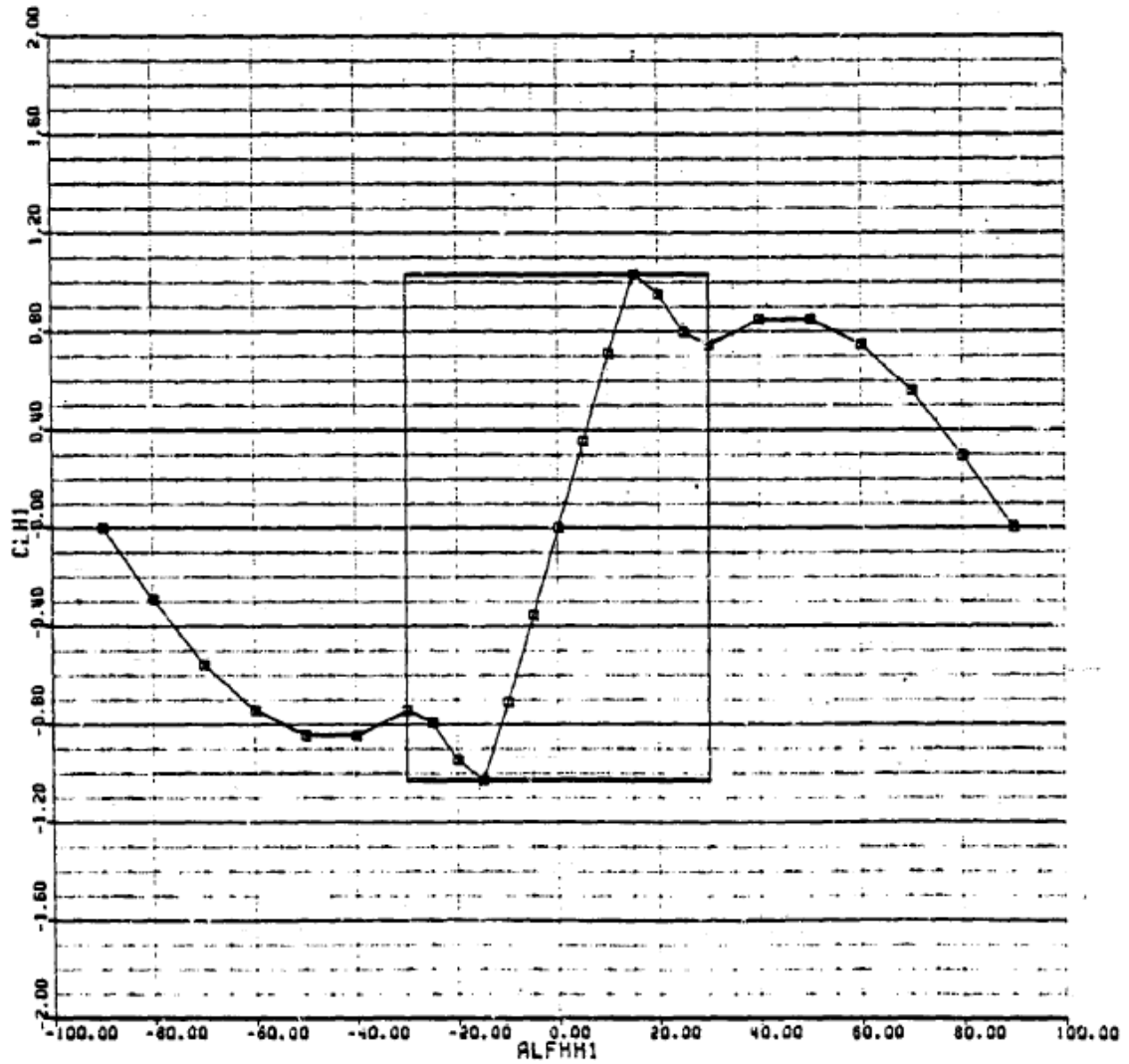


Figure B-1: Horizontal Tail Lift Coefficient Due to Angle of Attack [61]

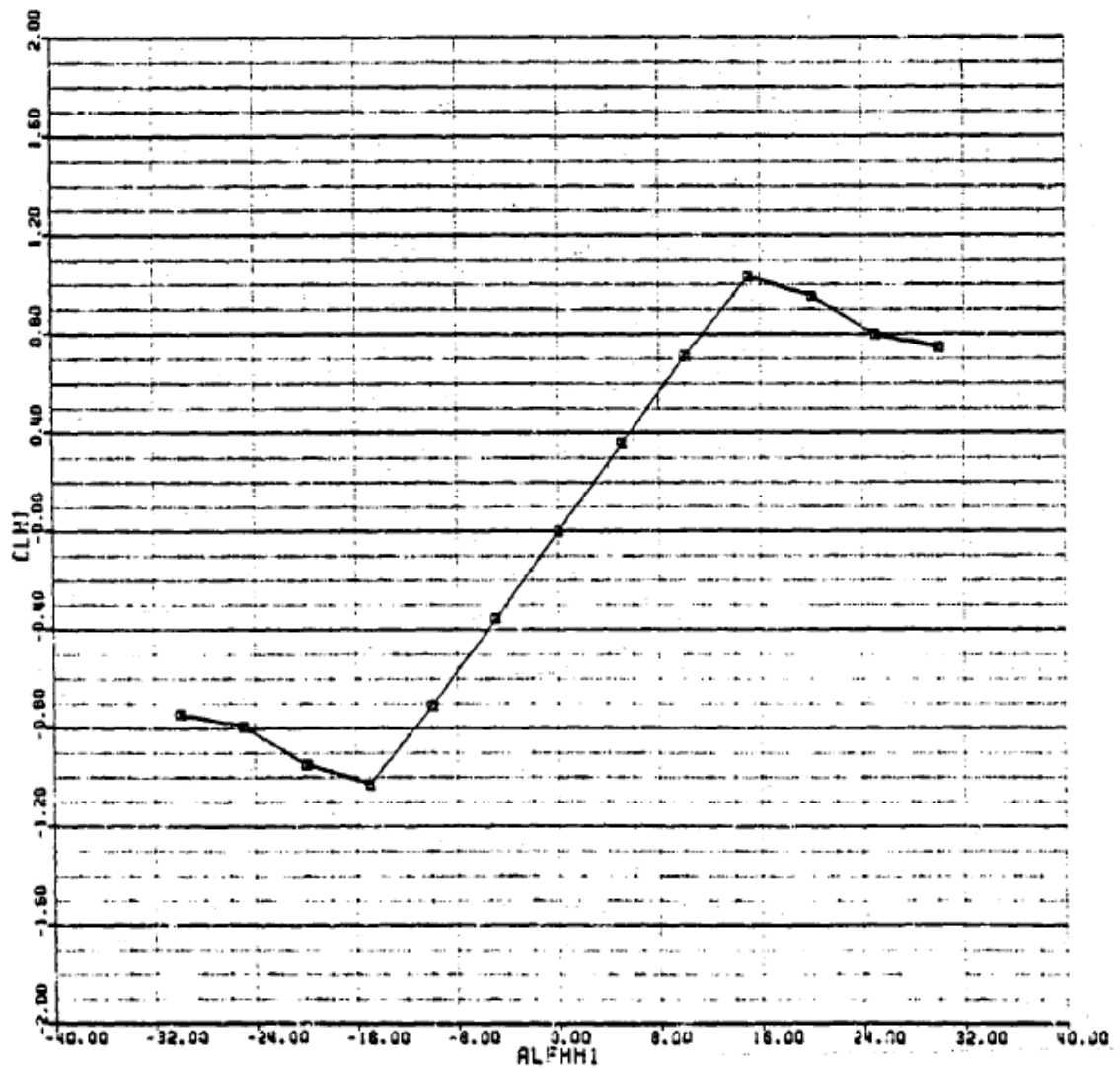


Figure B-2: Horizontal Tail Lift Coefficient Due to Angle of Attack [61]

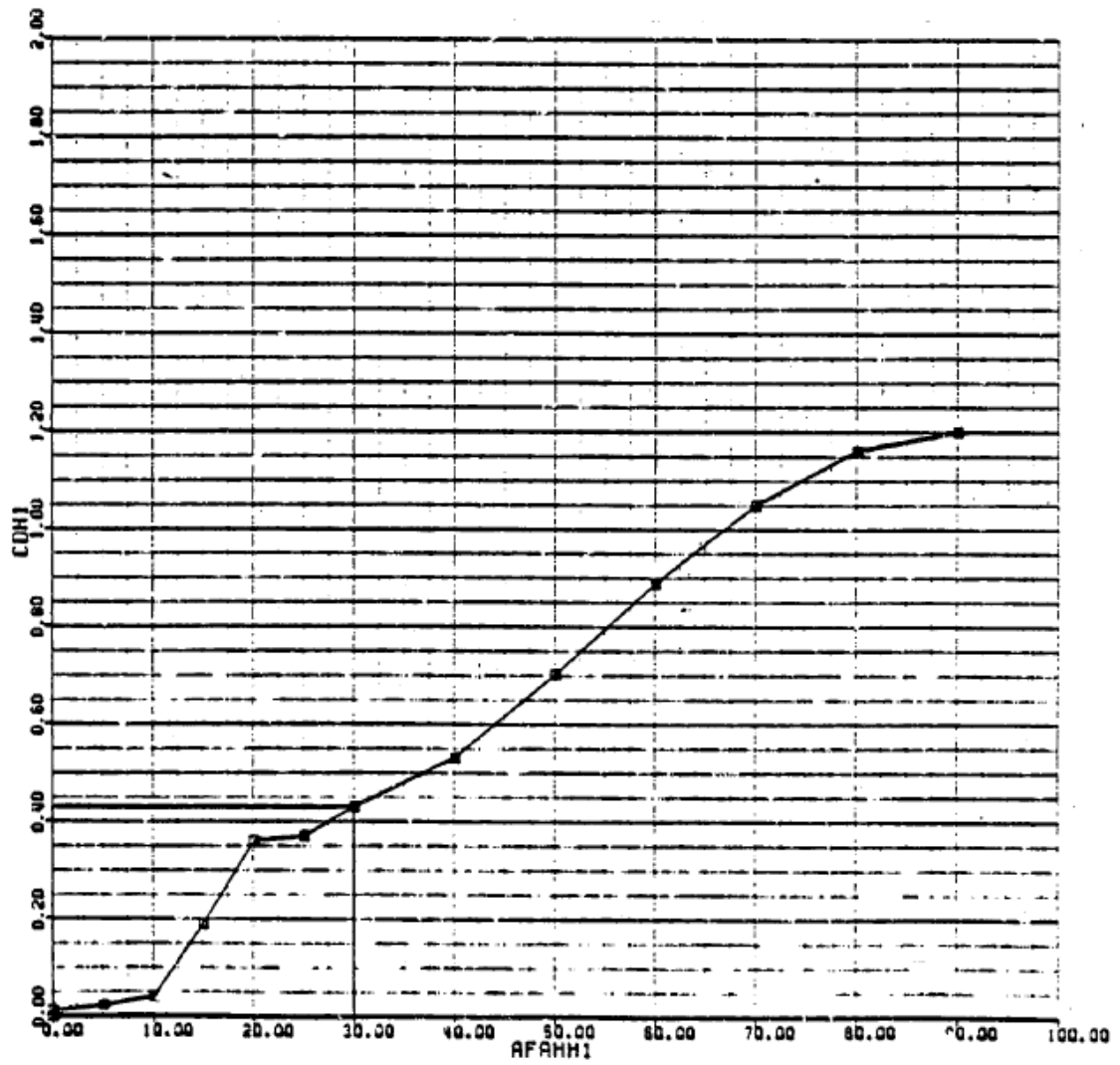


Figure B-3: Horizontal Tail Drag Coefficient Due to Angle of Attack [61]

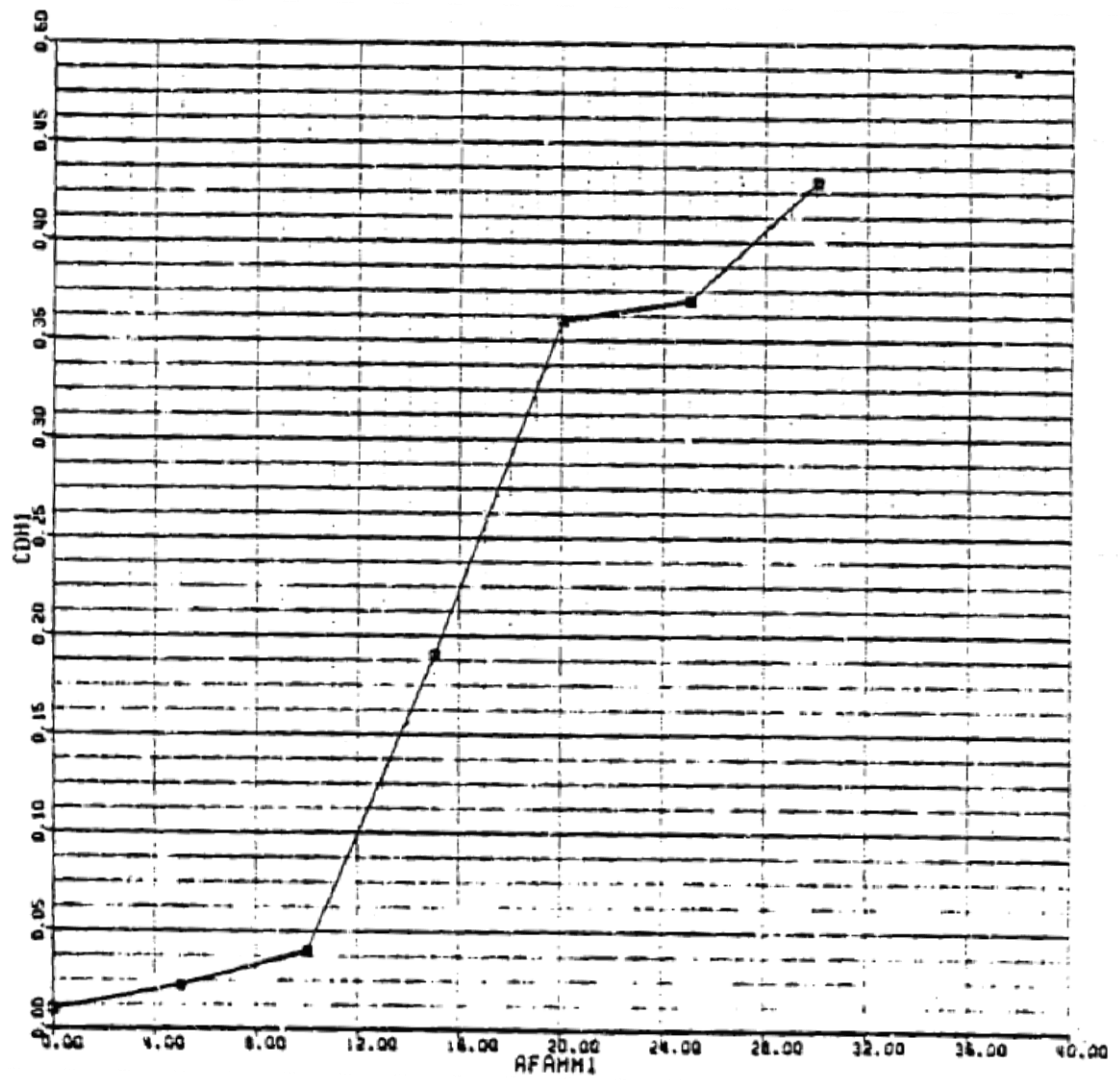


Figure B-4: Horizontal Tail Drag Coefficient Due to Angle of Attack [61]

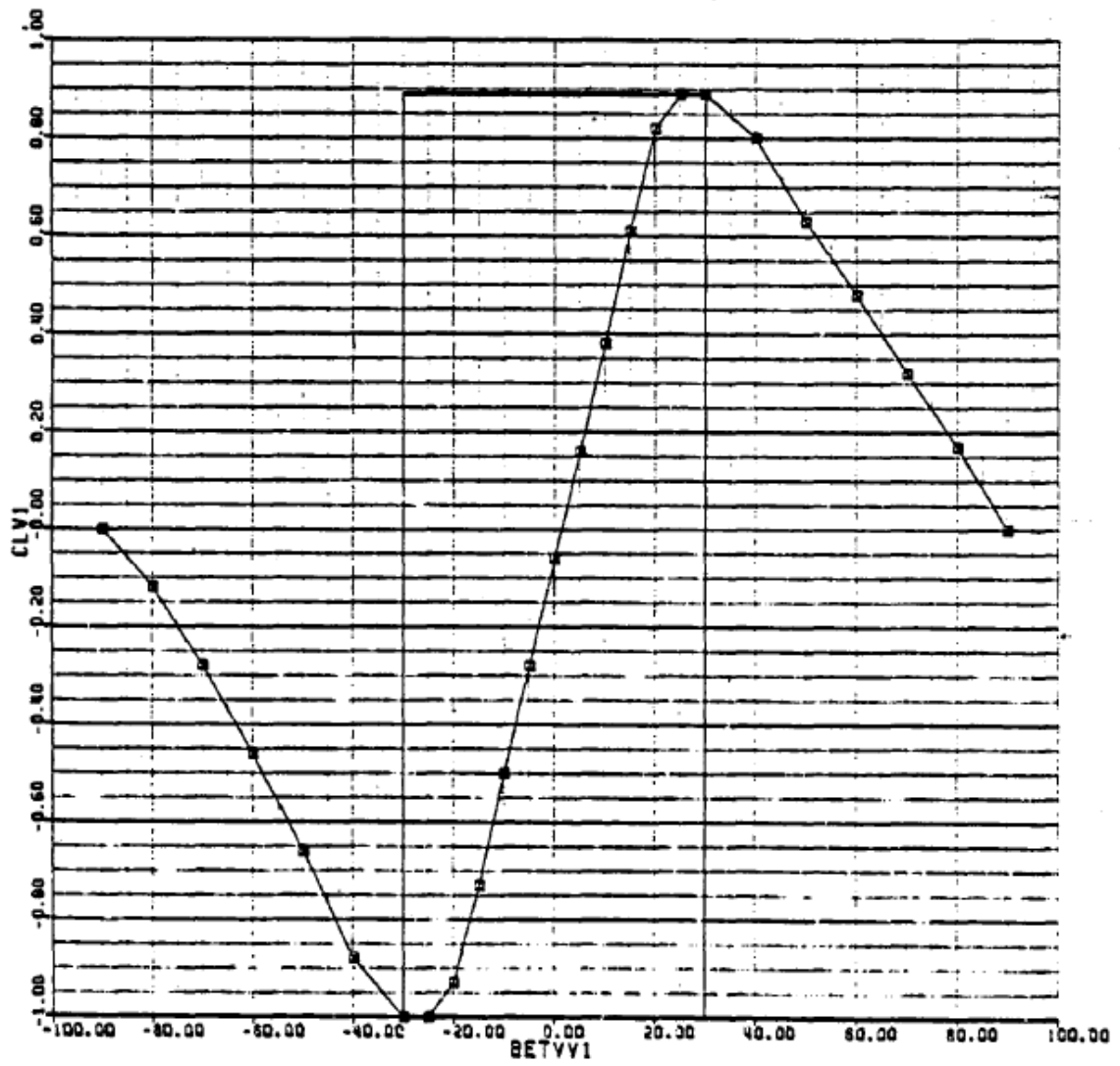


Figure B-5: Vertical Tail Lift Coefficient Due to Sideslip [61]

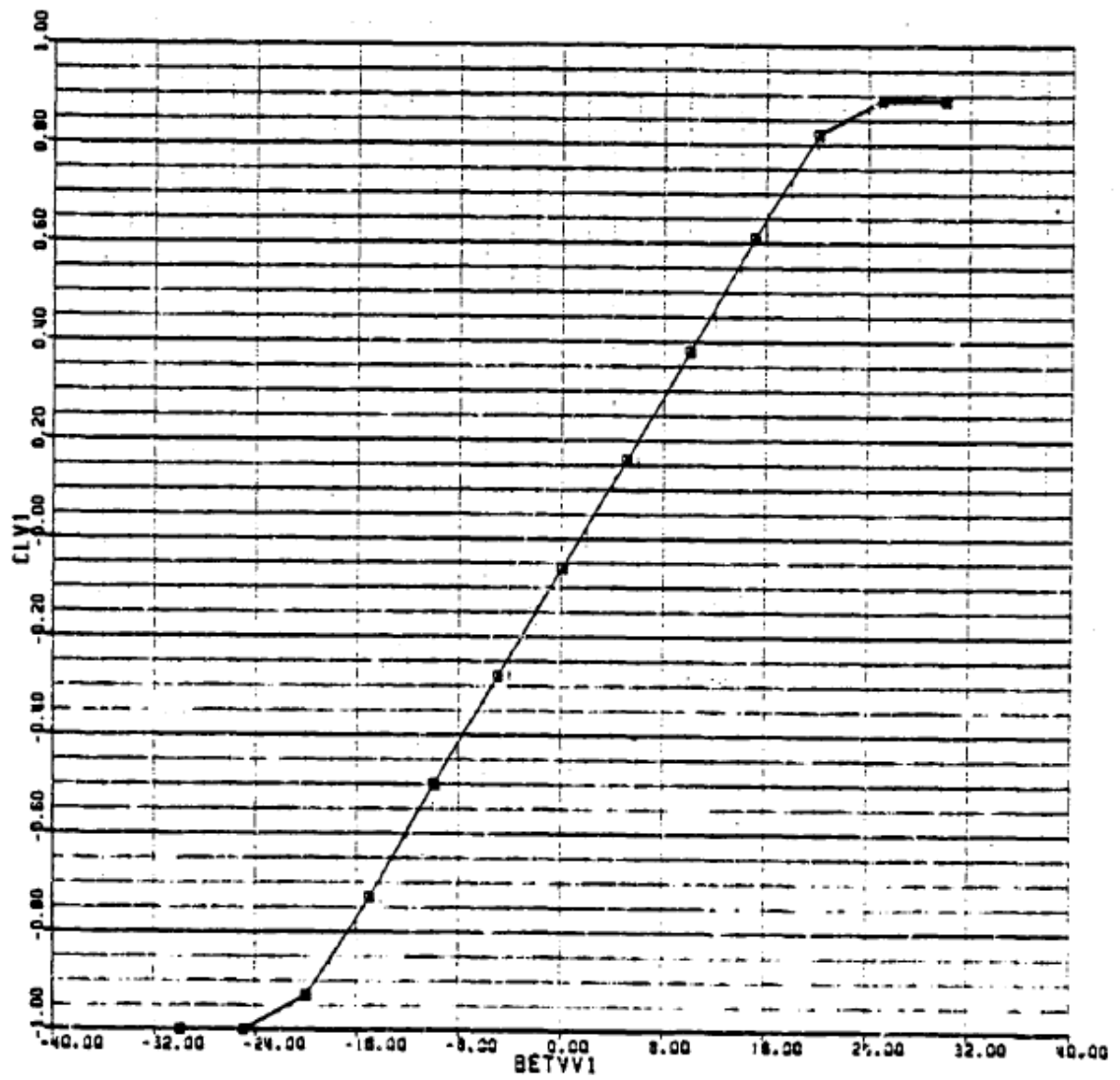


Figure B-6: Vertical Tail Lift Coefficient Due to Sideslip [61]

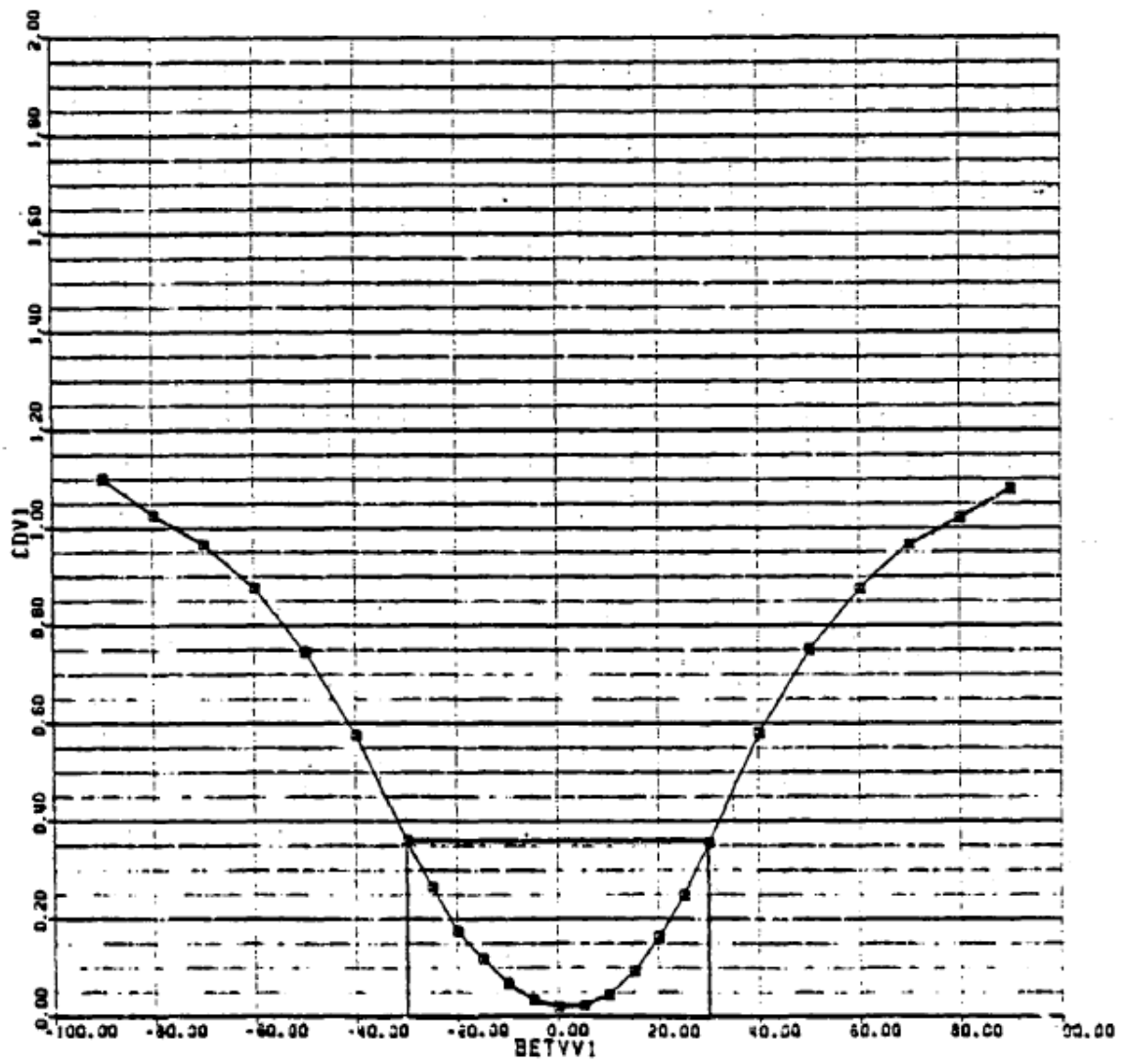


Figure B-7: Vertical Tail Drag Coefficient Due to Sideslip [61]

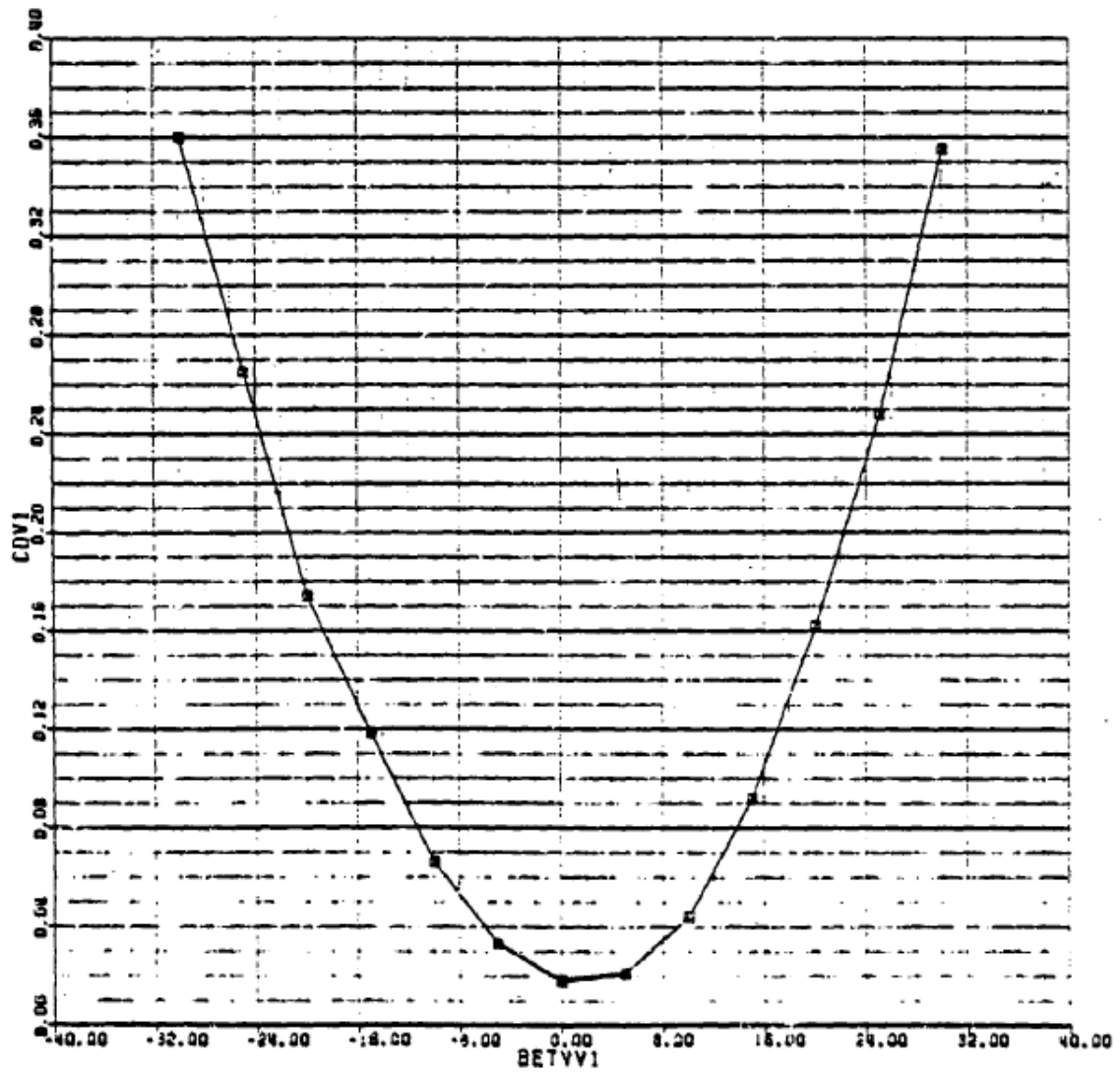


Figure B-8: Vertical Tail Drag Coefficient Due to Sideslip [61]

Appendix C

Lift, Drag and Pitching Moment Coefficients of the Wing

The 2D wing tables are developed by using XFOIL. The increments in lift, drag and pitching moment with flaps come from the NACA report of wind tunnel tests for the flaps [74].

Table C-1: Lift, Drag and Pitching Moment Coefficient of the Wing with -60° Flap Deflection

α	Cl	Cd	Cm
-180	-1.124	0.201	0.262
-170	-0.577	0.427	0.314
-160	-0.096	0.772	0.383
-150	0.261	1.197	0.465
-140	0.451	1.648	0.55
-130	0.451	2.072	0.626
-120	0.261	2.418	0.684
-110	-0.096	2.644	0.713
-100	-0.577	2.722	0.71
-90	-1.124	2.644	0.675
-80	-1.672	2.418	0.614
-70	-2.153	2.072	0.535
-60	-2.51	1.648	0.45
-50	-2.7	1.197	0.37
-40	-2.7	0.772	0.303
-35	-2.628	0.587	0.272
-30	-2.51	0.427	0.255
-25	-2.35	0.297	0.237
-20	-2.153	0.201	0.228
-18	-2.065	0.173	0.225
-16	-1.972	0.151	0.222
-14	-1.875	0.135	0.22
-12	-1.775	0.126	0.218
-10	-1.672	0.122	0.182
-8	-1.739	0.12	0.181
-6	-1.494	0.119	0.179
-4	-1.248	0.118	0.176
-2	-1.004	0.117	0.174
0	-0.77	0.118	0.173
2	-0.539	0.119	0.173
4	-0.306	0.12	0.176
6	-0.086	0.122	0.178
8	0.138	0.123	0.189
10	0.321	0.125	0.219
12	0.385	0.128	0.242
14	0.426	0.132	0.251
16	0.411	0.146	0.25
18	0.321	0.178	0.216
20	0.177	0.241	0.203
25	0.101	0.343	0.194
30	0.261	0.48	0.176
35	0.379	0.646	0.159
40	0.451	0.836	0.128
50	0.451	1.265	0.061
60	0.261	1.716	-0.019
70	-0.096	2.135	-0.104
80	-0.577	2.47	-0.183
90	-1.124	2.682	-0.244
100	-1.672	2.745	-0.279
110	-2.153	2.651	-0.282
120	-2.51	2.412	-0.252
130	-2.7	2.056	-0.195
140	-2.7	1.627	-0.119
150	-2.51	1.176	-0.034
160	-2.153	0.757	0.048
170	-1.672	0.421	0.118
180	-1.124	0.21	0.169

Table C-2: Lift, Drag and Pitching Moment Coefficient of the Wing with -45° Flap Deflection

α	Cl	Cd	Cm
-180	-0.974	0.156	0.253
-170	-0.426	0.382	0.304
-160	0.055	0.728	0.374
-150	0.412	1.152	0.456
-140	0.602	1.604	0.541
-130	0.602	2.028	0.617
-120	0.412	2.374	0.674
-110	0.055	2.599	0.703
-100	-0.426	2.678	0.7
-90	-0.974	2.599	0.666
-80	-1.521	2.374	0.605
-70	-2.002	2.028	0.526
-60	-2.359	1.604	0.441
-50	-2.549	1.152	0.36
-40	-2.549	0.728	0.293
-35	-2.477	0.542	0.262
-30	-2.359	0.382	0.246
-25	-2.199	0.252	0.227
-20	-2.002	0.156	0.218
-18	-1.914	0.128	0.215
-16	-1.821	0.106	0.213
-14	-1.725	0.091	0.21
-12	-1.624	0.081	0.209
-10	-1.521	0.078	0.172
-8	-1.588	0.076	0.172
-6	-1.343	0.074	0.169
-4	-1.098	0.073	0.167
-2	-0.853	0.073	0.165
0	-0.619	0.073	0.164
2	-0.388	0.074	0.163
4	-0.155	0.075	0.166
6	0.065	0.077	0.168
8	0.289	0.078	0.179
10	0.471	0.08	0.21
12	0.535	0.081	0.233
14	0.577	0.087	0.241
16	0.561	0.103	0.24
18	0.471	0.137	0.206
20	0.328	0.197	0.194
25	0.252	0.271	0.185
30	0.412	0.407	0.166
35	0.53	0.573	0.15
40	0.602	0.763	0.119
50	0.602	1.193	0.052
60	0.412	1.644	-0.029
70	0.055	2.062	-0.114
80	-0.426	2.398	-0.193
90	-0.974	2.61	-0.254
100	-1.521	2.673	-0.288
110	-2.002	2.579	-0.291
120	-2.359	2.34	-0.262
130	-2.549	1.984	-0.205
140	-2.549	1.554	-0.129
150	-2.359	1.103	-0.044
160	-2.002	0.685	0.038
170	-1.521	0.349	0.108
180	-0.974	0.137	0.159

Table C-3: Lift, Drag and Pitching Moment Coefficient of the Wing with -30° Flap Deflection

α	Cl	Cd	Cm
-180	-0.76	0.116	0.219
-170	-0.213	0.342	0.27
-160	0.268	0.688	0.34
-150	0.626	1.112	0.422
-140	0.816	1.564	0.507
-130	0.816	1.988	0.583
-120	0.626	2.334	0.64
-110	0.268	2.559	0.67
-100	-0.213	2.638	0.667
-90	-0.76	2.559	0.632
-80	-1.307	2.334	0.571
-70	-1.788	1.988	0.492
-60	-2.146	1.564	0.407
-50	-2.336	1.112	0.327
-40	-2.336	0.688	0.26
-35	-2.264	0.502	0.229
-30	-2.146	0.342	0.212
-25	-1.986	0.212	0.194
-20	-1.788	0.116	0.185
-18	-1.7	0.088	0.182
-16	-1.608	0.066	0.179
-14	-1.511	0.05	0.177
-12	-1.411	0.041	0.175
-10	-1.307	0.038	0.139
-8	-1.375	0.035	0.138
-6	-1.129	0.034	0.136
-4	-0.884	0.033	0.133
-2	-0.639	0.033	0.131
0	-0.405	0.033	0.13

α	Cl	Cd	Cm
2	-0.175	0.034	0.13
4	0.059	0.035	0.133
6	0.279	0.037	0.135
8	0.502	0.038	0.146
10	0.685	0.038	0.176
12	0.749	0.041	0.199
14	0.791	0.048	0.208
16	0.775	0.066	0.207
18	0.685	0.1	0.173
20	0.541	0.158	0.16
25	0.466	0.232	0.151
30	0.626	0.369	0.133
35	0.744	0.534	0.116
40	0.816	0.724	0.085
50	0.816	1.154	0.018
60	0.626	1.605	-0.062
70	0.268	2.024	-0.147
80	-0.213	2.359	-0.226
90	-0.76	2.571	-0.287
100	-1.307	2.634	-0.322
110	-1.788	2.54	-0.325
120	-2.146	2.301	-0.295
130	-2.336	1.945	-0.238
140	-2.336	1.516	-0.162
150	-2.146	1.064	-0.077
160	-1.788	0.646	0.005
170	-1.307	0.31	0.075
180	-0.76	0.098	0.126

Table C-4: Lift, Drag and Pitching Moment Coefficient of the Wing with -20° Flap Deflection

α	Cl	Cd	Cm
-180	-0.661	0.093	0.176
-170	-0.114	0.319	0.227
-160	0.367	0.664	0.297
-150	0.724	1.089	0.379
-140	0.914	1.54	0.464
-130	0.914	1.964	0.54
-120	0.724	2.31	0.597
-110	0.367	2.536	0.627
-100	-0.114	2.614	0.624
-90	-0.661	2.536	0.589
-80	-1.208	2.31	0.528
-70	-1.69	1.964	0.449
-60	-2.047	1.54	0.364
-50	-2.237	1.089	0.283
-40	-2.237	0.664	0.217
-35	-2.165	0.479	0.186
-30	-2.047	0.319	0.169
-25	-1.887	0.189	0.15
-20	-1.69	0.093	0.142
-18	-1.602	0.065	0.138
-16	-1.509	0.043	0.136
-14	-1.412	0.027	0.134
-12	-1.312	0.018	0.132
-10	-1.208	0.014	0.096
-8	-1.276	0.012	0.095
-6	-1.031	0.011	0.093
-4	-0.785	0.01	0.09
-2	-0.541	0.009	0.088
0	-0.306	0.01	0.087

α	Cl	Cd	Cm
2	-0.076	0.011	0.086
4	0.157	0.012	0.089
6	0.378	0.014	0.092
8	0.601	0.015	0.103
10	0.784	0.016	0.133
12	0.848	0.019	0.156
14	0.889	0.027	0.164
16	0.874	0.044	0.164
18	0.784	0.079	0.129
20	0.64	0.137	0.117
25	0.564	0.212	0.108
30	0.724	0.348	0.089
35	0.842	0.514	0.073
40	0.914	0.704	0.042
50	0.914	1.133	-0.025
60	0.724	1.584	-0.105
70	0.367	2.003	-0.191
80	-0.114	2.339	-0.269
90	-0.661	2.551	-0.33
100	-1.208	2.613	-0.365
110	-1.69	2.519	-0.368
120	-2.047	2.28	-0.339
130	-2.237	1.924	-0.282
140	-2.237	1.495	-0.205
150	-2.047	1.044	-0.12
160	-1.69	0.625	-0.038
170	-1.208	0.29	0.031
180	-0.661	0.078	0.083

Table C-5: Lift, Drag and Pitching Moment Coefficient of the Wing with -15° Flap Deflection

α	Cl	Cd	Cm
-180	-0.518	0.09	0.144
-170	0.029	0.316	0.196
-160	0.511	0.661	0.265
-150	0.868	1.086	0.347
-140	1.058	1.537	0.432
-130	1.058	1.961	0.508
-120	0.868	2.307	0.566
-110	0.511	2.533	0.595
-100	0.029	2.611	0.592
-90	-0.518	2.533	0.557
-80	-1.065	2.307	0.496
-70	-1.546	1.961	0.417
-60	-1.903	1.537	0.332
-50	-2.093	1.086	0.252
-40	-2.093	0.661	0.185
-35	-2.021	0.476	0.154
-30	-1.903	0.316	0.137
-25	-1.743	0.186	0.119
-20	-1.546	0.09	0.11
-18	-1.458	0.062	0.107
-16	-1.366	0.04	0.104
-14	-1.269	0.024	0.102
-12	-1.169	0.015	0.1
-10	-1.065	0.011	0.064
-8	-1.133	0.009	0.063
-6	-0.887	0.008	0.061
-4	-0.642	0.007	0.058
-2	-0.397	0.006	0.056
0	-0.163	0.007	0.055
2	0.068	0.008	0.055
4	0.301	0.009	0.058
6	0.521	0.011	0.06
8	0.744	0.012	0.071
10	0.927	0.014	0.101
12	0.991	0.018	0.124
14	1.033	0.027	0.133
16	1.017	0.044	0.132
18	0.927	0.078	0.098
20	0.783	0.136	0.085
25	0.708	0.21	0.076
30	0.868	0.347	0.058
35	0.986	0.513	0.041
40	1.058	0.703	0.01
50	1.058	1.132	-0.057
60	0.868	1.583	-0.137
70	0.511	2.002	-0.222
80	0.029	2.337	-0.301
90	-0.518	2.549	-0.362
100	-1.065	2.612	-0.397
110	-1.546	2.518	-0.4
120	-1.903	2.279	-0.37
130	-2.093	1.923	-0.313
140	-2.093	1.494	-0.237
150	-1.903	1.043	-0.152
160	-1.546	0.624	-0.07
170	-1.065	0.288	0
180	-0.518	0.077	0.051

Table C-6: Lift, Drag and Pitching Moment Coefficient of the Wing with -10° Flap Deflection

α	Cl	Cd	Cm
-180	-0.335	0.089	0.103
-170	0.212	0.315	0.154
-160	0.693	0.661	0.224
-150	1.05	1.085	0.306
-140	1.24	1.536	0.391
-130	1.24	1.961	0.467
-120	1.05	2.307	0.524
-110	0.693	2.532	0.553
-100	0.212	2.611	0.55
-90	-0.335	2.532	0.516
-80	-0.883	2.307	0.455
-70	-1.364	1.961	0.376
-60	-1.721	1.536	0.291
-50	-1.911	1.085	0.21
-40	-1.911	0.661	0.143
-35	-1.839	0.475	0.112
-30	-1.721	0.315	0.096
-25	-1.561	0.185	0.077
-20	-1.364	0.089	0.068
-18	-1.276	0.061	0.065
-16	-1.183	0.039	0.063
-14	-1.086	0.023	0.06
-12	-0.986	0.014	0.059
-10	-0.883	0.011	0.022
-8	-0.95	0.008	0.022
-6	-0.705	0.007	0.019
-4	-0.459	0.006	0.017
-2	-0.215	0.006	0.015
0	0.02	0.006	0.014
2	0.25	0.007	0.013
4	0.483	0.008	0.016
6	0.704	0.009	0.018
8	0.927	0.011	0.029
10	1.11	0.013	0.06
12	1.174	0.017	0.083
14	1.215	0.025	0.091
16	1.2	0.042	0.09
18	1.11	0.076	0.056
20	0.966	0.134	0.044
25	0.89	0.208	0.035
30	1.05	0.345	0.016
35	1.168	0.51	0
40	1.24	0.7	-0.031
50	1.24	1.13	-0.098
60	1.05	1.581	-0.179
70	0.693	2	-0.264
80	0.212	2.335	-0.343
90	-0.335	2.547	-0.404
100	-0.883	2.61	-0.438
110	-1.364	2.516	-0.441
120	-1.721	2.277	-0.412
130	-1.911	1.921	-0.355
140	-1.911	1.492	-0.279
150	-1.721	1.04	-0.194
160	-1.364	0.622	-0.112
170	-0.883	0.286	-0.042
180	-0.335	0.074	0.009

Table C-7: Lift, Drag and Pitching Moment Coefficient of the Wing with -5° Flap Deflection

α	Cl	Cd	Cm
-180	-0.154	0.089	0.056
-170	0.393	0.315	0.108
-160	0.875	0.661	0.177
-150	1.232	1.085	0.259
-140	1.422	1.536	0.344
-130	1.422	1.961	0.421
-120	1.232	2.306	0.478
-110	0.875	2.532	0.507
-100	0.393	2.611	0.504
-90	-0.154	2.532	0.469
-80	-0.701	2.306	0.408
-70	-1.182	1.961	0.33
-60	-1.54	1.536	0.244
-50	-1.73	1.085	0.164
-40	-1.73	0.661	0.097
-35	-1.657	0.475	0.066
-30	-1.54	0.315	0.05
-25	-1.38	0.185	0.031
-20	-1.182	0.089	0.022
-18	-1.094	0.061	0.019
-16	-1.002	0.039	0.016
-14	-0.905	0.023	0.014
-12	-0.805	0.014	0.012
-10	-0.701	0.011	-0.024
-8	-0.769	0.008	-0.025
-6	-0.523	0.007	-0.027
-4	-0.278	0.006	-0.03
-2	-0.033	0.006	-0.032
0	0.201	0.006	-0.033
2	0.432	0.007	-0.033
4	0.665	0.008	-0.03
6	0.885	0.01	-0.028
8	1.108	0.012	-0.017
10	1.291	0.015	0.013
12	1.355	0.018	0.036
14	1.397	0.027	0.045
16	1.381	0.043	0.044
18	1.291	0.078	0.01
20	1.147	0.136	-0.003
25	1.072	0.21	-0.011
30	1.232	0.346	-0.03
35	1.35	0.512	-0.047
40	1.422	0.702	-0.078
50	1.422	1.132	-0.144
60	1.232	1.583	-0.225
70	0.875	2.001	-0.31
80	0.393	2.337	-0.389
90	-0.154	2.549	-0.45
100	-0.701	2.612	-0.485
110	-1.182	2.518	-0.488
120	-1.54	2.279	-0.458
130	-1.73	1.923	-0.401
140	-1.73	1.493	-0.325
150	-1.54	1.042	-0.24
160	-1.182	0.624	-0.158
170	-0.701	0.288	-0.088
180	-0.154	0.076	-0.037

Table C-8: Lift, Drag and Pitching Moment Coefficient of the Wing with 0° Flap Deflection

α	Cl	Cd	Cm
-180	0	0.088	0.007
-170	0.547	0.314	0.058
-160	1.028	0.66	0.128
-150	1.386	1.084	0.21
-140	1.576	1.536	0.295
-130	1.576	1.96	0.371
-120	1.386	2.306	0.428
-110	1.028	2.532	0.457
-100	0.547	2.61	0.454
-90	0	2.532	0.42
-80	-0.547	2.306	0.359
-70	-1.028	1.96	0.28
-60	-1.386	1.536	0.195
-50	-1.576	1.084	0.114
-40	-1.576	0.66	0.047
-35	-1.504	0.474	0.016
-30	-1.386	0.314	-0.0001
-25	-1.226	0.184	-0.013
-20	-1.028	0.088	-0.028
-18	-0.94	0.06	-0.031
-16	-0.848	0.038	-0.033
-14	-0.751	0.023	-0.036
-12	-0.651	0.013	-0.037
-10	-0.547	0.01	-0.074
-8	-0.615	0.008	-0.075
-6	-0.369	0.006	-0.077
-4	-0.124	0.006	-0.079
-2	0.121	0.005	-0.081
0	0.355	0.006	-0.083
2	0.585	0.007	-0.083
4	0.819	0.007	-0.08
6	1.039	0.009	-0.078
8	1.262	0.01	-0.067
10	1.445	0.012	-0.036
12	1.509	0.016	-0.013
14	1.551	0.024	-0.005
16	1.535	0.041	-0.006
18	1.445	0.075	-0.04
20	1.301	0.133	-0.052
25	1.226	0.208	-0.067
30	1.386	0.344	-0.08
35	1.504	0.51	-0.096
40	1.576	0.7	-0.127
50	1.576	1.129	-0.194
60	1.386	1.58	-0.275
70	1.028	1.999	-0.36
80	0.547	2.334	-0.439
90	0	2.546	-0.5
100	-0.547	2.609	-0.534
110	-1.028	2.515	-0.537
120	-1.386	2.276	-0.508
130	-1.576	1.92	-0.451
140	-1.576	1.491	-0.375
150	-1.386	1.04	-0.29
160	-1.028	0.621	-0.208
170	-0.547	0.286	-0.138
180	0	0.074	-0.087

Table C-9: Lift, Drag and Pitching Moment Coefficient of the Wing with 5° Flap Deflection

α	Cl	Cd	Cm
-180	0.186	0.089	-0.036
-170	0.733	0.315	0.015
-160	1.214	0.661	0.084
-150	1.572	1.085	0.166
-140	1.762	1.536	0.251
-130	1.762	1.961	0.328
-120	1.572	2.307	0.385
-110	1.214	2.532	0.414
-100	0.733	2.611	0.411
-90	0.186	2.532	0.376
-80	-0.361	2.307	0.315
-70	-0.842	1.961	0.237
-60	-1.2	1.536	0.151
-50	-1.39	1.085	0.071
-40	-1.39	0.661	0.004
-35	-1.318	0.475	-0.027
-30	-1.2	0.315	-0.043
-25	-1.04	0.185	-0.062
-20	-0.842	0.089	-0.071
-18	-0.754	0.061	-0.074
-16	-0.662	0.039	-0.077
-14	-0.565	0.023	-0.079
-12	-0.465	0.014	-0.08
-10	-0.361	0.011	-0.117
-8	-0.429	0.008	-0.118
-6	-0.183	0.007	-0.12
-4	0.062	0.006	-0.122
-2	0.307	0.006	-0.124
0	0.541	0.007	-0.126
2	0.771	0.008	-0.126
4	1.005	0.009	-0.123
6	1.225	0.011	-0.121
8	1.448	0.012	-0.11
10	1.631	0.014	-0.08
12	1.695	0.018	-0.057
14	1.737	0.026	-0.048
16	1.721	0.043	-0.049
18	1.631	0.077	-0.083
20	1.487	0.135	-0.096
25	1.412	0.209	-0.104
30	1.572	0.346	-0.123
35	1.69	0.511	-0.14
40	1.762	0.701	-0.171
50	1.762	1.131	-0.237
60	1.572	1.582	-0.318
70	1.214	2	-0.403
80	0.733	2.336	-0.482
90	0.186	2.548	-0.543
100	-0.361	2.611	-0.578
110	-0.842	2.517	-0.58
120	-1.2	2.278	-0.551
130	-1.39	1.922	-0.494
140	-1.39	1.493	-0.418
150	-1.2	1.041	-0.333
160	-0.842	0.623	-0.251
170	-0.361	0.287	-0.181
180	0.186	0.075	-0.13

Table C-10: Lift, Drag and Pitching Moment Coefficient of the Wing with 10° Flap Deflection

α	Cl	Cd	Cm
-180	0.325	0.091	-0.075
-170	0.872	0.317	-0.024
-160	1.353	0.662	0.046
-150	1.71	1.087	0.128
-140	1.9	1.538	0.213
-130	1.9	1.962	0.289
-120	1.71	2.308	0.346
-110	1.353	2.534	0.376
-100	0.872	2.612	0.373
-90	0.325	2.534	0.338
-80	-0.223	2.308	0.277
-70	-0.704	1.962	0.198
-60	-1.061	1.538	0.113
-50	-1.251	1.087	0.032
-40	-1.251	0.662	-0.034
-35	-1.179	0.477	-0.065
-30	-1.061	0.317	-0.082
-25	-0.901	0.187	-0.101
-20	-0.704	0.091	-0.109
-18	-0.616	0.063	-0.113
-16	-0.523	0.041	-0.115
-14	-0.427	0.025	-0.117
-12	-0.326	0.016	-0.119
-10	-0.223	0.012	-0.155
-8	-0.29	0.01	-0.156
-6	-0.045	0.008	-0.158
-4	0.201	0.007	-0.161
-2	0.445	0.006	-0.163
0	0.679	0.006	-0.164

α	Cl	Cd	Cm
2	0.91	0.007	-0.165
4	1.143	0.008	-0.162
6	1.363	0.01	-0.159
8	1.587	0.01	-0.148
10	1.769	0.013	-0.118
12	1.833	0.016	-0.095
14	1.875	0.024	-0.087
16	1.86	0.041	-0.087
18	1.769	0.075	-0.122
20	1.626	0.133	-0.134
25	1.55	0.208	-0.143
30	1.71	0.344	-0.162
35	1.828	0.51	-0.178
40	1.9	0.7	-0.209
50	1.9	1.129	-0.276
60	1.71	1.581	-0.356
70	1.353	1.999	-0.442
80	0.872	2.335	-0.52
90	0.325	2.547	-0.581
100	-0.223	2.609	-0.616
110	-0.704	2.516	-0.619
120	-1.061	2.276	-0.59
130	-1.251	1.921	-0.533
140	-1.251	1.491	-0.456
150	-1.061	1.04	-0.371
160	-0.704	0.621	-0.289
170	-0.223	0.286	-0.22
180	0.325	0.074	-0.168

Table C-11: Lift, Drag and Pitching Moment Coefficient of the Wing with 15° Flap Deflection

α	Cl	Cd	Cm
-180	0.466	0.092	-0.113
-170	1.013	0.318	-0.062
-160	1.495	0.664	0.008
-150	1.852	1.088	0.09
-140	2.042	1.54	0.174
-130	2.042	1.964	0.251
-120	1.852	2.31	0.308
-110	1.495	2.536	0.337
-100	1.013	2.614	0.334
-90	0.466	2.536	0.3
-80	-0.081	2.31	0.238
-70	-0.562	1.964	0.16
-60	-0.919	1.54	0.075
-50	-1.109	1.088	-0.006
-40	-1.109	0.664	-0.073
-35	-1.037	0.478	-0.104
-30	-0.919	0.318	-0.12
-25	-0.759	0.188	-0.139
-20	-0.562	0.092	-0.148
-18	-0.474	0.064	-0.151
-16	-0.382	0.042	-0.154
-14	-0.285	0.027	-0.156
-12	-0.185	0.017	-0.157
-10	-0.081	0.014	-0.194
-8	-0.149	0.011	-0.195
-6	0.097	0.008	-0.197
-4	0.342	0.007	-0.199
-2	0.587	0.006	-0.201
0	0.821	0.007	-0.203
2	1.052	0.008	-0.203
4	1.285	0.009	-0.2
6	1.505	0.011	-0.198
8	1.728	0.012	-0.187
10	1.911	0.014	-0.157
12	1.975	0.017	-0.134
14	2.017	0.026	-0.125
16	2.001	0.042	-0.126
18	1.911	0.077	-0.16
20	1.767	0.135	-0.173
25	1.692	0.209	-0.181
30	1.852	0.345	-0.2
35	1.97	0.511	-0.217
40	2.042	0.701	-0.248
50	2.042	1.131	-0.314
60	1.852	1.582	-0.395
70	1.495	2	-0.48
80	1.013	2.336	-0.559
90	0.466	2.548	-0.62
100	-0.081	2.611	-0.654
110	-0.562	2.517	-0.657
120	-0.919	2.278	-0.628
130	-1.109	1.922	-0.571
140	-1.109	1.492	-0.495
150	-0.919	1.041	-0.41
160	-0.562	0.623	-0.328
170	-0.081	0.287	-0.258
180	0.466	0.075	-0.207

Table C-12: Lift, Drag and Pitching Moment Coefficient of the Wing with 20° Flap Deflection

α	Cl	Cd	Cm
-180	0.536	0.095	-0.133
-170	1.083	0.32	-0.082
-160	1.564	0.666	-0.012
-150	1.922	1.091	0.07
-140	2.112	1.542	0.155
-130	2.112	1.966	0.231
-120	1.922	2.312	0.288
-110	1.564	2.538	0.317
-100	1.083	2.616	0.314
-90	0.536	2.538	0.28
-80	-0.011	2.312	0.219
-70	-0.492	1.966	0.14
-60	-0.85	1.542	0.055
-50	-1.04	1.091	-0.026
-40	-1.04	0.666	-0.093
-35	-0.968	0.481	-0.124
-30	-0.85	0.32	-0.14
-25	-0.69	0.191	-0.159
-20	-0.492	0.095	-0.168
-18	-0.404	0.067	-0.171
-16	-0.312	0.045	-0.173
-14	-0.215	0.029	-0.176
-12	-0.115	0.02	-0.177
-10	-0.011	0.016	-0.214
-8	-0.079	0.014	-0.215
-6	0.167	0.013	-0.217
-4	0.412	0.012	-0.219
-2	0.657	0.012	-0.221
0	0.891	0.014	-0.223
2	1.121	0.015	-0.223
4	1.355	0.015	-0.22
6	1.575	0.017	-0.218
8	1.798	0.018	-0.207
10	1.981	0.021	-0.176
12	2.045	0.024	-0.153
14	2.087	0.032	-0.145
16	2.071	0.049	-0.146
18	1.981	0.083	-0.18
20	1.837	0.141	-0.192
25	1.762	0.216	-0.201
30	1.922	0.352	-0.22
35	2.04	0.518	-0.236
40	2.112	0.708	-0.267
50	2.112	1.137	-0.334
60	1.922	1.588	-0.415
70	1.564	2.007	-0.5
80	1.083	2.343	-0.579
90	0.536	2.554	-0.64
100	-0.011	2.617	-0.674
110	-0.492	2.523	-0.677
120	-0.85	2.284	-0.648
130	-1.04	1.928	-0.591
140	-1.04	1.499	-0.515
150	-0.85	1.048	-0.43
160	-0.492	0.629	-0.348
170	-0.011	0.294	-0.278
180	0.536	0.082	-0.227

Table C-13: Lift, Drag and Pitching Moment Coefficient of the Wing with 30° Flap Deflection

α	Cl	Cd	Cm
-180	0.67	0.117	-0.161
-170	1.217	0.343	-0.11
-160	1.698	0.689	-0.04
-150	2.055	1.113	0.042
-140	2.245	1.565	0.127
-130	2.245	1.989	0.203
-120	2.055	2.335	0.26
-110	1.698	2.561	0.29
-100	1.217	2.639	0.287
-90	0.67	2.561	0.252
-80	0.122	2.335	0.191
-70	-0.359	1.989	0.112
-60	-0.716	1.565	0.027
-50	-0.906	1.113	-0.053
-40	-0.906	0.689	-0.12
-35	-0.834	0.503	-0.151
-30	-0.716	0.343	-0.168
-25	-0.556	0.213	-0.186
-20	-0.359	0.117	-0.195
-18	-0.271	0.089	-0.198
-16	-0.178	0.067	-0.201
-14	-0.082	0.052	-0.203
-12	0.019	0.042	-0.205
-10	0.122	0.039	-0.241
-8	0.055	0.037	-0.242
-6	0.3	0.036	-0.244
-4	0.546	0.036	-0.247
-2	0.79	0.037	-0.249
0	1.024	0.037	-0.25

α	Cl	Cd	Cm
2	1.255	0.038	-0.25
4	1.488	0.039	-0.248
6	1.708	0.041	-0.245
8	1.932	0.042	-0.234
10	2.114	0.044	-0.204
12	2.178	0.048	-0.181
14	2.22	0.056	-0.173
16	2.205	0.073	-0.173
18	2.115	0.107	-0.207
20	1.971	0.165	-0.22
25	1.895	0.239	-0.229
30	2.055	0.375	-0.247
35	2.173	0.541	-0.264
40	2.245	0.731	-0.295
50	2.245	1.161	-0.362
60	2.055	1.612	-0.442
70	1.698	2.03	-0.527
80	1.217	2.366	-0.606
90	0.67	2.578	-0.667
100	0.122	2.641	-0.702
110	-0.359	2.547	-0.705
120	-0.716	2.308	-0.675
130	-0.906	1.952	-0.618
140	-0.906	1.523	-0.542
150	-0.716	1.071	-0.457
160	-0.359	0.653	-0.375
170	0.122	0.317	-0.305
180	0.67	0.105	-0.254

Table C-14: Lift, Drag and Pitching Moment Coefficient of the Wing with 45° Flap Deflection

α	Cl	Cd	Cm
-180	0.856	0.152	-0.229
-170	1.403	0.378	-0.178
-160	1.884	0.724	-0.108
-150	2.241	1.148	-0.026
-140	2.431	1.599	0.059
-130	2.431	2.024	0.135
-120	2.241	2.37	0.192
-110	1.884	2.595	0.222
-100	1.403	2.674	0.219
-90	0.856	2.595	0.184
-80	0.308	2.37	0.123
-70	-0.173	2.024	0.044
-60	-0.53	1.599	-0.041
-50	-0.72	1.148	-0.121
-40	-0.72	0.724	-0.188
-35	-0.648	0.538	-0.219
-30	-0.53	0.378	-0.236
-25	-0.37	0.248	-0.254
-20	-0.173	0.152	-0.263
-18	-0.085	0.124	-0.266
-16	0.008	0.102	-0.269
-14	0.105	0.088	-0.271
-12	0.205	0.079	-0.273
-10	0.308	0.077	-0.309
-8	0.241	0.076	-0.31
-6	0.486	0.076	-0.312
-4	0.732	0.075	-0.315
-2	0.976	0.075	-0.317
0	1.211	0.075	-0.318
2	1.441	0.076	-0.318
4	1.674	0.077	-0.316
6	1.895	0.079	-0.313
8	2.118	0.08	-0.302
10	2.301	0.082	-0.272
12	2.365	0.086	-0.249
14	2.406	0.094	-0.241
16	2.391	0.111	-0.241
18	2.301	0.145	-0.275
20	2.157	0.203	-0.288
25	2.081	0.277	-0.297
30	2.241	0.414	-0.315
35	2.359	0.579	-0.332
40	2.431	0.77	-0.363
50	2.431	1.199	-0.43
60	2.241	1.65	-0.51
70	1.884	2.069	-0.595
80	1.403	2.404	-0.674
90	0.856	2.616	-0.735
100	0.308	2.679	-0.77
110	-0.173	2.585	-0.773
120	-0.53	2.346	-0.743
130	-0.72	1.99	-0.686
140	-0.72	1.561	-0.61
150	-0.53	1.11	-0.525
160	-0.173	0.691	-0.443
170	0.308	0.355	-0.373
180	0.856	0.143	-0.322

Table C-15: Lift, Drag and Pitching Moment Coefficient of the Wing with 60° Flap Deflection

α	Cl	Cd	Cm
-180	0.961	0.195	-0.253
-170	1.508	0.421	-0.202
-160	1.989	0.767	-0.132
-150	2.346	1.191	-0.05
-140	2.536	1.643	0.035
-130	2.536	2.067	0.111
-120	2.346	2.413	0.168
-110	1.989	2.638	0.197
-100	1.508	2.717	0.194
-90	0.961	2.638	0.16
-80	0.413	2.413	0.099
-70	-0.068	2.067	0.02
-60	-0.425	1.643	-0.065
-50	-0.615	1.191	-0.146
-40	-0.615	0.767	-0.213
-35	-0.543	0.581	-0.244
-30	-0.425	0.421	-0.26
-25	-0.265	0.291	-0.279
-20	-0.068	0.195	-0.288
-18	0.02	0.169	-0.291
-16	0.113	0.149	-0.293
-14	0.209	0.135	-0.296
-12	0.31	0.127	-0.297
-10	0.413	0.126	-0.334
-8	0.346	0.124	-0.335
-6	0.591	0.123	-0.337
-4	0.837	0.122	-0.339
-2	1.081	0.121	-0.341
0	1.315	0.122	-0.343
2	1.546	0.123	-0.343
4	1.779	0.124	-0.34
6	1.999	0.126	-0.338
8	2.223	0.127	-0.327
10	2.405	0.129	-0.296
12	2.469	0.132	-0.273
14	2.511	0.141	-0.265
16	2.496	0.157	-0.266
18	2.406	0.192	-0.3
20	2.262	0.25	-0.312
25	2.186	0.324	-0.321
30	2.346	0.46	-0.34
35	2.464	0.626	-0.356
40	2.536	0.816	-0.387
50	2.536	1.246	-0.454
60	2.346	1.697	-0.535
70	1.989	2.115	-0.62
80	1.508	2.451	-0.699
90	0.961	2.663	-0.76
100	0.413	2.726	-0.794
110	-0.068	2.632	-0.797
120	-0.425	2.393	-0.768
130	-0.615	2.037	-0.711
140	-0.615	1.607	-0.635
150	-0.425	1.156	-0.55
160	-0.068	0.738	-0.468
170	0.413	0.402	-0.398
180	0.961	0.19	-0.347

Appendix D

Calculations of Thrust and Power Coefficients of the Propeller

Blade element theory was combined with Goldstein's classical vortex theory in order to create a refined model of the pusher propeller [67]. Blade element theory cannot comprehensively model a propeller, especially at low speeds. Blade stall for certain ranges of relatively high pitch inputs at low enough speeds also creates issues. Vortex Theory was introduced and incorporated into a baseline blade element model for a more accurate determination of inflow and sectional angles of attack.

To account for the helical trailing vortex system downstream of the propeller disk, the propeller inflow, λ , is iterated as a function of total induced velocity, w , and is given by equation D.1, where V_t is The total propeller induced velocity is further decomposed along the propeller blade segments into its axial, w_a , and tangential, w_t , components as shown in equations D.2 and D.3, where r is the local non-dimensional radial position, B is the number of propeller blades, Γ is the bound circulation, x is the local dimensional radial position and F is the total tip loss factor. Both components contribute to the resultant velocity, V_e , resolved along each blade segment given in equation D.4.

$$\lambda = \frac{V + w}{V_t} \quad \text{D.1}$$

$$w_a = \frac{V_t}{2} \left[\frac{-V}{V_t} + \sqrt{\left(\frac{V}{V_t}\right)^2 + 4 \frac{w_t}{V_t} \left(r - \frac{w_t}{V_t}\right)} \right] \quad \text{D.2}$$

$$w_t = \frac{B\Gamma}{4\pi x F} \quad \text{D.3}$$

$$V_e = V_t \sqrt{\left(\frac{V}{V_t} + \frac{w_a}{V_t}\right)^2 + \left(r - \frac{w_t}{V_t}\right)^2} \quad \text{D.4}$$

Both hub and tip loss correction factors are used on each blade element based on the radial position and local inflow angle to develop a total loss factor. Corrections for local angles of attack, α , based on section blade thickness, t , are also used along with a correction to camber to account for flow curvature. Each sectional angle of attack is ultimately computed using equation D.5 and then used to find the sectional lift, c_l and drag, c_d coefficients, where β is the local propeller pitch, ϕ is the local inflow angle, α_{0L} is the local zero-lift angle of attack, σ is the solidity and c is the chord.

$$\alpha = \beta - \tan^{-1}\left(\frac{w_t}{w_a}\right) - \phi - \alpha_{0L} - \frac{4}{15} \frac{\left(\frac{V}{V_t}\right) \sigma}{\left(\frac{V}{V_t}\right)^2 + r^2} \left(\frac{t}{c}\right) \quad \text{D.5}$$

The bound circulation at each radial station along the blade is computed in order to iterate on tangential induced velocity at each new value of total induced velocity. This entire process for inflow convergence is performed at a given advance ratio and propeller pitch. Calculations of the propeller thrust, C_T , and power coefficients, C_P , are based on equations D.6 and D.7 respectively, where r_s is the non-dimensional spinner radius.

$$C_T = \frac{\pi^3}{8} \int_{r_s}^1 \left\{ \left(\frac{V_e}{V_t}\right)^2 \sigma [c_l \cos(\phi + \alpha_i) - c_d \sin(\phi + \alpha_i)] \right\} dr \quad \text{D.6}$$

$$C_P = \frac{\pi^4}{8} \int_{r_s}^1 \left\{ \left(\frac{V_e}{V_t}\right)^2 \sigma [c_l \sin(\phi + \alpha_i) + c_d \cos(\phi + \alpha_i)] \right\} r dr \quad \text{D.7}$$

As far as airfoil property inputs, the model does not use a fixed Reynolds number but rather a varying local Reynolds number, including low speed corrections, at each blade segment and adjusts the stall angle of attack and zero-lift angle of attack as the Reynolds number varies. Areas of stall are modeled using quasi-steady lift and drag coefficients; there are clear and identifiable areas of blade stall that can be avoided when performing a full aircraft trim, while areas of reverse thrust at higher advance ratios and low pitch inputs are known and can be used in decelerating flight conditions.

References

- 1 Johnson, W. *Helicopter Theory*, Dover Publications, New York, NY, 1980.
- 2 Etkin, B. & Reid, L. D. *Dynamics of Flight Stability and Control*, John Wiley & Sons Inc., Hoboken, NJ, 1996.
- 3 Stevens, B. L. & Lewis, F. L., *Aircraft Control and Simulation*, John Wiley & Sons Inc., Hoboken, NJ, 2003.
- 4 Newman, Simon, "The Compound Helicopter Configuration and the Helicopter Speed Trap," *Aircraft Engineering and Aerospace Technology*, Vol. 69, No. 5, 1997, pp. 407-413.
- 5 Leishman, J. G., *Principles of Helicopter Aerodynamics*, Cambridge University Press, New York, NY, 2006.
- 6 Prouty, R. W., *Helicopter Performance, Stability and Control*, Krieger Publishing Company, Malabar, FL, 1986.
- 7 Geiger, B., "Flight Control Optimization on a Fully Compounded Helicopter with Redundant Control Effectors", M.S. Thesis, Dept. of Aerospace Engineering, The Pennsylvania State University, University Park, PA, May 2005.
- 8 Tanner, Watson H. and Berquist, Russel R., "Some Problems of Design and Operation of a 250-Knot Compound Helicopter Rotor," *Journal of Aircraft*, Vol. 1, No. 5, September, 1964, pp. 252-259.
- 9 Fradenburgh, E. A. and Segel, R. M., "Model and Full Scale Compound Helicopter Research," *Proceedings of the 21st Annual Forum of the American Helicopter Society*, Washington, D.C., May 1965, pp. 38-64.
- 10 Blackburn, W. E. "High Speed Helicopter Research with Jet Thrust Augmentation," *Proceedings of the 21st Annual Forum of the American Helicopter Society*, May 1965.
- 11 Prouty, Ray, "Induced Power-Not So Simple Part I," *Vertiflite*, Vol. 50, No. 3, Fall 2004, pp. 28-29.
- 12 Sekula, M. and Gandhi, F., "Evaluation of Vibration Reduction and Changes in Trim due to Helicopter Compounding," *Proceedings of the 57th Annual Forum of the American Helicopter Society*, Washington, D.C., May 2001, pp. 613-624.
- 13 Fenaughty, R. R. and Beno, E. A., "Airload, Blade Response, and Hub Force

- Measurements on the NH-3A Compound Helicopter," *Journal of Aircraft*, Vol. 6, No. 5, May 1969, pp. 386–392.
- 14 Spreuer, W. E., "Experimental Flight Tests of the XH-51A Compound Helicopter," *Journal of the American Helicopter Society*, Vol. 13, No. 3, July 1968, pp. 64-69.
 - 15 Wilbur, M. L. and Wilkie, W. K., "Active-Twist Rotor Control Applications for UAVs," Report from U.S. Army Research Laboratory Vehicle Technology Directorate, Hampton, VA, Dec. 2004.
 - 16 Cresap, W. L. and Van Wyckhouse, J. F., "Flight Research with Winged and Auxiliary Propulsion Compound Helicopters," *Proceedings of the 20th Annual Forum of the American Helicopter Society*, Washington, D.C., May 1964, pp. 1-10.
 - 17 Lynn, R. R., "Wing-Rotor Interactions," *Journal of Aircraft*, Vol. 3, No. 4, July 1966, pp. 326–332.
 - 18 Foulke, W. K. and Rhodes, J. E., "The XH-51A Rigid Rotor Compound Helicopter Program," *Proceedings of the 21st Annual Forum of the American Helicopter Society*, Washington, D.C. May 1965, pp. 1-8.
 - 19 Drees, J. M., "High Speed Helicopter Rotor Design," *Proceedings of the 19th Annual Forum of the American Helicopter Society*, Washington, D.C. May 1963, pp. 59-67.
 - 20 Lightfoot, R. B., et al., "VTOL – 1968," *Journal of Aircraft*, Vol. 6, No. 4, July-Aug. 1969, pp. 289-298.
 - 21 Carlson, R. M., "Possibilities of Compound Rotorcraft—Status 1968," *The Aeronautical Journal of the Royal Aeronautical Society*, Vol. 100, No. 72, Dec. 1968, pp. 1029-1044.
 - 22 Robinson, Jr. D. W., "Use of Thrust and Lift Augmentation for Increasing Helicopter Operating Speed," *31st Annual Meeting of the Institute of the Aerospace Sciences*, New York, NY Jan. 1963.
 - 23 Blackburn, W. E.; "Methods for Improving Flying Qualities of Compound Aircraft," *Journal of American Helicopter Society*, Washington, Vol. 13, No. 1, Jan. 1968, pp. 71-77.
 - 24 Segner, D. R., "XH-51A Compound Research Flight Test Program," *Canadian Aeronautics and Space Journal*, April 1967.
 - 25 Orchard, M. and Newman, S., "Some Design Issues for the Optimization of the Compound Helicopter Configuration," *Proceedings of the 56th Annual Forum of the*

- American Helicopter Society*, Virginia Beach, VA, May 2000, pp. 1357-1369.
- 26 Orchard, M. and Newman, S., "The Fundamental Configuration and Design of the Compound Helicopter," *Proceedings of the Institution of Mechanical Engineers Part G Journal of Aerospace Engineering*, Vol. 217, Dec. 2003, pp. 297–315.
 - 27 Sonneborn, W. G. O.; Hartwig, L. W., "Results of High-Speed Flight Research with the High Performance UH-1 Compound Helicopter," *Proceedings of the 27th Annual Forum of the American Helicopter Society*, Washington, D.C., May 1971, pp. 1-17.
 - 28 Balmford, D. E. H. and Benger, B. S., "The Compound Helicopter—A Concept Revisited," *Proceedings of the 17th European Rotorcraft and Powered Lift Aircraft Forum*, Berlin, Germany, Sept. 1991.
 - 29 Arcidiacono, Peter J., deSimone, Gary, and Occhiato, John J., "Preliminary Evaluation of RSRA Data Comparing Pure Helicopter, Auxiliary Propulsion and Compound Helicopter Flight Characteristics," *Journal of the American Helicopter Society*, Vol. 27, No. 1, Jan. 1982, pp. 42–51.
 - 30 Balmford, D. E. H., "Some Reflections on Trends in Rotorcraft Technology and Configurations—Into the 21st Century," *The Aeronautical Journal*, Vol. 98, No. 974, Apr. 1994, pp. 113–126.
 - 31 Orchard, M. and Newman, S., "A Generic Compound Helicopter Model," *Proceedings of the 25th European Rotorcraft Forum*, Rome, Italy, Sept. 1999.
 - 32 Fradenburgh, E. A. and Chuga, G. M., "Flight Program on the NH-3A Research Helicopter," *Journal of the American Helicopter Society*, Vol. 13, No. 1, Jan. 1968, pp. 44–62.
 - 33 Blackwell, R. and Millott, T., "Dynamics Design Characteristics of the Sikorsky X2 Technology™ Demonstrator Aircraft," *Proceedings of the 64th Annual Forum of the American Helicopter Society*, Montreal, Canada, April-May 2008.
 - 34 Bagai, A., "Aerodynamics Design of the X2 Technology Demonstrator™ Main Rotor Blade," *Proceedings of the 64th Annual Forum of the American Helicopter Society*, Montreal, Canada, April-May 2008.
 - 35 Robb, R. L. "Hybrid helicopters: Compounding the quest for speed", *Vertiflite*. Summer 2006, pp. 30-54.
 - 36 Ruddell, A. J., et al, "Advancing Blade Concept (ABC) Technology Demonstrator,"

- USAAVRADCOM-TR-81-D-5, Apr. 1981.
- 37 Coleman, C. P., "A Survey of Theoretical and Experimental Coaxial Rotor Aerodynamic Research," NASA TP-3675, Mar. 1997.
- 38 Eller, E., "X2™ Load Alleviating Controls," *Proceedings of the 68th Annual Forum of the American Helicopter Society*, Fort Worth, TX, May 2012.
- 39 Gandhi, F. and Sekula, M. K., "Helicopter Vibration Reduction using Fixed-System Auxiliary Moments," *Proceedings of the American Helicopter Society 58th Annual Forum*, Montreal, Canada, June 2002.
- 40 Gandhi, F. and Sekula, M. K., "Helicopter Vibration Reduction Using Fixed-System Auxiliary Moments," *AIAA Journal*, Vol. 42, No. 3, Mar. 2004, pp. 501-512.
- 41 Sekula, M. K. and Gandhi, F., "Effects of Auxiliary Lift and Propulsion on Helicopter Vibration Reduciton and Trim," *Journal of Aircraft*, Vol. 41, No. 3, May-June 2004, pp. 645-656.
- 42 Sekula, Martin K., "Helicopter Vibration Reduction Using Fixed-system Auxiliary Moments and Forces," Ph.D. Thesis, Dept. of Aerospace Engineering, The Pennsylvania State University, University Park, PA, May 2002.
- 43 F. N, Piasecki, A. S. Greenjack, J. F. Horn, "Compound Aircraft Control System and Method." U.S. Patent 7,438,259, Oct. 21, 2008.
- 44 Geiger, B., Horn, J.F., Greenjack, A., and Piasecki, F.W., "Trim and Maneuver Optimization Methods for Compound Rotorcraft," *Proceedings of the American Helicopter Society 60th Annual Forum*, Baltimore, MD, June, 2004.
- 45 Dominic Perry, *Flight International*, ISSN 0015-3710, 02/2012, Volume 181, Issue 5326, p. 6
- 46 Horn, J. F., Guo, W., and Ozdemir, G.T., "Use of Rotor State Feedback to Improve Closed-Loop Stability and Handling Qualities," *Proceedings of the American Helicopter Society 66th Annual Forum*, 2010.
- 47 Chen, Robert T.N., "An Exploratory Investigation of the Flight Dynamics Effects of Rotor RPM Variations and Rotor State Feedback in Hover", NASA-TM-103968, NASA Ames Research Center, Sept. 1992.
- 48 Lentine, F. P., Groth, W. P., and Oglesby, T. H. "Research in Maneuverability of the XH-51A Compound Helicopter," USAAVLABSTR-68-23, June 1968.

- 49 Ruddell, A. J., Groth, W., and McCutcheon, R., "Advancing Blade Concept (ABC) Technology Demonstrator Report," USAAVRADCOM-TR-81-D-5, Fort Eustis, VA, Apr. 1977.
- 50 Karem, A., "Hummingbird A160 and Optimum Speed Rotor (OSR)," *AHS International Specialists' Meeting - Unmanned Rotorcraft: Design, Control and Testing, Proceedings*, Phoenix, AZ, Jan. 2005, pp. 335-356.
- 51 Steiner J. and Farhan G., "An Investigation of Variable Rotor RPM on Performance and Trim", *Proceedings of the American Helicopter Society 64th Annual Forum*, Montreal, Canada, April-May 2008.
- 52 Horn, J. F. and Guo, W., "Flight Control Design for Rotorcraft with Variable Rotor Speed," *Proceedings of the American Helicopter Society 64th Annual Forum*, Montreal, Canada, April-May 2008.
- 53 Horn, J. F. and Guo, W., "Helicopter Flight Control with Variable Rotor Speed and Torque Limiting," *Proceedings of the American Helicopter Society 65th Annual Forum*, Grapevine, TX, May 2009.
- 54 Bodson, M., "Evaluation of Optimization Methods for Control Allocation," *Journal of Guidance, Control and Dynamics*, Vol. 25, No. 4, July-Aug. 2002, pp. 703-711.
- 55 Schultz, R. L. and Zagalsky, N. R., "Aircraft Performance Optimization," *Journal of Aircraft*, Vol. 9, No. 2, Feb. 1972, pp. 108-113.
- 56 G. Gilyard, "In-flight Adaptive Performance Optimization (APO) Control Using Redundant Control Effectors of an Aircraft." U.S. Patent 5,908,176, June 1, 1999.
- 57 Gilyard, G., "In-flight Transport Performance Optimization: An Experimental Flight Research Program and an Operational Scenario," *Proceedings of the AIAA/IEEE 16th Digital Avionics Systems Conference*, Irvine, CA, Oct. 1997, pp. 7.2.33-7.2.49.
- 58 Gilyard, G., "Development of a Real-Time Transport Performance Optimization Methodolgy", NASA-TM-4730, NASA Dryden Flight Research Center, Jan. 1996.
- 59 Gilyard, G., "Flight Test of an Adaptive Configuration Optimization System for Transport Aircraft", NASA-TM-1999-206569, NASA Dryden Flight Research Center, Jan. 1999.
- 60 Horn, J. F., Bridges, D. O., Lopes, L. V., and Brentner, K. S., "Development of a Low-Cost, Multi-Disciplinary Rotorcraft Simulation Facility." *Journal of Aerospace Computing, Information and Communication*, Vol. 2, No. 7, July 2005, pp. 267-284.

- 61 Howlett, J., UH-60A BLACK HAWK Engineering Simulation Program: Volume I – Mathematical Model, NASA CR-166309, Dec. 1981.
- 62 Swartzwelder, Matthew A., “Trim and Control Optimization of a Compound Helicopter Model”, M.S. Thesis, Dept. of Aerospace Engineering, The Pennsylvania State University, University Park, PA, Aug. 2003.
- 63 Guo, Wei, “Flight Control Design for Rotorcraft with Variable Rotor Speed”, Ph.D. Thesis, Dept. of Aerospace Engineering, The Pennsylvania State University, University Park, PA, Dec. 2009.
- 64 Ballin, M., “A High Fidelity Real-Time Simulation of a Small Turboshaft Engine”, NASA TM-100991, July 1988.
- 65 Moodie, Yeo, “Design of a Cruise Efficient Compound Helicopter.” *Proceedings of the American Helicopter Society 67th Annual Forum*, Virginia Beach, Virginia, May 3 - 5, 2011.
- 66 Thorsen, A., Horn, J.F., Ozdemir, G.T., “Optimizing Control of a Compound Rotorcraft in Quasi-Steady Maneuvers,” *Proceedings of the Fifth Decennial American Helicopter Society Aeromechanics Specialists’ Conference*, San Francisco, CA, Jan, 22-24, 2013.
- 67 McCormick, “Aerodynamics, Aeronautics, and Flight Mechanics.” John Wiley & Sons Inc., 1994
- 68 Theodorsen, Stickle, Brevoort, “Report No. 594: Characteristics of Six Propellers including the High Speed Range.” NACA-TR-594, 1937.
- 69 Padfield, Gareth D., *Helicopter Flight Dynamics: The Theory and Application of Flying Qualities and Simulation Modeling*, American Institutes of Aeronautics and Astronautics, Inc., Blackburn, VA, 1996.
- 70 Ormiston, R.A., “Rotor Aerodynamic Characteristics at High Advance Ratio Relevant to Compound Rotorcraft,” *Proceedings of the American Helicopter Society San Francisco Chapter Future Vertical Lift Aircraft Design Conference*, San Francisco, CA, Jan. 18-20, 2012.
- 71 Horn, J.F., Calise, A.J., Prasad, J.V.R. and O’Rourke, M., “Flight Envelope Cueing on a Tilt-Rotor Aircraft Using Neural Network Limit Prediction,” *Proceedings of the American Helicopter Society 54th Annual Forum*, Washington, DC, May 1998.
- 72 Johnson, J., Bender, G.L., McClellan, R.D., Burden, J.R., Larsen, M.E., “Attack Helicopter

- Evaluation AH-56A Cheyenne Compound Helicopter”, AD-771 914, US Army Aviation Systems Test Activity, Edwards Air Force Base, CA, June, 1972.
- 73 Dominick Jr., F.L., Bender, G.L., McClellan, R.D., Hall, G.C., Stringer, P.G., Buss, M.W., “Army Preliminary Evaluation I and Research and Development Acceptance Test I AH-56A Cheyenne Compound Helicopter”, AD-905 910, US Army Aviation Systems Test Activity, Edwards Air Force Base, CA, Mar., 1972.
- 74 Abbott, I.H., Greenberg, H., “Tests in the Variable-Density Wind Tunnel of the N.A.C.A. 23012 Airfoil with Plain and Split Flaps”, Report No. 661, Langley Memorial Aeronautical Laboratory, National Advisory Committee for Aeronautics, Langley Field, VA, Jan. 21, 1938.

VITA

Gurbuz Taha Ozdemir

Gurbuz Taha Ozdemir was born in 1987 in Ankara, Turkey. He obtained a Bachelor of Science degree in Aerospace Engineering in 2008 at Middle East Technical University at Ankara, Turkey. In 2008 he joined the Pennsylvania State University Aerospace Engineering department Vertical Lift Research Center of Excellence and obtained a Master of Science degree in Aerospace Engineering in 2010 under the supervision of Associated Professor Joe Horn. His M.Sc. work was on control of ducted fan air vehicle using redundant controls. Continuing in the same department, he pursued a Ph.D. degree in Aerospace Engineering. His Ph.D. work is on control of compound rotorcraft using redundant controls with in-flight performance optimization under the supervision of Associated Professor Joe Horn. He is a member of the American Helicopter Society and the American Institute of Aeronautics and Astronautics.